THE UNIVERSITY
of EDINBURGH

Motor Neuron Degeneration and Compensatory Sprouting in Mouse Models of Spinal Muscular Atrophy

Natalie Louise Courtney

A thesis submitted for the degree of PhD
The University of Edinburgh

2018

Declaration

I declare that the work presented in this thesis is entirely my own, unless otherwise stated in the text, and has not been submitted for any other degree or qualification.

Natalie L Courtney

Acknowledgements

There are many people that I'd like to acknowledge, for their help and support throughout my PhD.

Firstly, and most importantly, my supervisor Lyndsay Murray. I will never be able to find the words that appropriately describe how thankful I am for all of your help, support, guidance and time. Your encouragement has been invaluable and I thank you for being so patient and understanding. It is thanks to you that I continued in science and have genuinely enjoyed this PhD journey. You are an incredible teacher and a true role model.

Thank you also to my thesis committee; Tom Gillingwater and Mandy Jackson. Your help, advice and guidance over the course of my PhD has been very much appreciated.

Thank you to all of the past and present Murray lab members. Notably, Rachel Kline, Alannah Mole, Roxanna Munir and Ali Thomson. Thank you to you all for supporting and encouraging me, both professionally and personally. Specifically, thanks to Alannah for your help with the work on motor neuron pathology and to Roxanna for your help with the work on motor neuron sprouting. Thank you also to Shilpa Purushotham, for your help with looking at the effect of YFP on motor neuron pathology.

Thank you to all of the members of the Gillingwater and Paxton Labs, both past and present. Notably, thanks to Ewout Groen and Hannah Shorrock; you both played a huge part in my time at the University of Edinburgh and supported me from day one.

Thank you also to Yvonne Clarkson for your support, mentoring and advice. You really have kept me sane!

Thank you also to Viv Allison and Louise Dunn in the Histology Department of the Hugh Robson Building (HRB), Anisha of the Impact facility and the stores department of the HRB. In addition, thanks to the BRR facilities at both the HRB and Western General Hospital (WGH). Especially, John and Vicky, who helped me immensely with the P53 colony.

Of course, none of this would have been possible without the studentship provided by the Euan MacDonald Centre for Motor Neurone Disease Research. This is an incredible organisation that I am proud to be a part of and will always do my best to represent in such a way that it deserves.

Last but not at all least, thank you to all of my friends and family.

Thank you to my flatmate, Catriona MacLean, for helping me through the hard times but also for helping me celebrate the good times.

Thank you to Rachael Reid. I sometimes wonder how I ended up in the position I am now, but then I remember that it was you that told me of an opportunity at the University of Edinburgh that I might be interested in – so really, for all of this, I have to you to thank.

Thank you to my Mum and Dad, and to my brother Ross. I am so grateful to have such a loving family around me. Mum and Dad, you have given me the opportunity to fulfil my dreams and you have supported me every step of the way. I honestly cannot ever thank you enough.

Hamish, thank you for proof reading this thesis, for reminding me that I can do it, for making me dinner and for being unbelievably patient. I really do feel so lucky to have met you – here's to more beer and pizza!

Abstract

Spinal muscular atrophy (SMA) is a childhood onset form of motor neuron disease. It is characterised by the degeneration and loss of lower motor neurons with subsequent muscle weakness and atrophy. It has long been assumed that these motor neurons degenerate in a distal to proximal manner, with the neuromuscular junction (NMJ) being an early pathological target. However, it is unknown how the onset of pathology at the distal portion of the motor neuron (the NMJ) relates to the onset of pathology at the proximal portion of the motor neuron (motor neuron cell body (MNCB)). Therefore, the timing of the onset of NMJ and MNCB pathology, in the *Smn*$^{2B/-}$ mouse model of SMA, is addressed within this thesis. The results show that NMJ pathology begins between P5 and P7 in *Smn*$^{2B/-}$ mice and MNCB morphology is altered in *Smn*$^{2B/-}$ mice between P10 and P15. Furthermore, the up-regulation of transcripts involved in the P53 signaling pathway is shown to coincide with the onset of NMJ pathology. Therefore whether NMJ pathology is the cause or a consequence P53 activation is subsequently investigated. By using an inducible P53 knock down *Smn*$^{2B/-}$ mouse model, it is shown that reducing P53 in *Smn*$^{2B/-}$ mice can decrease denervation.

In this thesis, the possibility that the degeneration of motor neurons induces remaining motor neurons to sprout and whether it is this compensatory sprouting that allows certain muscles and mice to remain apparently 'resistant' to reduced Smn levels is also addressed. In mouse models and patients of SMA, some muscles are relatively spared, with lower levels of denervation even at late stages of disease. It is hypothesised that these 'resistant' muscles have increased motor neuron sprouting that compensates for ongoing denervation. To address this, degeneration and regeneration was quantified in resistant and vulnerable muscles in *Smn*$^{2B/-}$ mice as well as mouse models that have reduced Smn but are asymptomatic. The pathology of individual motor units was also assessed to determine whether there are

compensatory populations of motor units. Furthermore, degeneration and regeneration in mouse models that have reduced Smn but are asymptomatic was quantified. In both of these cases, it was found that sprouting is not compensating for denervation in these ‘resistant’ muscles and mice, suggesting that these NMJs remain stable.

Overall, these results provide an important insight into the pattern of motor neuron degeneration and remodeling in SMA and therefore provide significant contribution to the SMA research field.

Lay Summary

Motor neurons are long cells that connect the spinal cord to muscles and instruct muscles to contract. They have a cell body that lies within the spinal cord, a long axon that stretches from the spinal cord to the muscles and a neuromuscular junction (NMJ), which is where the motor neuron connects with the muscle. In motor neuron diseases, like spinal muscular atrophy (SMA), motor neurons breakdown, or degenerate. This means that there is a loss of the connections between motor neurons and muscles and as a result, muscles are no longer able to contract as efficiently. Patients experience muscle weakness and ultimately paralysis. It has long been assumed that, in SMA, motor neurons degenerate by withdrawing away from the muscle, as the NMJ is thought to be the first part of the motor neuron to breakdown. However, the relationship between the degeneration of the NMJ and the degeneration of the cell body is actually unknown. Therefore, in this thesis, degeneration at both the cell body and the NMJ is investigated, in a mouse model of SMA, to try and determine where exactly degeneration begins. In addition, work is performed to try and determine the relationship between motor neuron degeneration and the turning on of a 'switch' that is known to cause cells to die.

Further to this, not all muscles in SMA are equally affected by the degeneration and withdrawal of motor neurons. While some 'vulnerable' muscles are severely affected, others are 'resistant' and appear to be relatively unaffected. In this thesis, it is suggested that in 'resistant' muscles motor neurons that have not broken down grow new branches to make up for the motor neurons that have been lost. This process of growing new branches is called compensatory sprouting. Therefore whether compensatory sprouting is occurring in resistant muscles in a mouse model of SMA is investigated.

Table of Contents

List of Abbreviations

μm	Micrometer
AAL	Abductor Auris Longus
AAV	Adeno-associated virus
AChR	Acetylcholine Receptor
ALS	Amyotrophic Lateral Sclerosis
AS	Auricularis Superior
ASO	Antisense Oligonucleotide
BSA	Bovine Serum Albumin
BTX	Bungarotoxin
ChAT	Choline Acetyltransferase
CNS	Central nervous system
CSF	Cerebrospinal fluid
EO	External Oblique
ESE	Exon Splicing Enhancer
g	Grams
(p)H2AX	(phosphorylated) H2A histone family member X
LAL(c/r)	Levator Auris Longus (caudal/rostral bands)
mg	Milligram
mM	Microgram
MNCB	Motor neuron cell body
MND	Motor Neuron Disease
mRBP	mRNA binding proteins
mRNA	messenger RNA
NF(A)	Neurofilament (Accumulation)
NMJ	Neuromuscular Junction
P	Postnatal (i.e. Postnatal Day 5 = P5)
PBS	Phosphate Buffered Saline
PCR	Polymerase Chain Reaction
PFA	Paraformaldehyde

PLS	Primary Lateral Sclerosis
qPCR	Quantitative Reverse Transcription Polymerase Chain Reaction
RA	Rectus Abdominis
SMA	Spinal Muscular Atrophy
SMARD	Spinal Muscular Atrophy with Respiratory Distress
SMN/ Smn	Survival Motor Neuron gene (italisised) (HUMAN/ Murine)
SMN/ Smn	Survival Motor Neuron protein (HUMAN/ Murine)
snRNPs	small nuclear ribonuclear proteins
TA	Turn Around (test)
TMX	Tamoxifen
TS	Triangularis Sterni
TtR	Time to right (test)
TVA	Transverse Abdominis
WT	Wild Type
YFP	Yellow Fluorescent Protein

List of Figures

Chapter 1

Chapter 2

Chapter 3

3.1 Phenotypic analysis of the *Smn*$^{2B/-}$ mouse model of SMA shows that it becomes significantly different from control littermates around P9 to P10.

3.2 Representative images of NMJs in the TVA muscle of *Smn*$^{2B/-}$ and *Smn*$^{2B/+}$ mice displaying features of NMJ pathology.

3.3 There is significant pathology in the TVA muscle in *Smn*$^{2B/-}$ mice from P10.

3.4 At P7, there is significantly more pre-synaptic swelling at the NMJs in the TVA muscle of *Smn*$^{2B/-}$ mice compared to *Smn*$^{2B/+}$ mice.

3.5 Analysis of NMJs in the Rectus Abdominis (RA) muscle of *Smn*$^{2B/-}$ mice confirms that there is no pre-synaptic pathology observed at P5.

3.6 There is a loss of MNCBs in *Smn*$^{2B/-}$ mice between P10 and P15.

3.7 There is a significant difference in the area of MNCBs in *Smn*$^{2B/-}$ mice compared to controls at P15.

3.8 There is an increase in the percentage of activated caspase-3 positive cells in the ventral horn of the thoracic spinal cord of *Smn*$^{2B/-}$ mice at P15.

3.9 There is a significant increase in the expression of transcripts involved in the P53 signalling pathway in the spinal cords of *Smn*$^{2B/-}$ mice compared to controls at P7.

3.10 Derivation process to obtain experimental *Smn*$^{2B/-}$*;P53*$^{fl/fl}$*;Cre*$^{+}$ mice and control littermates.

3.11 Copy number genotyping separates *P53*$^{fl/+}$ mice and the desired *P53*$^{fl/fl}$ mice.

3.12 Reduction of P53 was confirmed using qPCR on spinal cord cDNA.

3.13 Reducing P53 does not improve the phenotype of *Smn*$^{2B/-}$ mice.

3.14 A reduction in P53 reduces denervation in the TVA of *Smn*$^{2B/-}$ mice.

3.15 A reduction in P53 in control *Smn*$^{2B/+}$ mice does not alter NMJ morphology.

3.16 Reducing P53 in *Smn*$^{2B/-}$ and *Smn*$^{2B/+}$ mice does not alter the

morphology of MNCBs in the ventral horn of their spinal cord.

3.17 Reducing P53 does not alter the number or size of MNCBs in the ventral horn of the thoracic spinal cord.

3.18 Reducing P53 does not alter the overall regulation of transcripts that are downstream of P53 in the P53 signalling pathway.

Chapter 4

4.1 Motor neurons sprouting can take to form of either terminal or nodal sprouting.

4.2 There are different suggestions for how compensatory sprouting of motor neurons could occur following denervation in MNDs.

4.3 The *YFP-H* transgene was crossed onto mouse models that express various levels of Smn protein.

4.4 A high number of YFP expressing axons entering a muscle means individual axonal inputs are untraceable.

4.5 Carrying the *YFP-H* transgene does not affect the severity of NFA in the $Smn^{2B/-}$ mouse model of SMA at P18.

4.6 Expressing YFP does not have an adverse effect on the NMJ, in terms of NFA, in $Smn^{2B/-}$ mice at P18.

4.7 Expressing YFP does increase the levels of pH2AX in motor neurons from $Smn^{2B/-}$ mice at P18.

4.8 The TS muscle of $Smn^{2B/-}$ mice exhibits significant denervation and pre-synaptic swelling when compared to $Smn^{2B/+}$ controls.

4.9 The LALr muscle of $Smn^{2B/-}$ mice exhibits increased pre-synaptic swelling but shows no significant denervation compared to controls

4.10 The TS muscle displays significantly more pathology than the LALr muscle in P18 $Smn^{2B/-}$ mice

4.11 There is no significant difference in sprouting between the TS and LALr muscles in P18 $Smn^{2B/-}$ mice

4.12 YFP allows individual motor neurons to be traced.

4.13 Features of denervation were visible using YFP expression in motor

neurons

4.14 Denervation was visible in 50% of LALr motor units analysed in *Smn$^{2B/-}$;YFP-H* mice.

4.15 Pre-synaptic swelling can be observed in motor neurons expressing YFP.

4.16 Pre-synaptic swelling severity is not synchronous within motor units of *Smn$^{2B/-}$;YFP-H* mice.

4.17 The area of post-synaptic endplates varies throughout a motor units of *Smn$^{2B/-}$;YFP-H* mice.

4.18 Endplate maturation varies within motor units of *Smn$^{2B/-}$;YFP-H* mice.

4.19 Sprouting can be observed in motor neurons expressing YFP.

4.20 Sprouting appears to be motor neuron dependent in *Smn$^{2B/-}$;YFP-H* mice.

Chapter 5

5.1 There is no significant difference in the number of MNCBs in *Smn$^{+/-}$* mice compared to *Smn$^{+/+}$* mice at 1 year old.

5.2 There is no significant degenerative or regenerative NMJ phenotype observed in *Smn$^{+/-}$* mice at 1 year old.

5.3 YFP positive NMJs of *Smn$^{+/-}$* mice were examined for morphological alterations.

5.4 There is no significant degenerative or regenerative phenotype in the LALr muscle of *Smn$^{+/-}$* mice at 1 year old compared to age matched *Smn$^{+/+}$* controls.

5.5 There is no significant difference in the number of MNCBs in *Smn$^{2B/2B}$* mice compared to *Smn$^{+/+}$* mice at 3 months old.

5.6 There is no significant degenerative or regenerative NMJ phenotype observed in *Smn$^{2B/2B}$* mice.

5.7 There is no significant degenerative or regenerative phenotype in the LALr muscle of *Smn$^{2B/2B}$* mice at 3 months old compared to age matched *Smn$^{+/+}$* controls.

5.8 There is no significant degenerative or regenerative phenotype in the TS muscle of *Smn*$^{2B/2B}$ mice at 3 months old compared to age matched *Smn*$^{+/+}$ controls.

List of Tables

Chapter 2

Chapter 4

Chapter 1

General Introduction

Motor neuron disease (MND) is an umbrella term that incorporates a variety of different disorders, all of which are caused by the degeneration of motor neurons within the brain and spinal cord. Upper motor neurons carry signals from the motor cortex to the brainstem or ventral horn of the spinal cord and lower motor neurons receive these signals from the upper motor neurons and carry them to the muscle where they elicit a contraction (Figure 1.1). The most common MND is Amyotrophic Lateral Sclerosis (ALS) (James & Talbot 2006). The terms ALS and MND are often used interchangeably, however, there are other types of MND, including Primary Lateral Sclerosis (PLS) and Spinal Muscular Atrophy (SMA). One of the differences between these three MNDs is the type of motor neuron degeneration they present with; while patients with ALS experience degeneration of both the upper and lower motor neurons, PLS patients experience purely upper motor neuron degeneration and SMA patients experience purely lower motor neuron degeneration (Talbot 2002).

In addition, the cause of the different MNDs varies; both ALS and PLS most commonly occur sporadically while SMA has a heritable genetic origin (James & Talbot 2006; Statland et al. 2015). Unlike sporadic diseases, where their cause is unknown, genetic diseases are often easier to study, mainly due to the ability to create animal models of these diseases (Fisher et al. 2009). The genetic cause of SMA is well documented and as a result various models have been developed to study this disease. By studying SMA, we will not only increase our knowledge of SMA but may also be able to provide an understanding of motor neuron degeneration that could be transferable amongst the other MNDs, to help in the search for therapeutic options for these devastating disorders (Bowerman et al. 2018).

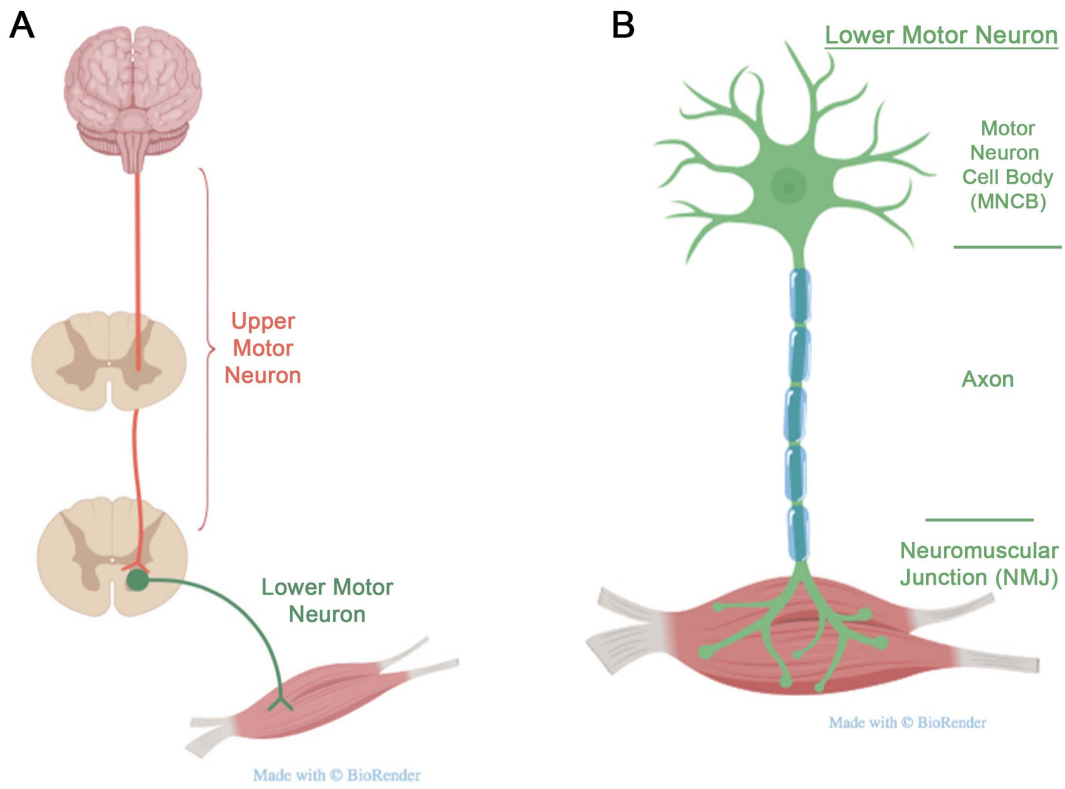

Figure 1.1: Upper and lower motor neurons are responsible for initiating muscle contraction. (**A**) Upper motor neurons carry signals from the brain to the spinal cord. These synapse onto lower motor neurons that carry the signal from the spinal cord to muscles. (**B**) The schematic shows the anatomy of the lower motor neuron. The motor neuron cell body (MNCB) is located within the ventral horn of the spinal cord and receives signals from the upper motor neurons. These signals are transmitted along the axon of the lower motor neuron where they reach the neuromuscular junction (NMJ). The NMJ consists of the pre-synaptic terminal of the motor neuron and the post-synaptic endplate of the muscle. Together, the motor neuron and all of the muscle fibres it innervates are called the motor unit.

1.1 Overview of SMA

Spinal muscular atrophy (SMA) is the leading genetic cause of infant mortality (Monani 2005). The commonly reported incidence is 1 in 6,000 - 10,000 live births however, recent data has found that the incidence is now 1 in ~12,000 live births (Lunn & Wang 2008; Verhaart et al. 2017). It is characterised by the loss of lower alpha motor neurons from the ventral horn

of the spinal cord that results in progressive muscle weakness and atrophy with subsequent paralysis.

As an autosomal recessive disorder, SMA is caused by mutations and deletions in the survival motor neuron 1 (*SMN1*) gene, which leads to a reduction in the ubiquitously expressed survival motor neuron (SMN) protein (Lefebvre 1995). Due to the presence of a second partially functionally copy of the *SMN* gene (SMN2; refer to section 1.3), SMN protein levels vary amongst patients, with lower levels of SMN protein resulting in severe SMA phenotypes and higher levels SMN protein resulting in more mild phenotypes. SMA is therefore separated into four different types based upon the severity of the phenotype patients exhibit (Munsat & Davies 1992; Taylor et al. 1998; Mailman et al. 2002).

1.2 Types of SMA

The severity and onset of SMA can vary considerably, with some patients being diagnosed early in infancy and others not diagnosed until adulthood. As a result, SMA was categorised into different types by the International SMA Consortium in 1992 (Munsat & Davies 1992). These types ranged from type I to type IV based on phenotypic severity and the milestones that were reached by SMA patients. A brief description of each is detailed below.

SMA type I is normally diagnosed within the first 6 months of life and, without treatment or respiratory support, most patients will not live past their second birthday (Wirth et al. 2006). Type I infants are unable to sit or hold their body weight, and from their appearance it is clear why SMA can also be referred to as ‘floppy baby syndrome’ (Wirth et al. 2006). Type I was the first type of SMA to be described in the literature when Guido Werdnig reported patients with SMA type I symptoms in 1891. John Hoffmann subsequently reviewed and added to these reports and as a result, SMA type I is also known as Werdnig-Hoffmann’s disease (Dubowitz 2009). With 60% of SMA patients

presenting with type 1, this is the most common of the various types of SMA (Ogino & Wilson 2004; Verhaart et al. 2017b).

Type II SMA is an intermediate form of the disease where infants are diagnosed after 6 months of age and live past 2 years of age. It is defined as having the ability to sit but not to stand and walk however, its manifestation has a large degree of variably (Wirth et al. 2006; Dubowitz 2009).

Type III is a milder form of SMA. Patients are not diagnosed until after 18 months of age, have the ability to sit and walk and do not have a shortened life expectancy. Type III SMA can be subcategorised into type IIIa and type IIIb based on age at diagnosis; with diagnosis between 18 months and 3 years of age defined as type IIIa SMA and diagnosis after 3 years defined as type IIIb SMA (Zerres & Rudnik-Schöneborn 1995; Wirth et al. 2006). Type III SMA was comprehensively described by Kugelberg and Welander in 1956 and as a result is also known as Kugelberg-Welander disease (Dubowitz 2009).

Type IV SMA is adult onset and patients are diagnosed around 30 years old. Although patients experience muscle weakness that results in mild disability later in life, patients do not experience a reduction in overall life span (Pearn 1978; Wirth et al. 2006).

These types of SMA described above (types I-IV) are all caused by mutations or deletions in the *SMN1* gene, leading to a reduction in SMN protein levels. However, the term spinal muscular atrophy is also sometimes used to refer to other disorders that are caused by different genetic mutations. These different types are also characterised by the loss of lower motor neurons and as a result, exhibit similar symptoms to types I-IV SMA. For example, SMA with respiratory distress (SMARD) is an autosomal recessive disorder caused by mutations in the *IGHMBP2* gene. It is first noticeable through breathing difficulties due to the paralysis of the diaphragm

from the degeneration of motor neurons supplying this muscle (Baumbach-Reardon et al. 2012). In addition, X-linked SMA is caused by mutations in the *UBA1* gene and due to the X-linked recessive nature of this disorder it primarily affects males (Baumbach-Reardon et al. 2012). Both SMARD and X-linked SMA are severe forms of this motor neuron disease with patients affected very early in infancy. They are also are much rarer than SMA type I-IV. In the context of this thesis, when SMA is used it will refer exclusively to types I-IV SMA, which are caused by mutations and deletions in the *SMN1* gene.

1.3 The genetics of SMA

In 1990, the gene responsible for SMA was mapped, using linkage analysis, to the 5q13 chromosome region (Figure 1.2A)(Brzustowicz et al. 1990; Gilliam et al. 1990; Melki et al. 1990; Verhaart et al. 2017). In 1995, it was reported that the *SMN1* gene was the disease determining gene in SMA after it was shown that this gene was either deleted, interrupted or mutated in all 229 SMA patients examined (Lefebvre 1995). Moreover, this study also showed that an almost identical gene, *SMN2*, was responsible for modifying the SMA phenotype in these patients (Lefebvre 1995).

Within chromosome 5q13, a portion of the genetic sequence is duplicated and inverted; while *SMN1* lies in the telomeric region, *SMN2* lies within the inverted centromeric copy (Figure 1.2A) (Lunn & Wang 2008). *SMN1* and *SMN2* are similar as both contain 9 exons separated by 8 introns, with only 5 nucleotide changes in *SMN2* when compared with *SMN1* (Figure 1.2B) (Bürglen et al. 1996). It is the C to T transition within exon 7 that is responsible for the disease modifying properties of *SMN2* (Lefebvre 1995; Lorson et al. 1999; Singh et al. 2017). While this transition is a silent mutation that would not result in an amino acid alteration, it does result in a G-U transition within *SMN2* pre-mRNA that is responsible for disrupting the exon splicing enhancer (ESE) site or creating a exon splicing silencer (ESS) in

exon 7 (Singh et al. 2017). This results in the alternative splicing and skipping of exon 7 in the *SMN2* pre-mRNA (Lorson et al. 1999). The exclusion of exon 7 does not alter the half-life and stability of the mRNA but does create a truncated, short-lived and non-functional protein known as *SMNΔ7* (Lefebvre 1995; Lorson et al. 1999; Monani et al. 1999). As exon 7 can be randomly included in some *SMN2* mRNA, approximately 10-15% of *SMN2* protein product is full-length, functional SMN protein (Figure 1.2C). This small production of SMN means that life, to some extent, can be sustained when there is a loss of *SMN1*.

This small production of SMN from the *SMN2* gene means that in those individuals with no functional *SMN1* gene, *SMN2* copy number is important in determining the severity of SMA phenotype; those with a greater copy number of *SMN2* often have an increased production of SMN protein (Taylor et al. 1998; Mailman et al. 2002). The number of copies of *SMN2* that an individual carries can vary. Within the general population, 14.4% have no copies of *SMN2*, 33% have one copy of *SMN2* while 50% have three copies of *SMN2* (Mailman et al. 2002; Oskoui et al. 2017). SMA patients with severe type I SMA tend to have only one or two copies of *SMN2* while type II-III patients tend to have ≥3 copies of *SMN2* (Harada et al. 2002; Calucho et al. 2018). This demonstrates a dose dependent effect of *SMN2* copy number.

However, it should be noted that although *SMN2* copy number is the predominant phenotypic modifier in SMA, it is not the only modifier of disease severity. Patients have previously presented with disease phenotypes that are milder than would be expected based on their *SMN2* copy number and this was shown to be caused by mutations within *SMN2* itself (Prior et al. 2009). In addition, in a case where two siblings were shown to have the same *SMN* genetics but one was symptomatic while the other was asymptomatic, it was the expression of Plastin 3, an actin-binding protein, that was found to be the modifying factor (Oprea et al. 2008). As a result,

although SMA is ultimately caused by mutations and deletions in *SMN1*, there are clearly other genetic factors that impact upon this disease.

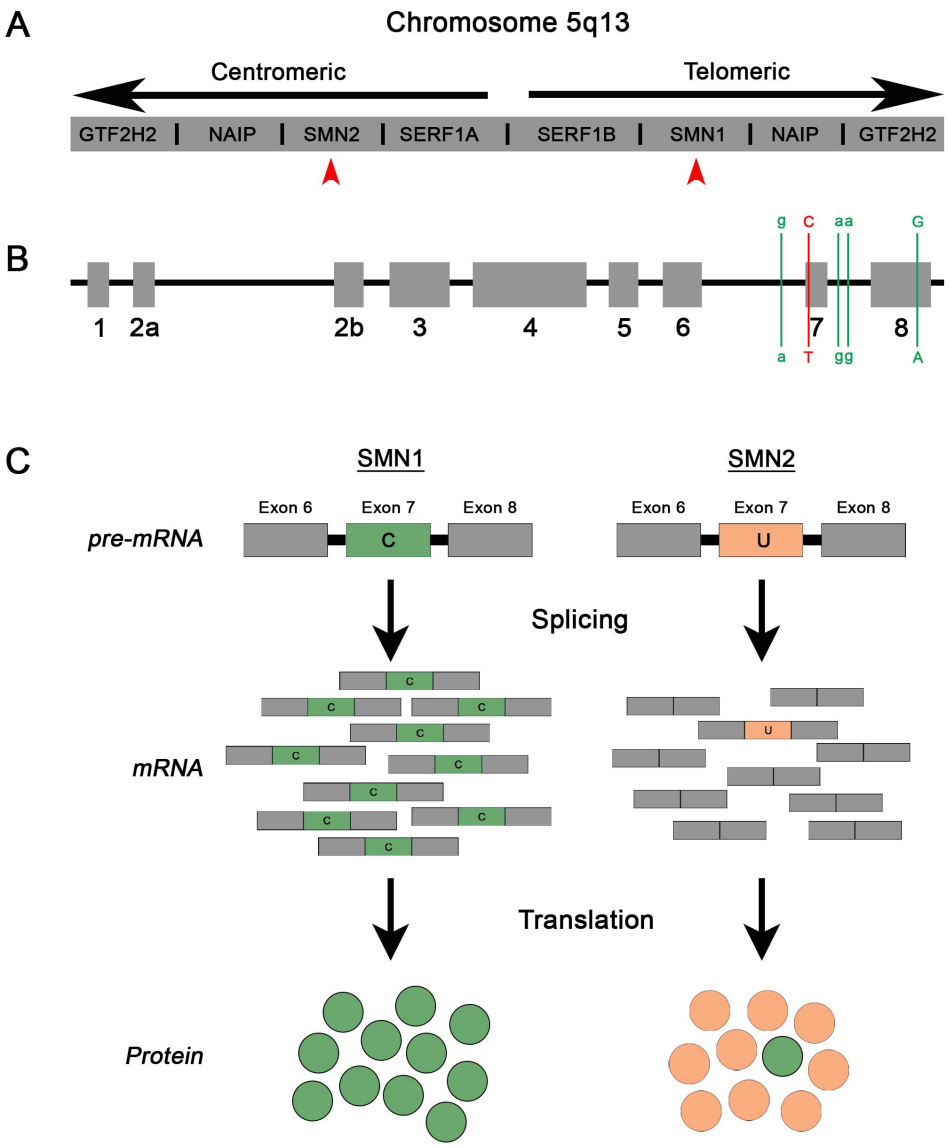

Figure 1.2: *SMN2* is alternatively spliced resulting in a reduction in the amount of functional SMN protein translated from this gene. (**A**) *SMN* genes are located on chromosome 5q13 with *SMN1* in the telomeric region and *SMN2* in the centeromeric region. Note that the centeromeric region is inverted when compared to the telomeric region of chromosome 5q13. (**B**) Both *SMN* genes have 8 exons separated by 9 introns. *SMN1* sequences are shown on top and the altered *SMN2* sequence on the bottom, this includes the C to T transition that is important in splicing. (**C**) The C to T substitution in exon 7 of *SMN2* causes a C to U alteration in pre-mRNA. This results in the alternative splicing of this gene. While all *SMN1* pre-mRNA is spliced to include exon 7, only 10% of SMN2 pre-mRNA is spliced to include exon 7. Therefore, only 10% of functional SMN protein is obtained from the *SMN2* gene. The majority of *SMN2* protein product is a short-lived and non-functional SMNΔ7 protein. *Figure based on Lung & Wang, 2008; Codey & Lorson, 2011; Butchbach, 2016.*

1.4 SMN protein

SMN protein contains 294 amino acids and has a predicted molecular weight of 32kDa, although subsequent western blotting has shown a molecular weight of ~38kDa (Lefebvre 1995; Giavazzi et al. 2006). This alteration is possibly as a result of post-translational modifications. The levels of SMN protein expressed can vary with age and between tissues, with a higher level of Smn in the CNS tissues observed in control mice (Coovert 1997; Groen et al. 2018a). At the cellular level, SMN is located in both the cytoplasm and the nucleus. In the nucleus, SMN is concentrated in “gems” (or Gemini of Cajal bodies) (Gubitz et al. 2004). As the name suggests these gems are often associated with Cajal bodies and are similar in size and number (Gubitz et al. 2004). The exact function of these gems remains unknown however due to their composition, it is thought that gems play a role in RNA processing (Gubitz et al., 2004; Q. Liu & Dreyfuss, 1996; Pellizzoni et al., 1998).

The best characterised role for SMN is in pre-mRNA splicing (reviewed by (Burghes & Beattie 2009)). Pre-mRNA splicing is the process whereby non-coding introns are removed from pre-mRNA and the remaining coding exons are rejoined to allow translation to progress. This process is facilitated by protein complexes known as spliceosomes and, from work in HeLa cells, it is known that SMN is involved in their assembly (Pellizzoni et al., 1998; Burghes & Beattie 2009). Specifically, SMN is involved in the assembly of snRNPs (small nuclear ribonuclear proteins), which are a major component of the spliceosome (Burghes & Beattie 2009). In its role in snRNP assembly, SMN exists as a complex, comprising of SMN and several Gemin proteins, specifically Gemins 2-8 and Unrip (Burghes & Beattie 2009). This SMN complex binds Sm proteins and snRNAs (small nuclear RNAs) that combine to create snRNPs (Burghes & Beattie 2009). Therefore, a lack of SMN will result in preventing snRNP assembly and subsequent insufficient production of spliceosomes (Burghes & Beattie 2009).

Although pre-mRNA splicing is the best-characterised role of SMN, it is not the only suggested role of this protein. In fact, due to the finding that splicing defects increased over disease progression it is thought that perhaps defective splicing is a secondary cause of the disease (Bäumer et al. 2009). It has been suggested that SMN can also function in the assembly of mRNPs (messenger ribonucleoproteins) from mRNA and mRNA binding proteins (mRBPs) (Fallini et al. 2012). It is in this form that mRNAs are transported within cells for their local translation within specific compartments of the cell. In neurons, local translation of mRNAs appears to be important as many of the proteins that are involved in synapse formation appear to be locally translated (Cajigas et al., 2012; Khalil et al., 2018). In motor neurons specifically, this transportation of mRNAs for local translation may be more important due to the substantial length of their axons (Czaplinski, 2014; Donlin-Asp et al., 2017; Fallini et al., 2016; Khalil et al., 2018). It is also postulated that SMN acts as an mRNA chaperone, supported by the finding that SMN is transported in both the anterograde and retrograde direction along the axon of motor neurons (Zhang et al. 2003).

In addition, a lack of SMN leads to impairment of the cytoskeleton and this has been shown to contribute to SMA pathogenesis. Levels of RhoA, a regulator of actin dynamics, is increased in an SMA mouse model and the inhibition of ROCK, a downstream effector of RhoA, using Y-27632 or Fasudil, has been shown to improve the phenotype of this mouse model (Bowerman et al. 2010; Bowerman et al. 2012b). As the cytoskeleton is important for the transport of mRNAs within motor neurons, it may be possible that this impairment of the cytoskeleton adversely impacts on local translation of mRNAs at the synapse.

It has also been suggested that SMN functions in DNA repair (Fayzullina & Martin 2014), stress granule formation (Hua & Zhou 2004), ubiquitin homeostasis (Groen & Gillingwater 2015) and synaptic vesicle release (Kong et al. 2009). However, despite the large number of suggested roles of SMN,

the disease-causing function of SMN ultimately remains unknown. It also remains unclear as to why a reduction in a ubiquitously expressed protein leads specifically to a motor neuron disease phenotype.

1.5 Selective and differential vulnerability of motor neurons in SMA

SMA is characterised by the selective degeneration of lower alpha-motor neurons. However, as SMN is a ubiquitously expressed protein, it is unclear why these motor neurons are selectively vulnerable. Defects in SMNs role in splicing are disputed as the causative factor of SMA due to splicing being a universal process that is not exclusive to motor neurons. However, one theory is that motor neurons have a greater requirement for transcripts that are spliced by the minor spliceosome (Gabanella et al. 2007). It is known that there are two types of spliceosome, major and minor, and these differ in their composition of snRNAs. Minor spliceosomes are responsible for splicing only 1% of transcripts but are thought to be more affected by a reduction in SMN (Gabanella et al. 2007). Therefore, it is suggested that motor neurons may require transcripts that are spliced by the minor spliceosome and as a result are more affected by a reduction in SMN protein than other tissue types.

It is also suggested that disruption in the transportation and local translation of mRNAs impacts on motor neurons to a greater extent than other tissues. This is due to motor neurons having extremely long axons, and as a result, having an increased requirement for local translation at their synapses (Czaplinski 2014; Fallini et al. 2016; Donlin-Asp et al. 2017; Khalil et al. 2018). By impairing the process of local translation, motor neurons are no longer able to translate proteins required at the synapse.

Another theory is that there is a threshold requirement for SMN, meaning that some tissues have a greater requirement for SMN than others (Sleigh et al. 2011). It would suggest that motor neurons require large amounts of SMN

compared to other tissues. This is supported by the recent report that neuronal tissues have a higher level of Smn in control mice compared to other tissue types (Groen et al. 2018a). In addition, heart defects have been seen in patients of severe type I SMA, where SMN levels are very low, but not in patients of type II-III SMA, where SMN levels are higher (Shababi et al. 2014; Deguise et al. 2016). Thus, suggesting that when SMN levels drop below a certain threshold for the heart it can no longer sustain normal function.

However, motor neurons are not only selectively vulnerable to degeneration, they are also differentially vulnerable. This means that not all motor neurons are equally affected by a decrease in SMN and while some motor neurons degenerate, others do not, even at a late stage in the disease. This is a phenomenon that is observed in SMA mouse models and in patients with SMA. In patients, the upper limbs are less affected that the lower limbs and distal musculature is less affected than proximal musculature (Dubowitz 1999). While the intercostal muscles are always affected, the diaphragm and facial muscles are comparatively spared (Dubowitz 1999). In mouse models, differential vulnerability of muscles varies between the different mouse models in the field. For example, in the *Smn*$^{2B/-}$ mouse model abdominal musculature displays vast denervation and pathology while cranial musculature shows less denervation (Murray et al. 2015). However, in the more severe mouse models of SMA, the vulnerability status of the muscle varies even between the four cranial muscles (Murray et al., 2008; Thomson et al., 2012). The reasons for this differential vulnerability remain unknown. Recent transcriptional analysis of the motor neurons supplying these differentially vulnerable muscle groups has highlighted pathways that are altered between the subpopulations of motor neurons (Murray et al. 2015). This revealed an up-regulation of transcripts involved in DNA repair in less vulnerable motor neurons providing one theory as to how protection against severe degeneration is obtained (Murray et al. 2015).

Ultimately, the reasons for this selective and differential vulnerability of motor neurons in SMA remains unclear and whether there is one particular reason for this or rather a multitude of different genetic disruptions between subpopulations has yet to be determined. However, investigation into these differences between motor neurons and in fact between motor neurons of different types of MND may highlight particular modifiers of motor neuron health that can be exploited as therapeutic targets (Murray et al. 2015; Kline et al. 2017).

1.6 Animal models of SMA

The discovery of the causative gene of SMA started the hunt for appropriate models of the disease. As *SMN2* is unique to humans, SMA is a disease that only affects the human species (Rochette et al. 2001). Genetic modification of various other species, including *Drosophila melanogaster* (Chan et al. 2003; Chang et al. 2008), *Dario renia* (zebrafish) (McWhorter et al. 2003; Boon et al. 2009) and *Mus musculus* (mouse) (Monani et al. 2000; Hsieh-Li et al. 2000; Le et al. 2005; Bowerman et al. 2012a), has been performed in order to create models of SMA. Each animal model has their strengths, and each provide different opportunities in SMA research. For example, *Drosophila* provides a quick screening tool for modifiers of the disease or for genetic mapping. However, it should be remembered that conclusions regarding the human disease cannot be drawn solely from findings within this relatively basic model (Schmid & DiDonato 2007; Burghes & Beattie 2009). A prime example of this is restoration of Smn in muscle; in *Drosophila* models of SMA, restoration of Smn in muscle provides a significant rescue of the disease whereas restoration of Smn in the muscles of mouse models has little effect on disease phenotype (Chan et al. 2003; Gavrilina et al. 2008; Burghes & Beattie 2009).

Moreover, zebrafish are popular in the research of neurodegeneration due to their highly conserved genome, their rapid development and transparent

morphology, which makes imaging very accessible (Babin et al. 2014). Again, as they only have a single *Smn* gene, modification is required to create an SMA-like phenotype. In zebrafish, knocking out *Smn* reduces survival to a mean of 12 day post-fertilization (Boon et al. 2009). This is in contrast to mice where *Smn* knockout is embryonically lethal (Schrank et al. 1997). In zebrafish, the increased survival of *Smn* knockout animals is thought to be caused by a higher dose of maternal Smn that is available in the early gestation period of zebrafish compared to mice (Boon et al. 2009). To further extend the survival of this zebrafish model of SMA, the transgenic expression of human *SMN2* was introduced. This *SMN2* expression on a null *Smn* background extended survival to 15 days post-fertilization (Hao et al. 2011).

An alternative method of reducing *Smn* expression in zebrafish is through the administration of modified antisense oligonucleotides, termed morpholinos, into embryos, rather than modifying the genome. This method targets protein production by inhibiting the translation of target mRNA. Injecting this morpholino into embryos resulted in a 61% reduction in Smn and abnormal axonal morphology (McWhorter et al. 2003).

With regards to mouse models of SMA, many different mouse models have been created through a variety of genetic modifications. The initial creation of the first mouse model of SMA began when exon 2 in the murine *Smn* gene was disrupted. However, it was found that disruption of both copies of this gene, resulting in a completely null background and a complete lack of Smn, was embryonically lethal (Schrank et al. 1997). Transgenic expression of human *SMN2* on this null background provided a small production of Smn protein that resulted in a mouse model with a phenotype that resembled that of SMA (Monani et al. 2000). With only one or two copies of *SMN2* mice display a very severe phenotype and have a short life span; with two copies of *SMN2* this mouse model will not survive past 6 days (Monani et al. 2000). However, with eight or more copies of *SMN2* mice are phenotypically normal,

demonstrating the dose dependent requirement of Smn (Monani et al. 2000). Due to the severe phenotype of those mice with only two copies of *SMN2*, this mouse model is known colloquially as the 'severe' mouse model of SMA.

The 'Taiwanese' mouse model of SMA is genetically similar to the 'severe' model. It also expresses *SMN2* on a null background, however in the 'Taiwanese' mouse model this null background is created through the disruption of exon 7 within the murine *Smn* gene, rather than exon 2 (Hsieh-Li et al. 2000). With the expression of two copies of *SMN2*, this mouse model has an expected survival of 8-10 days and with the expression of four copies mice have a normal lifespan (Hsieh-Li et al. 2000).

Approximately 5 years later, the *SMNΔ7* transgene, developed from human *SMN* cDNA that excluded exon 7, was introduced into the 'severe' mouse model of SMA (Le et al. 2005). This addition was originally developed to determine whether the non-functional SMNΔ7 protein that is produced by *SMN2* contributes to the SMA phenotype. However, it was found that incorporation of *SMNΔ7* in fact moderately reduced the severity of the SMA-like phenotype and extended life span to between 12 and 17 days (Le et al. 2005). As a result, this '*SmnΔ7'* mouse model of SMA is still used in SMA research.

A mouse model in which the Smn deletion was exclusive to motor neurons, achieved using the Cre-Lox system, was used to determine the effect of Smn reduction on motor neurons specifically (Cifuentes-Diaz 2002). However, since Smn is reduced ubiquitously in SMA, this mouse model is less representative of the disease than other mouse models. Despite this, it did provide some of the first reports of pathological features of the NMJ that have since been shown in other, perhaps more representative, mouse models of SMA (Cifuentes-Diaz 2002; Murray et al. 2008).

The *Smn*$^{2B/-}$ mouse model of SMA is created through the genetic modification of the murine *Smn* gene (Bowerman et al. 2012a). One of the *Smn* alleles in this mouse model is non-functional due to the disruption of exon 2 (Schrank et al. 1997). The other allele is known as the '*Smn2B*' allele and contains a three base pair substitution within exon 7 which causes it to mimic the effects of human *SMN2* (DiDonato et al. 2001; Hammond et al. 2010). It expresses approximately 15% of full-length SMN but, as in *SMN2*, its main protein product is SMNΔ7. This mouse model is often referred to as an 'intermediate' mouse model of SMA due to its extended life span, of approximately 28 days, compared to previously reported mouse models. It is also because of the lack of symptoms observed in the model until approximately 10 days old (Bowerman et al. 2012a).

Mice that have reduced Smn levels but have a normal life span, and remain asymptomatic throughout, have also been created and characterised (Bowerman et al. 2012a; Jablonka et al. 2000). The *Smn*$^{2B/2B}$ mouse model carries two copies of the *Smn2B* allele and, as one copy of this allele is responsible for producing ~15% of normal Smn levels, the *Smn*$^{2B/2B}$ mouse expresses ~30% of normal Smn protein (Bowerman et al. 2012a). Analysis of specific tissue has shown that expression does vary between tissues with ~36% in the spinal cord and ~25% in the brain (Bowerman et al. 2012a). Despite the reduction in Smn protein, this mouse model was shown to have no overt phenotype, with no significant difference in motor performance, NMJ morphology and motor neuron cell body (MNCB) number at both 6 months and 1 year of age (Bowerman et al. 2012a).

Furthermore, the *Smn*$^{+/-}$ mouse model has only one functional murine *Smn* gene and therefore expresses approximately 50% of normal SMN levels (Jablonka et al. 2000). This mouse model has been shown to have a loss of MNCBs in the ventral horn of the spinal cord, although the degree of loss appears to vary considerably within the published literature (Jablonka et al. 2000; Simon et al. 2010; Bowerman et al. 2014; Udina et al. 2017). While it

was initially reported that there was a 54% loss of MNCBs from the lumbosacral region of the spinal cord, subsequent reports saw a 40% and a 19% loss of MNCBs (Jablonka et al. 2000; Simon et al. 2010; Udina et al. 2017). One report also shows no loss of MNCBs from the lumbar region of the spinal cord in the *Smn*$^{+/-}$ mouse model (Bowerman et al. 2014). Those that have found a loss of motor neurons within this mouse model report that axonal sprouting is responsible for masking the loss and the resulting motor phenotype (Simon et al. 2010; Udina et al. 2017).

Having a variety of different models within SMA research provides an opportunity for us to strengthen findings regarding the pathogenesis of SMA and the reliability of therapeutic targets. Being able to replicate results in mouse models of different severities makes findings more promising. It also provides an opportunity to observe how alterations in genetics may influence outcomes, just as can occur in humans.

1.7 Motor neuron pathology in SMA

Motor neuron pathology has been investigated in both patients and mouse models of SMA. Motor neurons are extremely long cells that can be separated into distinct compartments; the cell body, located within the spinal cord, the axon, which extends from the spinal cord into the periphery, and the neuromuscular junction (NMJ), the point at which the pre-synaptic terminal of the motor neuron meets the post-synaptic endplate of the muscle (Figure 1.1). Defects have been reported in each of these compartments and some of these defects are detailed below.

A reduction in MNCB area and number has been documented in both patients and mouse models of the disease (Simic et al. 2000; Soler-Botija et al. 2002; d'Errico et al. 2013; Powis & Gillingwater 2016; Pérez-García et al. 2017). Analysis on fetuses from terminated pregnancies has shown that SMA fetuses have a reduced number of MNCBs in their spinal cords from as early

as 12 weeks of gestation, when compared to age matched control fetuses (Soler-Botija et al. 2002). While there are many studies that report a loss of MNCB in post-mortem tissue for patients of SMA, very few provide quantification in support of this. One study however, carried out by Soler-Botija *et. al.*, reported a 50-60% loss of MNCBs in the spinal cord of patients with SMA type I during post-mortem analysis (Soler-Botija et al. 2002). In mouse models of SMA, the loss of MNCBs appears to vary between the different models. While the Taiwanese mouse model showed a 20% loss of MNCBs compared to controls, the *SmnΔ7* and the $Smn^{2B/-}$ mouse models had a 40% and a 50% loss of MNCBs, respectively (Bowerman et al. 2012a; d'Errico et al. 2013; Powis & Gillingwater, 2016). In addition, there are reports of reduced excitatory inputs as well as abnormal morphology of mitochondria at the cell body of motor neurons (Neve et al. 2016).

The axon of the motor neuron extends from the spinal cord within the ventral root. By examining the ventral roots of SMA type I patients, it has been shown that they experience a reduction in the number of myelinated axons (Pérez-García et al. 2017). This loss of myelinated axons was also shown in sural nerve of SMA type I patients (Carpenter et al. 1978). In a mouse model of SMA, there was a 78% loss of axons from the ventral root showing that this degeneration of axons is conserved in both patients and mouse models (Cifuentes-Diaz 2002).

The NMJ has many well-reported defects that have become hallmarks of SMA pathology. Denervation has been shown to occur in a die-back manner in which the pre-synaptic terminal withdraws away from the muscle (Murray et al. 2008). Post-synaptic endplates become progressively denervated, as evidenced by the presence of partially occupied and vacant clusters of acetylcholine receptors (AChRs) (Murray et al. 2008; Murray et al. 2015).

Furthermore, NMJs also exhibit an abnormal accumulation of neurofilament (or neurofilament accumulation/ NFA), a component of the cytoskeleton, at

their pre-synaptic terminals (Cifuentes-Diaz 2002; Murray et al. 2008; Kariya et al. 2008). This is regarded as a pathological hallmark of SMA as it is widely observed in both patients and mouse models of SMA (Murray et al. 2008; Kariya et al. 2008; Kong et al. 2009). As NFs are the intermediate filaments of neurons, they are part of the cytoskeletal system (Yuan et al. 2012). They are predominately located within the axons of neurons, where they are important during development and in nerve conduction and axon diameter (Yuan et al. 2012). NFs are primarily made within the cell body and are transported into and along axons (Miller et al. 2002). Therefore, it has been suggested that the accumulation of NFs observed in SMA may be caused by impaired axonal transport (Boyd & Gillingwater 2017). However, it has been reported that NFA is due to synaptic alterations rather than axonal transport defects and therefore, the causes of NFA in SMA remain unknown (Dale et al. 2011).

In fact, NFA occurs in other neurodegenerative diseases such as ALS, Alzheimer's disease and Parkinson's disease in which the cause and resulting consequences of this NFA are yet to be determined (Yuan et al. 2012). However, in these diseases NFA occurs within the cell body and axon, therefore it appears that pre-synaptic NFA is unique to SMA (Kong et al. 2009; Cifuentes-Diaz 2002). Interestingly, mice that have been genetically modified to overexpress NFs exhibit motor neuron degeneration suggesting perhaps that NFA can be a causative factor of motor neuron degeneration (Côté et al. 1993). Despite this, it remains unclear how the onset of NFA relates to the degeneration of the NMJ in SMA (Cifuentes-Diaz 2002; Boyd & Gillingwater 2017).

The post-synaptic endplate is formed by acetylcholine receptors (AChRs) on muscle fibers. In development, AChRs reorder and perforate, altering their morphology from immature plaque-like to mature pretzel-like structures (Sanes & Lichtman 2001). They also develop molecularly with a shift in the expression of the fetal γ-subunit to the adult subunit during the first two

weeks of postnatal development (Mishina et al. 1986). In SMA, immature endplates persist. In the *SmnΔ7* mouse model of SMA, 50% of endplates were morphologically immature at P14 while only 10% of endplates in controls appeared immature at the same age (Kariya et al. 2008). In addition, there was also an increase in the endplates that expressed the fetal γ-subunit of AChRs in this mouse model (Kariya et al. 2008). This pathological feature is conserved in humans, as patients of SMA exhibit a decrease in endplates with mature morphology and increase in endplates expressing the immature fetal AChR γ-subunit (Harding et al. 2015).

Although these hallmarks of SMA motor neuron pathology are relatively well documented in the literature, how they are related is unknown. Despite speculation that motor neurons degenerate in a distal to proximal manner, due to the NMJ being an early pathological target in SMA (Murray et al. 2008), there is no literature that explicitly explores this idea.

In addition, since the NMJ is an early target in SMA, it has been proposed that degeneration of the NMJ is what causes the motor neuron to die. However, two recent studies have shown that transcripts involved in the P53 signaling pathway are up-regulated prior to symptom onset in vulnerable motor neurons of three different SMA mouse models (Murray et al. 2015; Simon et al. 2017). As the P53 signaling pathway is important in DNA repair and apoptosis and is activated upon excessive DNA damage (Williams & Schumacher 2016), it suggests that motor neuron death could be initiated prior to visible motor neuron pathology.

In order to determine when and where degeneration of the motor neuron begins, a coherent study that looks at the hallmark features of pathology in SMA over a time course would be required in order to draw conclusions on the relationship of motor neuron pathology in SMA.

1.8 Non-neuronal defects in SMA

SMA is characterised by the degeneration of motor neurons, which are reportedly selectively vulnerable to a reduction in SMN. However, there are now many reports of defects in other tissues, from both patients and mouse models of SMA, suggesting that SMN plays a role within non-neuronal tissues. Below, a few of the non-neuronal defects that have been reported to occur within SMA mouse models and/or patients are briefly detailed.

Skeletal muscle in SMA experiences atrophy and this is, at least in part, due to the loss of innervation following motor neuron degeneration. However, it has also been shown that Smn reduction causes intrinsic defects of sketal muscle. For example, Smn reduction in myoblast cell lines results in defective myotubule formation and reduced myoblast proliferation (Shafey et al. 2005). Furthermore, proteomic analysis of skeletal muscle has been carried out at a pre-symptomatic time point, when there is a lack of denervation, and this revealed that there are molecular changes in muscle from SMA mice compared to controls (Mutsaers et al. 2011). Specifically, there were abnormalities in the regulation of proteins involved in muscle function and pathology (Mutsaers et al. 2011).

Moreover, skeletal muscle has been shown to have an immature phenotype in both mouse models and patients of SMA, when compared with that of age-matched controls (Kariya et al. 2008; Kong et al. 2009; Lee et al. 2011; Boyer et al. 2014). Not only has it been shown that there is delayed maturation of the post-synaptic endplates of the muscle, but also the persistence of the immature form of the myosin heavy chain in the skeletal muscle of the *SmnΔ7* mouse model (Kariya et al. 2008; Kong et al. 2009; Lee et al. 2011). This is important to consider as it Is belived that delayed maturation of the motor unit can be detrimental for its survival (Hausmanowa-Petrusewicz & Vrbová 2005).

Bone defects have been reported in both patients and mouse models of SMA. The Taiwanese mouse model displayed significantly thinner and more porous cortical bone in their vertebrae than control mice (Shanmugarajan et al. 2009). Similarly, SMA patients have been shown to have a low bone mineral density, with high rates of osteopenia. In fact, SMA patients presented with the lowest average bone mineral density when compared to patients of other neuromuscular disorders, such as Duchene Muscular Dystrophy (DMD) (Khatri et al. 2008).

Furthermore, the density of vasculature in the Taiwanese mouse model is significantly reduced compared to controls, in a variety of different muscles (Somers et al. 2016). This finding was also observed in muscle biopsies from SMA patients (Somers et al. 2016). In the spinal cord, the density of capillary bed was decreased in both the Taiwanese and *SmnΔ7* mouse models of SMA and this was reported to cause hypoxia of motor neurons at a pre-symptomatic time point (Somers et al. 2016). Therefore, the authors suggest that SMN plays a role in the development of vasculature and that hypoxia of motor neurons may be contributing to their death (Somers et al. 2016).

Additionally, the density of capillaries within cardiac muscle is decreased and cardiac defects have been reported in both patients and mouse models of SMA (Shababi et al. 2014; Deguise et al. 2016; Maxwell et al. 2018). Both the intraventricular septum and the ventricular wall were thinner in the severe, *SmnΔ7 and* Taiwanese mouse models of SMA, when compared to controls (Shababi et al. 2014; Maxwell et al. 2018). Patients with severe SMA have an increased risk of developing congenital heart defects, including atrial and ventricular septal defects, suggesting a role for SMN in cardiac tissue (Rudnik-Schoneborn et al. 2008).

Moreover, the spleen has been shown to be significantly smaller in size with abnormal morphology in various mouse models of SMA (Deguise et al. 2017; Thomson et al. 2017; Khairallah et al. 2017). Preliminary observations of

spleens from those with SMA type I/II suggest that splenic defects may also be a symptom of SMA in patients (Thomson et al. 2017). SMN expression within the spleen is high in wild type mice, suggesting a greater requirement for this protein (Deguise et al. 2017). It has also been shown that introducing one copy of *SMN2* into the *Smn*$^{2B/-}$ mouse model of SMA rescued the splenic defects observed in this mouse model (Deguise et al. 2017). Therefore, it is thought that SMN plays an important role within this tissue.

An abnormal morphology of the thymus has also been reported in mouse models of SMA and since both the thymus and the spleen are involved in immunity, it is suggested that a lack of SMN may be detrimental to the immune system (Deguise & Kothary 2017). However, this idea remains relatively unexplored and warrants further investigation to determine whether SMA patients have a greater susceptibility to infections due to impairment of their immune system (Deguise & Kothary 2017).

Analysis of the liver from the Taiwanese mouse model of SMA revealed this tissue fails to develop normally, with an immature morphology persisting (Szunyogova et al. 2016). It also displayed abnormal accumulation of iron, which is consistent with previous reports that found that deletion of SMN from the liver exclusively, leads to embryonic death as a result of iron accumulation (Vitte et al. 2004; Szunyogova et al. 2016).

Furthermore, gastrointestinal problems are also reported in patients of SMA, with symptoms including reflux, bloating and constipation (Wang et al. 2007). Diarrhea was reported in the Taiwanese mouse model of SMA, which also had a decreased number of villi, that had an abnormal appearance compared to controls, within their small intestine (Schreml et al. 2013).

The pancreas has been assessed in patients of SMA and in the *Smn*$^{2B/-}$ mouse model (Bowerman et al. 2012c). This revealed that in both cases, the pancreas has an abnormal cellular composition, with an increase in the

percentage of alpha cells, that produce glucagon, and a decrease in percentage of beta cells, that produce insulin (Bowerman et al. 2012c). This observation is consistent with reports of metabolic abnormalities in SMA patients including abnormal fatty acid metabolism and hypoglycemia (Bruce et al. 1995; Crawford et al. 1999). Further investigation into the pancreas in *Smn*$^{+/-}$ mice, which, in this case, was found to have no overt phenotype, showed that even with SMN levels that appear sufficient to sustain survival, there were metabolic differences in these mice when they were placed under stressed conditions (Bowerman et al. 2014). Therefore, highlighting the importance of SMN in regulating metabolism, even when SMN levels are sufficient to sustain survival of motor neurons.

From this brief overview of some of the defects that have been reported in non-neuronal tissues, in both patients and mouse models of SMA, it is clear that when levels of SMN are severely low SMA is no longer exclusively a neuromuscular disorder. This is important to consider when looking at therapeutic options, as correction of all pathologies would be required in order to benefit patients of SMA.

1.9 Therapeutics in SMA

SMA has now been at the forefront of therapeutic research for a number of years. Since the discovery of *SMN*, the disease-causing gene, the main line of therapeutic research has looked to restore the production of SMN protein. This has been attempted by replacing the faulty *SMN1* gene, using gene therapy techniques, or by altering the aberrant splicing of *SMN2* pre-mRNA, using an antisense oligonucleotide (ASO) or splice-altering, small molecules. Thanks to this research, the SMA field reached a major milestone when the first SMA treatment, Spinraza, was approved initially in the USA in December 2016 and since in the European Union in May 2017. Spinraza (Nursinersen, Biogen/Ionis) is an ASO based therapy. ASOs are short, single stranded, synthetic oligodeoxynucleotides that bind to the pre-mRNA of *SMN2* to

enhance the inclusion of exon 7 during splicing. This results in an increase in the amount of full-length SMN protein synthesised from the *SMN2* gene (Shorrock et al. 2018). In clinical trials (ENDEAR and CHERISH) of Spinraza, patients with type I, II and III SMA showed a significant increase in motor performance and in patients with type I SMA, there was a significant increase in lifespan. In fact, these trials were so successful that they were both closed and all patients were enrolled onto an open-label trial, SHINE, that now looks at the long-term effects of Spinraza (Mercuri et al. 2017; Finkel et al. 2017).

Spinraza itself has not been associated with many adverse side effects but rather the delivery method is what appears to cause the majority of the side effects reported during clinical trials (Finkel et al. 2016). Spinraza is administered intrathecally, into the cerebrospinal fluid (CSF) of patients via a lumbar puncture, as ASOs cannot cross the blood brain barrier (Wood et al. 2017). This ensures that a large dose of the ASO is delivered to the CNS, and importantly, the motor neurons (Shorrock et al. 2018). Although, as CSF is reabsorbed into systemic circulation, Spinraza is also detectable within the liver and kidneys, showing delivery is not exclusively to the nervous tissues (Finkel et al. 2016). Patients receive a loading period of the drug whereby 3 treatments are given 14 days apart and the fourth is given 30 days after (Finkel et al. 2016). Patients will receive subsequent treatments every 4 months. Since lumbar punctures are a rather invasive treatment, side effects of which include back pain, headaches and post-lumbar puncture syndrome, the frequent treatment of Spinraza is less than desirable (Finkel et al. 2016; Shorrock et al. 2018). Therefore, despite the efficacy of Spinraza, a treatment that requires a less invasive procedure would be more desirable.

Gene therapy is an alternative method of restoring SMN protein that is currently in clinical trials (AVXS-101, AveXis). This involves the systemic administration of an adeno-associated virus (AAV) vector that contains SMN1, replacing the endogenous faulty version of the gene. In mouse models, this therapy showed promising results and therefore it was brought

into clinical trials that assessed its safety (Foust et al. 2010; Valori et al. 2010; Dominguez et al. 2011). This initial trial proved encouraging and AVXS-101 is now in long-term trials that assess its efficacy and look at long-term effects of gene therapy treatment (Shorrock et al. 2018). The clear advantage of this therapy is its delivery method; it requires only a single, intravenous injection, which removes the side effects associated with more invasive procedures.

Small molecule therapies target the alternative splicing of *SMN2* pre-mRNA. There are two small molecule drugs currently in clinical trials; Branaplam (LMI070, Novartis) and RG7916 (RO7034067, Roche). Although both of these therapeutics can be given orally, which is a much more desirable delivery method in the clinic, they have shown only a modest improvement in motor function in patients (Shorrock et al. 2018).

Valproic Acid (VPA) is a drug that is currently used to treat a variety of neurological disorders, including epilepsy. The mechanism of how it works therapeutically is unknown but as a histone deacetylase (HDAC) inhibitor it is involved in regulating gene expression. In terms of SMA, it is thought to alter splicing of *SMN2* and in turn increase SMN levels (Sumner et al. 2003). Although a study looking at an alternative HDAC inhibitor, Trichostatin A, disputes this claim, reporting that this substance does not increase SMN levels (Liu et al. 2014). Interestingly, clinical trials of VPA for SMA, showed mixed results among patients (Swoboda et al. 2009). While some patients experienced the desired increase in SMN protein levels, others had no increase or even decreased SMN levels during the treatment (Garbes et al. 2013). A subsequent comparison of fibroblasts from those that responded to the treatment and from those that did not showed that *CD36* RNA levels were significantly increased in those that did not responded to VPA treatment (Garbes et al. 2013). CD36 is a cell surface membrane protein that is known to be involved in the transportation of fatty acids (Garbes et al. 2013). By treating cultured cells, that had been transfected with *CD36*, with VPA the

authors were able to show that *CD36* had a negative effect on SMN production (Garbes et al. 2013). This highlights the genetic differences amongst the population that should not be forgetten when considering SMA treatments.

One of the key findings from mouse models of SMA is that early restoration of SMN is key to the successful treatment of SMA (Lutz et al. 2011; Robbins et al. 2014). As this is likely due to the fact that motor neuron death is irreversible, it is assumed that this will also be the case in patients. The NURTURE trial of Spinraza therefore looks at the effects of administering Spinraza to pre-symptomatic patients. Through genetic testing these patients have been diagnosed with SMA but have not yet displayed symptoms. After one-year of treatment, these patients are showing promising results with all attaining normal head control and most being able to sit and crawl (Hwu et al. 2017). However, only three out of nine were able to stand unaided suggesting that although early intervention is beneficial and that Spinraza shows promising improvement for patients, it is clearly still not a 'cure' for SMA (Hwu et al. 2017; Shorrock et al. 2018). The hope is that by finding other treatments, that could be given to patients in conjunction with Spinraza, it may be possible to enhance the therapeutic effects of this treatment.

Other therapeutics being investigated for SMA are SMN-independent and target the motor unit, either through muscle enhancing or neuroprotection, rather than SMN expression. These are certainly not as effective as SMN-dependent therapies but are the focus of research into combinatorial therapies. For example, SRK-015 (Scholar Rock) is a myostatin inhibitor. Myostatin is involved in the inhibition of muscle growth and differentiation and therefore inhibition of this protein results in increased muscle mass. In mouse models of SMA, SRK-015 improved muscle function and as a result, Scholar Rock have recently begun safety and tolerability trials of SRK-015 in healthy adult controls (ScholarRock 2017; Shorrock et al. 2018). Assuming success in this trial, a subsequent Phase II trial will look at the effects of SRK-015 in

SMA patients that have or have not been treated with Spinraza (ScholarRock 2017; Shorrock et al. 2018).

Olesoxime (Roche) has been shown to stop excessive permeability of mitochondria under stressful conditions and to prevent the release of pro-apoptotic factors from mitochondria, resulting in neuroprotection within mouse models of neurodegenerative diseases (Bordet et al. 2010; Sunyach et al. 2012). Therefore, Olesoxime was put into clinical trials for SMA (Bertini et al. 2017). However, following poor results, Roche ended these clinical trials in June 2018 (Marques Lopes 2018). Despite the poor results with Olesoxime, the idea of a neuroprotection drug is one that should perhaps be further explored as research into combinational therapies continues.

All research to date has been paramount in the success of SMA therapies. However, more research into SMA is still required while the long-term effects of Spinraza and other gene therapy treatments are awaited. Continuing to look into possible therapeutic modifiers may give rise to other combinational therapies. Furthermore, increasing our understanding of SMA pathogenesis, through fundamental scientific research, continues to be important as an increased knowledge of SMA will give us a better chance of finding further ways to improve the lives of SMA patients. It is for this reason that the aims of this thesis are presented below.

1.10 Aims

A number of aims that will be addressed in the remainder of this thesis are detailed below. These aims have been formulated in order to further our knowledge into the pathogenesis of SMA.

Aim 1: Investigate the timing and mechanism of motor neuron pathology onset in the *Smn$^{2B/-}$* mouse model of SMA

Hypothesis 1A: Motor neuron pathology occurs in a distal to proximal manner

1A Perform a temporal analysis of NMJ and MNCB pathology in the *Smn$^{2B/-}$* mouse model of SMA

Hypothesis 1B: The activation of the P53 signaling pathway causes NMJ degeneration

1B Investigate the effects of a reduction in P53 on pathology at the NMJ and the MNCB in the *Smn$^{2B/-}$* mouse model of SMA

Aim 2: Investigate whether there are compensatory subpopulations of motor neurons in the *Smn$^{2B/-}$* mouse model that are responsible for masking degeneration in muscles that are less vulnerable to degeneration

Hypothesis 2A: Compensatory sprouting is responsible for the lack of denervation observed in less vulnerable muscles of the Smn$^{2B/-}$ mouse model of SMA

2A Investigate NMJ degeneration in vulnerable and resistant muscles of the *Smn$^{2B/-}$* mouse model of SMA and determine whether sprouting could be responsible for masking degeneration in resistant muscles

Hypothesis 2B: There are subpopulations of motor neurons that are 'healthier' and compensate for the degeneration of other motor neurons in the $Smn^{2B/-}$ mouse model of SMA

2B Examine pathology of single motor units within $Smn^{2B/-}$ mice to determine whether there are divergent populations of motor neurons

Aim 3: Investigate motor unit pathology in mouse models that have reduced Smn but are asymptomatic

Hypothesis 3: Compensatory sprouting is responsible for the lack of denervation observed in mice that have reduced Smn but are asymptomatic

3A Investigate MNCB loss as well as degeneration and regeneration of the NMJ in the $Smn^{+/-}$ mouse model, which expresses only 50% of normal Smn protein levels

3B Investigate MNCB loss as well as degeneration and regeneration of the NMJ in the $Smn^{2B/2B}$ mouse model, which expresses only 30% of normal Smn protein levels

Chapter 2

Materials and Methods

2.1 Mouse breeding

2.1.1 *Smn$^{2B/-}$* mice

The *Smn$^{2B/-}$* mouse model of SMA, which had been established within our laboratory, was maintained at the University of Edinburgh animal facilities (Central Campus) in Individually Ventilated Cages (IVCs) on a C57BL/6 background. Male and female *Smn$^{2B/+}$* mice (mice with the *Smn2B* allele were originally obtained from the Kothary Laboratory, Ottawa) had been crossed to produce *Smn$^{2B/2B}$* mice, as well as *Smn$^{2B/+}$* and *Smn$^{+/+}$* littermates. Subsequently, *Smn$^{2B/2B}$* mice were bred with Smn$^{+/-}$ mice (Strain: 10921, Jackson Laboratories) to give experimental *Smn$^{2B/-}$* mice and control *Smn$^{2B/+}$* littermates (Bowerman et al. 2012a).

2.1.2 *Smn$^{2B/-}$;P53$^{fl/fl}$;Cre^{+}* mice

Smn$^{2B/-}$;P53$^{fl/fl}$;Cre^{+} mice were established within our laboratory (for the establishment of this colony please refer to Figure 3.10 within Chapter 3). They were maintained at the University of Edinburgh animal facilities (Western General Hospital Campus) in open caging on a C57BL/6 background.

To establish this colony, *Smn$^{+/+}$;P53$^{fl/+}$;Cre^{-}* mice were kindly donated to our laboratory by Dr Luke Boulter and Dr Kevin Myant (University of Edinburgh). These were bred with mice carrying CAG-Cre-ER, a tamoxifen inducible Cre that is ubiquitously expressed (strain: 004682, Jackson Laboratories), which had been kindly donated by Dr You-Ying Chau (University of Edinburgh).

Using *Smn*$^{2B/2B}$ and *Smn*$^{+/-}$ from our own colony, the *Smn*$^{2B/2B}$;*P53*$^{fl/fl}$;*Cre*$^{-}$ and *Smn*$^{+/-}$;*P53*$^{fl/fl}$;*Cre*$^{+}$ mice were derived (Figure 3.10) and were bred to give experimental litters containing mice of the following genotypes;

- *Smn*$^{2B/-}$;*P53*$^{fl/fl}$;*Cre*$^{+}$ mice
- *Smn*$^{2B/-}$;*P53*$^{fl/fl}$;*Cre*$^{-}$ mice
- *Smn*$^{2B/+}$;*P53*$^{fl/fl}$;*Cre*$^{+}$ mice
- *Smn*$^{2B/+}$;*P53*$^{fl/fl}$;*Cre*$^{-}$ mice

2.1.3 *Thy-1-YFP-H* mice

Thy1-YFP-H mice were purchased from Jackson Laboratories (Strain: 003782). These mice were wild type for *Smn* and so had the genotype *Smn*$^{+/+}$;*YFP-H*. They were crossed with *Smn*$^{+/-}$ to produce *Smn*$^{+/-}$;*YFP-H* and *Smn*$^{+/+}$;*YFP-H mice* that were aged at Charles River Laboratories, East Lothian, in IVCs.

Additionally, *Smn*$^{+/+}$;*YFP-H* mice were bred with *Smn*$^{2B/2B}$ mice at the University of Edinburgh animal facilities (Central Campus) in IVCs. *Smn*$^{2B/+}$;*YFP-H* mice were interbred to produce *Smn*$^{2B/2B}$;*YFP-H* mice. By crossing these with *Smn*$^{+/-}$;*YFP-H* mice, *Smn*$^{2B/-}$;*YFP-H* mice and control *Smn*$^{2B/+}$;*YFP-H* mice were obtained.

2.2 Genotyping

2.2.1 DNA Extraction

DNA was extracted from tail tips or ear clips by digesting the tissue in 500µl of Tail Tip Lysis Buffer (TTLB; 0.5M EDTA, 1M Triz-HCl, 1M NaCl, 10% SDS, ddH2O) and 2.5µl of Proteinase K (1mg/ml) for 24 hours at 55^{o}C. DNA was precipitated in Isopropanol and washed in 70% ethanol. It was re-suspended

in 50µl of ddH2O for ear clips and 200µl of ddH_2O for tail tips to give a concentration of approximately 200ng/µl.

2.2.2 *Smn*$^{2B/-}$ mice

Smn2B gene

To determine what mice carried the *Smn2B* allele, PCR was carried out using the Invitrogen Taq Polymerase kit with a forward and reverse primer (please refer to Table 2.6 for primer sequences; sequences originally obtained from the Kothary Laboratory). Temperature cycling was as shown in Table 2.1.

Gel electrophoresis, using a 1.5% agarose gel that contained 0.01% SYBRSafe DNA stain (Invitrogen), separated the DNA strands created by this PCR protocol. An upper 700bp band denoted the *Smn2B* allele and a lower 500bp band denoted the murine *Smn* (*mSmn*) allele (Figure 2.1).

As the primers for this protocol bind within exon 7 of the *Smn* gene and the mutation that results in this gene being null is within exon 2 (Schrank et al. 1997), this protocol does not determine whether the m*Smn* allele is non-functional (null) or functional. A non-functioning *Smn* allele would result in no Smn product from this allele, as in the case of *Smn*$^{2B/-}$ *mice*. Therefore, to separate *Smn*$^{2B/+}$ (functioning *Smn* allele) and *Smn*$^{2B/-}$ (null *Smn* allele) mice the '*mSmn* gene' protocol, shown below, must be used.

Table 2.1: PCR temperature cycling for *Smn2B* genotyping protocol

Step	Temperature (°C)	Duration
1	94	3 minutes
2	94	45 seconds
3	58	45 seconds
4	72	45 seconds
5	*Repeat steps 2-4*	*35 times*
6	72	5 minutes
7	4	Hold

mSmn gene

To determine whether the *mSmn* allele *Smn2B* mice carried was functional or non-functional (null), PCR was preformed using the Invitrogen Taq Polymerase kit, a common forward primer and two reverse primers, one that binds to the wild-type genetic sequence and another that binds to the inserted cassette that creates the null allele (Table 2.6; sequences obtained from Jackson Laboratories). Table 2.2 displays the temperature cycling protocol.

As above, gel electrophoresis separated the DNA strands created from this PCR protocol and these are shown in Figure 2.1. An upper 800bp band represents the wild-type *Smn* allele and a lower 500bp band represents the null-*Smn* allele.

Table 2.2: PCR temperature cycling for *mSmn* genotyping protocol

Step	Temperature (°C)	Duration
1	94	3 minutes
2	94	30 seconds
3	58	1 minute
4	72	1 minute
5	*Repeat steps 2-4*	*35 times*
6	72	2 minutes
7	4	Hold

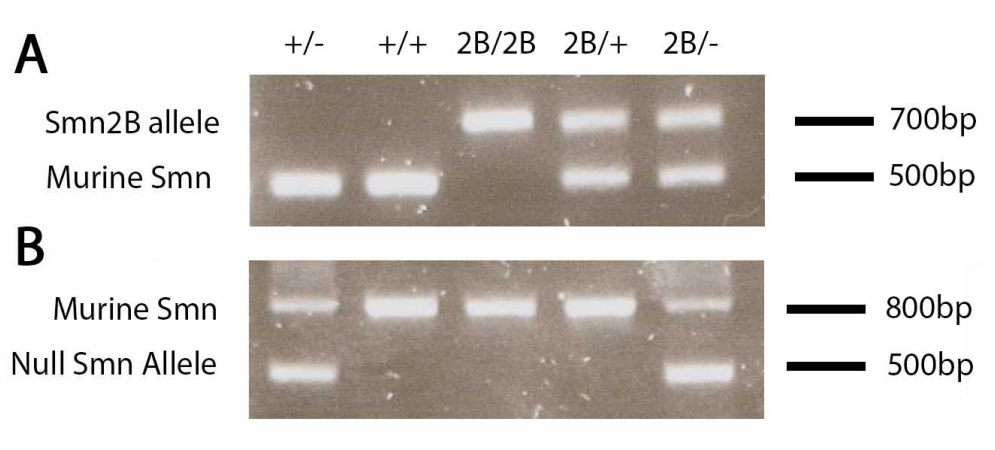

Figure 2.1: PCR and gel electrophoresis determines the *Smn* genotype of a mouse (**A**) Image of a gel showing the results of the *Smn2B* PCR protocol. The *Smn2B* allele is amplified to give a 700bp band and the *mSmn* gene is amplified to give a 500bp band. (**B**) To determine whether this *mSmn* allele was functional or non-functional (null), the *mSmn* PCR protocol was performed. The gel shows a 500bp band where the mouse carries a null *Smn* allele.

2.2.3 *Smn$^{2B/-}$;P53$^{fl/fl}$;Cre^{+}* mice

Throughout the breeding of this colony several genotyping protocols were required. Genotyping for the *Smn2B* and null *mSmn* alleles followed the same protocols noted above under '*Smn$^{2B/-}$* mice'. In addition to this, genotyping was required for *Cre* and the *P53-floxed* allele.

Cre

Mice were bred to only express only one or no copies of Cre and therefore genotyping was required to separate those positive or negative for Cre. PCR was carried out using the Invitrogen Taq Polymerase kit, and two primer sets; one that amplifies a control sequence within interleukin-2 (Primer-BLAST, NCBI), to show a successful PCR, and another that amplifies the Cre sequence (primer sequences are shown in Table 2.6; sequences obtained from Dr Luke Boulter). The temperature cycling for this PCR protocol is shown in Table 2.3.

Subsequent gel electrophoresis was preformed and shows the control band, denoting a successful PCR, at 300bp and, if positive for Cre, a band is displayed at 100bp (Figure 2.2).

Table 2.3: PCR temperature cycling for *Cre* genotyping protocol

Step	Temperature (°C)	Duration
1	94	3 minutes
2	94	30 seconds
3	51.7	1 minute
4	72	1 minute
5	*Repeat steps 2-4*	*35 times*
6	72	2 minutes
7	4	Hold

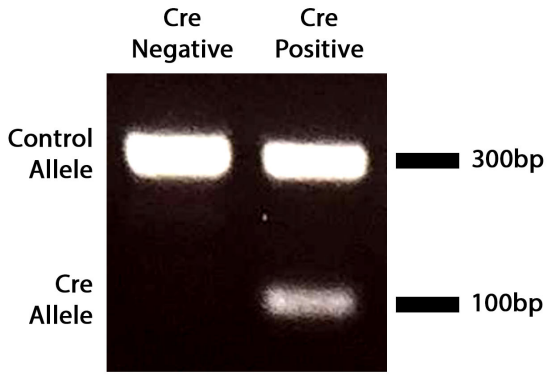

Figure 2.2: PCR and gel electrophoresis reveals the presence or absence of Cre. The image of a gel displays the result of the *Cre* PCR protocol. A control band at 300bp denotes a successful PCR run and a band at 100bp represents positivity for *Cre*.

P53-floxed

To differentiate between mice that carried a P53-floxed (*P53fl*) allele and those that did not, PCR was carried out using the KAPA2G Robust PCR kit with dNTPs (KAPA Biosystems Ltd) and two sets of primers. One set amplified a control sequence, within a non-floxed region of the *P53* gene, and the other amplified a region of the *P53fl* allele (Table 2.6; sequences obtained from Dr Luke Boulter). The temperature cycling programme was as shown in Table 2.4.

Again, gel electrophoresis separated the two products giving a lower 100bp control band, denoting a successful PCR, and an upper 300bp band if positive for *P53fl* (Figure 2.3).

Homozygosity for the *P53fl* allele was required to ensure the maximum knockdown of P53. In order to separate homozygous and heterozygous mice, copy number genotyping, using qPCR, was required. To preform qPCR, all DNA samples were diluted to 10ng/ul. SYBR green-based qPCR was preformed using Kapa SYBR Fast Universal (Kapa Biosystems) and the CFX Connect Real-time PCR Detection system (Biorad). The *P53fl* primers detailed in Table 2.6 were optimised for quantitative use (please refer to Figure 3.11 in Chapter 3). The primers that amplified the control sequence and the primers that amplified the *P53fl* sequence were separated and each run in technical triplicate in separate wells. The Cq values for each sample

were collated in Microsoft Excel and the mean for each technical triplicate calculated. The mean Cq value of the *P53fl* amplicon was subtracted from the internal control amplicon Cq value for each sample. GraphPad Prism was used to produce a graph that plotted the difference between the mean Cq values of the two primer sets to compare unknown samples to samples that were known to be from heterozygous mice. Detailed results for this can be found in Chapter 3 (Figure 3.11).

Table 2.4: PCR temperature cycling for *P53fl* genotyping protocol

Step	Temperature (°C)	Duration
1	94	2 minutes
2	94	20 seconds
3	65	15 seconds
4	68	10 seconds
5	Repeat steps 2-4	10 times
6	94	15 seconds
7	60	15 seconds
8	72	10 seconds
9	Repeat steps 6-8	28 times
10	72	10 minutes
11	4	Hold

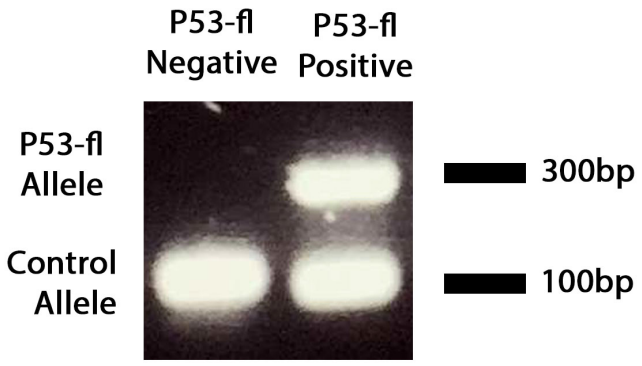

Figure 2.3: PCR and gel electrophoresis reveals the presence or absence of the *P53fl* allele. The image of a gel displays the result of the *P53fl* PCR protocol. A control band at 100bp denotes a successful PCR run and a band at 300bp would mean at least one of the *P53* alleles is *P53fl*.

2.2.4 *Thy-1-YFP-H* mice

Mice that were bred to express *YFP-H* were either $Smn^{+/+}$, $Smn^{+/-}$, $Smn^{2B/2B}$, $Smn^{2B/+}$ or $Smn^{2B/-}$. The genotyping of for these *Smn* genotypes can be found above under the '$Smn^{2B/-}$ mice' section.

YFP

To separate mice positive for YFP and mice negative for YFP the following PCR protocol was obtained from Jackson Laboratories. It was optimised using the GoTaq Flexi DNA polymerase kit with the four primer sequences given in their protocol. A forward and a reverse primer set that amplified the transgene itself and a forward and reverse primer set that displays mice negative for *YFP-H* (Table 2.6; sequences obtained from Jackson Laboratories). The temperature cycling programme shown in Table 2.5 was used.

Gel electrophoresis separated the two DNA sequences giving an upper 500bp band that represents the *YFP-H* positive mice and a lower 300bp band represented mice negative for the *YFP-H* transgene (Figure 2.4).

Table 2.5: PCR temperature cycling for *YFP-H* genotyping protocol

Step	Temperature (°C)	Duration
1	94	2 minutes
2	94	20 seconds
3	65	15 seconds
4	68	10 seconds
5	*Repeat steps 2-4*	*10 times*
	Decreasing the temperature of Step 3 by 0.5°C each	
6	94	15 seconds
7	60	15 seconds
8	72	10 seconds
9	*Repeat steps 6-8*	*28 times*
10	72	10 minutes
11	4	Hold

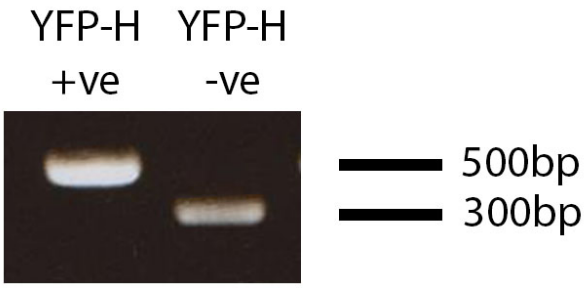

Figure 2.4: PCR and gel electrophoresis separates mice positive and negative for *YFP-H*. The image of a gel displays the result of the *YFP-H* PCR protocol. A mouse positive for *YFP-H* will show a 500bp band and a mouse negative for *YFP-H* will show a 300bp band.

Table 2.6: Primer sequences used in genotyping protocols

(all from Sigma)

Protocol	Sequence
Smn2B	Forward: 5'- AAC TCC GGG TCC TCC TTC CT -3' Reverse: 5'- TTT GGC AGA CTT TAG CAG GGC -3'
mSmn	Forward: 5'- CTC CGG ATA TTG GGA TTG -3' Reverse (for wildtype *mSmn*): 5'-TTT CTT CTG GCT GTG CCT TT -3' Reverse (for null *mSmn*): 5'- GGT AAC GCC AGG GTT TTC C -3'
Cre	Forward (Control): 5'-CTA GGC CAC AGA ATT GAA AGA TCT-3' Reverse (Control): 5'-GTA GGT GGA AAT TCT AGC ATC ATC C-3' Forward (Cre): 5'-GCG GTC TGG CAG TAA AAA CTA TC-3' Reverse (Cre): 5'-GTG AAA CAG CAT TGC TGT CAC TT-3'
P53-floxed	Forward (Control): 5'- CTC AGC AGT AAG GAA GAC AAA GTC A-3' Reverse (Control): 5'- CCA TGA GAC AGG GTC TTG CTA TT-3' Forward (P53-floxed): 5'-CTG TGC CCT CCG TCC TTT T -3' Reverse (P53-floxed): 5'-GGC TGC AGA TAA CTT CGT ATA GCA T-3'
YFP	Forward (Control): 5'- CTA GGC CAC AGA ATT GAA AGA TCT -3' Reverse (Control): 5'- GTA GGT GGA AAT TCT AGC ATC ATC C -3' Forward (YFP): 5'- ACA GAC ACA CAC CCA GGA CA -3' Reverse (YFP): 5'- CGG TGG TGC AGA TGA ACT T -3'

2.3 Tamoxifen dosing

To induce Cre production in *Smn*$^{2B/-}$;*P53*$^{fl/fl}$;*Cre*$^{+}$ and *Smn*$^{2B/+}$;*P53*$^{fl/fl}$;*Cre*$^{+}$ mice, experimental litters were treated with a tamoxifen solution. Tamoxifen (Sigma-Aldrich) was dissolved in corn oil, to give a 20mg/ml solution, using a sonicating water bath. The solution was exposed to the water bath for 45 minutess at room temperature. Pups in experimental litters were dosed 75mg/kg of this tamoxifen solution by modified oral gavage at P4 and P5. Following dosing, body weights were recorded and motor tests were performed as detailed below.

2.4 Phenotypic analysis

Motor testing of mice involved two tests. The first was the 'time to right' test that was carried out on mice younger than P11-P12. Mice were placed on their back and the time it took for them to right themselves (turn to be on all four paws) was noted. The test was stopped when mice had been attempting to do this for 30 seconds. This test was repeated 3 times with a two-minute rest period between testing. Mice were nested together during rest period to reduce the risk of hypothermia.

As all mice aged over 11 days were able to perform this task well, including experimental *Smn*$^{2B/-}$ mice, a second test was created to test motor performance in older pups. This second test, which was termed the 'turn around test', involved placing mice, head down on a gridded cage top that was at a 45^{o} angle. The time it took for mice to turn 180^{o} to face up was noted. This test was also stopped at 30 seconds. If mice were unable to remain on the angled cage top then this was noted as the maximum time of 30 seconds.

Body weight was also tracked over time and any phenotypic abnormalities were recorded.

2.5 Euthanasia

Mice housed at the Central Campus facilities were sacrificed by overdose of anaesthetic (IsoFlo, Abbott, Quèbec, Canada) and death was confirmed using exsanguination of the carotid artery. Mice housed at this campus that were under the age of P7 were sacrificed by decapitation following anaesthesia (IsoFlo, Abbott, Quèbec, Canada).

$Smn^{2B/-}$;$P53^{fl/fl}$;Cre^{+} and control mice that were housed at the Western General Hospital Campus were sacrificed by overdose of CO_2 and death was confirmed using exsanguination of the carotid artery.

All procedures were carried out in accordance with the procedures approved and licensed by the Home Office, United Kingdom.

2.6 Immunofluorescence

2.6.1 Immunofluorescence for NMJ Analysis

Preparation of muscles

Several different muscles have been used in various aspects of this thesis, including cranial, abdominal and thoracic musculature. This is due to the status of differential vulnerability to pathology that these muscles express. For example, while the abdominal musculature is vulnerable to the degeneration of motor neurons, cranial musculature has significantly less degeneration of motor neurons (Figure 4.10; Murray et al. 2012).

Cranial musculature includes the Levator Auris Longus caudal band (LALc), Lavator Auris Longus rostral band (LALr), Abductor Auris Longus (AAL) and Auricularis Superior (AS) muscles, which are located superficially at the base of the skull and are involved in moving the ear. They originate from a

tendonous raphae that connects to the midline of the skull and insert onto the cartilage of the ear (Murray et al. 2010). To obtain these muscles, the muscles themselves and the tissue that surrounds them were gross dissected from the mouse and fixed for 15 minutes in 4% Paraformaldehyde (PFA; Electron Microscopy Science) in Phosphate Buffered Saline (PBS). Following fixation, muscles were finely dissected out of the surrounding tissue and prepared for immunofluorescent staining by removing excess fascia (Figure 2.5).

Abdominal musculature forms the abdominal wall of the mouse and includes the Rectus Abdomins (RA), External Oblique (EO) and Transverse Abdominis (TVA) muscles. The abdominal wall was gross dissected from the mouse and fixed in 4% PFA in PBS for 15 minutes. These muscles were finely dissected from the abdominal wall and prepared for immunofluorescent staining by removing excess fascia (Figure 2.6).

The Triangularis Sterni (TS) is a thoracic muscle that lies deep to the ribs and intercostal muscles. Therefore, the ribcage was grossly dissected and was fixed in 4% PFA in PBS for 15 minutes. The TS muscle was fine dissected by removal of the ribs and intercostal muscles (Figure 2.7).

Staining of Muscles for NMJ Analysis

Muscles were permeabilised in 2% Triton X-100 in PBS for 30 minutes and blocked in 4% Bovine Serum Albumin (BSA), 1% Triton X-100 in PBS for 30 minutes. They were subsequently incubated in primary antibody (Neurofilament (2H3) at 1:50 and SV2 (Synaptic Vesicle 2) at 1:100, Developmental Hybridoma Bank) in blocking solution for 72 hours at $4^{o}C$ on a rocking platform. Following three 10-minute PBS washes, muscles were immersed in secondary antibody (AlexaFluor-488 rabbit anti-mouse (green) at 1:250, Jackson) in PBS for 24 hours at room temperature. Subsequently, muscles were incubated in α- bungarotoxin (tetramethylrhodimine conjugate,

Life Technologies) in PBS for 2 hours at room temperature to label post-synaptic acetylcholine receptors. Following another three 10-minute PBS washes, muscles were mounted in Mowiol (Sigma).

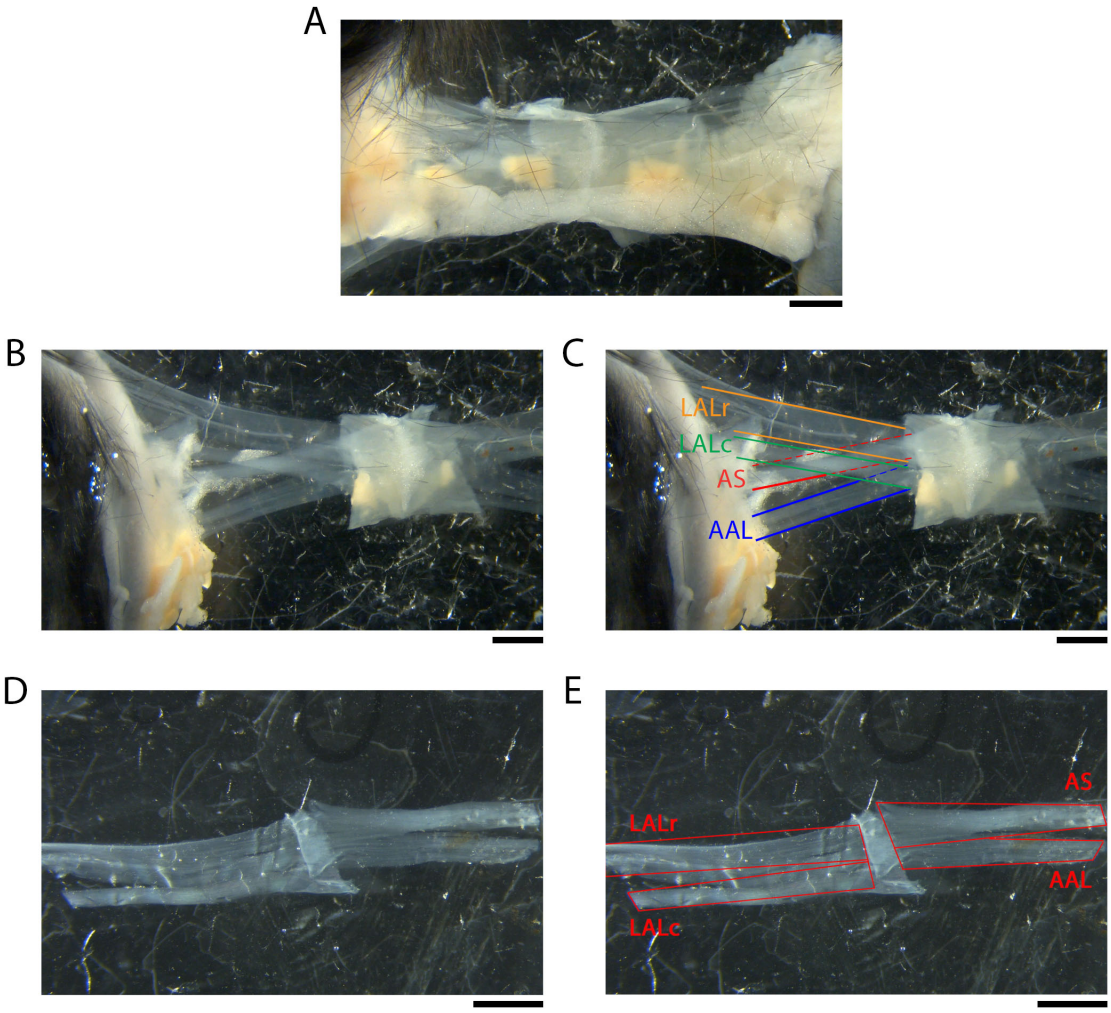

Figure 2.5: Cranial musculature was dissected for subsequent NMJ analysis. (**A**) Image shows gross dissected muscles following fixation. Note the large amount of surrounding tissue that obscures a clear view of the muscles of interest. (**B**) Image shows cranial muscles that connect to the skin of the mouse (left) and the midline (right in the image) following the fine dissection of tissue seen in A. (**C**) Image is the same as is seen in B with an overlay of the muscles of interest. (**D**) Image shows the muscles that have been removed from the skin of the mouse and opened from the midline to lie flat on the surface of the dish. At this point excess fascia is removed. (**D**) This image is the same as that seen in C but with an overlay labelling the individual cranial muscles. All scale bars = 25mm.

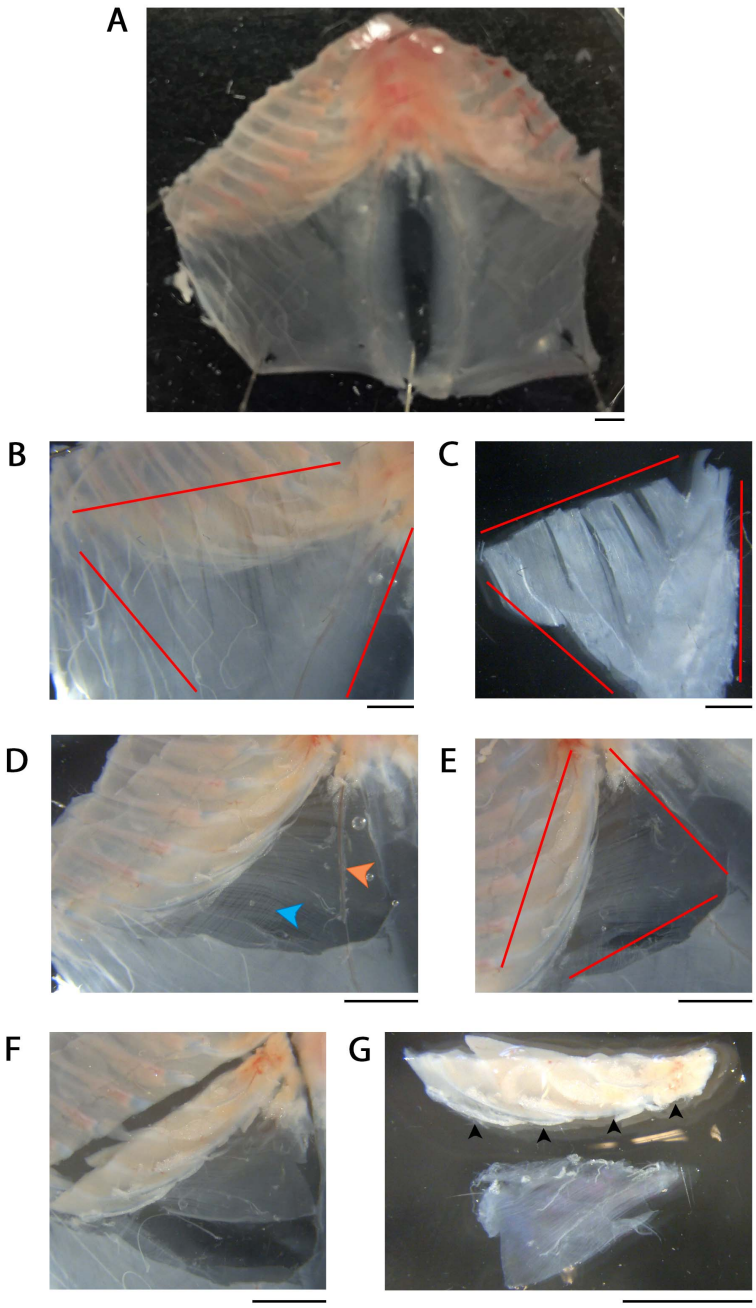

Figure 2.6: Abdominal musculature was dissected for subsequent NMJ analysis. The process of dissection is laid out from A-G (**A**) Image shows gross dissected abdominal wall following fixation. (**B**) Red lines indicate where the superficial RA and EO will be cut. (**C**) Image shows the RA muscle (thick vertical band of muscle on the far right) and the EO muscle (splayed out on the left from the RA muscle) following removal from the abdominal wall. (**D**) Image shows the abdominal wall following removal of the RA and EO muscles. Note the blood vessel (orange arrowhead) and the internal oblique (blue arrowhead) that are superficial to the TVA and will be removed. (**E**) By cutting along the red lines shown in the image, the TVA muscle and a proportion of the rib cage is removed from the abdominal wall as shown in F. (**G**) The ribs are removed from the TVA muscle and excess fascia is removed in preparation for immunostaining. All scale bars = 2.5mm.

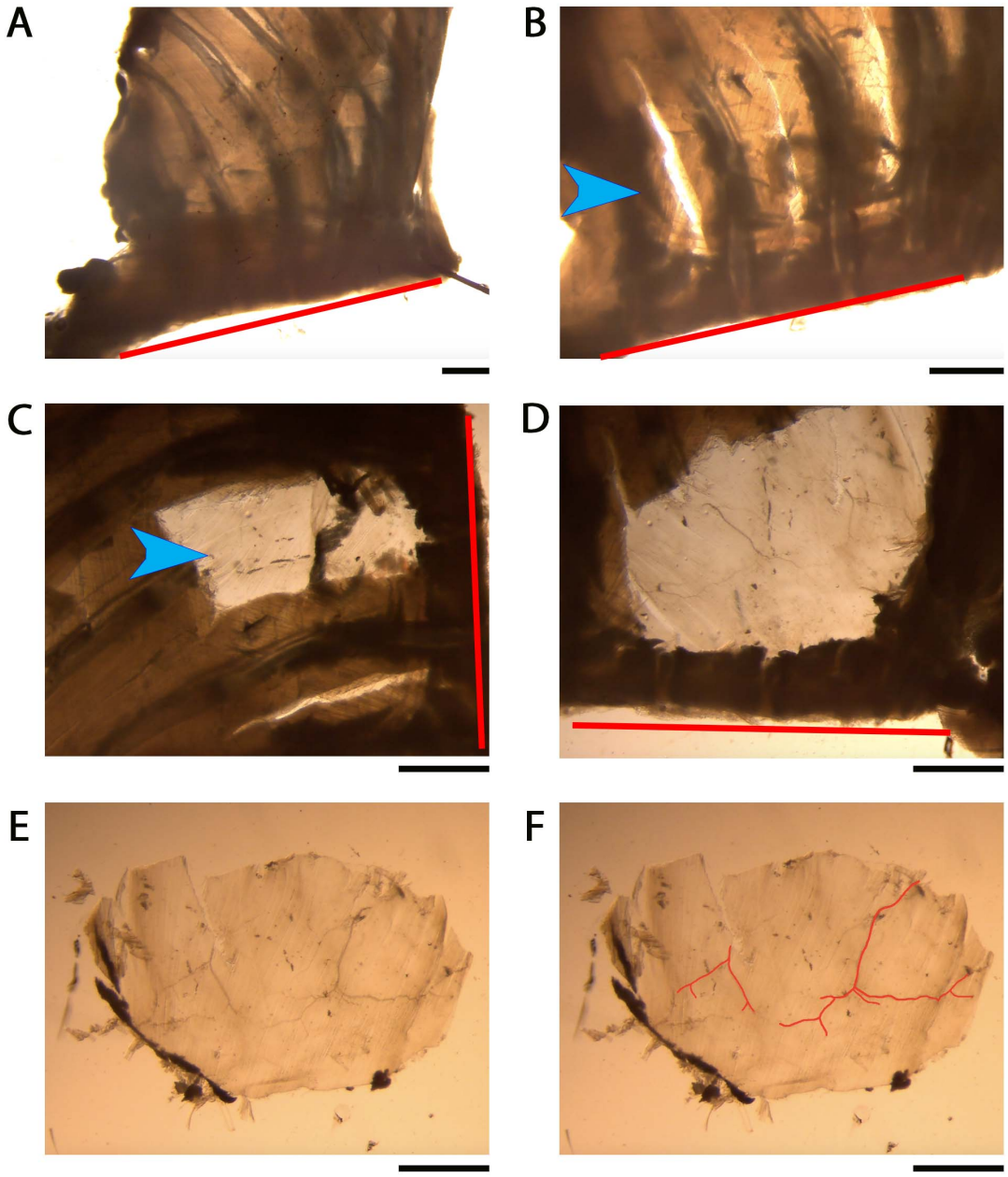

Figure 2.7: The thoracic TS muscle was dissected for subsequent NMJ analysis. The process of dissection is laid out from A-E. The red line in images A-D indicates the midline of the ribcage. (**A**) Image shows half of the gross dissected ribcage following fixation. The ribcage has been cut down its midline (red line) and the two halves separated (**B**) Between the ribs, intercostal muscles are cut to expose the underlying TS muscle (blue arrowhead). (**C**) Ribs are cut from the sternum and peeled from the underlying TS muscle (blue arrowhead). (**D**) Once exposed, excess fascia is removed from the TS muscle and it is cut from the ribcage around its exposed periphery. (**E**) The TS muscle, as seen in this image, is processed for immunostaining. (**F**) Note that the red line shows the axonal layout within this muscle. All scale bars = 1mm.

Staining of Muscles for Motor Unit Analysis

Muscles that should contain YFP were dealt with quickly to avoid fading of the YFP. Muscles that had been removed from recently sacrificed mice were pinned and fixed for 15 minutes in 4% PFA. Muscles were at room temperature and on a rocking platform in the dark. Fine dissection was completed immediately after and muscles were incubated in BTX at 1:250 for 1 hour at room temperature, in the dark and on a rocking platform. Muscles were mounted in mowiol (Sigma) on glass slides and stored at 4^{o}C.

2.6.2 Immunofluorescence on spinal cord sections

Preparation of spinal cords

Spinal columns were removed from recently sacrificed mice in order to retrieve the spinal cord. Spinal cords were ejected from the column by forcing PBS from a syringe through a needle placed within the lumbar end of the spinal column. For all mice used in Chapter 3, the left and right sides of the spinal cord were separated down the midline as one half was prepared for immunofluorescence and the other was frozen on dry ice and stored at -80^{o}C for use in qPCR analysis. For mice used in Chapter 4 and 5, whole spinal cords were prepared for immunofluorescence. Spinal cords processed for immunofluorescence were fixed in 4% PFA in PBS for 4 hours before washing in PBS. They were immersed in 30% sucrose for 48 hours prior to embedding in 50% OCT; 30% sucrose in PBS mixture.

For mice used in the characterisation of pathology work carried out in Chapter 3 (i.e MNCB number and size), spinal cords were trimmed at the lumbar enlargement prior to embedding to ensure that those from $Smn^{2B/-}$ mice and from $Smn^{2B/+}$ littermate controls were the same length. The embedding method for these spinal cords varied depending on the age of the mouse from which the spinal cord was obtained from. P1 and P5 spinal cords

were embedded medial side down and so sagittal sections were obtained. P10 and P15 spinal cords were embedded first in agar and once set, the agar block was embedded so the ventral surface of the spinal cord was facing down. This would allow coronal sections of the spinal cord to be cut. This was to ensure that the maximum number of motor neurons was obtained in the fewest sections. This method of embedding was initially carried out and refined by Alannah Mole.

For mice carrying the *P53fl* gene in Chapter 3, spinal columns were trimmed at vertebrae T4 prior to the ejection of the spinal cord. T4 was located by counting ribs starting at the 12th rib. Spinal cords were immersed in 30% sucrose for 48 hours prior to embedding in 50% OCT; 30% sucrose in PBS mixture. This method was also used for P18 mice used in Chapter 4. For the mice aged 3 months or older that were used in Chapter 5, spinal columns were trimmed at vertebrae T8 prior to the ejection of the spinal cord. Again, T8 was located by counting ribs starting at the 12th rib. T8 was the vertebrae chosen in this case as it was below the lordosis curvature of the upper spinal column that makes ejection of the spinal cord difficult. As before, these spinal were immersed in 30% sucrose for 48 hours prior to embedding in 50% OCT; 30% sucrose in PBS mixture. The thoracic spinal cord was used for analysis, as this is the region where motor neurons that supply the thoracic and abdominal musculature and are vulnerable to degeneration lie.

Regardless of the preparation method that was used, all embedded tissue was snap frozen on dry ice and stored at -80^{o}C. Frozen sections were cut at 10μm on a cryostat (Leica).

For characterisation work carried out in Chapter 3, longitudinal sections were collected on alternating glass slides to give two sets of slides, an A set and B set. All sections were collected.

For work relating to the investigation of P53 in SMA in Chapter 3 and for all mice used in Chapter 4 and 5, spinal cords were sectioned transversely. Every 10th section was collected on one slide. This was carried out in triplicate to provide three sets of slides. Approximately 2mm of the spinal cord was sectioned.

All slides were stored at -20^{o}C until they were processed for immunofluorescent staining.

Staining of spinal cord sections

Staining of slides was done in the Sequenza Immunostaining Centre (Fisher) and all reagents were applied at a volume of 300μl per slide. Two staining protocols were used; one for ChAT and anti-active caspase 3 and the other for pH2AX.

For ChAT and anti-active caspase 3

Sections were washed in PBS, permeabilised in 0.3% Triton X-100 in PBS for 30 minutes and blocked in 0.1% Power Block (100x, Biogenex Laboratories, HK085-5K) in PBS for 10 minutes. Following two 2-minute PBS washes, sections were incubated in ChAT or anti-active caspase 3 primary antibody (detailed in Table 2.7) in 0.3% Triton X-100; 1% Bovine Serum Albumin (BSA) in PBS at 4^{o}C, for 72 hours. Following this, slides were washed twice with 0.2% Triton X-100 for 5 minutes. Secondary antibody (detailed in Table 2.7) was applied for 2 hours at a dilution of 1:250 at room temperature. Sections were then stained with DAPI (Life Technologies) at 1:1000 for 10 minutes, washed with 0.2% Triton X-100 three times for 5 minutes and stained with the fluorescent Nissl stain NeuroTrace (Either 500/525 (Green) or 530/615 (Red), both Life Technologies, depending upon the fluorophore of the secondary antibody that had been used) at 1:100 for

30 minutes. Sections were subsequently washed twice with 0.2% Triton X-100 for 5 minutes before mounting in Mowiol (Sigma).

For anti-pH2AX

Sections were washed in PBS, permeabilised in 0.3% Triton X-100 in PBS for 30 minutes and blocked in 0.3% Triton X-100; 4% BSA in PBS for 30 minutes. Sections were incubated in anti-pH2AX primary antibody (detailed in Table 2.7) in blocking solution (0.3% Triton X-100; 4% BSA) that had been diluted 1:250 in PBS. Slides were left for 24 hours at 4^{o}C. Following this, slides were washed three times with PBS for 5 minutes. Secondary antibody (detailed in Table 2.7) was diluted in 0.3% Triton X-100 at 1:250 and applied for 2 hours at room temperature. Sections were then stained with DAPI (Life Technologies) and NeuroTrace as above before washing with PBS and mounted in Mowiol (Sigma).

Table 2.7: Antibodies, and their associated information, used in the immunofluorescent staining of spinal cord sections

Primary Antibody	Supplier	Dilution	Duration	Secondary Antibody	Supplier	Dilution
Goat anti-choline acetyl-transferase (ChAT)	Merck Millipore	1:100	72 hours	AlexaFluor 555 Donkey anti-Goat	Life Tech-nologies	1:250
Rabbit anti-active caspase 3	BD Bioscience	1:100	72 hours	AlexaFluor 488 Donkey anti-Rabbit	Life Tech-nologies	1:250
Rabbit anti-P53	Leica	1:250	24 hours	AlexaFluor 488 Donkey anti-Rabbit	Life Tech-nologies	1:250
Rabbit anti-pH2AX	Cell Signaling Technology	1:350	24 hours	AlexaFluor 555 Goat anti-Rabbit	Life Tech-nologies	1:200

2.7 Quantification and Statistics

2.7.1 NMJ Analysis

Occupancy

The occupancy of post-synaptic endplates was assessed and graded using specific criteria (Table 2.8; Figure 2.8). At least three fields of view were analysed with >50 NMJs quantified per muscle. All analysis was done on a standard fluorescent microscope (Leica DM8) at 40x magnification. Representative images were taken on a confocal microscope (Nikon A1R FLIM) at 40x magnification. All data was collated and analysed using Microsoft excel (Mac 2011) and GraphPad Prism (Version 6 for Mac OS X). The percentage of NMJs displaying each stage of occupancy was calculated and a Mann Whitney-U test compared these between experimental mice and their relevant controls.

Table 2.8: The criteria used to determine endplate occupancy of post-synaptic endplates

Occupancy Category	Criteria
Full	Pre-synaptic terminal completely covers the post-synaptic terminal
Partial	Pre-synaptic terminal partially covers the post-synaptic terminal, leaving some areas of the post-synaptic terminal denervated
Vacant	No axonal input to the post-synaptic endplate

Pre-synaptic Swelling

The level of pre-synaptic swelling at NMJs was graded (Table 2.9; Figure 2.8). As above, at least three fields of view were analysed with >50 NMJs quantified per muscle. All analysis was done on a standard fluorescent microscope and representative images were taken on a confocal microscope, both at 40x magnification. All data was collated and analysed using Microsoft excel (Mac 2011) and GraphPad Prism (Version 6 for Mac OS X). The percentage of NMJs with each grade of swelling was calculated and a Mann Whitney-U test compared each grade of pre-synaptic swelling between experimental mice and their relevant controls.

Table 2.9: The criteria used to determine the level of pre-synaptic swelling in NMJ analysis

Stage of Pre-synaptic swelling	Criteria
None	No evidence of pre-synaptic or axonal swelling
Mild	Evidence of some axonal swelling and/or pre-synaptic swelling that does not obscure the end plate
Moderate	Evidence of clear axonal swelling and significant pre-synaptic swelling that is beginning to obscure the end plate
Severe	Significant and obvious swelling along the length of the axon and severe swelling around the pre-synaptic terminal, which obscures the endplate

Endplate Size

Images of endplates within each muscle were captured on a standard fluorescent microscope (Leica DM8). The number of images depended upon the number of endplates within each image. Enough images were captured in order to measure >50 endplates. In Fiji Image Processing Software, the periphery of each endplate was traced and the area within measured. Microsoft Excel was used to collate the measurement information and this was subsequently analysed in GraphPad Prism. The average endplate area for a muscle was calculated and an unpaired t-test compared the average endplate size between experimental mice and their relevant controls.

Endplate Maturation

A criterion was established to stage the maturity of individual endplates (Table 2.10; Figure 2.8). As above, at least three fields of view were analysed with >50 NMJs quantified per muscle. All analysis was done on a standard fluorescent microscope. All data was collated and analysed using Microsoft excel (Mac 2011) and GraphPad Prism (Version 6 for Mac OS X). The percentage of NMJs displaying each stage of maturation was calculated and a Mann Whitney-U test compared each stage of maturity between experimental mice and their relevant controls.

Table 2.10: The criteria used to determine the stage of endplate maturation in NMJ analysis

Stage of Endplate Maturation	Criteria
Stage 4	Immature endplate; endplate has a plaque-like appearance
Stage 3	Endplate is developing from a plaque-like structure and 'highlights' are visible on the plaque
Stage 2	Endplate is developing into a pretzel-like structure, 'highlights' remain and there is now 'spaces' within the endplate
Stage 1	Fully mature endplate; endplate has a pretzel-like appearance

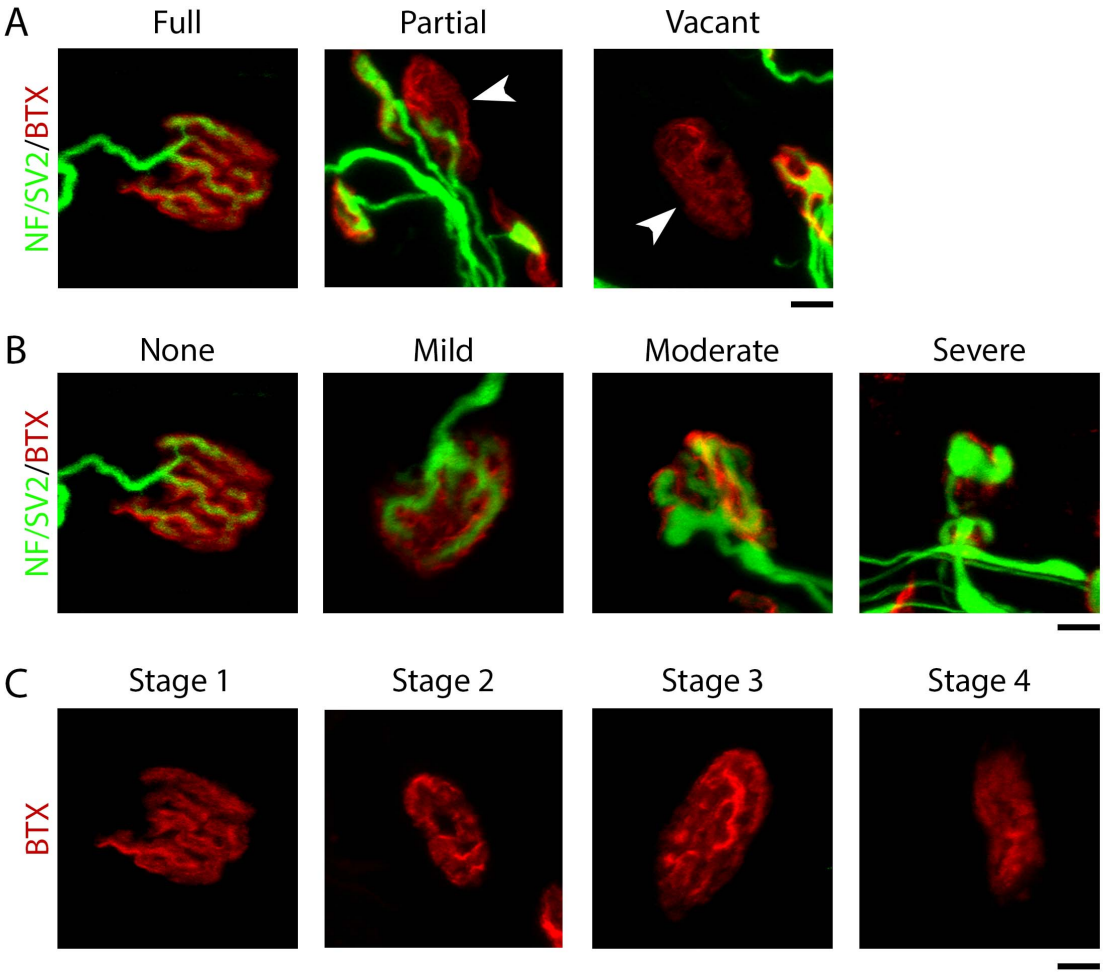

Figure 2.8: Features of NMJ morphology can be categories for analytical purposes. (**A**) Images show examples of fully occupied (full), partially occupied (partial) or vacant post-synaptic endplates. White arrowheads point out the NMJs that display the category of occupancy noted above their image. The criteria used to describe each of the stages can be seen in Table 2.8 (**B**) Images show examples of NMJs with none, mild, moderate and severe pre-synaptic swelling. The criteria used to describe each of the stages can be seen in Table 2.9 (**C**) Images show examples of stage 1-4 endplate maturity. The criteria used to describe each of the stages can be seen in Table 2.10. All scale bars = 10um

2.7.2 Whole Motor Unit Analysis

Images of the motor unit were taken at x20 magnification on a standard fluorescent microscope (Leica DM8, Leica Application Suite X). These were assembled in Adobe Photoshop to allow the whole motor unit to be traced. Areas of ambiguity were checked on the fluorescent microscope to confirm the layout of the motor unit. Once traced the morphology at the NMJs of the motor unit were assessed on the fluorescent microscope. Various features were quantified; Pre-synaptic swelling, occupancy, endplate maturation and evidence of sprouting. Endplate size was determined by imaging the endplates of interest and measuring the area of these in Fiji Image Analysis Software. NMJs that were not quantifiable due to being misaligned or, in terms of endplate size, out of focus in the images were excluded. The branching pattern of the traced motor unit was simplified into a tree diagram on Adobe Photoshop. A tree diagram was made for each parameter measured for each motor unit traced. Data was collated in Microsoft Excel (Mac 2011) and GraphPad Prism (Version 6 for Mac OS X) was used to generate graphs.

2.7.3 Motor Neuron Cell Body Analysis

Motor Neuron Number

For characterisation work carried out in Chapter 3, longitudinal sections were collected on alternating glass slides to give two sets of slides, an A set and B set. One set was stained with ChAT to labels motor neurons. This allow the counting of motor neuron cell bodies (MNCBs) within the ventral horn of the spinal cord. Using a standard fluorescent microscope (Leica DM8), the number of MNCBs within each field of view was counted. MNCBs were distinguished from other neuronal material by their large size, irregular shape and were double stained with Nissl and ChAT. Only MNCBs that conformed

to this criterion and had a visible nucleus and nucleoli were counted. The numbers were collated in Microsoft excel and analysed in GraphPad Prism. A paired t-test compared the absolute number of MNCBs in *Smn*$^{2B/-}$ mice compared to *Smn*$^{2B/+}$ controls.

For work relating to the investigation of P53 in SMA in Chapter 3 and for all mice used in Chapter 4 and 5, where spinal cords were sectioned transversely, one slide (which contained every 10th section) was stained with ChAT. Again, only MNCBs that conformed to the criterion above were counted. The numbers were collated in Microsoft excel and analysed in GraphPad Prism. Using the number of MNCBs counted an approximate number was calculated for the whole area in which every 10th section was collected. This was then compared by unpaired t-test between experimental mice and their relevant controls.

Motor Neuron Size

To assess the size of MNCBs and their nuclei images of MNCBs (see the criterion above) were captured on a standard fluorescent microscope (Leica DM8). Images were opened in Fiji Image Processing Software and the periphery of each MNCB was traced. The area within was measured. In addition, the area of the nuclei was measured using the same method. Microsoft Excel was used to collate the measurement information and this was subsequently analysed in GraphPad Prism. The average area of MNCB or their nuclei, for each mouse, was calculated and a Mann Whitney-U test compared experimental mice and their relevant controls.

Activated Caspase 3 Quantification

The second set of slides collected from *Smn*$^{2B/+}$ and *Smn*$^{2B/-}$ mice in Chapter 3 were stained with anti-active caspase 3. Cells that stained positive for active caspase 3 and that fell within a motor neuron rich area were counted.

This number was used along with the total number of motor neurons counted on the ChAT stained slides to calculate the percentage of positive cells within the ventral horn of the spinal cord. Again, this data was collated in Microsoft Excel and analysed in GraphPad Prism. A Mann Whitney-U test compared the percentage of activated caspase-3 positive cells in *Smn*$^{2B/-}$ and *Smn*$^{2B/+}$ mice.

pH2AX Quantification

In Chapter 4, spinal cord sections from *Smn*$^{2B/-}$*;YFP-H* mice were stained for pH2AX. Images of MNCBs in these spinal cord sections were taken on a confocal microscope (Nikon A1R FLIM). The intensity of pH2AX staining was measured in Fiji imaging software, using mean grey value, in MNCBs that were YFP positive and YFP negative. Approximately 40 motor neurons per group were measured in three different *Smn*$^{2B/-}$*;YFP-H* mice. The data was collated in Microsoft Excel and was analysed in GraphPad Prism. An unpaired t-test compared the intensity of pH2AX staining in YFP positive and YFP negative MNCBs.

2.8 qPCR

Spinal cords were removed from recently sacrificed mice (see above for method), snap frozen on dry ice and were stored at -80^{o}C. RNA was extracted using a mini RNeasy kit (Qiagen), according to the manufacture's instructions. Briefly, tissue was homogenised in a mixture of 2-mercaptoethanol and the RLT buffer that was supplied within the kit. This was centrifuged and the supernatant was removed and mixed with 70% ethanol (prepared with RNase-free water). This mixture was added to the spin columns provided within the RNeasy kit prior to centrifugation. The spin columns are designed to collect RNA on their membrane while flow-through can be discard from the collection tube. The application of wash buffers and subsequent centrifugation ensured the RNA was clean. In addition, an

RNase-free DNase kit (Qiagen) was used during the RNA extraction process to remove any genomic DNA. Prior to their storage at -80^{o}C, the concentration of RNA samples was tested using a nanodrop (NanoDrop 2000, Thermo Scientific).

RNA was subsequently converted to cDNA using the QuantiTect Reverse Transcription kit (Qiagen), as per the manufacturer's instructions. Two sets of each sample were made, one that had reverse transcriptase added and one that did not. This means that one would have RNA converted to cDNA and one would not, thus controlling for genomic DNA contamination.

Kapa SYBR Fast Universal (Kapa Biosystems) and the CFX Connect Real-time PCR detection system (Biorad) was used to preform SYBR green-based qPCR. Primers obtained from Sigma had been previously optimised for use (Table 2.11). Primers from Qiagen were pre-optimised (Table 2.11). All cDNA samples were run in technical triplicate and the 'no reverse transcriptase' samples were run to check for genomic DNA contamination. The relative expression of housekeeping genes remained consistent between sample groups.

Table 2.11: Summary of primers used for transcriptional analysis by qPCR

Primer	Supplier	Sequence
ACTIN	Sigma	F: CCGTCAGGCAGCTCATAGCTCTTC R: CTGAACCCTAAGGCCAACCGT
GUSB	Sigma	F: GGCTGGTGACCTACTGGATTT R: TTGGCACTGGGAACCTGAAGT
YWHAZ	Sigma	F: TTGATCCCCAATGCTTCGC R: CAGCAACCTCGGCCAAGTAA
CDKN1A	Qiagen	Pre-optimised primer against mouse CDKN1A
FAS	Qiagen	Pre-optimised primer against mouse FAS
PMAIP1	Qiagen	Pre-optimised primer against mouse PMAIP1

Chapter 3

Investigating the timing and mechanism of motor neuron pathology onset in the *Smn$^{2B/-}$* mouse model of SMA

Summary

In this chapter, the time course of motor neuron pathology in the *Smn$^{2B/-}$* mouse model of SMA is investigated in order to determine the relationship between pathological hallmarks of motor neurons in SMA. Both NMJ pathology (including pre-synaptic terminal swelling and post-synaptic endplate occupancy and area) and MNCB pathology (including number and area) are quantified and transcriptional analysis of the spinal cord is performed. Furthermore, by genetically modifying the *Smn$^{2B/-}$* mouse model of SMA, P53 is ubiquitously reduced in this mouse model to determine the effects of P53 on motor neuron pathology.

The results that are detailed in the following chapter show that:

1. The onset of NMJ pathology occurs between P5 and P7 in the *Smn$^{2B/-}$* mouse model of SMA
2. There is a decrease in the number and area of MNCBs between P10 and P15 in the *Smn$^{2B/-}$* mouse model of SMA
3. The onset of NMJ pathology coincides with the up-regulation of transcripts involved in the P53 signaling pathway in the spinal cords of *Smn$^{2B/-}$* mice
4. A reduction in P53 in the *Smn$^{2B/-}$* mouse model of SMA does not improve the overall phenotype of the mouse model or reduce motor neuron loss but does result in a decrease in denervation

3.1 Introduction

In SMA, motor neurons are selectively vulnerable to degeneration. This degeneration causes denervation of muscles resulting in muscle atrophy, weakness and subsequent paralysis. It is thought that motor neurons degenerate in a 'die-back' manner, as the pre-synaptic terminal appears to withdraw from the post-synaptic endplate, leaving partially occupied endplates (Murray et al. 2008). In support of this, a study found that there was a 78% loss of axons in the ventral roots while there was only a 30% loss of MNCB in the ventral horn of the lumbar spinal cord suggesting distal to proximal degeneration of the motor neuron (Cifuentes-Diaz 2002). Further to this, NMJ defects occur prior to symptom onset in mouse models of SMA and therefore, it is reported that the NMJ is an 'early pathological target' in SMA (Murray et al. 2008; Murray et al. 2015).

However, the temporal relationship between NMJ degeneration and the loss of MNCBs remains unknown. Reports of MNCB loss tend to be from mid- to late- symptomatic stage studies where motor neuron degeneration is already clearly evident. For example, Le *et al* reported a 20% loss of MNCB in the lumbar spinal cord of *SmnΔ7* mouse model at P9, with the average life span of these mice being 14 days (Le et al. 2005). They also report significant denervation in the gastrocnemius muscle at P14 however, as these time points are different, conclusions regarding the relationship between these two pathologies cannot be drawn. In the $Smn^{2B/-}$ mouse model of SMA, Bowerman *et. al.* report both a loss of MNCB, of approximately 50%, in the lumbar spinal cord and significant denervation in the TVA muscle at P21 compared to controls (Bowerman et al. 2012a). However, this is again a symptomatic time point, with both ends of the motor neuron displaying significant pathology compared to controls.

What also remains unknown is the relationship of motor neuron degeneration to the onset of cell death pathways. Recently, it has been shown that there is an up-regulation of transcripts involved in the P53 signaling pathway in motor

neurons in SMA prior to the onset of NMJ pathology (Murray et al. 2015; Simon et al. 2017; Nichterwitz et al. 2018). The P53 signaling pathways is known to be involved in cell cycle control, DNA repair and apoptosis (Elmore 2007; Li & Yuan 2008; Williams & Schumacher 2016). Furthermore, in post-mortem analysis of SMA patients, there was shown to be an increase in P53 within their spinal cords (Simic et al. 2000). Therefore, it has been suggested that the activation of P53 may be causing the initiation of motor neuron degeneration (Murray et al. 2015; Simon et al. 2017; Nichterwitz et al. 2018).

P53 has previously been shown to co-localise with SMN (Young et al. 2002). In this study, the authors found that under normal circumstances, where P53 was not active in control cells, P53 was at low levels and was dispersed evenly throughout the nucleus. However, upon activation of P53 in these control cells, P53 co-localised with SMN in both cajal bodies of the nucleus and in the nucleolus (Young et al. 2002). In fibroblasts derived from SMA patients, P53 was found to accumulate only in the nucleolus and not in cajal bodies. Furthermore, it was reported that while functional full-length SMN can interact with P53, mutated SMN and SMNΔ7 had a reduction in their ability to interact with P53 (Young et al. 2002). The mutated forms of SMN tested were from three different patients with three unique mutations and the binding affinity of these three different mutated SMNs for P53 correlated with the disease severity of the patients they were obtained from (Young et al. 2002). This therefore suggests that SMN plays a role in regulating P53.

It is widely accepted that during development, apoptosis is responsible for the death of cells, including motor neurons, however, whether apoptosis is responsible for the death of motor neurons in SMA pathogenesis remains disputed (Oppenheim 1991; Pérez-García et al. 2017). During the search for the genetic cause of SMA, initial findings pointed towards a role of the Neuronal Apoptosis Inhibitory Protein in pathogenesis (Pérez-García et al. 2017). Approximately 45% of SMA type I cases also have a homozygous deletion of the NAIP gene and this lead many to believe that SMA motor

neuron loss was as a result of uncontrolled apoptosis (Roy et al. 1995; Biros & Forrest 1999). Tsai *et. al.* report increased apoptosis in SMA mouse model spinal cord through an increase in positive TUNEL staining, which labels DNA fragmentation (Tsai et al. 2006a). TUNEL staining has also been performed in post-mortem patient samples of spinal cord and this showed an increase in DNA fragmentation of cells in the ventral horns (Simic et al. 2000). However, it has been previously reported that TUNEL is not able to distinguish between different types of cell death including apoptosis and necrosis (Grasl-Kraupp et al. 1995).

Sareen *et. al.*, 2012, observed apoptotic morphology, specifically nuclear condensation and increased caspase-3 activation, in iPSCs derived from SMA patients compared to iPSCs derived from controls (Sareen et al. 2012). The loss of motor neurons, observed in cultured SMA iPSCs, was decreased by blocking apoptosis through the Fas receptor (Sareen et al. 2012). Despite this, post-mortem analysis of patient motor neurons in the spinal cord revealed that motor neurons in the spinal cords of SMA patients appeared to be swollen and present features more consistent with necrotic cell death rather than apoptotic cell death (Kato & Hirano 1990; Korinthenberg et al. 1997; Simic et al. 2000; Ito et al. 2011; Harding et al. 2015; Pérez-García et al. 2017). Therefore, the mechanism of motor neuron death in SMA remains unclear.

From the literature presented within this introduction, it is clear that there are gaps in our knowledge regarding motor neuron pathology, including the relationship of NMJ and MNCB pathology, in SMA. In order to address this, I aimed to carry out a time course analysis of pathology of both the NMJ and the MNCBs within the *Smn*$^{2B/-}$ mouse model of SMA. This mouse model is described as an intermediate mouse model of SMA due to its extended pre-symptomatic period compared to other mouse models in the field. As a result, any subtle pre-symptomatic changes that may be occurring and may

be missed in other mouse models that have a more rapid decline can be observed.

Further to this, I genetically modified the *Smn*$^{2B/-}$ mouse model of SMA in order to induce a reduction of ubiquitously expressed P53. In doing so, I aimed to determine what effect P53 has on motor neuron pathology. If indeed the activation of the P53 signaling pathway is responsible for the degeneration of the motor neuron, then I would hypothesise that a reduction in P53 would have a positive impact on motor neuron pathology. To address this, analysis of NMJs and MNCBs was performed at a symptomatic time point following the pre-symptomatic knockout of P53.

3.2 Results

3.2.1 Phenotypic Analysis of *Smn$^{2B/-}$* mice

The phenotype of the *Smn$^{2B/-}$* mouse model has previously been described in the literature however, many factors can affect the severity and phenotypic features of mouse models (Bowerman et al. 2012a). For example, genetic background has a huge bearing on phenotype (Eshraghi et al. 2016) as well as the type of caging in which animals are housed (Logge et al. 2014). Therefore, a basic assessment of the phenotype of the *Smn$^{2B/-}$* mouse model of SMA that was used within this study was performed.

Firstly, the body weight of *Smn$^{2B/-}$* and control *Smn$^{2B/+}$* mice was measured. This showed that the body weight of *Smn$^{2B/-}$* mice is significantly lower than that of control *Smn$^{2B/+}$* littermates from P10 (Figure 3.1B). The *Smn$^{2B/-}$* mice fail to gain weight at the same rate as *Smn$^{2B/+}$* mice and in the later stages of the disease *Smn$^{2B/-}$* mice begin to lose weight.

Secondly, motor performance was assessed, using the time to right (TtR) test, on *Smn$^{2B/-}$* and *Smn$^{2B/+}$* mice between P8 and P12. This was the critical time window in which the onset of an SMA like phenotype was occurring. It was found that, although the performance of both *Smn$^{2B/-}$* and *Smn$^{2B/+}$* mice improves over time, *Smn$^{2B/-}$* mice do not perform as well as *Smn$^{2B/+}$* mice. The time to right for *Smn$^{2B/-}$* and *Smn$^{2B/+}$* mice was significantly different at P9 (Figure 3.1C).

It was also noted that *Smn$^{2B/-}$* mice develop distinguishing features as the disease progresses. By P15, *Smn$^{2B/-}$* mice have a short dark tail and small ears (Figure 3.1A).

Furthermore, the life span of the *Smn*$^{2B/-}$ mouse model is commonly reported as 28 days (Bowerman et al. 2012a). This mouse model is on a mixed genetic background but recently published data shows that on a pure genetic background, life span of the *Smn*$^{2B/-}$ mouse model is shorter, with death occurring from P19 (Eshraghi et al. 2016). This is consistent with the findings in this study as *Smn*$^{2B/-}$ were presenting with a severe phenotype at P18-P19. To ensure there were no fatalities, in keeping with Home Office regulations, *Smn*$^{2B/-}$ mice were not kept alive longer than 19 days.

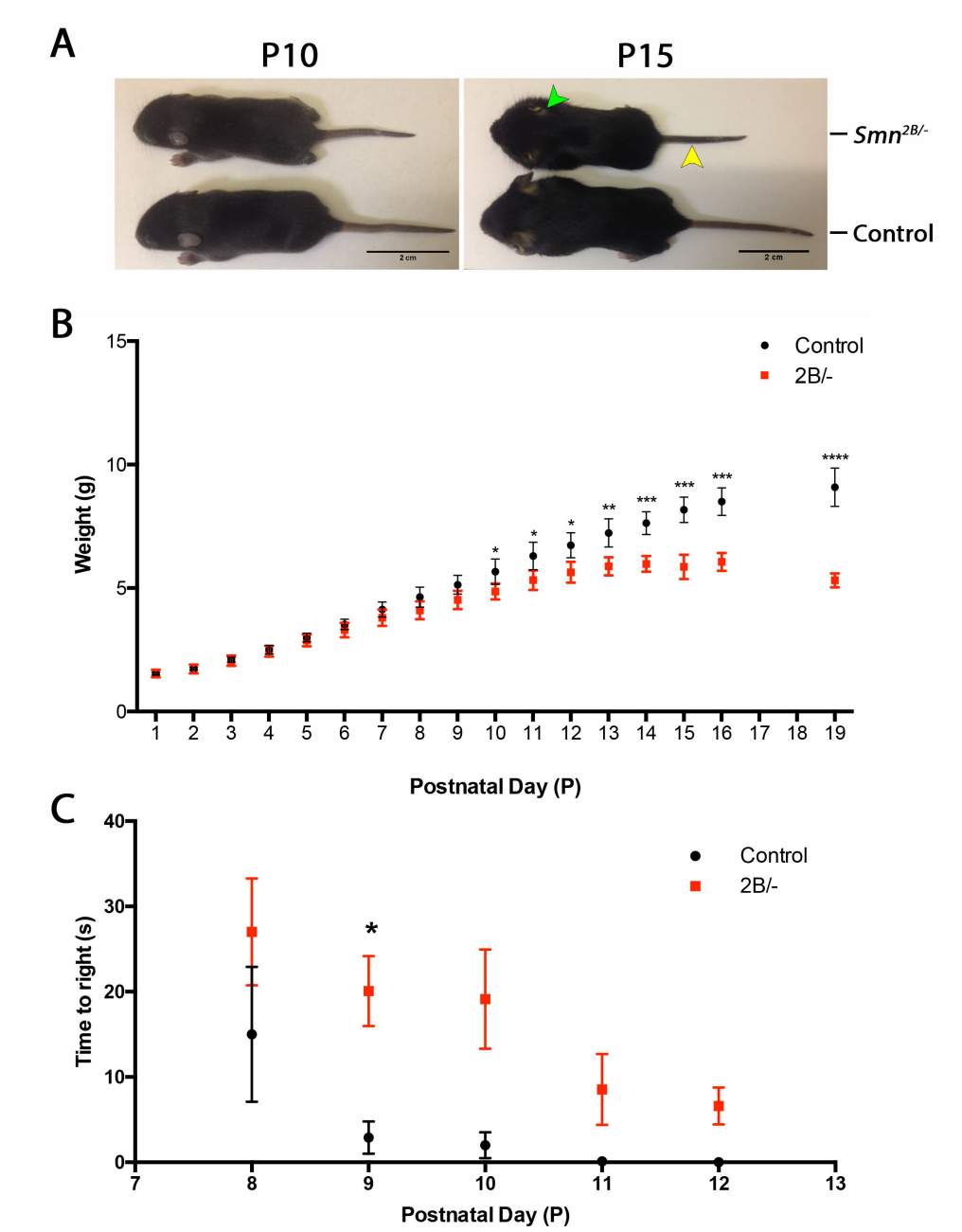

Figure 3.1: Phenotypic analysis of the *Smn*$^{2B/-}$ mouse model of SMA shows that it becomes significantly different from control littermates around P9 to P10. (**A**) Representative images showing a *Smn*$^{2B/-}$ mouse and a control *Smn*$^{2B/+}$ littermate at P10 and P15. Note that the yellow arrowhead highlights the short dark tail and the green arrowhead highlights the small ears. (**B**) The graph (Mean±SEM) shows that the weights of *Smn*$^{2B/-}$ mice are significantly different from their *Smn*$^{2B/+}$ littermate controls at P10 with an increase in the level of significance thereafter (n=4, unpaired t-test, *p<0.05, **p<0.01, ***p<0.005, ****p<0.001). (**C**) The graph (Mean ± SEM) shows the time it took for *Smn*$^{2B/-}$ and *Smn*$^{2B/+}$ mice to right themselves between P8 and P12. There was a significant difference in the time to right of *Smn*$^{2B/-}$ mice compared to *Smn*$^{2B/+}$ mice at P9 (n=4, unpaired t-test, *p<0.05).

3.2.2 Investigating the onset of pathology in motor neurons of the *Smn$^{2B/-}$* mouse model of SMA

In order to try and determine whether pathology in motor neurons begins first at the NMJ or at the MNCB, a comprehensive morphological assessment of both the NMJ and the MNCB in the *Smn$^{2B/-}$* mouse model of SMA was carried out at various time points that ranged from pre-symptomatic to late symptomatic. Below, NMJ pathology (at both the pre- and post-synapse), MNCB number and size as well as molecular alterations in the spinal cord of *Smn$^{2B/-}$* mice were assessed and compared to *Smn$^{2B/+}$* mice.

3.2.2.1 Analysis of NMJs in Smn$^{2B/-}$ mice shows that the onset of pathology at the NMJ occurs between P5 and P7

I aimed to comprehensively assess the level of NMJ pathology over the disease progression in the *Smn$^{2B/-}$* mouse model of SMA. For this analysis, the transverse abdominis (TVA) muscle was used. This is a thin, flat muscle that is ideal for NMJ analysis as, when using immunofluorescence techniques, NMJs are clearly visible in the whole mounted muscle. This eliminates the need for the muscle to be sectioned, even when it is larger in older mice. In addition, the TVA is a known vulnerable muscle in the *Smn$^{2B/-}$* mouse model of SMA (Murray et al. 2012). There are several pathological hallmarks of SMA that can be quantified in order to assess alterations in NMJ morphology. These include occupancy of the post-synaptic endplate, pre-synaptic swelling and endplate size. These features were quantified at P1, P5, P10 and P15 in *Smn$^{2B/-}$* and *Smn$^{2B/+}$* mice to determine when NMJ morphology begins to differ in the *Smn$^{2B/-}$* mouse model of SMA (Figure 3.2).

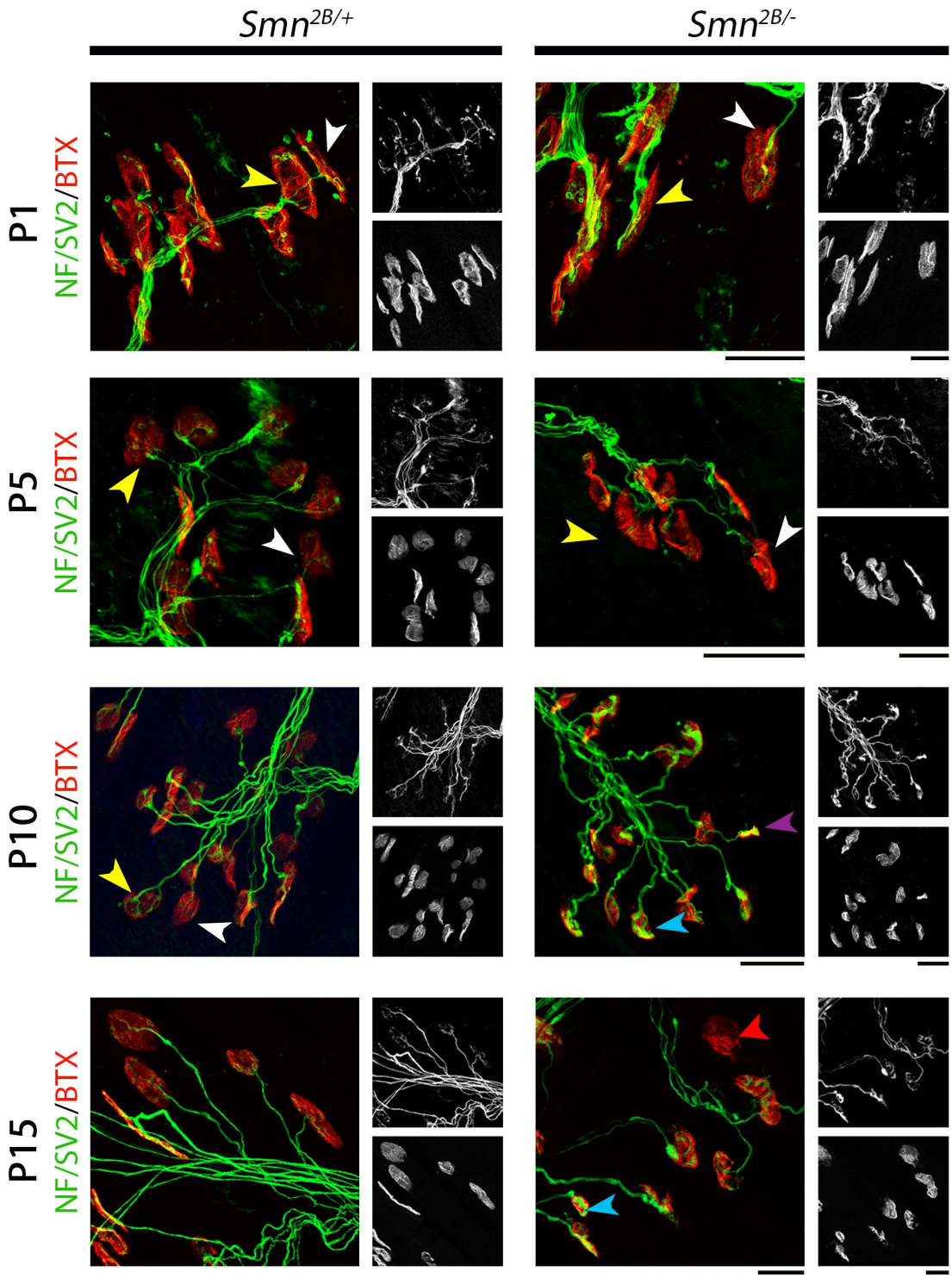

Figure 3.2: Representative images of NMJs in the TVA muscle of *Smn*$^{2B/-}$ and *Smn*$^{2B/+}$ mice displaying features of NMJ pathology. Representative images of NMJs in the TVA muscle of *Smn*$^{2B/+}$ and *Smn*$^{2B/-}$ mice at P1, P5, P10 and P15. Note that white arrowheads show no pre-synaptic swelling, yellow arrowheads show mild pre-synaptic swelling, blue arrowheads show moderate pre-synaptic swelling and the purple arrowhead shows severe pre-synaptic swelling. Vacant endplates (red arrowhead) are seen at P15 in the *Smn*$^{2B/-}$ mouse model of SMA (Scale bars = 20μm).

Occupancy measures the innervation of the post-synaptic endplate and determines the level of denervation within a muscle. The complete criteria for assessing occupancy can be found in Chapter 2. Briefly, endplates are fully occupied if they are completely covered by the pre-synaptic terminal, partially occupied if the pre-synaptic terminal only partially covers the endplate and vacant if they have no innervation from the pre-synaptic terminal (Figure 3.2). At P1 and P5 all endplates, in both *Smn*$^{2B/-}$ and *Smn*$^{2B/+}$ mice, were fully occupied by the pre-synaptic terminal (Figure 3.3A). By P10, there was a significant decrease in the percentage of fully occupied endplates in *Smn*$^{2B/-}$ mice; some pre-synaptic terminals had begun to withdraw leaving a small but significant percentage of endplates only partially occupied. This withdrawal of the pre-synaptic terminal continued through the disease progression and by P15, there is a significant percentage of partially occupied and vacant endplates, compared to *Smn*$^{2B/+}$ controls (Figure 3.3A).

Another hallmark of pathology in SMA mouse models is pre-synaptic swelling. The level of pre-synaptic swelling was staged using the criteria detailed in Chapter 2: Methods; pre-synaptic swelling ranged from none to severe (Figure 3.2). This staging of pre-synaptic swelling was carried out in *Smn*$^{2B/-}$ and *Smn*$^{2B/+}$ control mice over the disease progression of the *Smn*$^{2B/-}$ mouse model at the same time points used for occupancy: P1, P5, P10 and P15 (Figure 3.3B). At P1 and P5, there was no significant difference in the level of pre-synaptic swelling in *Smn*$^{2B/-}$ mice compared to *Smn*$^{2B/+}$ mice. However, at P10 there was a significant decrease in the percentage of NMJs with no pre-synaptic swelling and a significant increase in the percentage of NMJs with mild and moderate pre-synaptic swelling in *Smn*$^{2B/-}$ mice compared to controls. At P15, there is again a significant increase in mild and moderate pre-synaptic swelling in *Smn*$^{2B/-}$ mice compared to controls but at this time point there is also significant percentage of NMJs displaying severe pre-synaptic swelling in *Smn*$^{2B/-}$ mice.

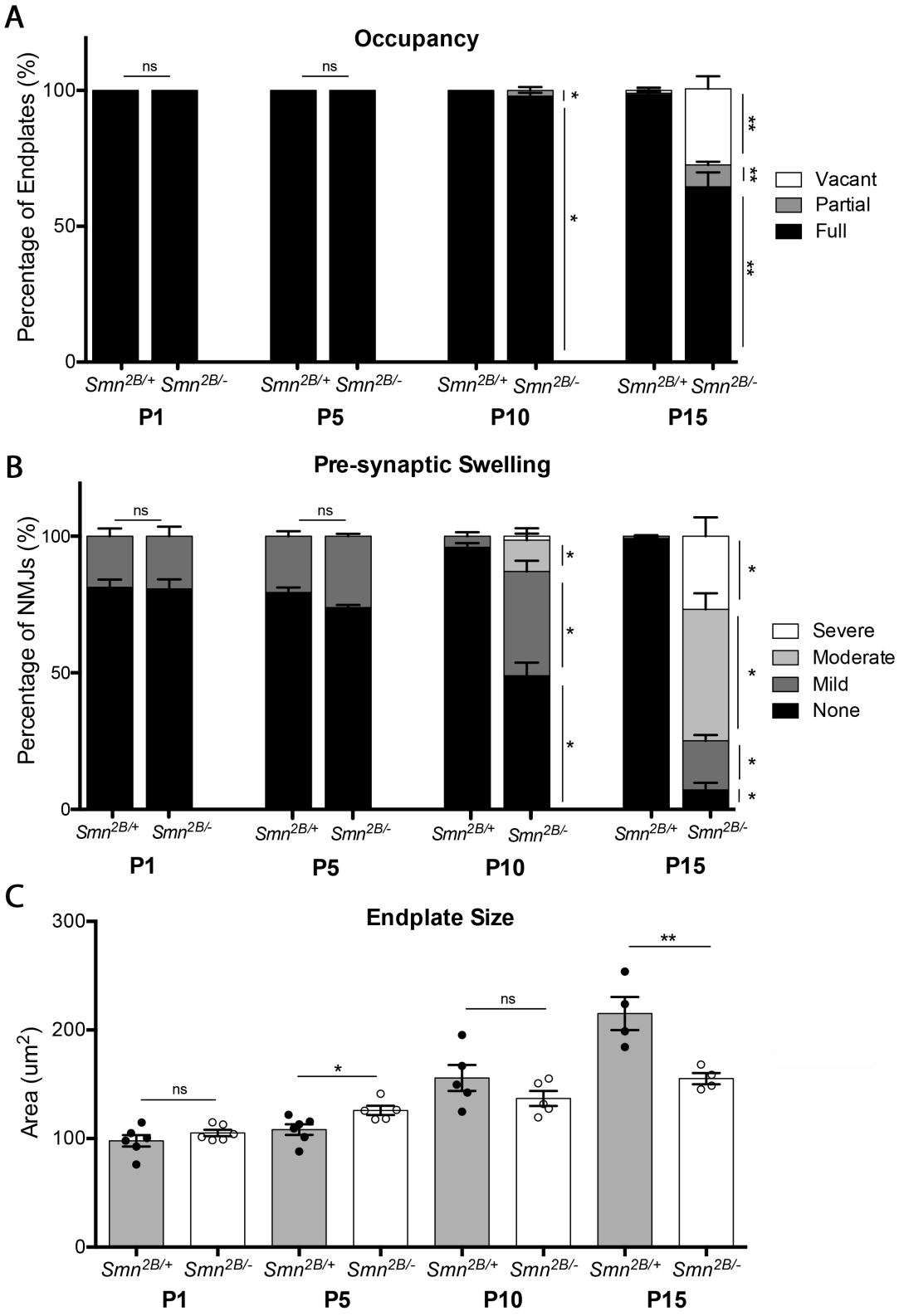
A
Occupancy
Percentage of Endplates (%)
100
50
0
ns
ns
*
*
**
**
**
Vacant
Partial
Full
Smn2B/+ Smn2B/-
P1
P5
P10
P15
B
Pre-synaptic Swelling
Percentage of NMJs (%)
100
50
0
ns
ns
*
*
*
*
*
*
Severe
Moderate
Mild
None
Smn2B/+ Smn2B/-
P1
P5
P10
P15
C
Endplate Size
Area (um2)
300
200
100
0
ns
*
ns
**
Smn2B/+ Smn2B/-
P1
P5
P10
P15

Figure 3.3: There is significant pathology in the TVA muscle in *Smn$^{2B/-}$* mice from P10. (**A**) Bar chart (Mean ± SEM) compares the percentage of full, partial and vacant endplates in *Smn$^{2B/-}$* mice compared to *Smn$^{2B/+}$* controls. At P1 and P5, all of the endplates quantified in *Smn$^{2B/-}$* and *Smn$^{2B/+}$* mice were fully occupied by the pre-synaptic terminal. At P10, there is significant increase in the percentage of partially occupied endplates and at P15, there is a significant increase in the percentage of both vacant and partially occupied endplates in *Smn$^{2B/-}$* compared to *Smn$^{2B/+}$* mice (Mann Whitney-U test, ns>0.05, *p<0.05, **p<0.01; n=4 mice per genotype). *P15 data acquired in collaboration with Alannah Mole during a placement project.* (**B**) Bar chart (Mean ± SEM) compares the stages of pre-synaptic swelling in *Smn$^{2B/-}$* and *Smn$^{2B/+}$* mice. There is no significant difference in the level of swelling in *Smn$^{2B/-}$* mice compared to controls at P1 and P5. At P10, there is a significant increase in the percentage of NMJs with mild and moderate swelling in *Smn$^{2B/-}$*mice. At P15, there is a significant increase in the percentage of pre-synaptic terminals with mild, moderate and severe swelling in *Smn$^{2B/-}$* mice compared to *Smn$^{2B/+}$* controls (Mann Whitney-U test, ns>0.05, *p<0.05; n=4 mice per genotype). *P15 data acquired in collaboration with Alannah Mole during a placement project.* (**C**) Bar chart (Mean ± SEM) compares the average size of endplates in the TVA of *Smn$^{2B/-}$* mice compared to controls. At P1 and P10 there is no significant difference in the area of post synaptic endplates in *Smn$^{2B/-}$* mice compared to controls. At P5, there is a small but significant increase in endplate area in *Smn$^{2B/-}$* mice. At P15 there is a significant decrease in the size of endplates in *Smn$^{2B/-}$* mice compared to controls (unpaired t-test, ns>0.05, *p<0.05, **p<0.01; n=4-6 muscles per genotype).

Additionally, the area of post-synaptic endplates in the TVA muscle was measured in P1, P5, P10 and P15 *Smn$^{2B/-}$* and *Smn$^{2B/+}$* mice. At P1 and P10, there was no significant difference between control and *Smn$^{2B/-}$* mice. However, at P5 there was a significant increase and at P15, there was a significant decrease in the area of endplates in *Smn$^{2B/-}$* mice compared to controls (Figure 3.3C). This increase in the area of endplates in *Smn$^{2B/-}$* mice compared to controls could potentially be caused by a developmental delay. Under normal circumstances, the post-synaptic endplate experiences a temporary decrease in area during postnatal synapse elimination (Marques et al. 2000). It is possible that there is a delay in this process in the *Smn$^{2B/-}$* mice and as a result they appear to have larger endplates than controls.

Ultimately, when taking all of this NMJ analysis into consideration, it is clear that pathological alterations at the NMJ occur at the pre-synaptic terminal

somewhere between P5 and P10. In order to narrow the time window in which pathological changes at the NMJ are occuring, occupancy and pre-synaptic swelling analysis was carried out at P7. This showed that although there was no evidence of denervation (all endplates were fully occupied), there was a significant decrease in the percentage of NMJs displaying no swelling and an increase in the percentage of pre-synaptic terminals with mild swelling (Figure 3.4). This not only identifies this as an earlier time point for the onset of pathology but also shows that pre-synaptic swelling precedes the onset of pre-synaptic withdrawal.

The rectus abdominis (RA) is a muscle that appears to be more affected in end-stage *Smn*$^{2B/-}$ mice (Murray et al. 2015). The RA muscle is significantly thicker than the TVA and, although easily quantifiable as a whole mount muscle in young pups, it becomes progressively more difficult to reliably quantify NMJ pathology as these pups mature. Therefore, it was felt that this was not an appropriate muscle of choice when wishing to carry out NMJ analysis over time. However, to confirm that there was indeed no NMJ pathology present at P5 in *Smn*$^{2B/-}$ mice, pre-synaptic swelling and occupancy was quantified in the RA muscle (Figure 3.5). No significant difference in pre-synaptic swelling or occupancy was observed in *Smn*$^{2B/-}$ mice compared to *Smn*$^{2B/+}$ controls. This therefore agrees with the finding that the onset of NMJ pathology occurs between P5 and P7.

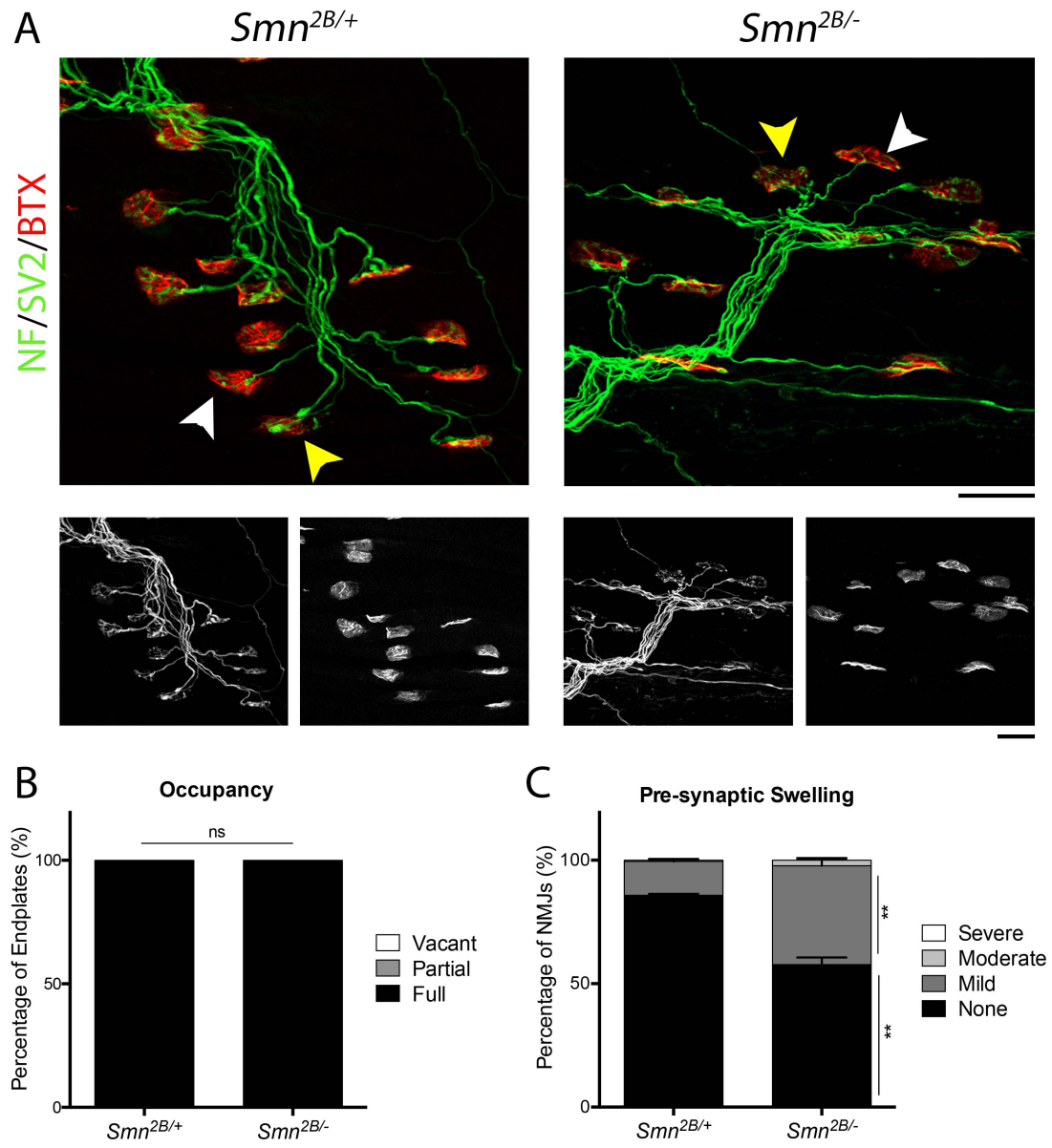

Figure 3.4: At P7, there is significantly more pre-synaptic swelling at the NMJs in the TVA muscle of *Smn*$^{2B/-}$ mice compared to *Smn*$^{2B/+}$ mice. (**A**) Representative micrographs of the NMJs in the TVA of P7 *Smn*$^{2B/-}$ and *Smn*$^{2B/+}$ mice. White arrowheads show NMJs with no swelling and yellow arrowheads show NMJs with mild pre-synaptic swelling (Scale bars = 20μm). (**B**) Bar chart (Mean ± SEM) shows that at P7, 100% of endplates in the TVA of *Smn*$^{2B/-}$ and *Smn*$^{2B/+}$ mice were fully occupied by the pre-synaptic terminal of an axon (by Mann Whitney-U test, ns>0.05; n=4 mice per genotype) (**C**) Bar chart (Mean ± SEM) compares the stages of pre-synaptic swelling in *Smn*$^{2B/-}$ mice compared to *Smn*$^{2B/+}$ controls. There is a significant decrease in the percentage of pre-synaptic terminals with no swelling and increase in mild swelling in the TVA of *Smn*$^{2B/-}$ mice compared to *Smn*$^{2B/+}$ controls at P7 (by Mann Whitney-U test, **p<0.01; n=4 mice per genotype).

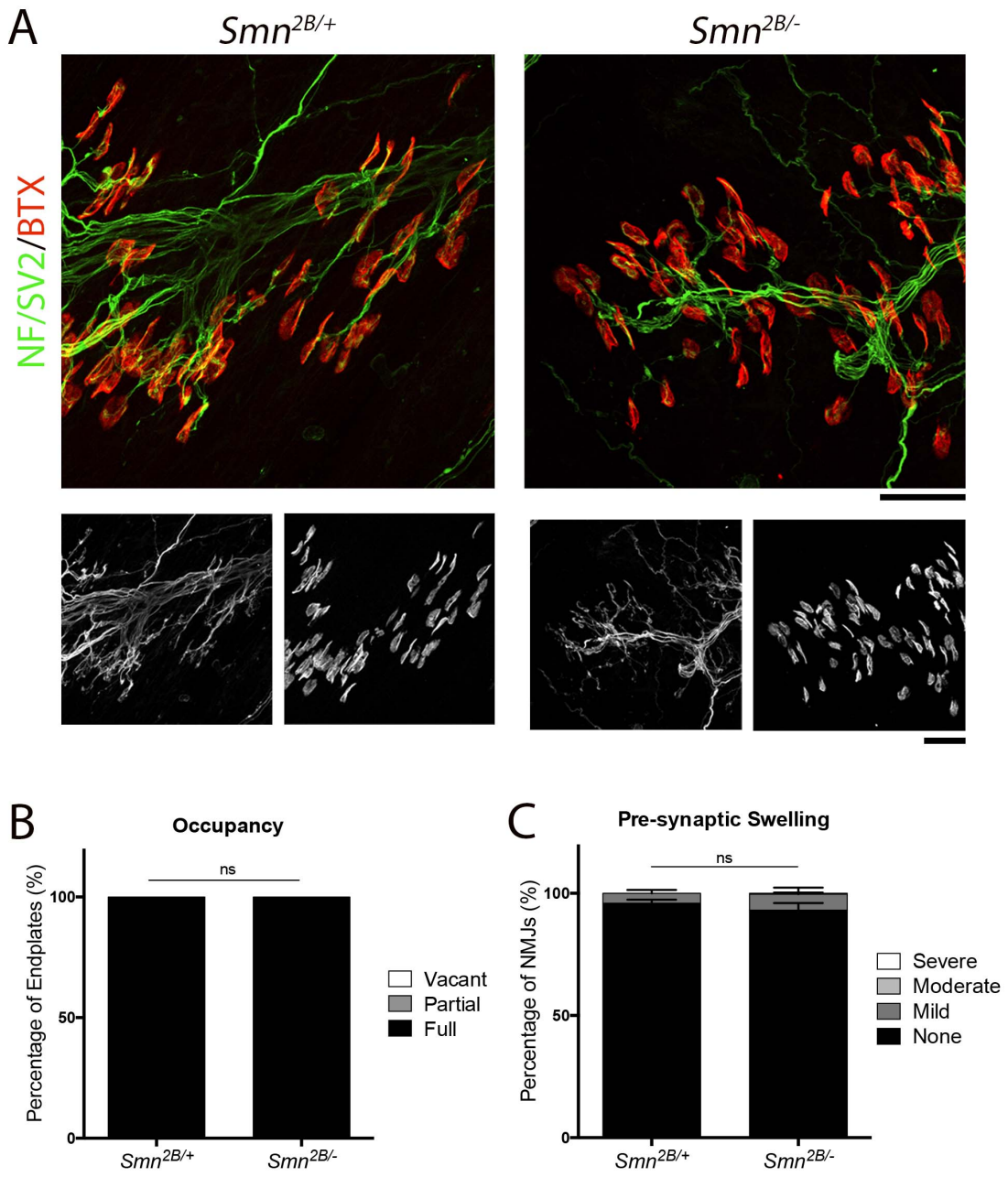

Figure 3.5: Analysis of NMJs in the Rectus Abdominis (RA) muscle of *Smn*$^{2B/-}$ mice confirms that there is no pre-synaptic pathology observed at P5 (**A**) Representative micrographs of the NMJs in the RA of *Smn*$^{2B/-}$ and control mice showing no significant difference in appearance (Scale bars = 40μm). (**B**) Bar chart (Mean ± SEM) shows that at P5, 100% of endplates in the RA of *Smn*$^{2B/-}$ and *Smn*$^{2B/+}$ mice were fully occupied by the pre-synaptic terminal (by Mann Whitney-U test, ns>0.05; n=4 mice per genotype) (**C**) Bar chart (Mean ± SEM) compares the stages of pre-synaptic swelling in *Smn*$^{2B/-}$ mice compared to *Smn*$^{2B/+}$. There is no significant difference in the level of pre-synaptic swelling in the RA of *Smn*$^{2B/-}$ mice compared to *Smn*$^{2B/+}$ controls at P5 (by Mann Whitney-U test, ns>0.05; n=4 mice per genotype).

3.2.2.2 $Smn^{2B/-}$ mice begin to lose MNCBs between P10 and P15

A temporal analysis of the number of MNCBs in the ventral horn of $Smn^{2B/-}$ and $Smn^{2B/+}$ thoracic spinal cords was carried out. Spinal cord sections were stained with ChAT, Nissl and DAPI. Motor neurons were identifiable by their large size, irregular shape and were doubled stained with ChAT and Nissl. Only those with a visible nucleus and nucleolus were counted to avoid double counting the same motor neuron on different sections.

No significant change in the number of MNCBs in the ventral horn of $Smn^{2B/-}$ and $Smn^{2B/+}$ spinal cords was observed at P1 and P10 (Figure 3.6). However, at P5 there was a significant increase of 22% in the number of MNCBs in the ventral horn of $Smn^{2B/-}$ spinal cords compared to $Smn^{2B/+}$ controls and at P15 there was a significant decrease of 51% in the number of MNCBs in $Smn^{2B/-}$ mice compared to littermate $Smn^{2B/+}$ controls.

The increase in the number of MNCBs in $Smn^{2B/-}$ mice compared to controls that was observed at P5 is potentially a very interesting finding and will be addressed within the discussion section of this chapter. However, ultimately, the phenotype of SMA is associated with a loss of motor neurons and these findings show that the loss of MNCBs in $Smn^{2B/-}$ mice occurs between P10 and P15. This is after the onset of pathology at the NMJ.

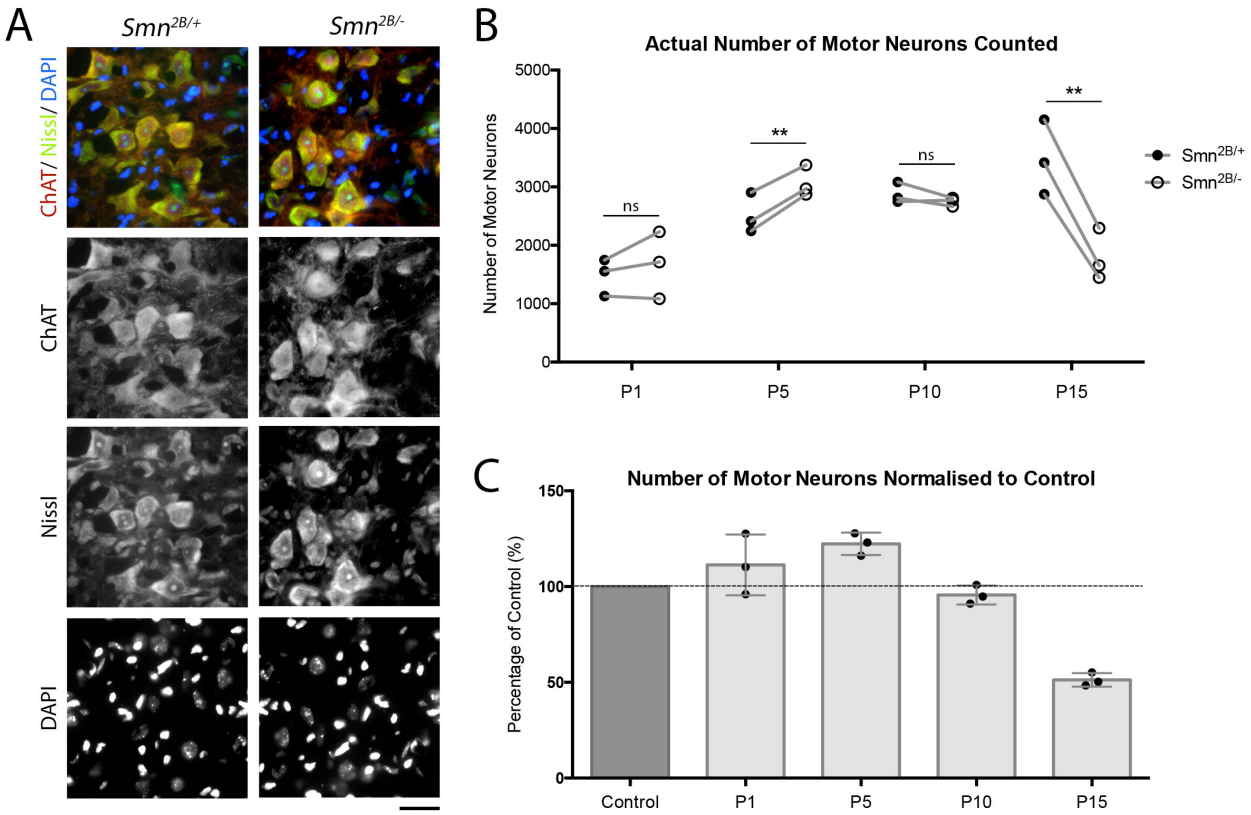

Figure 3.6: There is a loss of MNCBs in *Smn*$^{2B/-}$ mice between P10 and P15. (**A**) Representative images showing the ventral horn of the spinal cord of P1 *Smn*$^{2B/+}$ and *Smn*$^{2B/-}$ mice. Note the large and irregular shape of the ChAT and Nissl stained MNCBs, which also have a prominent, spherical nucleolus in the centre of the nucleus. (Scale bar = 40μm) (**B**) Graph plotting the absolute number of MNCBs counted in the ventral horn of the thoracic spinal cord of *Smn*$^{2B/-}$ and control mice. Note that only points that are linked by a grey line can be compared, as these spinal cords are size matched. At P1 and P10 there is no significant difference between *Smn*$^{2B/-}$ and *Smn*$^{2B/+}$ pairs. At P5 there is a significant increase in the number of MNCBs in *Smn*$^{2B/-}$ mice and at P15 there is a significant decrease in the number of MNCBs in *Smn*$^{2B/-}$ mice compared to *Smn*$^{2B/+}$ controls (Paired T-test, **p<0.01, n=3 per genotype per time point) (**C**) Bar chart (Mean±SEM) displaying the number of MNCBs in the ventral horn of the spinal cord of *Smn*$^{2B/-}$ mice as a percentage of controls. *Smn*$^{2B/-}$ absolute numbers are normalised to their paired control. Note that time points cannot be compared.

3.2.2.3 The area of MNCBs in Smn$^{2B/-}$ mice becomes significantly smaller compared to controls between P10 and P15

The area of MNCBs at P1, P5, P10 and P15 was also assessed in *Smn*$^{2B/-}$ and *Smn*$^{2B/+}$ control mice (Figure 3.7B). This analysis revealed that there is no significant difference in MNCB area at P1, P5 and P10. However, at P15 there is a significant decrease in MNCB area in *Smn*$^{2B/-}$ mice compared to controls. While the area of MNCBs in *Smn*$^{2B/+}$ mice increases over time, with a significant difference in area between P1 and P15, MNCB area in *Smn*$^{2B/-}$ mice does not change across the time course assessed (Figure 3.7).

The same method for measuring MNCB area was used to measure the nuclear area of MNCBs. This showed that there is no significant difference in the nuclear area of MNCBs of *Smn*$^{2B/-}$ and *Smn*$^{2B/+}$ mice at P1, P5, P10 and P15 (Figure 3.7C). This quantification also validates the counting method used for determining MNCB number. Since only MNCBs with a visible nucleus were counted, it is unlikely that motor neurons would have been excluded due to a reduction in their nuclear area.

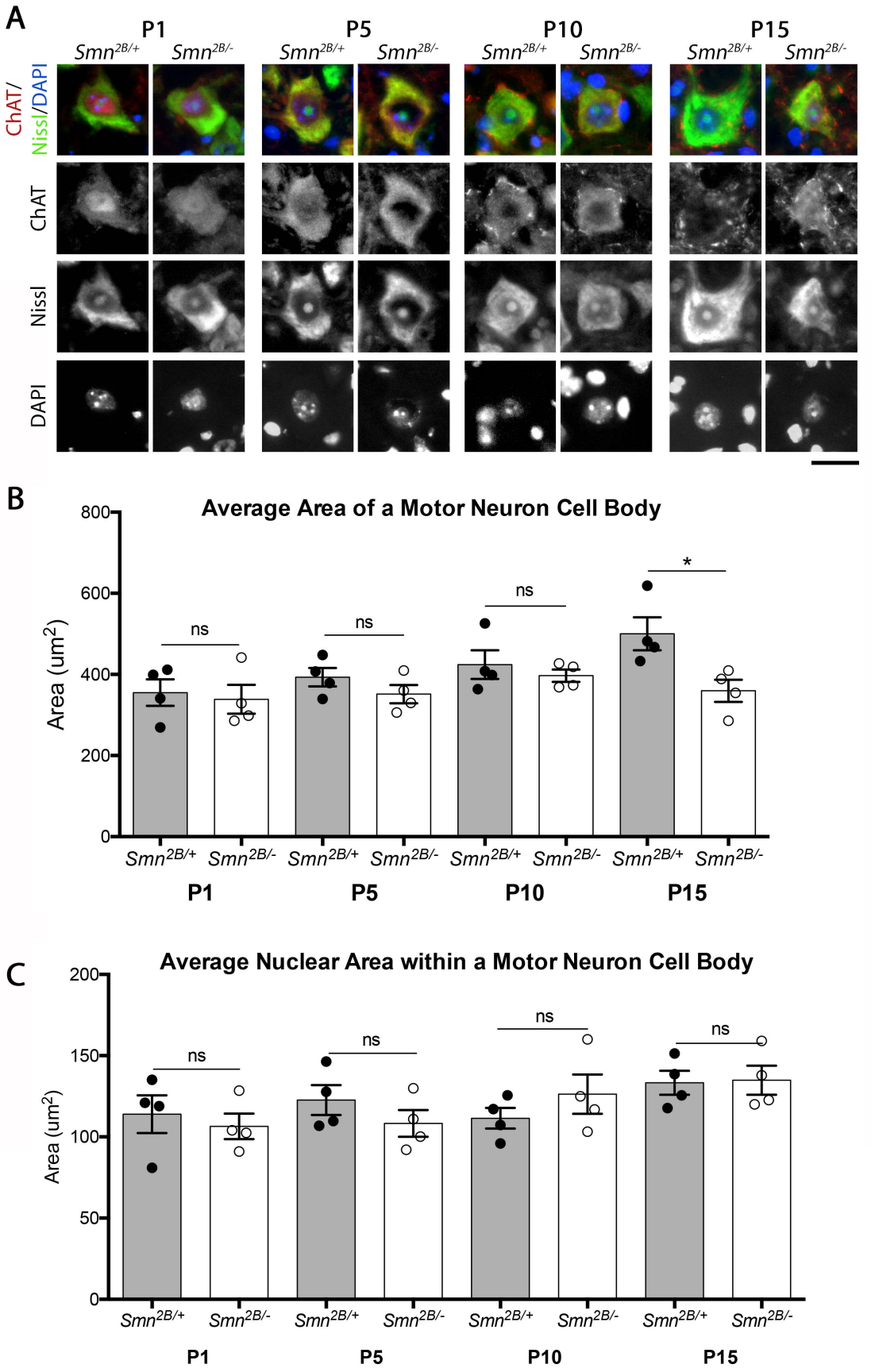
A
P1
P5
P10
P15
Smn2B/+
Smn2B/-
ChAT/
Nissl/DAPI
ChAT
Nissl
DAPI
B
Average Area of a Motor Neuron Cell Body
Area (um2)
800
600
400
200
0
ns
ns
ns
*
Smn2B/+
Smn2B/-
P1
P5
P10
P15
C
Average Nuclear Area within a Motor Neuron Cell Body
Area (um2)
200
150
100
50
0
ns
ns
ns
ns

Figure 3.7: There is a significant difference in the area of MNCBs in *Smn$^{2B/-}$* mice compared to controls at P15 (**A**) Representative images showing MNCBs from *Smn$^{2B/-}$* and *Smn$^{2B/+}$* control mice at P1, P5, P10 and P15. Note the relative decrease in area in *Smn$^{2B/-}$* compared to *Smn$^{2B/+}$* mice at P15 (Scale bar = 20μm). (**B**) The graph (Mean ± SEM) shows that at P1, P5 and P10 there is no significant difference in the average area of MNCBs in the ventral horn of the spinal cord of *Smn$^{2B/-}$* and *Smn$^{2B/+}$* mice. However, there is a significant decrease in the average area of MNCBs in *Smn$^{2B/-}$* mice compared to *Smn$^{2B/+}$* mice at P15 (by unpaired t-test, ns>0.05, *p<0.05, n= 4 mice per genotype). Statistical analysis has also shown that there is a significant increase in the area of MNCBs in *Smn$^{2B/+}$* controls between P1 and P15 (by one-way ANOVA, p<0.05) but no significant difference over time in *Smn$^{2B/+}$* mice (by one-way ANOVA, p>0.05). (**C**) The graph (Mean ± SEM) shows that there is no significant difference in the area of MNCB nuclei in *Smn$^{2B/-}$* compared to *Smn$^{2B/+}$* controls at any of the time points measured (by unpaired t-test, ns>0.05; n=4 mice per genotype).

3.2.2.4 There is an increase in the percentage of activated caspase-3 positive cells in the ventral horn of spinal cords of P15 Smn$^{2B/-}$ mice

Caspase-3 is a protein involved in the execution of apoptosis (Vila & Przedborski 2003). Therefore, I wished to consider the activation of caspase-3 in MNCBs of *Smn$^{2B/-}$* mice. Spinal cord sections from P1, P5, P10 and P15 *Smn$^{2B/-}$* and *Smn$^{2B/+}$* mice were stained for activated caspase-3. Positive cells in the ventral horn of the spinal cord were counted. During analysis, it was found that cells positive for activated caspase-3 could have different appearances (Figure 3.8A). For this analysis, all cell-like structures that lay within the ventral horn and still displayed a DAPI stained nucleus were counted.

When spinal cord sections were cut, they were alternated between two sets of slides; one was used for ChAT staining (and MNCB counting) while the other was used for activated caspase-3 staining. Therefore, the number of MNCBs counted in the ventral horn of spinal cords was used to normalise the number of activated caspase-3 positive cells to the number of motor neurons present.

It was found that at P1 there was significantly less activated caspase-3 positive cells in the ventral horns of *Smn*$^{2B/-}$ spinal cords (Figure 3.8B). This suggests that there is a decrease in apoptosis in *Smn*$^{2B/-}$ mice at P1. At P5 and P10, there was no significant difference in the percentage of activated caspase-3 positive cells. At P15, there was an increase in the percentage of activated caspase-3 positive cells in the ventral horn of *Smn*$^{2B/-}$ mice compared to *Smn*$^{2B/+}$ controls (Figure 3.8B). Furthermore, over time there is a statistically significant decrease in the percentage of activated caspase-3 positive cells in *Smn*$^{2B/+}$ mice that is not observed in *Smn*$^{2B/-}$ mice (Figure 3.8).

Whether these cells are exclusively motor neurons or not cannot be confirmed, as they were not stained using a motor neuron specific marker. Preliminary work to double staining for both activated caspase-3 and ChAT was unsuccessful however, it is likely that the use of ChAT as a motor neuron specific marker when looking for dying motor neurons may not be appropriate as loss of function in motor neurons results in reduced expression of ChAT (Wu & Hersh 1994; Pérez-García et al. 2017).

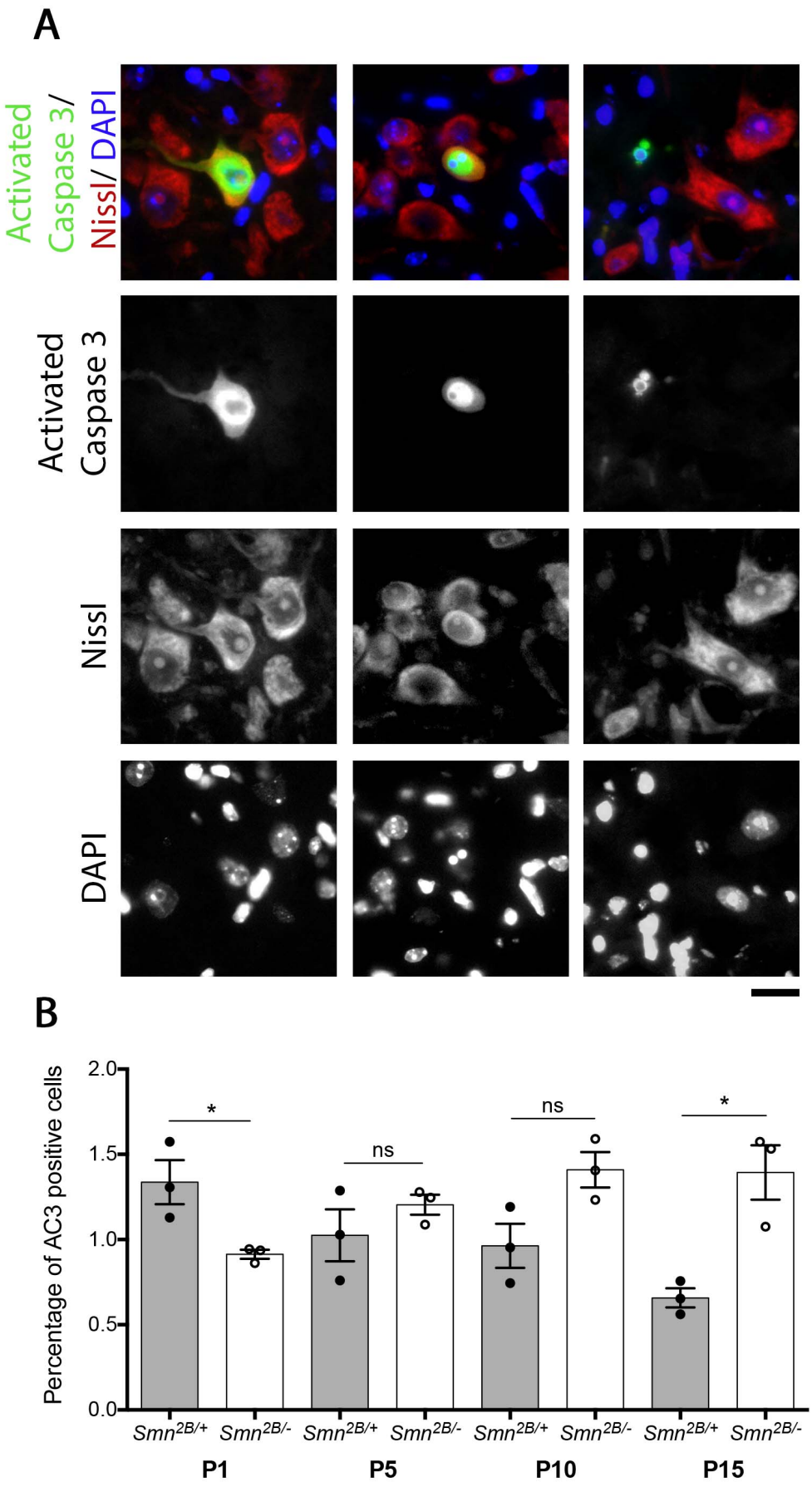
A
Activated Caspase 3/ Nissl/ DAPI
Activated Caspase 3
Nissl
DAPI
B
Percentage of AC3 positive cells
2.0
1.5
1.0
0.5
0.0
*
ns
ns
*
Smn2B/+
Smn2B/-
Smn2B/+
Smn2B/-
Smn2B/+
Smn2B/-
Smn2B/+
Smn2B/-
P1
P5
P10
P15

Figure 3.8: There is an increase in the percentage of activated caspase-3 positive cells in the ventral horn of the thoracic spinal cord of *Smn$^{2B/-}$* mice at P15 (**A**) Representative images showing the different appearances that positive active caspase-3 cells can take. All cells with these appearances were counted in this analysis (Scale bar = 20μm). (**B**) The graph (Mean ± SEM) shows that at P1 there is a significant increase in the percentage of activated caspase-3 positive cells in control, *Smn$^{2B/+}$* mice. At P5 and P10 there is no significant difference in the percentage of active caspase-3 positive cells between *Smn$^{2B/-}$* and *Smn$^{2B/+}$* mice. At P15 there is a significant increase in the percentage of activated caspase-3 positive cells in the ventral horn of *Smn$^{2B/-}$* spinal cords compared to controls (by Mann Whitney-U test; ns>0.05, *p<0.05; n= 3 mice per genotype). Statistical analysis has also shown that there is a significant decrease in the percentage of active caspase-3 positive cells in *Smn$^{2B/+}$* controls between P1 and P15 (by one-way ANOVA, p<0.05) that is not observed *Smn$^{2B/-}$* mice (by one-way ANOVA, p>0.05).

3.2.2.5 Transcripts involved in the P53 signalling pathway are upregulated in the spinal cords of Smn$^{2B/-}$ mice between P5 and P7

Previous work by Murray *et. al.* showed that transcripts involved in the P53 signalling pathway were pre-symptomatically up-regulated in motor neurons of two different mouse models of SMA (Murray et al. 2015). Therefore, I aimed to determine the relationship between the onset of NMJ pathology and the up-regulation of transcripts involved in the P53 signalling pathway in the *Smn$^{2B/-}$* mouse model of SMA. As motor neurons that supply the vulnerable abdominal musculature (notably the TVA muscle), which was used for NMJ analysis above, lie within the thoracic portion of the spinal cord, cDNA from the thoracic spinal cord of *Smn$^{2B/-}$* and *Smn$^{2B/+}$* mice was used to perform qPCR. Transcripts of interest were *Cdkn1A*, *Fas* and *Pmaip1*, all of which are involved in the P53 signalling pathway.

qPCR analysis was performed first at P5. As shown above, at this time point there is no sign of pathological features at the NMJ or MNCBs. At P5, qPCR analysis showed that there is no significant change in the regulation of these transcripts in the spinal cords of *Smn$^{2B/-}$* compared to *Smn$^{2B/+}$*mice (Figure 3.9A).

Therefore, the regulation of these transcripts of interest was assessed at P7. This revealed an up-regulation of *Fas* and *Pmaip1* in $Smn^{2B/-}$ compared to $Smn^{2B/+}$ mice. There was no significant difference in the regulation of *Cdkn1A* (Figure 3.9B).

In conclusion, the up-regulation of these transcripts of interest in the spinal cord of $Smn^{2B/-}$ mice is occurring between P5 and P7, the same time window in which the onset of NMJ pathology was observed. These two events appear to be coinciding with each other and warrant further investigation to determine whether NMJ pathology is a consequence of the activation of the P53 signalling pathway or the cause of the activation of the P53 signalling pathway.

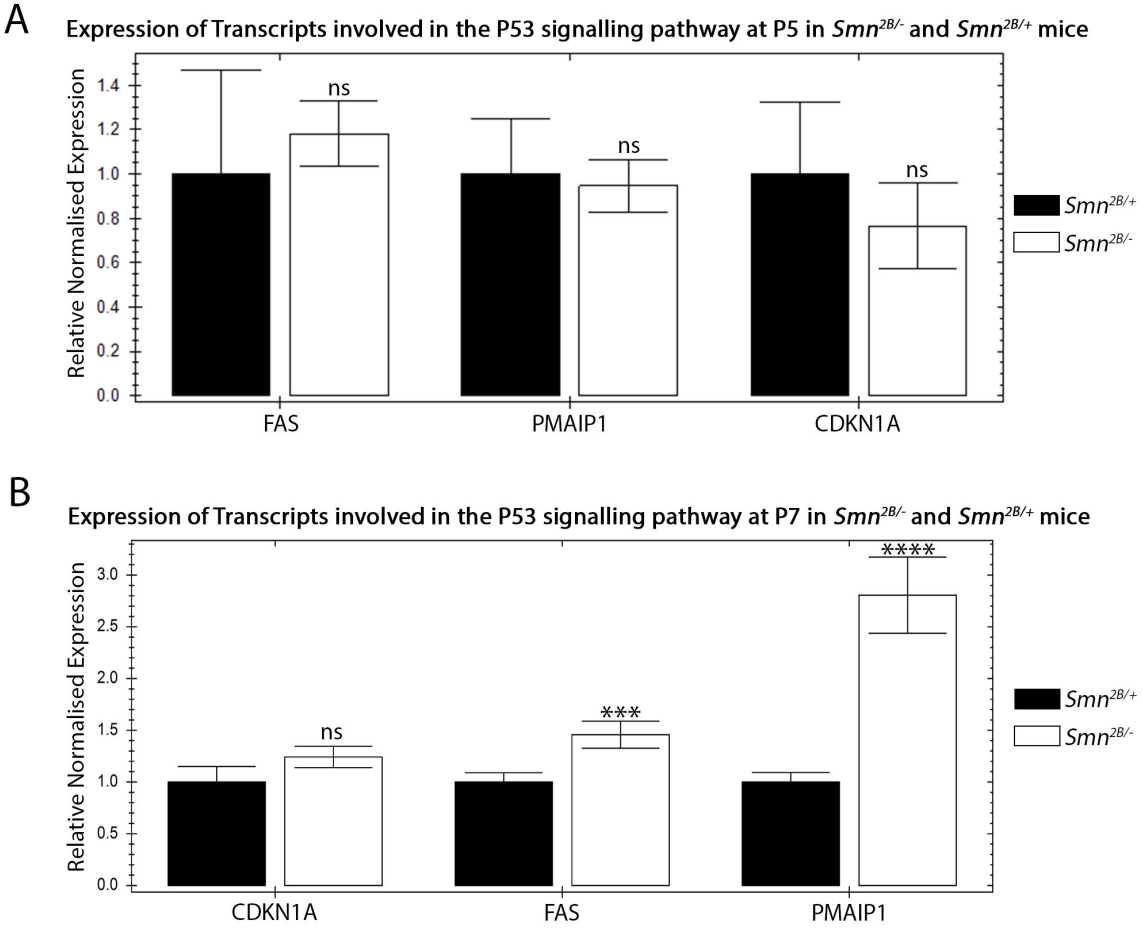

Figure 3.9: There is a significant increase in the expression of transcripts involved in the P53 signalling pathway in the spinal cords of *Smn*$^{2B/-}$ mice compared to controls at P7 (**A**) The bar chart (Mean ± SEM) shows that there is no significant difference in the expression of transcripts involved in the P53 signalling pathway in the thoracic spinal cord of *Smn*$^{2B/-}$ mice compared to *Smn*$^{2B/+}$ mice at P5 (by Mann Whitney-U test; ns>0.05;n=4 per genotype) (**B**) The bar chart (Mean ± SEM) shows that there is a significant increase in the expression of transcripts involved in the P53 signalling pathway in the thoracic spinal cord of *Smn*$^{2B/-}$ mice compared to *Smn*$^{2B/+}$ mice at P5 (by Mann Whitney-U test; ns>0.05;n=4 per genotype). Specifically, there is an increase in Fas and Pmaip1.

3.2.3 Investigating the relationship of the activation of the P53 signalling pathway and NMJ pathology

To investigate whether NMJ pathology is a consequence of the activation of the P53 signalling pathway or the cause of the activation of the P53 signalling pathway a mouse model in which the levels of P53 could be decreased was created. It was hypothesised that NMJ pathology was caused by the activation of the P53 signalling pathway and by reducing P53 the level of pathology at the NMJ observed at P15 would be decreased.

3.2.3.1 Reduction of P53 was confirmed using qPCR following derivation of the $Smn^{2B/-};P53^{fl/fl};Cre^{+}$ mouse model

The $Smn^{2B/-};P53^{fl/fl};Cre^{+}$ mouse model is a conditional knockout $Smn^{2B/-}$ mouse model of SMA in which P53 levels can be reduced using the Cre-LoxP system (Figure 3.10). This mouse model carries a P53-floxed gene (referred to as *P53fl* hereafter) that when in the presence of Cre-recombinase (Cre) will recombine and will essentially be 'knocked out'. In this case, mice carry the *CAG-CreER* allele. This is a tamoxifen inducible allele that leads to ubiquitous expression of Cre when tamoxifen is administered (Hayashi & McMahon 2002). Mice were bred to carry only one copy of *Cre* to exclude the need for *Cre* copy number genotyping and to ensure comparable recombination across mice.

In addition, mice were derived to be homozygous for *P53fl*, maximising the knockdown of P53 in this mouse model. To determine *P53fl* copy number, qPCR was performed using primers targeted against *P53fl* (see section 2.2.3 in Chapter 2). These primers were optimised for quantitative use and were shown to have an efficiency of 100% and 100.5% for *P53fl* primers and the control primer set, respectively (Figure 3.11A).

Here SYBR qPCR is used. SYBR green is a dye that binds to synthesised double stranded DNA and when it does so it begins to fluoresce. Therefore, when this dye is incorporated into the double stranded DNA synthesised during PCR, a fluorescent output can determine the quantity of DNA product within a sample (and therefore this is termed quantitative-PCR (qPCR)). Samples from homozygous mice will produce a greater fluorescent output, due to the increased starting quantity (two copies), than samples from heterozygous mice (one copy). The greater the starting quantity of DNA, the lower the number of cycles required for detection of the fluorescent output.

Samples from mice that were known to be heterozygous for *P53fl* were compared with samples from mice with an unknown copy number of *P53fl*. DNA samples were exposed to primers for the *P53fl* allele and a standard control allele. By subtracting the mean Cq (number of cycles required to detect the fluorescence intensity) obtained from control primers and the mean Cq obtained from *P53fl* primers, for each sample, homozygous and heterozygous mice could be seperated. Those homozygous for *P53fl* had a difference of approximately 0.5 cycles whereas those heterozygous had a difference of 1.5 cycles (Figure 3.11B&C). This enabled us to select for $P53^{fl/fl}$ mice.

Experimental litters contained mice of four genotypes; $Smn^{2B/+}$ mice that are $P53^{fl/fl}$ and do not carry *Cre* ($Smn^{2B/+};P53^{fl/fl};Cre^{-}$), $Smn^{2B/-}$ mice that are $P53^{fl/fl}$ and do not carry Cre^{+} ($Smn^{2B/-};P53^{fl/fl};Cre$-), $Smn^{2B/+}$ mice that are $P53^{fl/fl}$ and carry Cre^{+} ($Smn^{2B/+};P53^{fl/fl};Cre^{+}$) and $Smn^{2B/-}$ mice that are $P53^{fl/fl}$ and carry Cre^{+} ($Smn^{2B/-};P53^{fl/fl};Cre$+) (Figure 3.11). All pups were treated with tamoxifen however only those that carried *Cre* would experience recombination of *P53*. This makes use of all pups within one litter and provides us with appropriate controls. For simplicity, hereafter, mice that were Cre^{-}, and so did not experience *P53* recombination, will be referred to as $P53^{+/+}$ and mice that were Cre^{+}, and did experience *P53* recombination, will be referred to as $P53^{-/-}$.

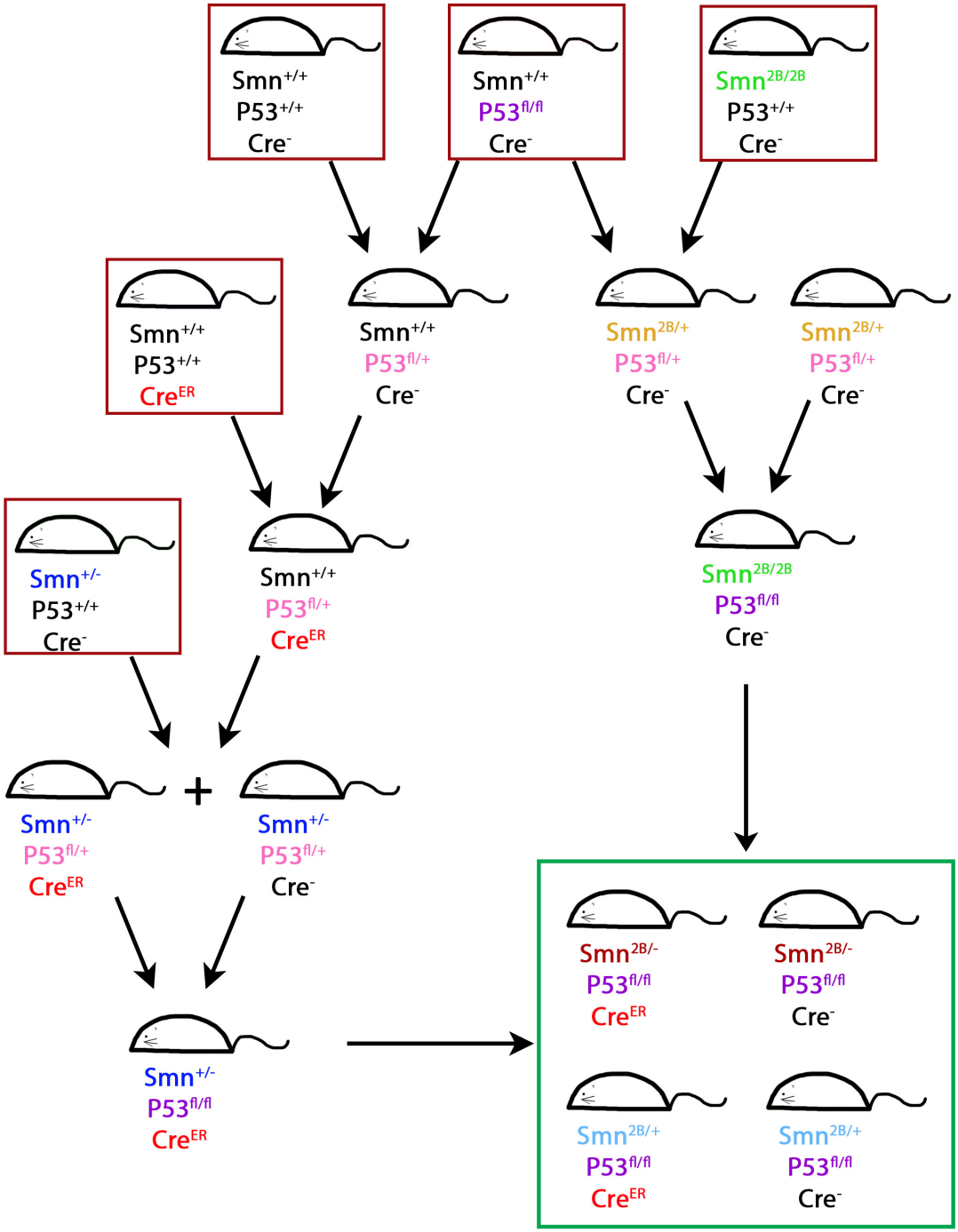

Figure 3.10: Derivation process to obtain experimental *Smn$^{2B/-}$;P53$^{fl/fl}$;Cre^{+}* mice and control littermates. Mice shown in red boxes are those that were within previously established colonies (*Smn$^{+/+}$* mice, *Smn$^{2B/2B}$* mice and *Smn$^{+/-}$* mice) or were donated to our lab (*P53$^{fl/fl}$* mice and *Cre^{ER}* mice). These mice were required to begin this colony. The arrows show the crosses that were carried out to obtain the next generation of desirable mice. Only desirable genotypes are shown, other genotypes were obtained from crossed in keeping with mendelian genetics. The mice in the green box represent an experimental litter. All mice in these litters were treated with tamoxifen and those that expressed *Cre^{ER}* would have P53 knocked down (Please note that *Cre^{ER}* will now be referred to as 'Cre^{+}').

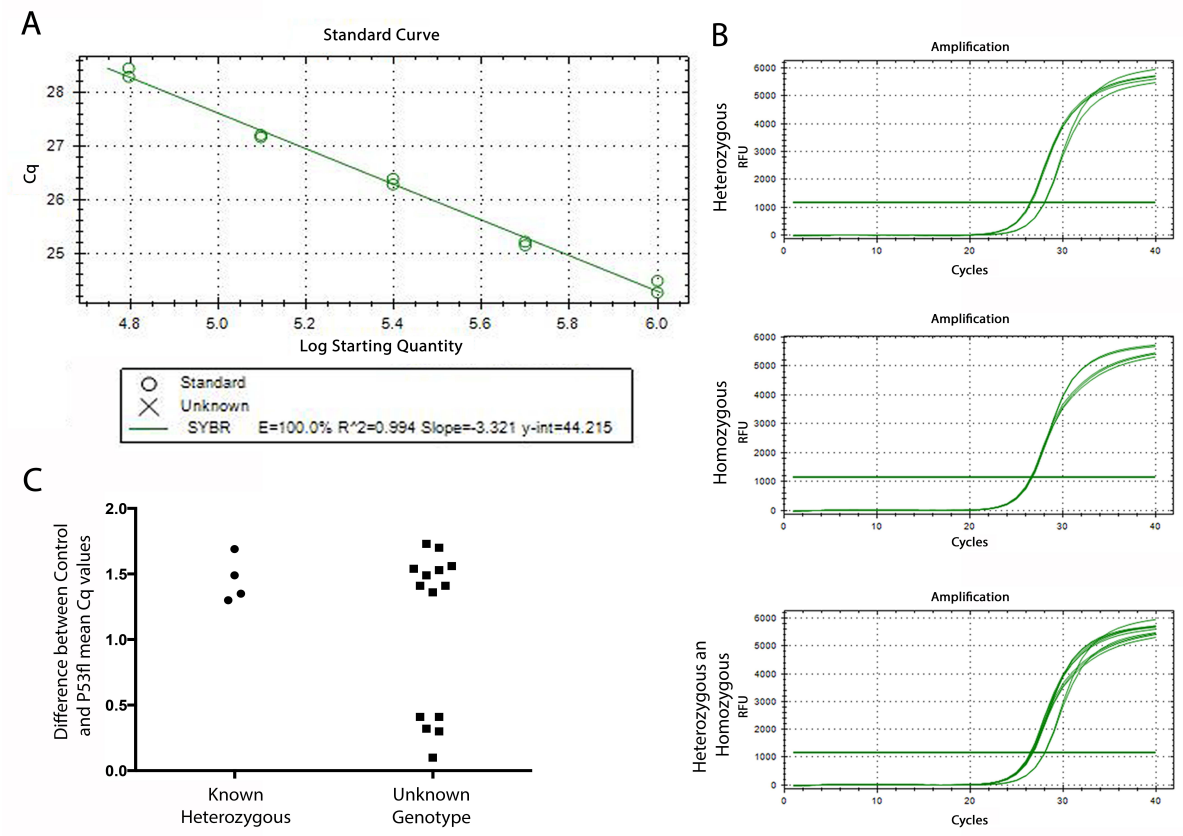

Figure 3.11: Copy number genotyping separates *P53*$^{fl/+}$ mice and the desired *P53*$^{fl/fl}$ mice. (A) The standard curve (created by plotting the fluorescence intensity (Cq) against the log of the relative starting quantity of DNA) shows that the efficiency of P53 primer set is 100%. An efficacy of 90-110% is desirable and so these primers are appropriated for quantitative use. **(B)** The graphs show amplification cycles for DNA samples from mice that have now been shown to be homozygous or heterozygous for the P53fl allele. Exponential amplification curves for control primers and P53 primers are shown in each of the three graphs. Note that in heterozygous samples these curves appear separated. This is due to a lower starting concentration of P53fl DNA (i.e one copy rather than two copies) meaning the amplification of this requires more cycles that if there were two copies of this allele. In addition, for reference, the Cq value is the number of cycles at which the amplification curve crosses the green horizontal threshold line that can be seen in these three graphs **(C)** The graph shows the difference between the mean Cq of control primers and *P53fl* primers, for each sample. Samples that were known to be heterozygous were used as reference. Those heterozygous consistently showed a difference of approximately 1.5 cycles and those homozygous for *P53fl* consistently showed a difference of approximately <0.5 cycles.

To confirm that *P53*$^{-/-}$ mice did express reduced P53, qPCR was performed using spinal cord cDNA and primers targeted against P53, which had been previously used by Simon *et. al.* (Simon et al. 2017). Optimisation of these primers showed an efficiency of 94%. This qPCR analysis revealed a reduction in *P53* in *Smn*$^{2B/-}$*;P53*$^{-/-}$ mice compared to *Smn*$^{2B/-}$*;P53*$^{+/+}$ mice at P15. This reduction was also seen in *Smn*$^{2B/+}$*;P53*$^{-/-}$ when compared to *Smn*$^{2B/+}$*;P53*$^{+/+}$ mice (Figure 3.12). Although this was not a complete knockdown, a reduction of 40% of *P53* mRNA was achieved in both *Smn*$^{2B/-}$ and *Smn*$^{2B/+}$ mice. It should be noted that this is a reduction in *P53* mRNA expression rather than in the levels of functional protein. In order to confirm that this reduction is also observed at the protein level, western blotting should be performed. Unfortunately, this was not possible due to time constraints.

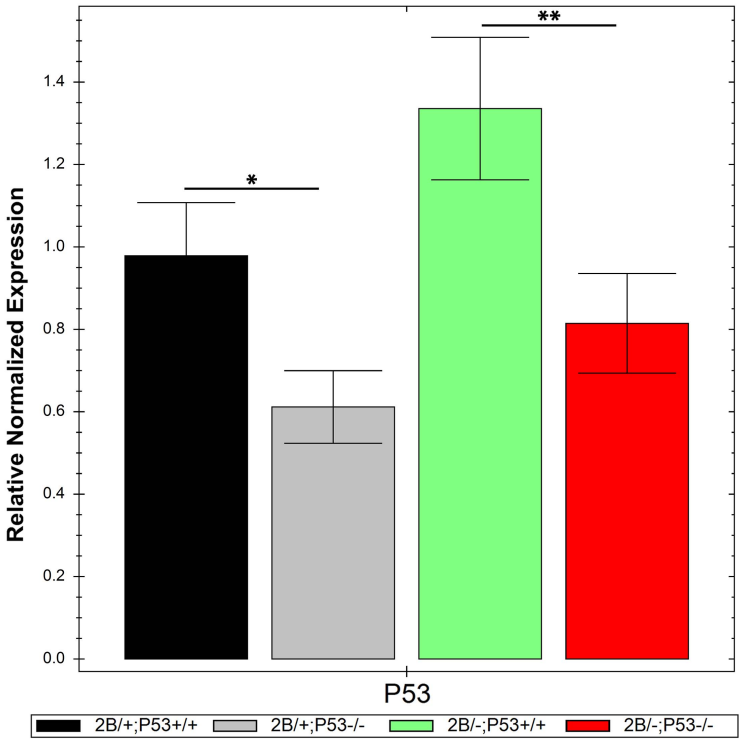

Figure 3.12: Reduction of P53 was confirmed using qPCR on spinal cord cDNA. Bar chart (Mean ± SEM) shows that there is a significant decrease in P53 at the transcript level in the spinal cord of *Smn*$^{2B/+}$*;P53*$^{-/-}$ mice compared to *Smn*$^{2B/+}$*;P53*$^{+/+}$ mice and in *Smn*$^{2B/-}$*;P53*$^{-/-}$ mice compared to *Smn*$^{2B/-}$*;P53*$^{+/+}$ mice (by Mann Whitney-U test, *p<0.05, **p<0.001; n=3 for *Smn*$^{2B/-}$*;P53*$^{+/+}$, n=4 for all other genotypes.)

3.2.3.2 Reducing P53 does not improve the phenotype of $Smn^{2B/-}$ mice

In order to investigate whether a reduction in P53 expression affects the phenotype of $Smn^{2B/-}$ mice (and control $Smn^{2B/+}$ *mice*) both weight and motor performance of $Smn^{2B/-};P53^{-/-}$, $Smn^{2B/-};P53^{+/+}$, $Smn^{2B/+};P53^{-/-}$ and $Smn^{2B/+};P53^{+/+}$ mice were monitored, following tamoxifen treatment at P4 and P5. In both $Smn^{2B/-}$ and $Smn^{2B/+}$ mice a separation in the body weights of $P53^{+/+}$ and $P53^{-/-}$ mice was observed (Figure 3.13). $Smn^{2B/-};P53^{-/-}$ and $Smn^{2B/+};P53^{-/-}$ displayed a decrease in body weight compared to their respective $P53^{+/+}$ controls. There was a significant difference in the body weights of $Smn^{2B/+};P53^{-/-}$ mice compared to $Smn^{2B/+};P53^{+/+}$ mice at P5 and a significant difference in the body weights of $Smn^{2B/-};P53^{-/-}$ mice compared to $Smn^{2B/-};P53^{+/+}$ mice at P6 (Figure 3.13B).

In order to investigate the effect of reduced P53 levels on motor performance, an age appropriate motor test was applied ('Time to Right' (TtR) test or the 'Turn Around' (TA) Test, both of which are explained fully in Chapter 2). The TtR test, used on pups aged between P7 and P11, involves the pups being place on their back and recording the time it takes for them to right themselves, or turn onto all four paws. There was no significant difference between $Smn^{2B/+};P53^{-/-}$ and $Smn^{2B/+};P53^{+/+}$ mice and also no significant difference between $Smn^{2B/-};P53^{-/-}$ and $Smn^{2B/-};P53^{+/+}$ mice (Figure 3.13C). Therefore, a reduction in P53 does not affect the ability of mice to right themselves.

To assess motor ability in mice aged between P12 and P15, the TA test was performed. This involves placing the mouse in a downward facing position on a grid that is placed at a 45^{o} angle and recording the time it takes for the mouse to turn 180^{o} to face upwards on the grid. There was no significant difference between $Smn^{2B/+};P53^{-/-}$ and $Smn^{2B/+};P53^{+/+}$ mice and between $Smn^{2B/-};P53^{-/-}$ and $Smn^{2B/-};P53^{+/+}$ mice (Figure 3.13D). This would imply that reducing P53 levels does not improve motor performance. Indeed, there is a

significant decrease in the ability of *Smn$^{2B/-}$;P53$^{-/-}$* mice to perform this test when compared to *Smn$^{2B/-}$;P53$^{+/+}$* mice at P13.

Overall this shows that knocking down P53 does not improve the phenotype of *Smn$^{2B/-}$* mice and if anything, it has a negative impact on the phenotype of both *Smn$^{2B/-}$* and *Smn$^{2B/+}$* mice.

3.2.3.3 A reduction in P53 decreases denervation in the TVA of Smn$^{2B/-}$ mice but does not improve the overall health of the NMJ

The hypothesis of this investigation was that by reducing P53 levels in *Smn$^{2B/-}$* mice NMJ pathology at P15 would improve. Therefore, NMJ analysis, as previously performed in *Smn$^{2B/-}$* mice, was performed at P15 in *Smn$^{2B/-}$;P53$^{-/-}$* and *Smn$^{2B/-}$;P53$^{+/+}$* mice. This involved assessing occupancy, pre-synaptic swelling and endplate size in the TVA muscle.

Firstly, the occupancy of post-synaptic endplates of *Smn$^{2B/-}$;P53$^{-/-}$* and *Smn$^{2B/-}$;P53$^{+/+}$* mice was assessed. This showed a significant increase in the percentage of fully occupied endplates and a decrease in the percentage of vacant endplates seen in *Smn$^{2B/-}$;P53$^{-/-}$* mice compared to *Smn$^{2B/-}$;P53$^{+/+}$*. This indicates that there is a decrease in denervation when P53 is reduced (Figure 3.14B).

Pre-synaptic swelling at the NMJs of *Smn$^{2B/-}$;P53$^{-/-}$* and *Smn$^{2B/-}$;P53$^{+/+}$* mice was also assessed. As before, the level of pre-synaptic swelling was staged from ‘none’ to ‘severe’. This showed that there was no significant difference in the level of swelling at pre-synaptic terminals in the TVA of *Smn$^{2B/-}$;P53$^{-/-}$* mice compared to *Smn$^{2B/-}$;P53$^{+/+}$* mice (Figure 3.14C).

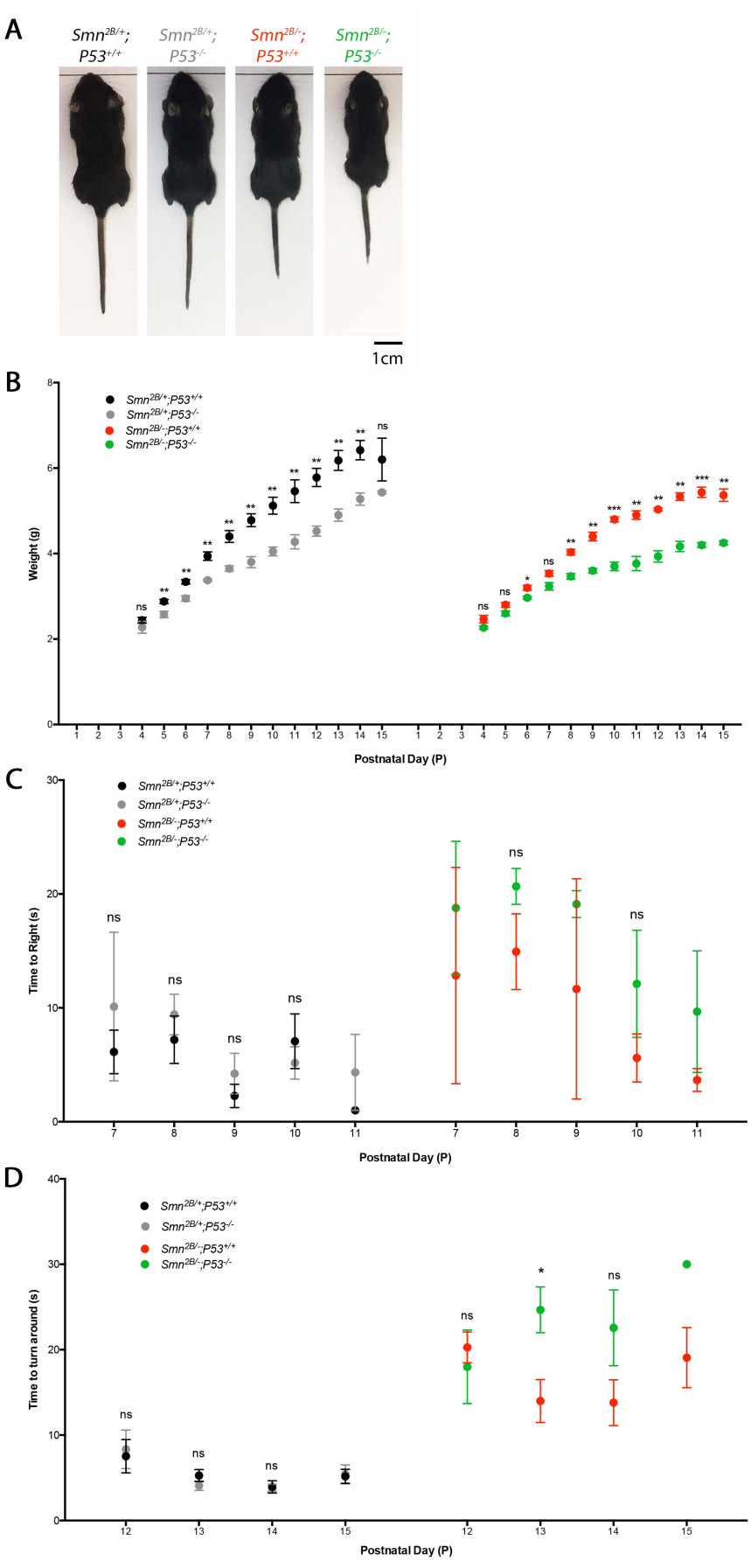
A
Smn2B/+; P53+/+
Smn2B/+; P53-/-
Smn2B/-; P53+/+
Smn2B/-; P53-/-
1cm
B
Smn2B/+;P53+/+
Smn2B/+;P53-/-
Smn2B/-;P53+/+
Smn2B/-;P53-/-
Weight (g)
Postnatal Day (P)
C
Time to Right (s)
Postnatal Day (P)
D
Time to turn around (s)
Postnatal Day (P)

Figure 3.13: Reducing P53 does not improve the phenotype of *Smn$^{2B/-}$* mice. (**A**) Representative images of mice with the various genotypes within experimental litters at P15. (**B**) Graph (Mean ± SEM) shows body weight in *Smn$^{2B/+}$;P53$^{+/+}$* and *Smn$^{2B/+}$;P53$^{-/-}$* on the left and *Smn$^{2B/-}$;P53$^{+/+}$* and *Smn$^{2B/-}$;P53$^{-/-}$* on the right. There is a significant difference in weight between those that are *P53$^{+/+}$* and *P53$^{-/-}$* in *Smn$^{2B/+}$* from P5 and in *Smn$^{2B/-}$* from P6 (**C**) Graph (Mean ± SEM) shows time to right for *Smn$^{2B/+}$;P53$^{+/+}$* and *Smn$^{2B/+}$;P53$^{-/-}$* on the left and *Smn$^{2B/-}$;P53$^{+/+}$* and *Smn$^{2B/-}$;P53$^{-/-}$* on the right. There is no significant difference between the time to right for *Smn$^{2B/+}$;P53$^{+/+}$* and *Smn$^{2B/+}$;P53$^{-/-}$* and also for *Smn$^{2B/-}$;P53$^{+/+}$* and *Smn$^{2B/-}$;P53$^{-/-}$* mice. Note that where no statistics are shown on the graph for particular time points is where there was not a sufficient n number to perform statistical analysis. (**D**) Graph (Mean ± SEM) shows performance in the time to turn around for *Smn$^{2B/+}$;P53$^{+/+}$* and *Smn$^{2B/+}$;P53$^{-/-}$* on the left and *Smn$^{2B/-}$;P53$^{+/+}$* and *Smn$^{2B/-}$;P53$^{-/-}$* on the right. There is no significant difference between the time to turn around for *Smn$^{2B/+}$;P53$^{+/+}$* and *Smn$^{2B/+}$;P53$^{-/-}$*. There is a significant difference between the time to turn around for *Smn$^{2B/-}$;P53$^{+/+}$* and *Smn$^{2B/-}$;P53$^{-/-}$* mice at P13 but not at any other time point, on which statistical analysis was performed. There may be a trend to *Smn$^{2B/-}$;P53$^{-/-}$* mice performing poorly compared to *Smn$^{2B/-}$;P53$^{+/+}$* mice. (For all graphs, where statistical analysis was possible, it was by unpaired t-test; ns>0.05, *p<0.05, **p<0.01, ***p<0.005; n=3-5 (n=2 where no statistics are shown)).

Maturation of the NMJ, including its post-synaptic endplate, is activity dependent and so maturity of the endplate is related to the activity and function of an NMJ (Darabid et al. 2014). Therefore, to gain an idea as to the functioning ability of NMJs in *Smn$^{2B/-}$;P53$^{-/-}$* the maturity of endplates in the TVA of *Smn$^{2B/-}$;P53$^{-/-}$* and *Smn$^{2B/-}$;P53$^{+/+}$* mice was assessed. A staging system that categorised endplates into groups based on their maturity was devised. Stage 1 was most mature, displaying a pretzel-like structure whereas stage 4 was the least mature where the endplate has a plaque-like appearance (see Chapter 2 for the full criteria). This showed that there is no significant difference in the maturity of endplates in the TVA of *Smn$^{2B/-}$;P53$^{-/-}$* mice when compared to *Smn$^{2B/-}$;P53$^{+/+}$* mice (Figure 3.14D). This suggests that although there is a decrease in denervation in *Smn$^{2B/-}$;P53$^{-/-}$* mice there is not necessarily an improvement in function.

The area of endplates in the TVA of *Smn*$^{2B/-}$;*P53*$^{-/-}$ and *Smn*$^{2B/-}$;*P53*$^{+/+}$ mice was also measured. This showed that reducing P53 decreases the area of endplates of *Smn*$^{2B/-}$;*P53*$^{-/-}$ mice compared to *Smn*$^{2B/-}$;*P53*$^{+/+}$ mice (Figure 3.14E). It is possible that this decrease in area may be caused by the decrease in size of the mouse and/or muscle. Further investigation into muscle fibre size would be required to confirm this.

Additionally, to confirm that a reduction in P53 did not cause alterations in NMJ morphology in control *Smn*$^{2B/+}$ mice, occupancy, pre-synaptic swelling and endplate maturation and size were assessed in *Smn*$^{2B/+}$;*P53*$^{-/-}$ and *Smn*$^{2B/+}$;*P53*$^{+/+}$ mice. This showed that there was no significant difference in any of these features between *Smn*$^{2B/+}$;*P53*$^{-/-}$ and *Smn*$^{2B/+}$;*P53*$^{+/+}$ mice (Figure 3.15).

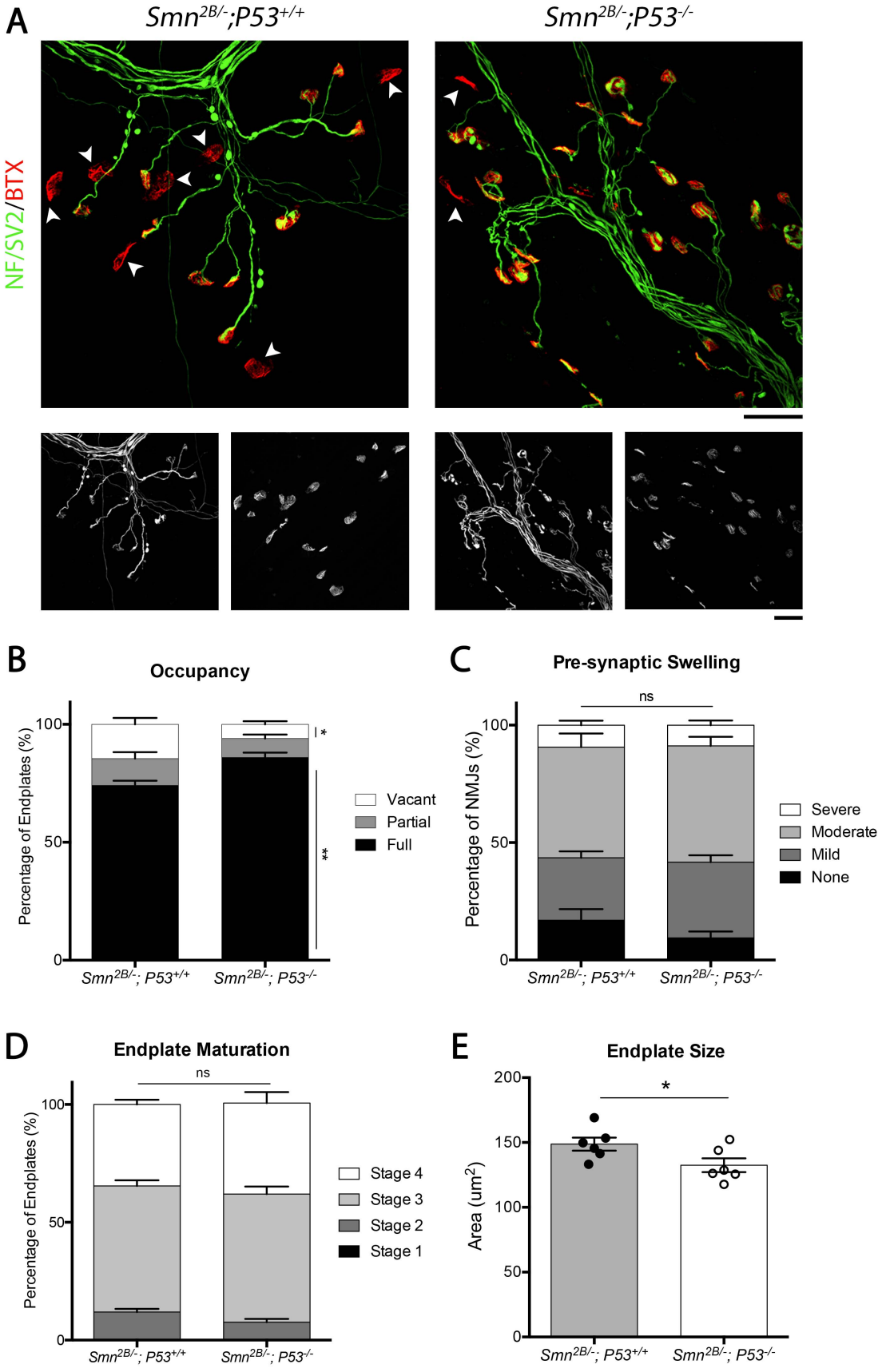
A
Smn2B/-;P53+/+
Smn2B/-;P53-/-
NF/SV2/BTX
B
Occupancy
Percentage of Endplates (%)
100
50
0
*
**
Vacant
Partial
Full
Smn2B/-; P53+/+
Smn2B/-; P53-/-
C
Pre-synaptic Swelling
ns
Percentage of NMJs (%)
Severe
Moderate
Mild
None
D
Endplate Maturation
ns
Percentage of Endplates (%)
Stage 4
Stage 3
Stage 2
Stage 1
E
Endplate Size
*
Area (um2)
200
150
100
50
0

Figure 3.14: A reduction in P53 reduces denervation in the TVA of *Smn$^{2B/-}$* mice (**A**) Representative confocal images showing NMJs from the TVA of *Smn$^{2B/-}$;P53$^{+/+}$* and *Smn$^{2B/-}$;P53$^{-/-}$* mice. Note that the white arrowheads point out vacant endplates (Scale bar = 40μm). (**B**) The graph (Mean ± SEM) shows that there is a significant increase in the percentage of fully occupied endplates and a significant decrease in vacant endplates in *Smn$^{2B/-}$;P53$^{-/-}$* compared to *Smn$^{2B/-}$;P53$^{+/+}$* (by Mann Whitney-U test; *p<0.05, **p<0.01). (**C**) The graph (Mean ± SEM) shows that there is no significant difference in the level of pre-synaptic swelling in the TVA of *Smn$^{2B/-}$;P53$^{+/+}$* and *Smn$^{2B/-}$;P53$^{-/-}$* mice (by Mann Whitney-U test; ns>0.05). **(D)** The graph (Mean ± SEM) shows that there is no significant difference in the maturity of endplates in the TVA of *Smn$^{2B/-}$;P53$^{+/+}$* and *Smn$^{2B/-}$;P53$^{-/-}$* mice (by Mann Whitney-U test; ns>0.05). (**E**) The graph (Mean ± SEM) shows that there is a small but significant decrease in the area of endplates in the TVA of *Smn$^{2B/-}$;P53$^{+/+}$* and *Smn$^{2B/-}$;P53$^{-/-}$* mice (by Unpaired T-test; *p<0.05; n=6 muscles per genotype for all analysis).

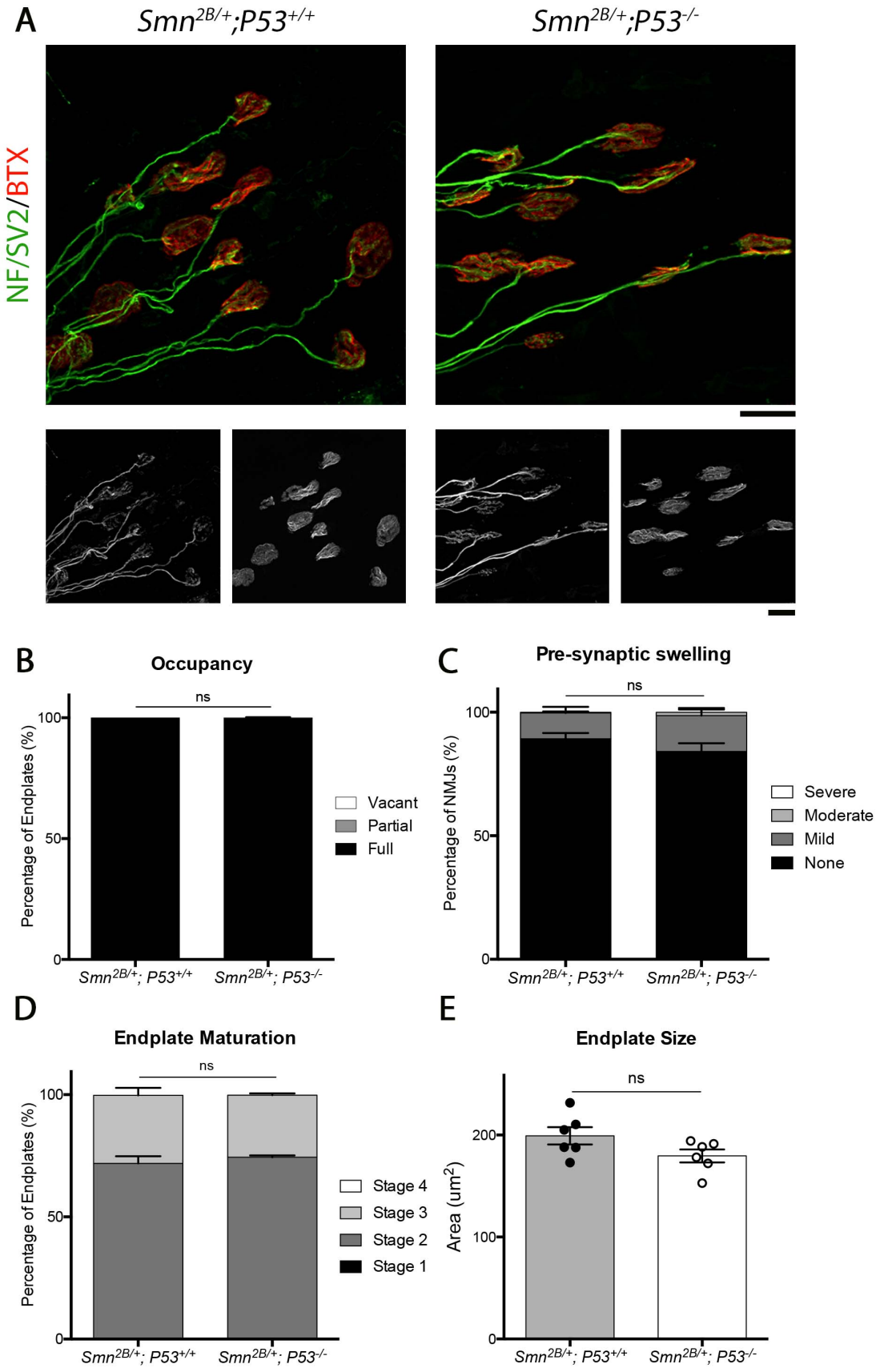
A
Smn2B/+;P53+/+
Smn2B/+;P53-/-
NF/SV2/BTX
B
Occupancy
ns
Percentage of Endplates (%)
100
50
0
Vacant
Partial
Full
Smn2B/+; P53+/+
Smn2B/+; P53-/-
C
Pre-synaptic swelling
ns
Percentage of NMJs (%)
100
50
0
Severe
Moderate
Mild
None
Smn2B/+; P53+/+
Smn2B/+; P53-/-
D
Endplate Maturation
ns
Percentage of Endplates (%)
100
50
0
Stage 4
Stage 3
Stage 2
Stage 1
Smn2B/+; P53+/+
Smn2B/+; P53-/-
E
Endplate Size
ns
Area (um2)
200
100
0
Smn2B/+; P53+/+
Smn2B/+; P53-/-

Figure 3.15: A reduction in P53 in control *Smn$^{2B/+}$* mice does not alter NMJ morphology. (**A**) Representative confocal images showing NMJs from the TVA of *Smn$^{2B/+}$;P53$^{+/+}$* and *Smn$^{2B/+}$;P53$^{-/-}$* mice (Scale bar = 20μm). (**B**) The graph (Mean ± SEM) shows that when P53 is knocked down there is no significant difference in the occupancy of endplates in the TVA of *Smn$^{2B/+}$;P53$^{-/-}$* compared to *Smn$^{2B/+}$;P53$^{+/+}$* mice *(*ns>0.05 by Mann Whitney-U test*)*. (**C**) The graph (Mean ± SEM) shows that there is no significant difference in the level of pre-synaptic swelling in the TVA of *Smn$^{2B/+}$;P53$^{+/+}$* mice compared to *Smn$^{2B/+}$;P53$^{-/-}$* mice (by Mann Whitney-U test; ns>0.05). (**D**) The graph (Mean ± SEM) shows that there is no significant difference in the maturity of endplates in the TVA of *Smn$^{2B/+}$;P53$^{+/+}$* mice compared to *Smn$^{2B/+}$;P53$^{-/-}$* mice (by Mann Whitney-U test; ns>0.05). (**E**) The graph (Mean ± SEM) shows that there is no significant difference in the area of endplates in the TVA of *Smn$^{2B/+}$;P53$^{+/+}$* mice compared to *Smn$^{2B/+}$;P53$^{-/-}$* mice (by Unpaired T-test; ns>0.05; n=6 muscles per genotype for all analysis).

3.2.3.4 A reduction in P53 does not alter the number or size of MNCBs in Smn$^{2B/-}$ mice at P15

To determine whether reducing P53 in *Smn$^{2B/+}$ and Smn$^{2B/-}$* mice had any effect on the number of MNCBs in the ventral horn of the spinal cord, MNCBs were counted in the thoracic segments T4-T8. Spinal cord sections from *P53$^{+/+}$* and *P53$^{-/-}$*, *Smn$^{2B/+}$ and Smn$^{2B/-}$* mice were stained for ChAT and Nissl and counterstained with DAPI. MNCBs were counted if they conformed to the criteria set out in Chapter 2; they would have a large, irregular shape and would be double stained with ChAT and Nissl. They would lie within the ventral horn of the spinal cord and have a visible nucleus and nucleoli (Figure 3.16). By following this criteria, it was found that there was no significant difference in the number of MNCBs in *Smn$^{2B/+}$;P53$^{-/-}$* compared to *Smn$^{2B/+}$;P53$^{+/+}$* mice or in *Smn$^{2B/-}$;P53$^{-/-}$* compared to *Smn$^{2B/-}$;P53$^{+/+}$* mice (Figure 3.17A). However, there was a significant difference between *Smn$^{2B/+}$ and Smn$^{2B/-}$* mice (Figure 3.17A) which is consistent with what had been previously seen earlier in this chapter (Figure 3.6).

Imaging of these MNCB allowed their cytoplasmic and nuclear area to be measured. This showed no significant difference in both the cytoplasmic area and in the area of the nucleus of MNCB between *Smn*$^{2B/+}$;*P53*$^{-/-}$ and *Smn*$^{2B/+}$;*P53*$^{+/+}$ mice as well as *Smn*$^{2B/-}$;*P53*$^{-/-}$ and *Smn*$^{2B/-}$;*P53*$^{+/+}$ mice (Figure 3.17 B&C).

3.2.3.5 Reducing P53 does not decrease the levels of transcripts downstream of P53 in Smn$^{2B/-}$ *mice at P15*

Transcripts involved in the P53 signalling pathway were of interest as Murray *et. al.* had shown that they were up-regulated pre-symptomatically in two different mouse models of SMA (Murray et al. 2015). As detailed above, it was also found that their up-regulation, in the *Smn*$^{2B/-}$ mouse model, coincided with the onset of NMJ pathology. I wished to determine the effect of reducing P53 on the regulation of these transcripts that are downstream of P53. The transcripts of interest were *Cdkn1A*, *Pmaip1* and *Fas*. It was found that there was no significant difference in mRNA level of these transcripts in *Smn*$^{2B/-}$;*P53*$^{-/-}$ compared to *Smn*$^{2B/-}$;*P53*$^{+/+}$ mice (Figure 3.18). The reasons for this remain unclear and provide an interesting discussion topic (refer to section 3.3.5).

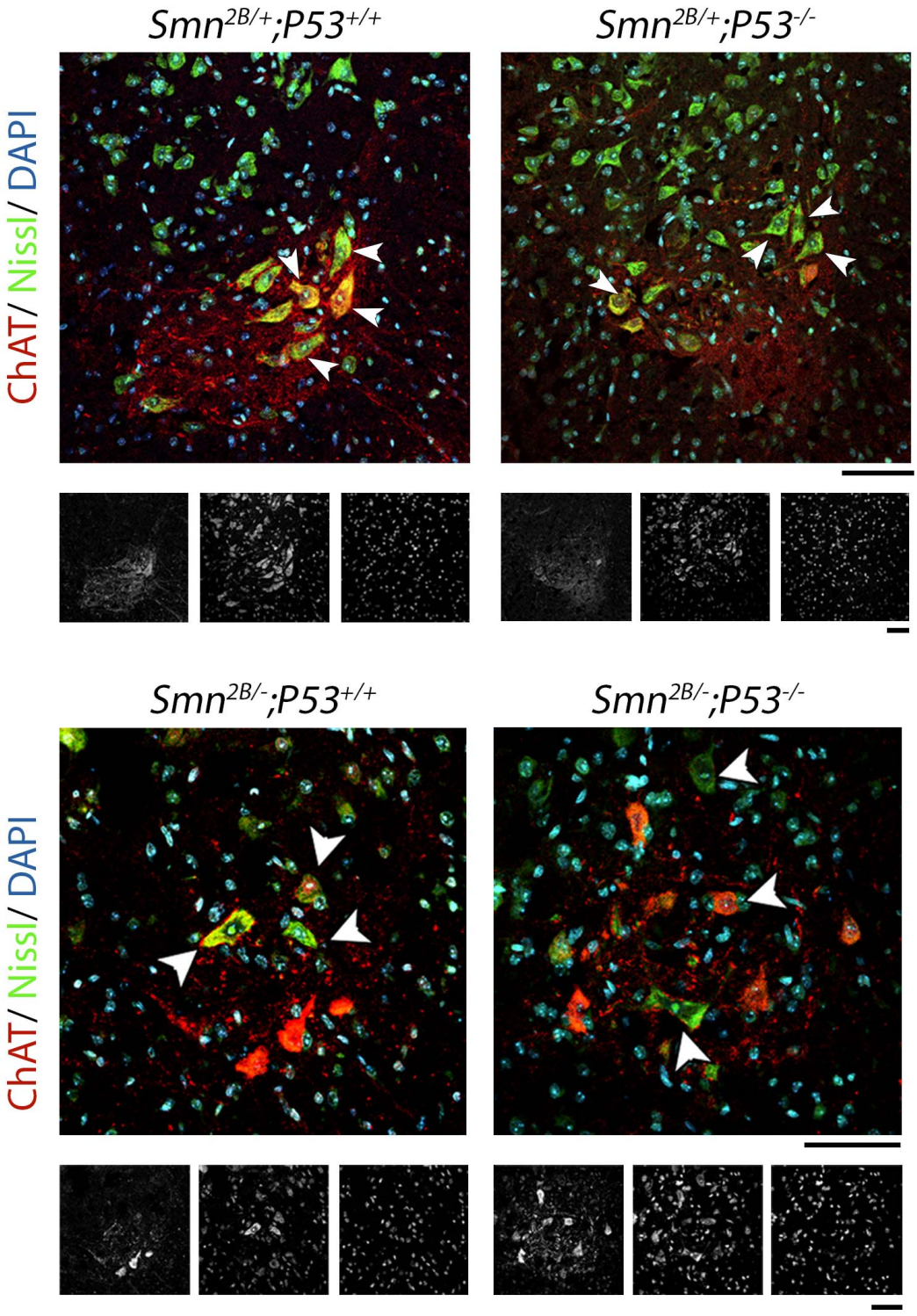

Figure 3.16: Reducing P53 in *Smn*$^{2B/-}$ and *Smn*$^{2B/+}$ mice does not alter the morphology of MNCBs in the ventral horn of their spinal cord (**A**) Representative images showing MNCBs in the ventral horn of the spinal cord of *Smn*$^{2B/+}$;*P53*$^{+/+}$ and *Smn*$^{2B/+}$;*P53*$^{-/-}$ mice and *Smn*$^{2B/-}$;*P53*$^{+/+}$ and *Smn*$^{2B/-}$;*P53*$^{-/-}$ mice. White arrowheads highlight MNCBs in the thoracic spinal cord of *Smn*$^{2B/-}$ and *Smn*$^{2B/+}$ mice that have normal P53 levels (*P53*$^{+/+}$) and have had P53 reduced (*P53*$^{-/-}$) (Scale bar = 40μm).

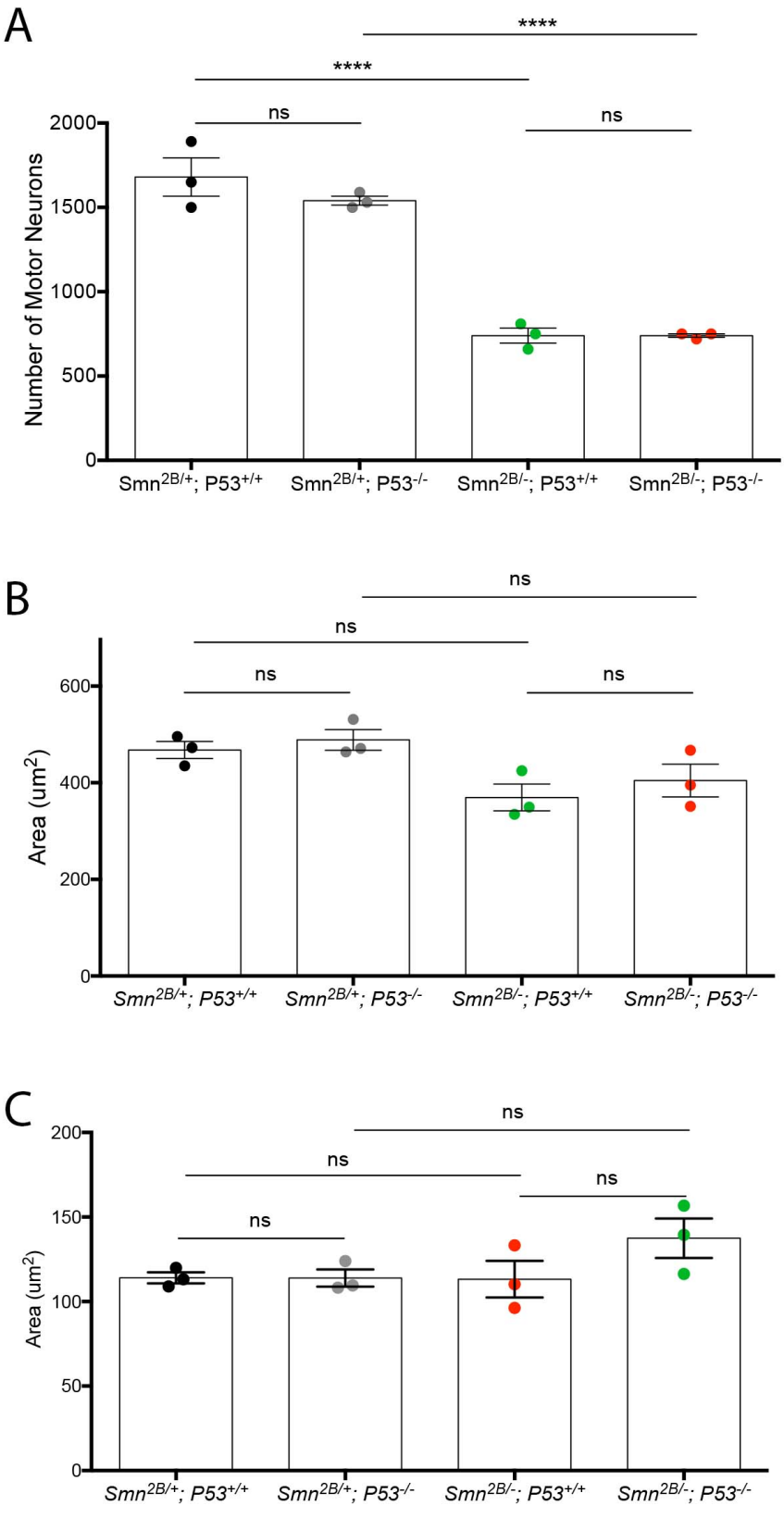
A
****
****
ns
ns
Number of Motor Neurons
2000
1500
1000
500
0
Smn2B/+; P53+/+
Smn2B/+; P53-/-
Smn2B/-; P53+/+
Smn2B/-; P53-/-
B
ns
ns
ns
ns
Area (um2)
600
400
200
0
Smn2B/+; P53+/+
Smn2B/+; P53-/-
Smn2B/-; P53+/+
Smn2B/-; P53-/-
C
ns
ns
ns
ns
Area (um2)
200
150
100
50
0
Smn2B/+; P53+/+
Smn2B/+; P53-/-
Smn2B/-; P53+/+
Smn2B/-; P53-/-

Figure 3.17: Reducing P53 does not alter the number or size of MNCBs in the ventral horn of the thoracic spinal cord. (**A**) The graph (Mean ± SEM) shows that when P53 is reduced there is no significant difference in the number of MNCBs in the ventral horn of both *Smn*$^{2B/+}$ and *Smn*$^{2B/-}$ spinal cords. There is a significant difference in the loss of MNCBs in *Smn*$^{2B/-}$ mice compared to *Smn*$^{2B/+}$ mice (by One-way ANOVA*;* ns>0.05, ****p<0.001; n=3 mice per genotype). (**B**) The graph (Mean ± SEM) shows that when P53 is reduced there is no significant difference in the area of MNCBs in the ventral horn of both *Smn*$^{2B/+}$ and *Smn*$^{2B/-}$ spinal cords (by One-way ANOVA*;* ns>0.05; n=3 mice per genotype). (**C**) The graph (Mean ± SEM) shows that when P53 is reduced there is no significant difference in the area of the nuclei of MNCBs in the ventral horn of both *Smn*$^{2B/+}$ and *Smn*$^{2B/-}$ spinal cords (by One-way ANOVA*;* ns>0.05; n=3 mice per genotype).

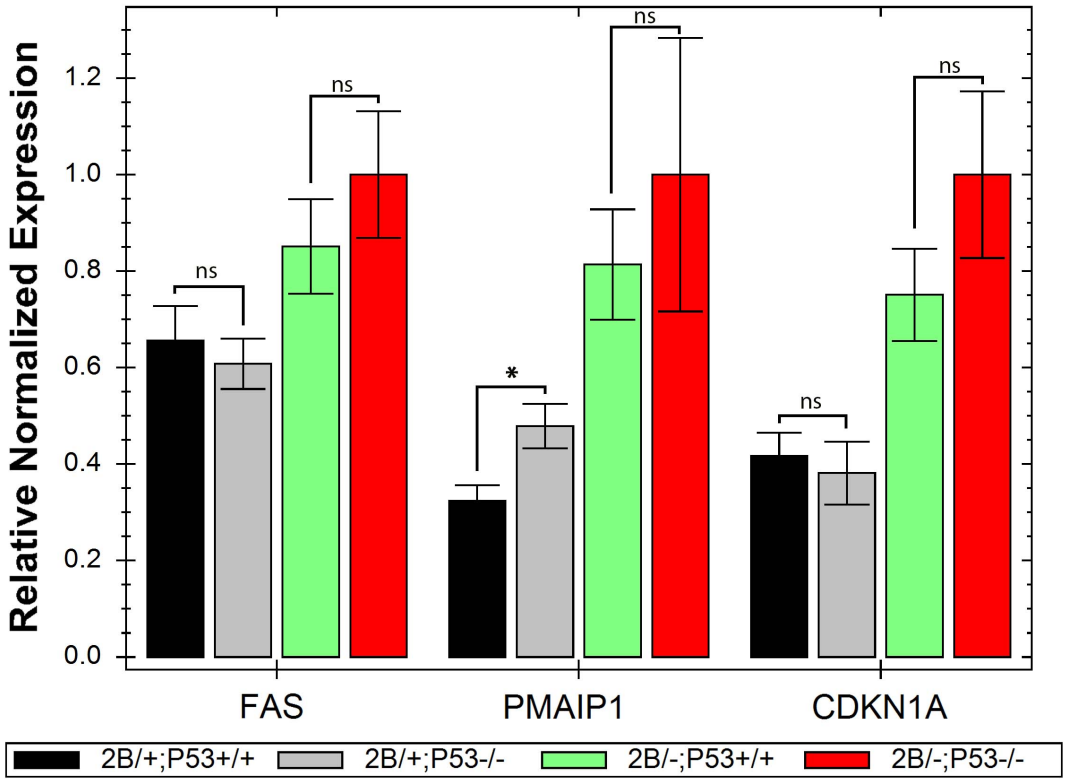

Figure 3.18: Reducing P53 does not alter the overall regulation of transcripts that are downstream of P53 in the P53 signalling pathway (**A**) The bar chart (Mean ± SEM) shows the relative normalised expression of Fas, Pmaip1 and Cdkn1A in the spinal cords of *Smn*$^{2B/+}$*;P53*$^{-/-}$, *Smn*$^{2B/+}$*;P53*$^{+/+}$, *Smn*$^{2B/-}$*;P53*$^{+/+}$ and *Smn*$^{2B/-}$*;P53*$^{-/-}$ mice. It compares *Smn*$^{2B/+}$*;P53*$^{-/-}$ and *Smn*$^{2B/+}$*;P53*$^{+/+}$ mice as well as *Smn*$^{2B/-}$*;P53*$^{-/-}$ and *Smn*$^{2B/-}$*;P53*$^{-/-}$ mice. There is a significant increase in the expression of Pmaip1 in *Smn*$^{2B/+}$*;P53*$^{-/-}$ mice compared to *Smn*$^{2B/+}$*;P53*$^{+/+}$ mice but there is no significant difference in all other comparisons *(*by Mann Whitney-U test*;* ns>0.05, *p<0.05; n=3 for *Smn*$^{2B/-}$*;P53*$^{+/+}$, n=4 for all other genotypes).

3.3 Discussion

3.3.1 Overview of Results

In this chapter, I first investigated the time course of motor neuron pathology in the *Smn*$^{2B/-}$ mouse model of SMA, in order to determine the relationship between the pathological hallmarks of motor neurons in SMA. It was found that, in the *Smn*$^{2B/-}$ mouse model of SMA, the onset of NMJ pathology coincides with the onset of phenotypic symptoms and precedes a decrease in the number and area of MNCBs. This therefore demonstrates that motor neurons degenerate in a distal to proximal manner.

Furthermore, I have shown that the onset of NMJ pathology coincides with the up-regulation of transcripts involved in the P53 signalling pathway in the spinal cords of *Smn*$^{2B/-}$ mice. By reducing the expression of P53 in the *Smn*$^{2B/-}$ mouse model of SMA, it was found that, although this does not improve the overall phenotype of the mouse model or decrease the loss of MNCBs, it does result in a decrease in the level of denervation observed at the level of the NMJ. This implies that P53 plays a role in synaptic withdrawal in this mouse model of SMA.

3.3.2 Understanding the temporal relationship of motor unit pathology in SMA

It has commonly been assumed that motor neurons in SMA degenerate in a distal to proximal manner, based on the fact that the pre-synaptic terminal appears to withdraw from the post-synaptic endplate, leaving partially occupied endplates (Murray et al. 2008). However, there is no literature that explicitly explores the relationship of NMJ and MNCB pathology in SMA. Therefore, by performing a temporal analysis of motor units in the *Smn*$^{2B/-}$

mouse model, I was able to determine that pre-synaptic pathology, including withdrawal of the pre-synaptic terminal, occurs prior to MNCB shrinkage and loss, with the earliest pathological feature to occur being an increase in abnormal pre-synaptic swelling. It was found that the onset of NMJ defects coincides with the onset of a symptomatic phenotype in the *Smn*$^{2B/-}$ mouse model of SMA, which is supported by findings in an ALS mouse model that show the onset of a symptomatic phenotype is caused by degeneration of the distal compartment of the motor neuron (Gould et al. 2006). As a result, these findings support the idea that degeneration of the motor neuron occurs in a distal to proximal manner.

Interestingly, the quantification of pre-synaptic swelling indicated that, at early time points, there was mild swelling at the NMJs of *Smn*$^{2B/+}$ mice as well as *Smn*$^{2B/-}$ mice. Over the time course, pre-synaptic swelling progressively decreased in *Smn*$^{2B/+}$ control mice but increased in *Smn*$^{2B/-}$ mice. It is worth considering the possibility that poly-innervation of post-synaptic endplates may contribute to the swollen appearance of axons and pre-synaptic terminals early in post-natal life. Poly-innervation of a post-synaptic endplate is observed in early postnatal life (Sleigh et al. 2014). However, following axonal pruning post-synaptic terminals are left with only a single axonal input (Sleigh et al. 2014). In mice, the process of axonal pruning is complete within the first two weeks of post-natal life (Sleigh et al. 2014). As swelling decreases in *Smn*$^{2B/+}$ mice, with almost all of the pre-synaptic terminals displaying no swelling by P15, it is possible that axonal pruning is responsible for eliminating the mild swollen appearance of the pre-synaptic terminal.

At a late symptomatic time point, after NMJ pathology had been observed, MNCB area in the *Smn*$^{2B/-}$ mouse model of SMA was decreased in comparison to *Smn*$^{2B/+}$ controls. It could be suggested that MNCBs are undergoing cytoplasmic shrinkage, which is known to be a feature of apoptosis (Ernest et al. 2008; d'Errico et al. 2013). However, by looking at

the temporal analysis for both *Smn*$^{2B/-}$ and *Smn*$^{2B/+}$ mice it was observed that while the area of MNCBs in *Smn*$^{2B/+}$ mice shows an increasing trend over time, MNCB area in *Smn*$^{2B/-}$ mice does not change. In cultured neurons, cell body area was shown to increase with maturation and therefore, this morphological alteration that was observed in *Smn*$^{2B/-}$ mice compared to *Smn*$^{2B/+}$ mice may be due to a lack of motor neuron growth and development. In support of this, the production of growth factors from astrocytes is thought to be reduced in SMA (McGivern et al. 2013).

An increase in activated caspase-3 staining at P15 was observed in *Smn*$^{2B/-}$ mice compared to *Smn*$^{2B/+}$ controls. The majority of the caspase-3 positive cells that were observed, exclusively within motor neuron rich regions, had an abnormal, shrunken appearance (Figure 3.8). As caspase-3 is responsible for degrading cellular components, which is thought to result in the altered structure of the cell, it is likely that these cells were undergoing apoptosis (Vila & Przedborski 2003; Fink & Cookson 2005). Whether these activated capase-3 positive cells are motor neurons or not cannot be confirmed, due to the lack of a motor neuron specific marker as double staining of spinal cord sections, for both ChAT and activated caspase-3, was unsuccessful. It is predicted that the use of ChAT as a motor neuron specific marker when looking for dying motor neurons may not be appropriate as loss of function in motor neurons results in reduced expression of ChAT (Wu & Hersh 1994; Pérez-García et al. 2017).

It has been suggested that SMN has an anti-apoptotic role (Kerr et al. 2000; Vyas et al. 2002; Wang et al. 2005; Parker et al. 2008; Anderton et al. 2011). In a study by Kerr *et. al.*, cells infected with an apoptotic-causing virus are given SMN resulting in an increase in cell survival. When alternatively spliced variants of SMN are given to these cells there is a decrease in cell survival (Kerr et al. 2000). It has also been shown that SMN interacts with Bcl-2, an anti-apoptotic factor, and by doing so it inhibits Bax and Fas mediated apoptosis (Iwahashi et al. 1997; Sato et al. 2000). Furthermore, SMN is also

thought to play an anti-apoptotic role by inhibiting cytochrome-C release from the mitochondria as well as inhibiting caspase-3 activation (Vyas et al. 2002; Wang et al. 2005; Parker et al. 2008; Anderton et al. 2011). SMA fibroblasts were more susceptible to cell death, than control fibroblasts, following treatment with camptothecin, which causes cell death through DNA damage, however they were no more susceptible to death than controls when treated with menadione, which causes cell death through oxidative stress (Wang et al. 2005). This therefore suggests that the pathway that results in cell death following DNA damage is compromised in SMA fibroblasts (Wang et al. 2005).

3.3.3 Early motor unit alterations may be consistent with a developmental delay

During the temporal analysis of pathology within the motor unit an increase in MNCB number in the ventral horn of *Smn*$^{2B/-}$ spinal cords was observed at P5, when compared to *Smn*$^{2B/+}$ controls. It is believed that this finding is suggestive of a developmental delay. As part of normal development, the nervous system undergoes programmed cell death (PCD) to compensate for an excess number of cells (Oppenheim 1991). If this process is delayed in *Smn*$^{2B/-}$ mice, this may be why an increase in the number of MNCBs in their spinal cords when compared to the number of MNCBs in *Smn*$^{2B/+}$ mice was seen. While *Smn*$^{2B/+}$ mice have already undergone this process, the delay in *Smn*$^{2B/-}$ mice would see a greater number of MNCB in their spinal cords. It has previously been suggested that the wave of PCD may be defective in SMA and that this process is somewhat uncontrolled, therefore highlighting that problems in this process are known to occur (Soler-Botija et al. 2002).

Furthermore, at P1 a decrease in activated caspase-3 staining in *Smn*$^{2B/-}$ mice was observed and may represent the natural wave of PCD occurring in *Smn*$^{2B/+}$ mice but not in *Smn*$^{2B/-}$ mice. It is believed that the developmental wave of PCD is caspase-3 dependent, which supports this idea (Raoul et al.

1999). In addition, it has been suggested that Bcl-2, which is thought to be involved in the regulation of developmental PCD, is down-regulated in post-mortem tissue from SMA patients, supporting the idea that this process may be defective in SMA (Soler-Botija et al. 2002).

In support of this theory, it was found that there was an increase in the area of post-synaptic endplates in the *Smn*$^{2B/-}$ mouse model of SMA compared to *Smn*$^{2B/+}$ controls at P5. Under normal circumstances, the post-synaptic endplate experiences a temporary decrease in area during postnatal synapse elimination and therefore, there may be a delay in this process in *Smn*$^{2B/-}$ mice and as a result they appear to have larger endplates than controls (Marques et al. 2000).

Since many believe that developmental delays may contribute to the pathogenesis of SMA, the observations from this study are potentially very interesting (Hausmanowa-Petrusewicz & Vrbová 2005).

3.3.4 A role for P53 in synaptic withdrawal in SMA

During the temporal analysis of pathology within the motor unit it was noted that the up-regulation of transcripts involved in the P53 signalling pathway coincides with the early onset of NMJ pathology in the *Smn*$^{2B/-}$ mouse model of SMA. Although this was in the whole spinal cord and not within motor neurons specifically, it is in keeping with results from other studies that show, using laser capture microdissection techniques, that these transcriptional changes occurred in motor neurons specifically at pre-symptomatic time points (Murray et al. 2015; Simon et al. 2017; Nichterwitz et al. 2018). This therefore led to the investigation into what role P53 plays on motor unit pathology and whether P53 was responsible for the degeneration of the NMJ.

When P53 was reduced in the *Smn*$^{2B/-}$ mouse model, no difference in MNCB number was observed. This is in contrast to recent reports from Simon *et. al.* showing a reduction in both denervation and MNCB loss when P53 expression was reduced in the *SmnΔ7* mouse model of SMA (Simon et al. 2017). However, it is consistent with reports from Tsai *et. al.* who also found that there was no significant improvement in their tiawanese SMA mouse model when P53 was knocked out (Tsai et al. 2006b). These three studies all show varying results however, they are difficult to compare due to experimental differences that exist between them, notably, the mouse models and methods of P53 reduction that are used. For example, Simon *et. al.* used the *SmnΔ7* mouse model, which has a shorter lifespan in comparison to the *Smn*$^{2B/-}$ mouse model. Therefore, if there are compensatory mechanisms of cell death that could be initiated when P53 is reduced, it could be speculated that, even with treating this mouse model at P1, there is not sufficient time for these to be initiated (Jacobs et al. 2006; Simon et al. 2017). In the study by Tsai *et. al.*, P53 was knocked out from conception and therefore, it mat be possible that this allows suffiecient time for compensatory mechanisms to be recruited and as a result lead to the continued loss of motor neurons (Jacobs et al. 2006; Tsai et al. 2006b). In the case of the *Smn*$^{2B/-}$ mouse model, there is an extended life span giving the same effects as that seen by Tsai *et. al.* (Tsai et al. 2006b).

However, our findings do show that reducing P53 in the *Smn*$^{2B/-}$ mouse model of SMA decreases denervation. This implies that P53 plays an important role in moderating the withdrawal of the pre-synaptic terminal in motor neuron degeneration. It is speculated that there may be a compartment specific requirement for P53 in motor neuron degeneration. The 40% reduction in P53 mRNA levels obtained in the *Smn*$^{2B/-}$ mouse model may not prevent the loss of MNCBs but could be sufficient to ameliorate the loss of synaptic connections of those motor neurons that remain. Furthermore, P53 is located within the synapse and is involved in the regulation of genes associated with synaptic function (Gilman et al. 2003;

Merlo et al. 2014). Moreover, it has been reported that P53 plays a major role in pre-synaptic degeneration following activation of apoptosis (Gilman et al. 2003). It has also been shown that the apoptotic cascade can be involved in localised axon degeneration, for example axonal pruning that is important during development, which does not lead to overall neuronal death (Cusack et al. 2013; Geden & Deshmukh 2016). It is reported that axon pruning involves the expression of Bax and the release of cytochrome c from the mitochondria, two events that are well known for their role in apoptosis (Geden & Deshmukh 2016). Perhaps surprisingly, due to its well-known role as an executor of apoptosis, caspase-3 is also activated during axonal pruning (Cusack et al. 2013; Geden & Deshmukh 2016). It is believed that although caspase-3 is activated ubiquitously within the neuron, its role is regulated within the various compartments of the cell, ensuring selective degeneration of the axon, by the proteasome system (Cusack et al. 2013).

3.3.5 Dissociation of P53 and its downstream regulators

Upon investigating the reduction in P53 within the *Smn*$^{2B/-}$*;P53*$^{-/-}$ mouse model it was found that, despite the reduction in P53 expression, downstream targets of P53 did not decrease. Based on this result it is perhaps possible that upon the reduction of P53, other transcriptional factors are able to compensate, initiating the expression of these downstream targets and ultimately causing motor neuron cell death. From work investigating development in *P53*$^{-/-}$ mice, it has been suggested that family members of P53, P63 and P73, could compensate for a lack of P53 during development (Jacobs et al. 2006). Interestingly, *PMAIP1,* also known as *NOXA*, is thought to lie downstream of and be activated by P73, as well as P53 (Roos & Kaina 2006; Ploner et al. 2008). *PMAIP1* has also been shown to be up-regulated in *P53*$^{-/-}$ mice following γ-irradiation, demonstrating that its activation can indeed occur independently of P53 (Fei et al. 2002; Ploner et al. 2008). Furthermore, *Cdkn1A*, often referred to as *p21*, has been up-regulated, by over expression of the cell cycle checkpoint and tumour

suppressor gene Chk2 kinase, in tumour cells that are P53-deficient. Suggesting that *Cdkn1A* can also be regulated by other transcriptional factors, and not solely by P53 (Aliouat-Denis et al. 2005).

However, it is thought that when DNA damage occurs, that these compensatory pathways are less sensitive to DNA damage than P53 (Merritt et al. 1997). When low levels of DNA damage were induced, via radiation, these pathways were not initiated (Merritt et al. 1997). Furthermore, some studies have shown that loss of P53 only has a temporary effect and that there is a delayed, P53-independent mechanism of cell death that can be initiated (Merritt et al. 1997). This is consistent with the finding that inhibition of PCD delays but does not prevent neurodegeneration (Kostic et al. 1997; Li et al. 2000; Gould et al. 2006). Therefore, it is perhaps possible that the effects that were observed in the $Smn^{2B/-};P53^{-/-}$ mouse model of SMA is a delayed onset of motor neuron death and/or synaptic withdrawal as compensatory mechanisms are employed. One possible way to investigate this would be to determine whether, when P53 is reduced, there is an increase in phosphorylated, and therefore activated, P73 and P63.

This P53-independent mechanism of cell death is also thought to be tissue specific as while some tissues in $P53^{-/-}$ mice are resistant to radiation induced cell death, other are not (Merritt et al. 1997). Fei *et. al.* have shown that P53-independent, up-regulation of *PMAIP1* is tissue specific (Fei et al. 2002). They report that while *PMAIP1* was up-regulated in the thymus, following γ-irradiation, it was not up-regulated in the spleen. Interestingly, our lab has recently begun investigating P53 in non-neuronal tissues of the $Smn^{2B/-}$ mouse model of SMA. In contrast to the spinal cord, where a, perhaps unexpected, sustained increase in transcripts involved in the P53 signalling pathway was observed, it was found that in the liver of $Smn^{2B/-};P53^{-/-}$ mice, these transcripts of interest returned to a level that was not significantly different from $Smn^{2B/+}$ controls (*Murray Laboratory, Unpublished data*). This finding shows that there may be differences in the control of cell

death in different tissues, which could potentially contribute to the selective vulnerability of neurons compared to other non-neuronal tissues in SMA.

It is perhaps due to this sustained increase in these transcripts that an overall improvement in the MNCB loss and phenotype of this mouse model was not seen. Inhibiting other members of the P53 family, specifically P73, may be interesting to determine whether there is a compensatory effect from this.

3.3.6 Conclusion

The temporal analysis of motor unit pathology that was performed has clarified an important issue in the field and the idea that motor neuron degeneration in SMA occurs in a distal to proximal manner can now be confirmed. Furthermore, the role that P53 plays in motor neuron degeneration has been addressed. Although the reduction in *P53* was only confirmed at the mRNA level and not at the level of the functional protein, this reduction was still able to prevent, or delay, the withdrawal of the pre-synaptic terminal. Due to the complex nature, the degree of overlap and the possibility of compensatory mechanisms that appears to occur in cellular death, it is acknowledged that untangling this pathway and its role in SMA may be difficult and require further work.

Chapter 4

Investigating compensatory sprouting of motor neurons in differentially vulnerable muscles of the Smn$^{2B/-}$ mouse model of SMA

Summary

In this chapter, I aimed to investigate whether compensatory sprouting could be responsible for the differential vulnerability of muscles in the *Smn*$^{2B/-}$ mouse model of SMA. NMJ morphology and sprouting in a muscle that displays vast denervation (Triangularis Sterni [TS]) is compared to a muscle that displays lower levels of denervation (Levator Auris Longus [LALr]), in the *Smn*$^{2B/-}$ mouse model of SMA. In terms of NMJ morphology, pre-synaptic terminal swelling and post-synaptic endplate occupancy and area are assessed and in terms of sprouting, both nodal and terminal sprouting are quantified.

In addition, Schaefer *et. al.* previously reported that, in a mouse model of ALS, there were two populations of motor units (refer to Figure 1.1 for motor unit description); one that was small compared to controls and another that was significantly larger than controls (Schaefer et al. 2005). They suggest that these small motor units have been degenerating and the large motor units have been compensating for this by sprouting. Therefore, I also aimed to examine the synchronicity of pathology within motor units and investigate whether there were compensatory subpopulations of motor neurons in *Smn*$^{2B/-}$ mice. It is reasoned that if some, 'healthy', motor neurons were compensating for degenerating motor neurons by sprouting, then pathology would be synchronous within motor units; some would have severe pathology while others would appear normal and healthy. In order to assess individual motor units, the *Thy1-YFP-H* transgene is crossed onto the *Smn*$^{2B/-}$

mouse model of SMA. Motor units within the LALr muscle were reconstructed and various features of pathology within each motor unit were assessed.

This chapter begins with the assessment of the YFP expression pattern in different muscles of mice of different ages. Based on this analysis a description of the usefulness and limitations of this model for our purposes is provided. Reports that YFP is not biologically inert are also considered by assessing the effect that YFP has on motor units of the *Smn*$^{2B/-}$ mouse model of SMA.

The results that are detailed in the following chapter show that:

1. *Thy1-YFP-H* expression is age dependent and varies between muscles.
2. *Thy1-YFP-H* expression does not have an adverse effect on NMJ pathology in the *Smn*$^{2B/-}$ mouse model of SMA.
3. The TS muscle displays vast denervation and pre-synaptic swelling as well as smaller post synaptic endplates.
4. The LALr muscle displays little denervation but does exhibit pre-synaptic swelling and smaller post-synaptic endplates.
5. Sprouting is ongoing in both the TS and LALr muscles but the level of sprouting in the LALr cannot account for the significant decrease in denervation observed within this muscle.
6. Pathologically divergent subpopulations of motor units are not observed in the LALr of the *Smn*$^{2B/-}$ mouse model of SMA.

4.1 Introduction

In SMA, the NMJ is targeted early in the disease progression (See Chapter 3; Murray et al. 2008). Under normal, non-pathological conditions, when NMJ degeneration, and resulting muscle fiber denervation occurs, neighboring motor neurons sprout, sending out new axonal branches, in order to re-innervate the muscle fiber (Slack et al. 1983). Sprouting has been shown to occur in mouse models and patients of SMA (Crawford & Pardo 1996; Murray et al. 2012). Sprouting was observed in the *Smn*$^{2B/-}$ mouse model of SMA and although it was shown that the rate of axon growth was unaffected by a reduction in Smn in this mouse model, the level of paralysis induced sprouting was decreased (Murray et al. 2012). In patients, EMG results from those with milder forms of SMA suggest that they have large motor units that are indicative of sprouting while those with severe SMA show EMG results that suggest ongoing denervation rather than sprouting (Crawford & Pardo 1996). This could suggest that sprouting is a disease modifier in SMA.

In 1950, Hoffman described two different types of sprouting; terminal and nodal (Hoffman 1950). Terminal sprouts extend from the pre-synaptic terminal of an innervated NMJ whereas nodal, or collateral, sprouts extend from the internodes of axons (Figure 4.1) (Hoffman 1950; Slack et al. 1979). It is unclear how these different types of sprouts are initiated as terminal sprouting can occur independently of nodal sprouting (Slack et al. 1979; English 2003). Inactivity of a muscle, which is induced by botulinum toxin, does not appear to induce nodal sprouting but does induce terminal sprouting (Slack et al. 1979). Therefore, it is thought that while terminal sprouting is induced by factors released from the muscle following inactivity, nodal sprouting is induced by the degeneration of the motor neuron (Slack et al. 1983).

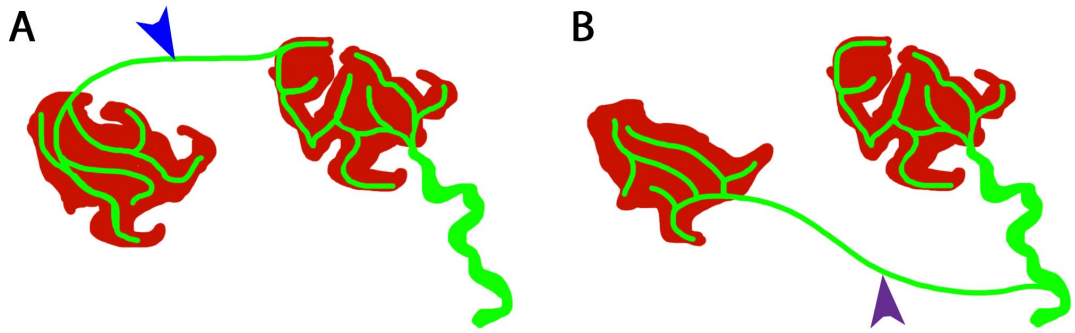

Figure 4.1: Motor neurons sprouting can take to form of either terminal or nodal sprouting. (**A**) The blue arrow in the schematic highlights a terminal sprout, which extends from the synaptic terminal of a motor neuron to re-innervate a vacant neighboring endplate. (**B**) The purple arrow in the schematic shows a nodal sprout, also known as a collateral sprout, which extends from the internode of a motor axon to re-innervate a vacant neighboring endplate.

These neurotrophic factors that induce sprouting do so by initiating the creation of Schwann cell bridges, from innervating motor neurons, that extend towards denervated endplates and eventually carry within them new axonal branches (Gordon et al. 2004). Neurotrophic factors include CNTF, GDNF and IGF, which are released from the Schwann cells, neuron and muscle respectively (English 2003). Although IGF is reported as being released from the muscle it is interesting that increased IGF2 expression in motor neurons correlates with neuroprotection (Allodi et al. 2016). This study found that in oculomotor neurons, which are resistant to degeneration in ALS, IGF2 levels were increased in both patients and the $SOD1^{G39A}$ mouse model (Allodi et al. 2016). Further to this, IGF2 was up-regulated in motor neurons that supply muscles with decreased susceptibility to denervation in the $Smn^{2B/-}$ mouse model of SMA (Murray et al. 2015). This finding suggested that sprouting could be a phenotypic modifier of differentially vulnerable muscles in SMA. It is possible that, in those muscles that appear to be less susceptible to degeneration of motor neurons, an increased level of compensatory sprouting means that on-going denervation is masked. In contrast, in those muscles that show vast denervation, the level of sprouting occurring is not sufficient to mask denervation.

In ALS, it has also been reported that while some motor neurons degenerate others compensate for this by sprouting and as a result enlarging (Schaefer et al. 2005). Schaefer *et. al.* presented different models for how motor units could be altered during the disease progression in their ALS mouse model (Figure 4.2). One suggestion is that there are compensatory subpopulations of motor neurons that sprout while others degenerate (Figure 4.2A). The other was that motor units contain both a mixture of degeneration and compensatory sprouting (Figure 4.2B). Based on their results, that showed that sprouting and degeneration did not occur within the same motor unit, they concluded that in their ALS mouse model there were compensatory subpopulations of motor neurons (ie Figure 4.2A) (Schaefer et al. 2005). It is unknown is whether this phenomenon is exclusive to ALS or whether it is observed in other MNDs like SMA.

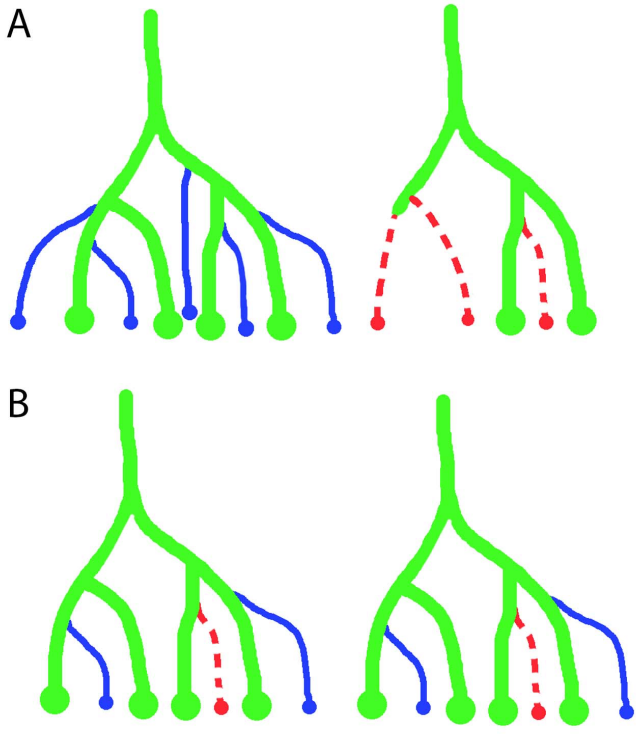

Figure 4.2: There are different suggestions for how compensatory sprouting of motor neurons could occur following denervation in MNDs. (**A**) The schematic shows the method of compensatory sprouting that Schaefer *et. al.* believe occurs during motor neuron degeneration in ALS. One motor unit enlarges following sprouting to compensate for the degeneration of another motor unit. (**B**) The schematic shows an alternative model in which motor units all show signs of both denervation and sprouting. *Adapted from Schaefer et. al., 2005*.

To investigate motor unit synchronicity, Schaefer *et. al.* utilised the *Thy1-YFP-H* transgene (Feng et al. 2000; Schaefer et al. 2005). Expression of this transgene results in in a subset of motor neurons exhibiting cytoplasmic expression of yellow fluorescent protein (YFP), which is a variant of green fluorescent protein (GFP) that was originally isolated and cloned from the jellyfish, *Aequorea victoria* (Feng et al. 2000). In this case, YFP expression is under the control of the *Thy1* gene (Feng et al. 2000). *Thy1* is normally expressed in a variety of neuronal and non-neuronal cells, however by deleting a specific intron within this gene it was found that expression of this gene became almost exclusively neuronal (Vidal et al. 1990; Kelley et al. 1994). *Thy1* expression is also developmentally regulated and as a result YFP expression is known to increase postnatally (Feng et al. 2000). During the creation of this transgene, many mouse embryos were transfected with the *Thy1-YFP* vector and the insertion point of this vector within the genome was random in each embryo. The different insertion sites resulted in a different YFP expression pattern within 8 mouse lines (Feng et al. 2000). Specifically, the *Thy1-YFP-H* mouse line expresses YFP in only a few of their motor neurons allowing the visualisation of individual motor neurons within a muscle (Feng et al. 2000).

Both YFP and GFP have been reported as being inert proteins that had no adverse effect when expressed *in vivo* (Okabe et al. 1997; Feng et al. 2000). However, others have disputed this belief (Huang et al. 2000; Comley et al. 2011). Expression of GFP within the hearts of mice was shown to increase the likelihood of a cardiomyopathy (Huang et al. 2000). Comley *et. al.* reported that YFP expression was associated with increased expression of transcripts associated with cell stress in the spinal cords of *Thy1-YFP*-16 mice (Comley et al. 2011). They also reported that there was abnormal neurofilament accumulation (NFA) present in YFP expressing motor axons of 2-4 month old *Thy1-YFP-H* mice.

Therefore, to consider this uncertainty in the toxicity of YFP, it is worth assessing the effects of this transgene and its expression when using YFP as an experimental tool.

The *Thy1-YFP-H* transgene, was utilised to examine motor unit pathology in the *Smn*$^{2B/-}$ mouse model. I aimed to examine motor units in the *Smn*$^{2B/2B}$ and *Smn*$^{+/-}$ mouse models, which have reduced Smn but are asymptomatic, in the subsequent chapter of this thesis (Bowerman et al. 2012a; Simon et al., 2010). Therefore, this chapter begins with the assessment of YFP expression in various muscles of mice of different ages. Whether carrying the *Thy1-YFP-H* transgene and expressing YFP in motor neurons has an adverse effect on the pathology of the NMJ, in terms of NFA, was also assessed in the *Smn*$^{2B/-}$ mouse model of SMA. In addition, the possibility that expressing YFP can cause increased stress in motor neurons of the *Smn*$^{2B/-}$ mouse model of SMA is addressed.

Secondly, I question whether sprouting can account for the decreased amount of denervation in muscles that are less susceptible to degeneration of motor neurons. This is investigated by comparing NMJ morphology and sprouting in a muscle that displays vast denervation to a muscle that displays lower levels of denervation, in the *Smn*$^{2B/-}$ mouse model of SMA.

Thirdly, I examine the synchronicity of pathology within motor units by tracing individual motor units in the LALr muscle of *Smn*$^{2B/-}$ mice and mapping NMJ pathology across the motor unit. I look to determine whether pathology is synchronous across motor units and whether there are divergent populations of motor neurons in the *Smn*$^{2B/-}$ mouse model of SMA, with some displaying severe pathology whilst others display no or mild pathology.

4.2 Results

4.2.1 Characterisation of the *Thy1-YFP-H* gene

4.2.1.1 Crossing of the Thy1-YFP-H gene onto the $Smn^{2B/-}$ mouse model of SMA

In order to investigate whether compensatory motor units are present within the $Smn^{2B/-}$ mouse model of SMA, the *Thy1-YFP-H* transgene (referred to as *YFP-H* hereafter) was crossed onto this mouse model. This transgene results in the expression of Yellow Fluorescent Protein (YFP) in the cytoplasm of a random subset of motor neurons (Feng et al. 2000). Due to this expression pattern of YFP, individual motor units are visible and potentially traceable within muscles (Schaefer et al. 2005; Murray et al. 2008).

The *YFP-H* transgene was crossed onto the $Smn^{2B/-}$ mouse model by initially breeding $Smn^{2B/+}$ and $Smn^{+/-}$ mice with $Smn^{+/+}$*;YFP-H* mice (strain: 003782, Jackson Laboratories) (Figure 4.3). $Smn^{2B/2B}$*;YFP-H* and $Smn^{+/-}$*;YFP-H* mice were selected to cross together and obtain $Smn^{2B/-}$*;YFP-H* mice; an SMA mouse model that expresses YFP in an apparently random subset of motor neurons.

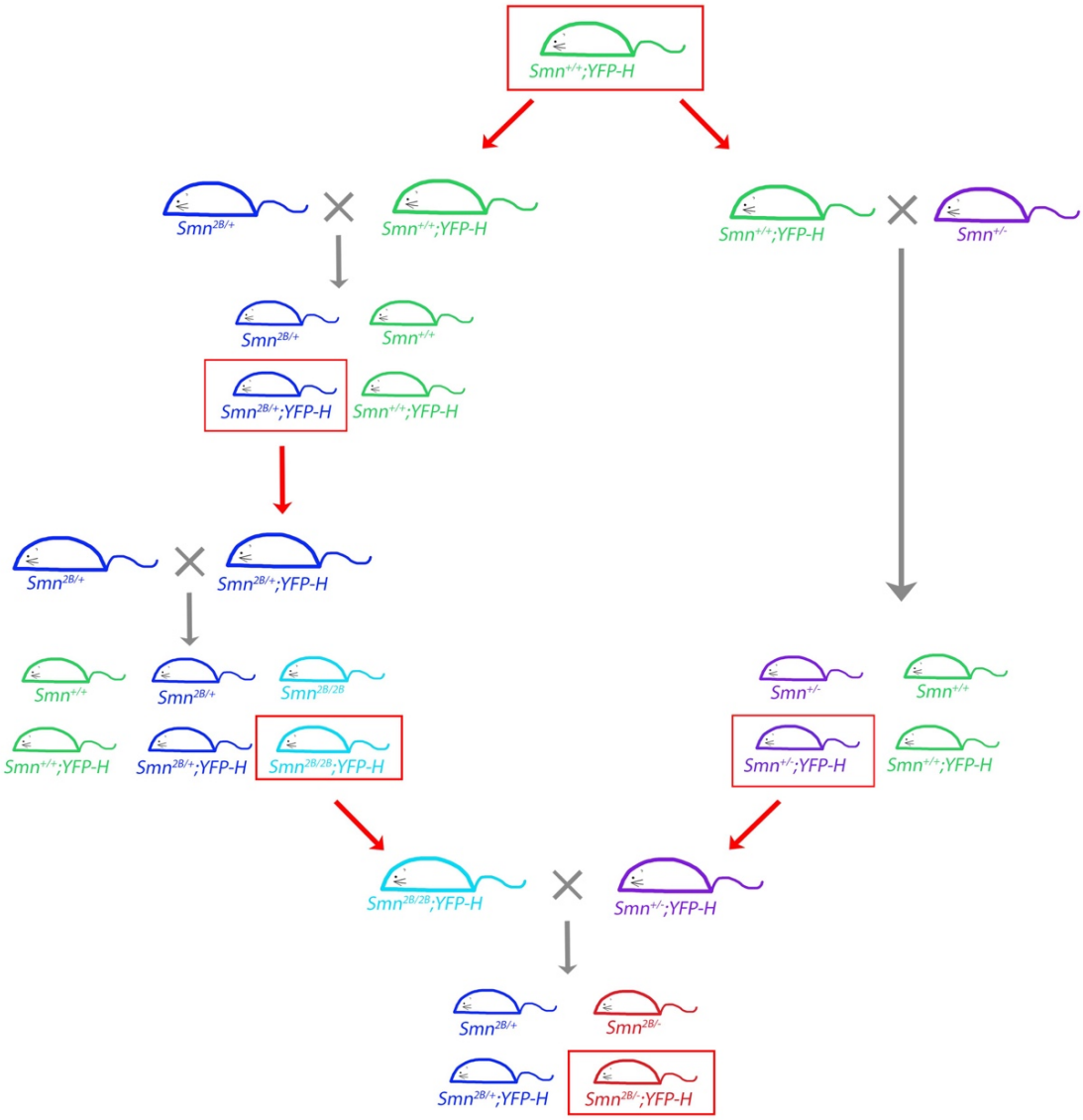

Figure 4.3: The *YFP-H* transgene was crossed onto mouse models that express various levels of Smn protein. The schematic shows the process of crossing the YFP-H transgene onto various mouse models of interest. *Smn*$^{+/+}$*;YFP-H* mice were originally obtained from Jackson Laboratories. These were crossed with *Smn*$^{2B/+}$ mice, which had been established within our laboratory, to produce *Smn*$^{2B/+}$*;YFP-H* (left side of the schematic). Subsequently, *Smn*$^{2B/+}$*;YFP-H* mice were bred to obtain *Smn*$^{2B/2B}$*;YFP-H* mice. In addition, *Smn*$^{+/+}$*;YFP-H* mice were also crossed with *Smn*$^{+/-}$ mice to produce *Smn*$^{+/-}$*;YFP-H* mice (right side of the schematic). Finally, *Smn*$^{2B/2B}$*;YFP-H* and *Smn*$^{+/-}$*;YFP-H* mice were crossed to produce *Smn*$^{2B/-}$*;YFP-H* mice. The red boxes highlight the mice with desirable genotypes, either in terms of subsequent breeding or for tissue analysis.

4.2.1.2 Characterisation of YFP-H

YFP-H expression patterns vary in mice of different ages and between muscles

Previous work has shown that the level of *YFP-H* expression can vary with age and between muscles (Feng et al. 2000). Therefore, as I aimed to examine individual motor units in various muscles from mice of various ages, I sought to determine the level of *YFP-H* expression in the different muscles that I had aimed to use for motor unit analysis, and the impact that age has on expression.

I aimed to examine motor units from differentially vulnerable muscles, in the $Smn^{2B/-}$ mouse model at P18 as well as examining motor units in the $Smn^{2B/2B}$ and $Smn^{+/-}$ mouse models, which have reduced Smn but are asymptomatic, in the subsequent chapter of this thesis (Bowerman et al. 2012a; Simon et al. 2010). These asymptomatic mouse models would be examined at aged time points, including 3 months, 6 months and 1 year, to determine whether compensatory sprouting had been employed to mask degeneration (please refer to Chapter 5 for background) (Simon et al. 2010). Therefore, to determine how aging affects *YFP-H* expression, the number of muscles that expressed YFP, within cranial musculature, in $Smn^{+/+}$*;YFP-H* mice at 3 months, 6 months and 1 year of age was quantified. It was found that in all four cranial muscles *YFP-H* expression increased with age. An increase in the percentage of muscles that had YFP positive axons was observed at 6 months compared to 3 months and a subsequent increase at 1 year of age. (Table 4.1). Of the four cranial muscles, the LALr had the greatest YFP expression. At 3 months, 50% of LALr muscles had positive YFP axons and this increased to 100% of LALr muscles examined expressing YFP. In contrast, no AS muscles at 3 months and 6 months expressed YFP and only 50% of the AS muscles examined at 1 year of age expressed YFP.

In addition, the number of YFP positive axons entering a muscle increased with age (Table 4.1). For example, in the LALr, there were an average of 3 YFP positive axons entering the muscle at 3 months of age, while there was an average of 4.75 at 6 months and an average of 9 YFP positive axons entering the muscle at 1 year of age.

To trace individual motor units, muscles should ideally express YFP in only one or two motor units. This allows the axon of the motor unit to be followed and all of its NMJs to be assessed. If the muscle contains two or more YFP expressing motor units, untangling the pattern of these to determine what branches and NMJs belong to each motor unit becomes more difficult (Figure 4.4). Where two motor units are expressed, varying intensities of YFP expression can often allow the two motor units to be separated from each other (Murray et al. 2008).

Table 4.1: YFP expression increases with age in *Smn$^{+/+}$;YFP-H*

Muscle	Percentage of positive muscles (%)			Number of axonal inputs in YFP positive muscles		
	3 months	**6 months**	**1 year**	**3 months**	**6 months**	**1 year**
LALr	50	80	100	**Avg. 2** Min.1 Max. 3	**Avg. 4.75** Min.2 Max.7	**Avg.9** Min. 5 Max. 10
LALc	0	80	100	**Avg. 0** Min. 0 Max. 0	**Avg. 2.75** Min. 1 Max. 4	**Avg. 5.75** Min. 3 Max. 8
AAL	0	0	75	**Avg. 0** Min. 0 Max. 0	**Avg. 0** Min. 0 Max. 0	**Avg. 5.67** Min. 4 Max. 7
AS	0	0	50	**Avg. 0** Min. 0 Max. 0	**Avg. 0** Min. 0 Max. 0	**Avg. 10.5** Min. 10 Max. 11

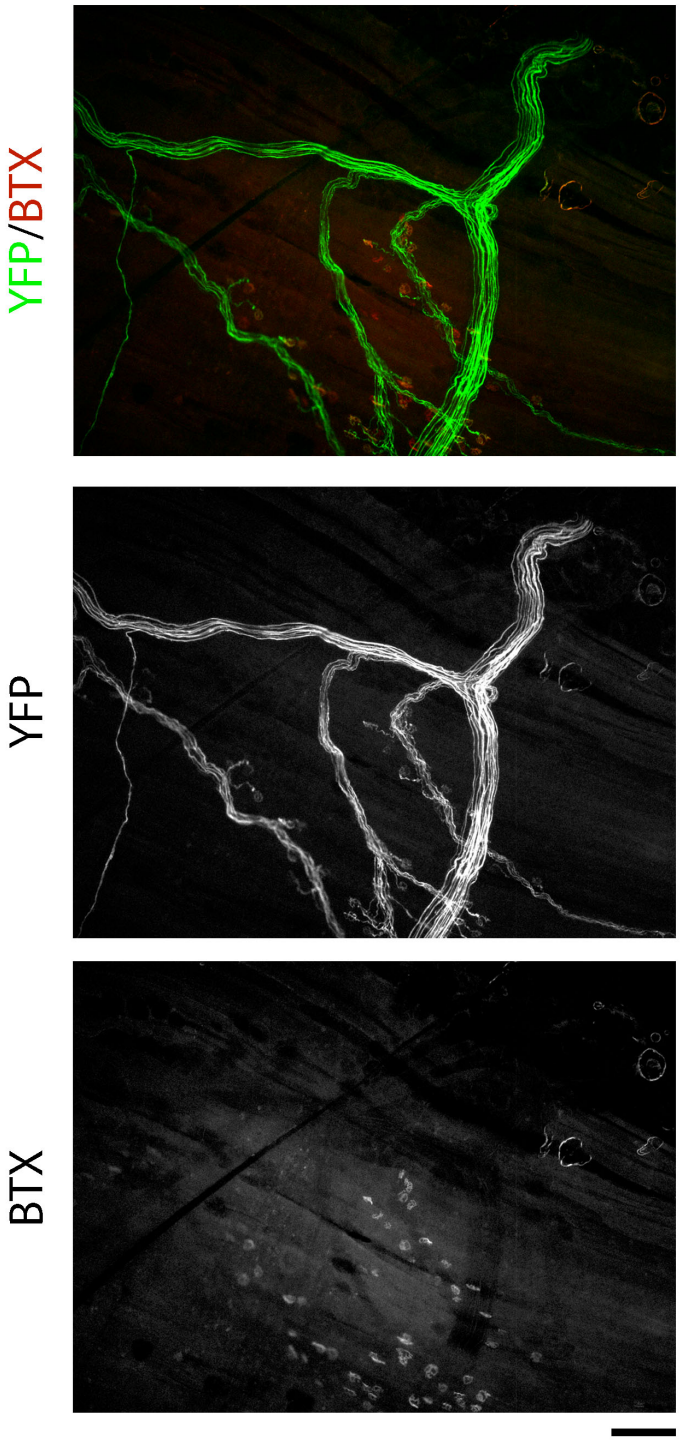

Figure 4.4: A high number of YFP expressing axons entering a muscle means individual axonal inputs are untraceable. Images show an axonal bundle entering a muscle in the top right corner. Due to the high number of YFP-expressing axonal inputs entering the muscle it is no possible to trace and follow individual motor units and determine what motor unit individual NMJs belong to. Scale bar =150μm.

In the cranial musculature of P18 *Smn*$^{2B/-}$ mice, there were no YFP positive AS and AAL muscles from 13 *Smn*$^{2B/-}$ mice and only one YFP positive LALc (3.8%). The LALr showed increased YFP expression, with 11/28 muscles (39.3%) positive for YFP expressing motor neurons.

Upon comparing the expression of YFP in the LALr of *Smn*$^{2B/-}$ to the level of YFP expression in the LALr of *Smn*$^{2B/+}$ mice, it was found that there was a decrease in the percentage of LALr muscle that were positive for YFP in *Smn*$^{2B/-}$ mice compared to *Smn*$^{2B/+}$. While 53.8% (14/26) of LALr muscle from *Smn*$^{2B/+}$ mice were YFP positive, only 39.3% (11/28) of LALr muscles from *Smn*$^{2B/-}$ mice were positive for YFP. This may suggest that there is a decrease in expression when Smn is reduced.

In the TVA of the abdominal musculature, there was no YFP expression throughout this investigation. As a vulnerable muscle that is thin and expresses YFP was desirable for whole motor unit analysis, the triangularis sterni (TS) muscle was also examined for YFP expression. This is a thoracic muscle that lies deep to the ribs but in close proximity to the TVA muscle. There was also no evidence of YFP expression in the TS muscle of *Smn*$^{2B/-}$ mice at P18.

From this analysis, it can be concluded that YFP expression in *Smn*$^{+/+}$*;YFP-H* mice does increase with age. Younger *Smn*$^{+/+}$*;YFP-H* mice have fewer YFP positive motor axons, within a particular muscle, than older *Smn*$^{+/+}$*;YFP-H* mice. This was true for all four of the cranial muscles that were assessed. YFP expression also differed between muscles with some muscles exhibiting many YFP positive motor axons while others had no YFP positive motor axons. It was found that individual motor units are traceable in the LALr muscle of the *Smn*$^{2B/-}$ mouse model but not in the TVA muscle or in the thoracic TS muscle. In older mice, motor units are untraceable due to either there being a lack of YFP expression at that age or an increase in the number of YFP positive axonal inputs entering the muscle.

YFP-H expression does not adversely affect motor unit pathology in Smn$^{2B/-}$ mice

Comley *et. al.* previously reported that YFP expression could induce cell stress (Comley et al. 2011). They reported that genes involved in cell stress are up-regulated in spinal cords of *YFP-16* mice and that YFP expression caused abnormal NFA. Therefore, I aimed to investigate whether the introduction of the *YFP-H* transgene had any impact on the motor neurons in *Smn$^{2B/-}$* mice.

Firstly, I sought to determine whether carrying the *YFP-H* transgene affected NFA at the NMJ in the *Smn$^{2B/-}$* mouse model of SMA. NFA in the TVA muscle of P18 *Smn$^{2B/-}$* and *Smn$^{2B/-}$;YFP-H* mice was quantified. This was an ideal muscle to use due to the absence of YFP expression. Therefore, whether simply carrying the *YFP-H* transgene affects NFA at the pre-synaptic terminal could be determined, excluding the possibility that expressing YFP within a motor unit affects NFA. TVA muscles from *Smn$^{2B/-}$* and *Smn$^{2B/-}$;YFP-H* mice were stained for neurofilament (NF) and the level of NFA was quantified from 'none' to 'severe'. It was found that there was no significant difference in the level of NFA in the TVA muscle of *Smn$^{2B/-}$;YFP-H* mice compared to *Smn$^{2B/-}$* mice (Figure 4.5). This suggests that carrying the *YFP-H* transgene does not alter NFA at the pre-synaptic terminals of *Smn$^{2B/-}$* mice.

Secondly, I aimed to address whether expressing YFP within a motor neuron could impact upon the NFA observed at its NMJ. To do so, cranial musculature was used due to the increased likelihood of YFP expression. Although these muscles are known to have relatively low levels of denervation, they still show pathology in their motor units (Figure 4.9; Murray et al. 2012). Cranial muscles that were positive for YFP expression were immunostained for NF. NFA at pre-synaptic terminals was staged from 'none' to 'severe', before determining whether the terminal belonged to a non-YFP expressing motor neuron or to a YFP-expressing motor neuron.

Quantification showed that there is a small but significant decrease in the level of moderate NFA at the pre-synaptic terminals of YFP-expressing motor neurons compared to motor neurons that do not express YFP (Figure 4.6B). Although all other severities showed no significant change, there is a trend for an increase in the percentage of YFP-expressing pre-synaptic terminals with no NFA. Overall, this data suggests that expressing YFP does not increase the severity of NFA, and there may be a slight reduction in NFA in YFP positive pre-synaptic terminals. This small but significant change in NFA in YFP-expressing motor neurons should still be considered when using *YFP-H* mice in further investigations. This is contrary to what may have been expected as YFP was thought to have an adverse effect on motor neurons (Comley et al. 2011). It may be possible that motor units that express YFP are those that are less affected by the neuromuscular pathology observed in SMA mouse models therefore appearing as if YFP expression have a positive effect on pathology.

Endplate area of YFP positive and YFP negative NMJs was also quantified. Again, endplate area was measured before determining whether or not it was associated with a YFP positive or a YFP negative motor neurons. There was no significant difference in the area of post-synaptic endplates of YFP positive motor neurons compared to YFP negative motor neurons (Figure 4.6C).

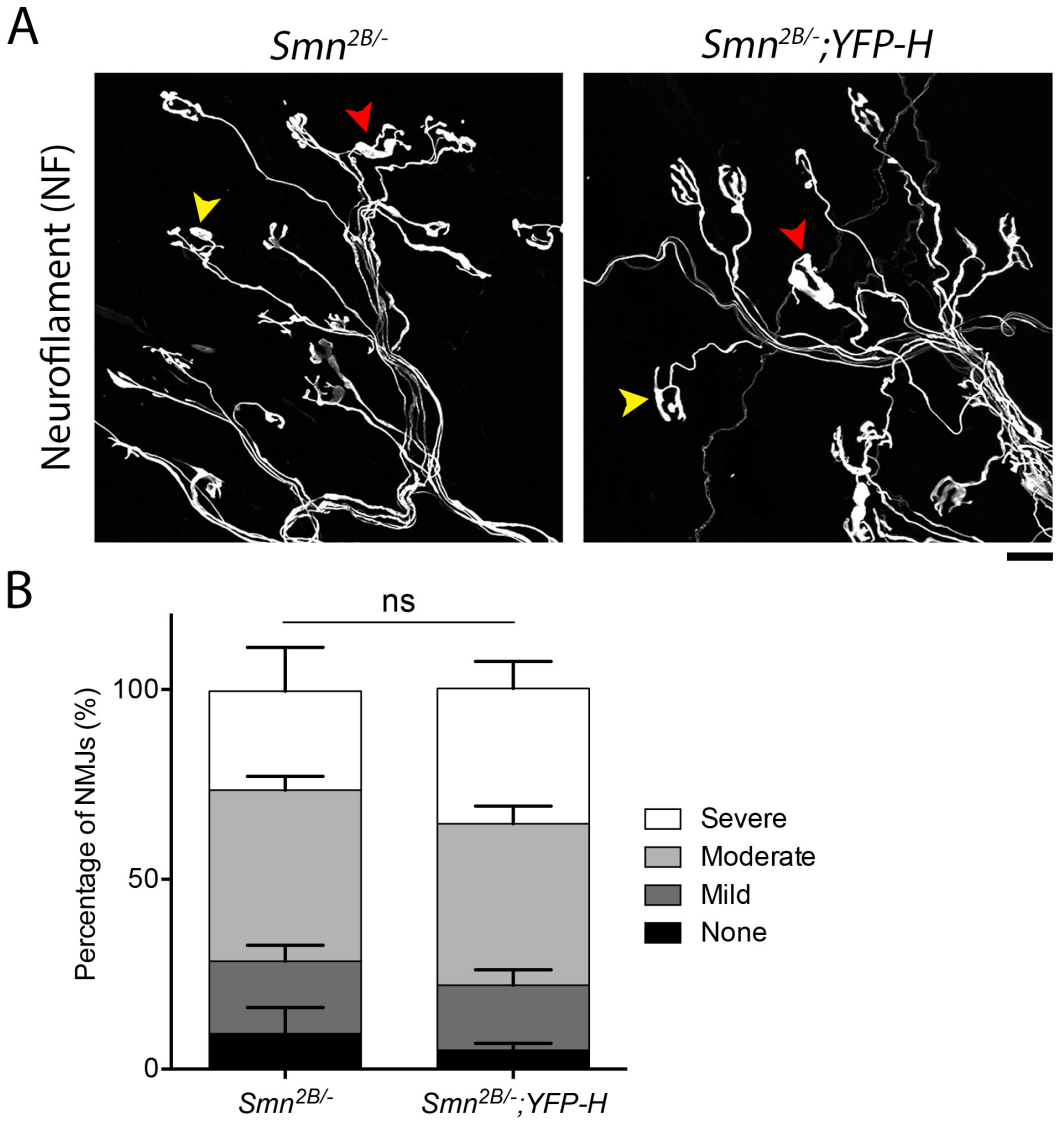

Figure 4.5: Carrying the *YFP-H* transgene does not affect the severity of NFA in the *Smn$^{2B/-}$* mouse model of SMA at P18. (**A**) Representative images of pre-synaptic terminals in the TVA of *Smn$^{2B/-}$* and *Smn$^{2B/-}$;YFP-H* mice. Note the red arrowheads highlight moderate NFA and yellow arrowheads highlight mild NFA. Scale bar = 10μm. (**B**) Bar chart (Mean±SEM) compares the severity of NFA in *Smn$^{2B/-}$* mice compared to *Smn$^{2B/-}$;YFP-H* mice. There is no significant difference in the severity of NFA between the two mouse models (by Mann Whitney-U Test, ns>0.05, n=3 mice per genotype). D*ata acquired in collaboration with Shilpa Purushotham (MSc student).*

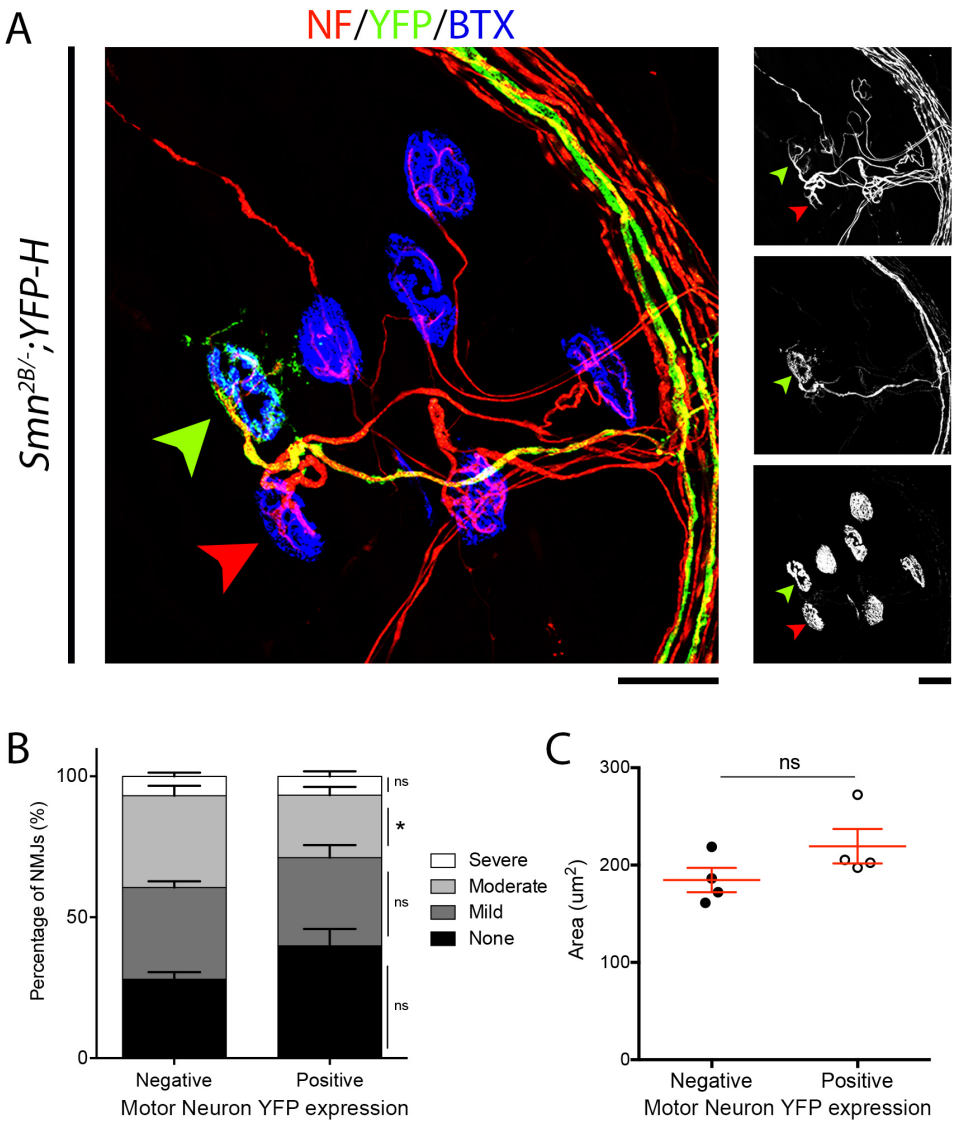

Figure 4.6: Expressing YFP does not have an adverse effect on the NMJ in *Smn$^{2B/-}$* mice at P18. (**A**) Representative image of NMJs in the LALr of *Smn$^{2B/-}$;YFP-H* mice. Note that the green arrows highlight the NMJ of a motor neuron that expresses YFP and the red arrow highlights the NMJ of a motor neuron that does not express YFP. Grey scale images are the separate channels of the image; top is NF, middle is YFP, bottom is BTX. Scale bar = 20μm. (**B**) Bar chart (Mean±SEM) compares the severity of NFA at pre-synaptic terminals in the LALr of *Smn$^{2B/-}$;YFP-H* mice. There is a small but significant decrease in the percentage of NMJs with moderate NFA in YFP positive motor neurons (by Mann Whitney-U Test, ns>0.05, *p<0.05; n=3 mice per genotype). (**C**) The graph (Mean±SEM) shows that there is no significant difference in the area of post-synaptic endplates that are supplied by motor neurons that express YFP and motor neurons that do not express YFP (by Unpaired T-test, ns>0.05; n= 4 mice per genotype). *Data acquired in collaboration with Shilpa Purushotham (MSc student).*

Thirdly, I wished to examine whether expressing YFP impacts on cellular stress of *Smn*$^{2B/-}$*;YFP-H* motor neurons. This was done by quantifying and comparing the intensity of phosphorylated H2AX (pH2AX) in MNCBs that expressed YFP and MNCBs that did not. H2AX is a protein that is recruited to and phosphorylated at sites of DNA damage and so an increase in pH2AX may be attributed to an increase in cell stress (Fulda et al. 2010). Sections of spinal cord from P18 *Smn*$^{2B/-}$*; YFP-H* mice were stained for pH2AX. Images of MNCBs that were YFP positive and YFP negative were taken and the intensity of pH2AX staining in each was subsequently measured. The intensity of pH2AX was compared (Figure 4.7) and showed no significant difference between MNCBs that expressed YFP and MNCBs that did not. Therefore, expressing the *YFP-H* transgene does not cause an increase in the levels of pH2AX, suggesting no increased stress on motor neurons expressing YFP.

Overall, carrying the *YFP-H* transgene and expressing YFP in motor neurons does not have an adverse effect on the pathology of the NMJ in the *Smn*$^{2B/-}$ mouse model of SMA. In addition, expressing YFP does not cause increased stress, as evidenced by no change in the level of pH2AX, in motor neurons in the *Smn*$^{2B/-}$ mouse model of SMA.

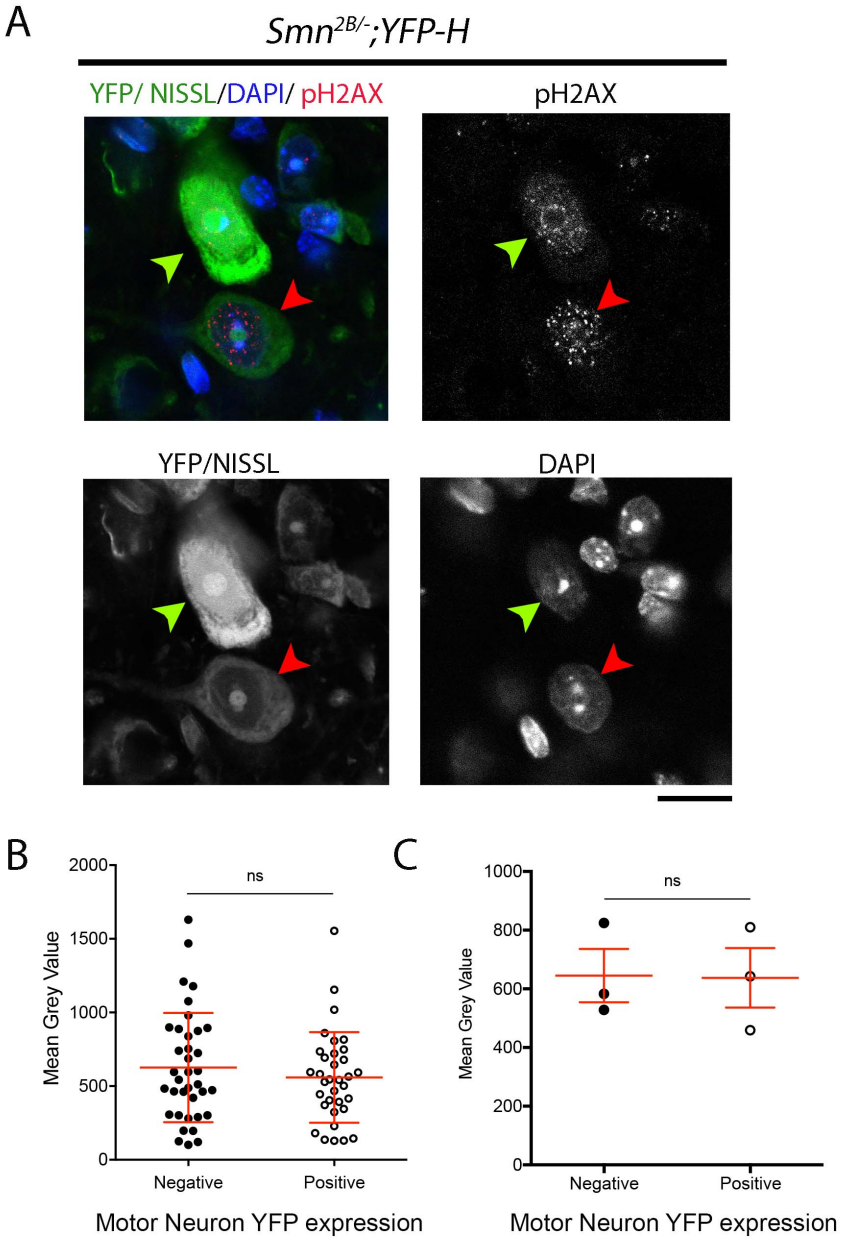

Figure 4.7: Expressing YFP does increase the levels of pH2AX in motor neurons from *Smn*$^{2B/-}$ mice at P18. (**A**) Representative images of MNCBs in the ventral horn of the thoracic region of the spinal cord of an *Smn*$^{2B/-}$*;YFP-H* mouse. The green arrow highlights a MNCB that expresses YFP and the red arrow highlights a MNCB that does not. Note that sections were stained with Nissl and although this was visible on the same channel as YFP, the intensity of YFP was substantially stronger. Scale bar = 20μm. (**B**) The graph (Mean±SEM) shows that there is no significant difference in the intensity of pH2AX staining in motor neurons that express YFP and motor neurons that do not express YFP (by Unpaired T-test, ns>0.05; n= 3 mice). (**C**) There is also no significant difference in the average intensity of pH2AX staining in motor neurons that express YFP and motor neurons that do not express YFP for each mouse (by Unpaired T-test, ns>0.05; n= 3 mice). D*ata acquired in collaboration with Shilpa Purushotham (MSc student).*

4.2.2 Sprouting cannot account for a reduction in denervation in the LALr muscle of *Smn*$^{2B/-}$ mice

Muscles of SMA mouse models fall on a spectrum of denervation; while some show high levels of denervation and pathology, others show considerably less (Thomson et al. 2012). I aimed to compare muscles of the *Smn*$^{2B/-}$ mouse model of SMA that show vast motor neuron degeneration to those that display considerably less, to address whether compensatory sprouting was responsible for this reduction in denervation. Both NMJ and motor unit morphology would be assessed in the LALr and TS muscles of the *Smn*$^{2B/-}$ mouse model to compare sprouting.

Firstly, the level of denervation and pathology that occurs within the TS muscle of *Smn*$^{2B/-}$ mice had to be determined. This muscle was originally examined for YFP expression however its vulnerability status had never been determined in the *Smn*$^{2B/-}$ mouse model of SMA. Therefore endplate occupancy, pre-synaptic swelling and post-synaptic endplate area was quantified in *Smn*$^{2B/-}$ mice and *Smn*$^{2B/+}$ controls at P18. It was found that there was a significant decrease in the percentage of fully occupied endplates, to an average of 31%, in the TS muscle of *Smn*$^{2B/-}$ mice when compared to controls (Figure 4.8). There was also a significant increase the severity of pre-synaptic swelling and a significant decrease in post-synaptic endplate area in the TS of *Smn*$^{2B/-}$ mice compared to controls (Figure 4.8). This muscle could therefore be classed as being vulnerable to degeneration.

In addition, I wished to confirm the pathological status of the LALr muscle in *Smn*$^{2B/-}$ mice at P18 by endplate occupancy analysis as well as performing further NMJ morphological analysis, specifically, pre-synaptic swelling and endplate size analysis, within this muscle. As one of the cranial muscles, this muscle has been shown to be display lower levels of degeneration (Murray et al. 2015). This analysis showed that ~96% of endplates in the LALr muscle of *Smn*$^{2B/-}$ mice were fully occupied by a pre-synaptic terminal and so confirmed previous reports (Figure 4.9). In addition, despite this low level of

denervation, this muscle displays a significant increase in severity of the pre-synaptic swelling observed in *Smn*$^{2B/-}$ mice compared to *Smn*$^{2B/+}$ controls. There was also a significant decrease in endplate area in the LALr of *Smn*$^{2B/-}$ mice compared to *Smn*$^{2B/+}$ controls (Figure 4.9). The pathology observed in the TS muscle was subsequently compared to pathology in the LALr muscle of P18 *Smn*$^{2B/-}$ mice (Figure 4.10). This showed that there was a significant decrease in the percentage of fully occupied endplates in the TS muscle compared to the LALr muscle of *Smn*$^{2B/-}$ mice and a significant increase in the severity of pre-synaptic swelling in the TS muscle compared to the LALr (Figure 4.10 A&B). There was no significant difference in the area of post-synaptic endplates in the TS muscle compared to the LALr in *Smn*$^{2B/-}$ mice. There was also no significant difference in endplate occupancy, pre-synaptic swelling or endplates area in the TS muscle compared to the LALr of *Smn*$^{2B/+}$ control mice (Figure 4.10).

Following the investigation into degeneration in the TS and LALr muscles, I wished to investigate whether sprouting could account for the reduced levels of denervation that is observed in the LALr compared to the TS. Therefore, nodal and terminal sprouting in the TS and LALr muscles of *Smn*$^{2B/-}$ mice as well as *Smn*$^{2B/+}$ control littermates was quantified. Nodal sprouts extend from an axon while terminal sprouts extended from a presynaptic terminal. Nodal sprouts were classified based on their thin axonal appearance that differed from other axonal branches (Refer to Figure 4.11, 4.19 and 5.3). There was no significant difference in the percentage of both nodal and terminal sprouting between the TS and LALr muscles in *Smn*$^{2B/-}$ mice (Figure 4.11). As sprouting was observed, albeit a small amount, in both the TS and LALr, there is evidence that sprouting is masking some denervation in the LALr muscle. However, as there was no significant difference in the level of sprouting between the TS and LALr, sprouting cannot account for the significant difference in denervation that is observed between the TS and the LALr muscle in *Smn*$^{2B/-}$ mice at P18.

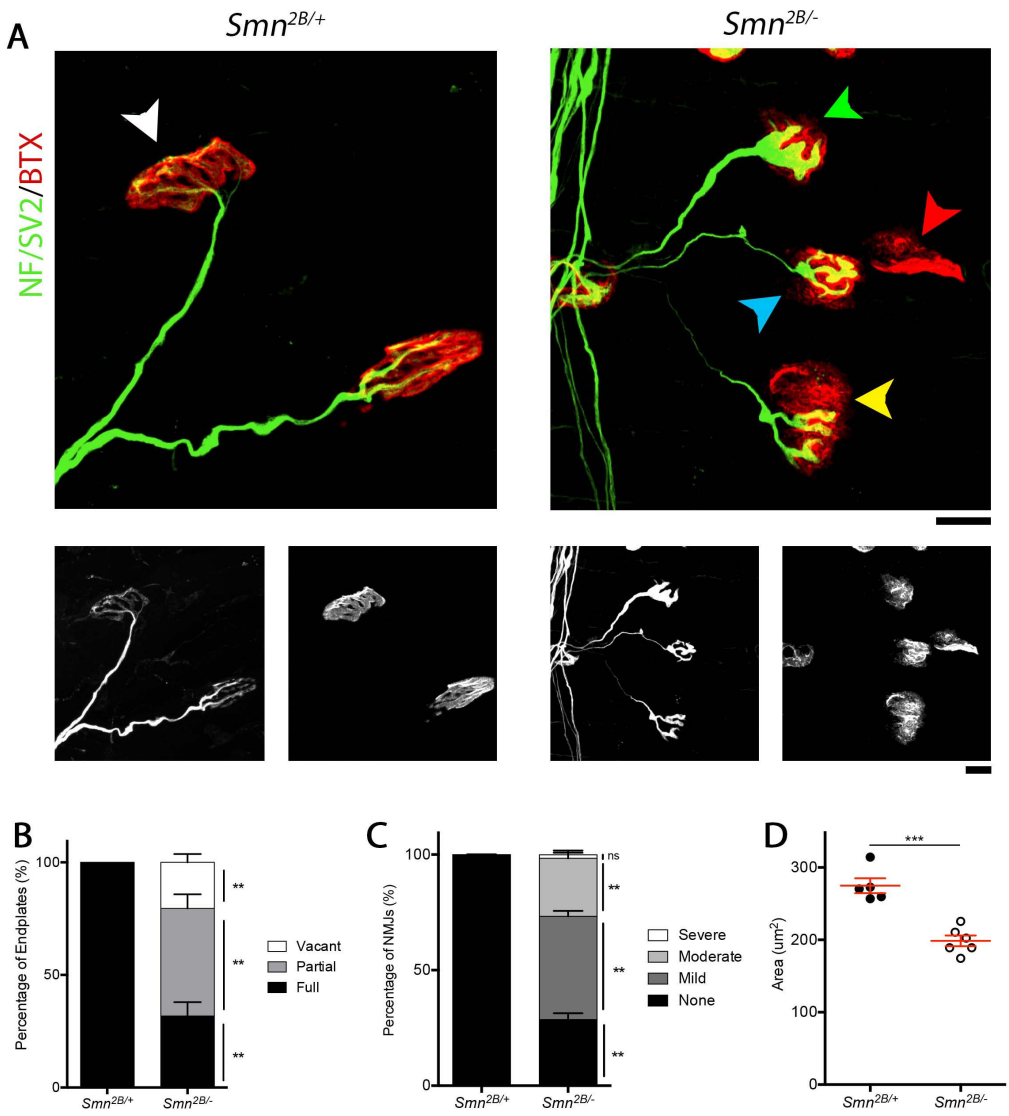

Figure 4.8: The TS muscle of *Smn*$^{2B/-}$ mice exhibits significant denervation and pre-synaptic swelling when compared to *Smn*$^{2B/+}$ controls. (**A**) Representative images of NMJs in the TS muscle of *Smn*$^{2B/-}$ and *Smn*$^{2B/+}$ mice. White arrowhead = normal NMJ with no swelling; blue arrowhead = NMJ with mild pre-synaptic swelling; green arrowhead = NMJ with moderate pre-synaptic swelling; yellow arrowhead = partially occupied endplate; red arrowhead = vacant endplate. Scale bar = 10μm. (**B**) The bar chart (Mean ± SEM) shows that there is a significant decrease in the percentage of fully occupied endplates and a significant increase in the percentage of partially occupied and vacant endplates in the TS of *Smn*$^{2B/-}$ mice compared to *Smn*$^{2B/+}$ mice (by Mann Whitney-U test; *p<0.01; n=6 muscles per genotype). (**C**) The bar chart (Mean ± SEM) shows that there is a significant decrease in the percentage of NMJs with no pre-synaptic swelling and an increase in the percentage displaying mild and moderate pre-synaptic swelling in the TS of *Smn*$^{2B/-}$ mice compared to *Smn*$^{2B/+}$ mice (by Mann Whitney-U test; ns>0.05, **p<0.01; n= 6 muscles per genotype). (**D**) The graph (Mean ± SEM) shows that there is a significant difference in the average post-synaptic endplate area of the TS in *Smn*$^{2B/-}$ mice when compared to the average endplate area of the TS of *Smn*$^{2B/+}$ mice (by Unpaired t-test, ***p<0.005; n= 5/6 muscles for *Smn*$^{2B/+}$/ *Smn*$^{2B/-}$ respectively). *Data acquired in collaboration with Roxanna Munir during a MSc project.*

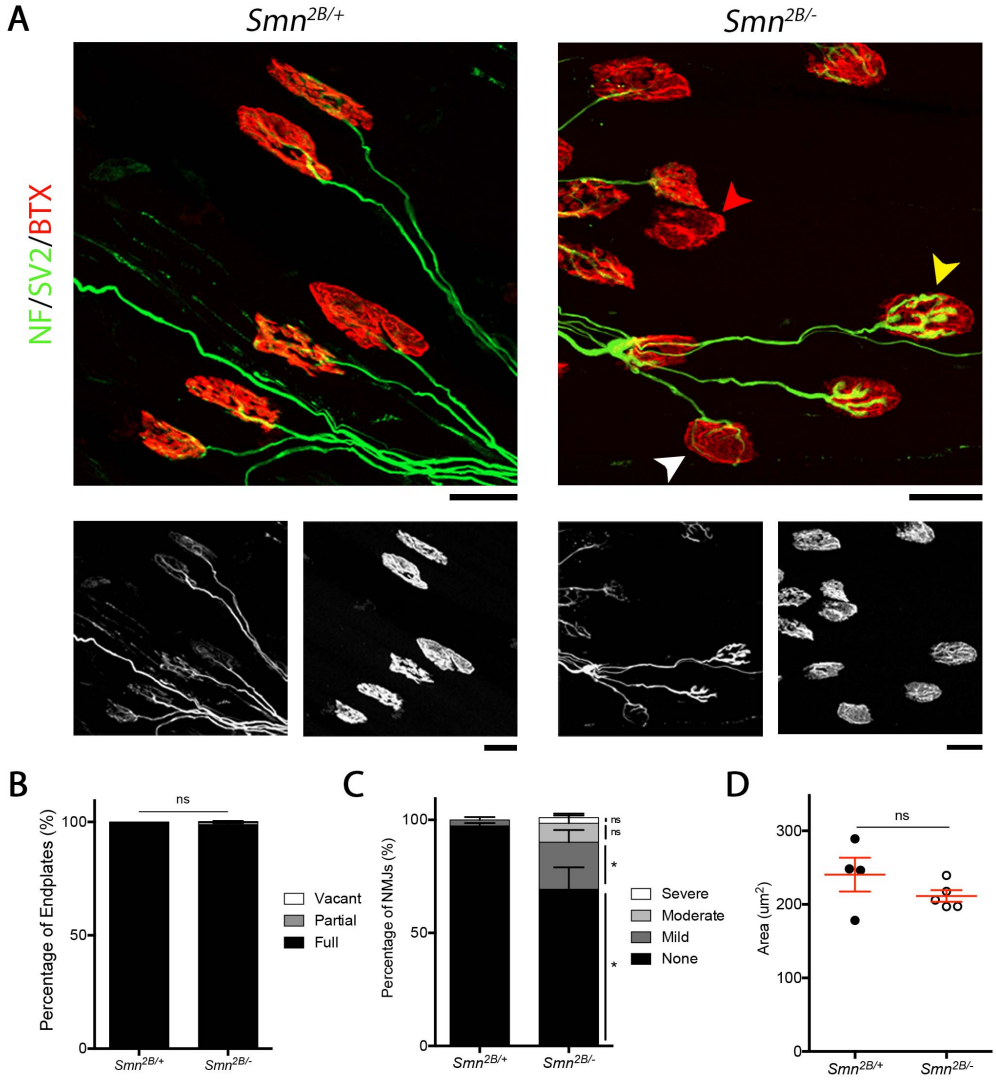

Figure 4.9: The LALr muscle of *Smn*$^{2B/-}$ mice exhibits increased pre-synaptic swelling but shows no significant denervation compared to controls. (**A**) Representative images display the increase in pre-synaptic swelling observed in the LALr of *Smn*$^{2B/-}$ mice compared to controls (White arrow = no swelling, yellow arrow = moderate swelling of the pre-synaptic terminal). Although there is some denervation (red arrowhead highlights a vacant endplate) in the LALr of *Smn*$^{2B/-}$ mice, this is not significantly different to controls. Scale bar = 10μm. (**B**) The bar chart (Mean ± SEM) shows that there is no significant difference in the occupancy of endplates in the LALr of *Smn*$^{2B/-}$ mice compared to the LALr of *Smn*$^{2B/+}$ controls (by Mann Whitney-U test; ns>0.05; n= 4 for *Smn*$^{2B/+}$, 6 for *Smn*$^{2B/-}$). (**C**) The bar chart (Mean ± SEM) shows that there is a significant decrease in the percentage of NMJs with no pre-synaptic swelling and an increase in the percentage displaying mild pre-synaptic swelling in the LALr of *Smn*$^{2B/-}$ mice compared to *Smn*$^{2B/+}$ mice (by Mann Whitney-U test; ns>0.05, *p<0.05; n= 4 for *Smn*$^{2B/+}$, 6 for *Smn*$^{2B/-}$). (**D**) The graph (Mean ± SEM) shows that there no significant difference in the average post-synaptic endplate area of the LALr in *Smn*$^{2B/-}$ mice when compared to the average endplate area of the LALr of *Smn*$^{2B/+}$ mice (by Unpaired t-test, *p<0.05; n= 4 for *Smn*$^{2B/+}$, 5 for *Smn*$^{2B/-}$).

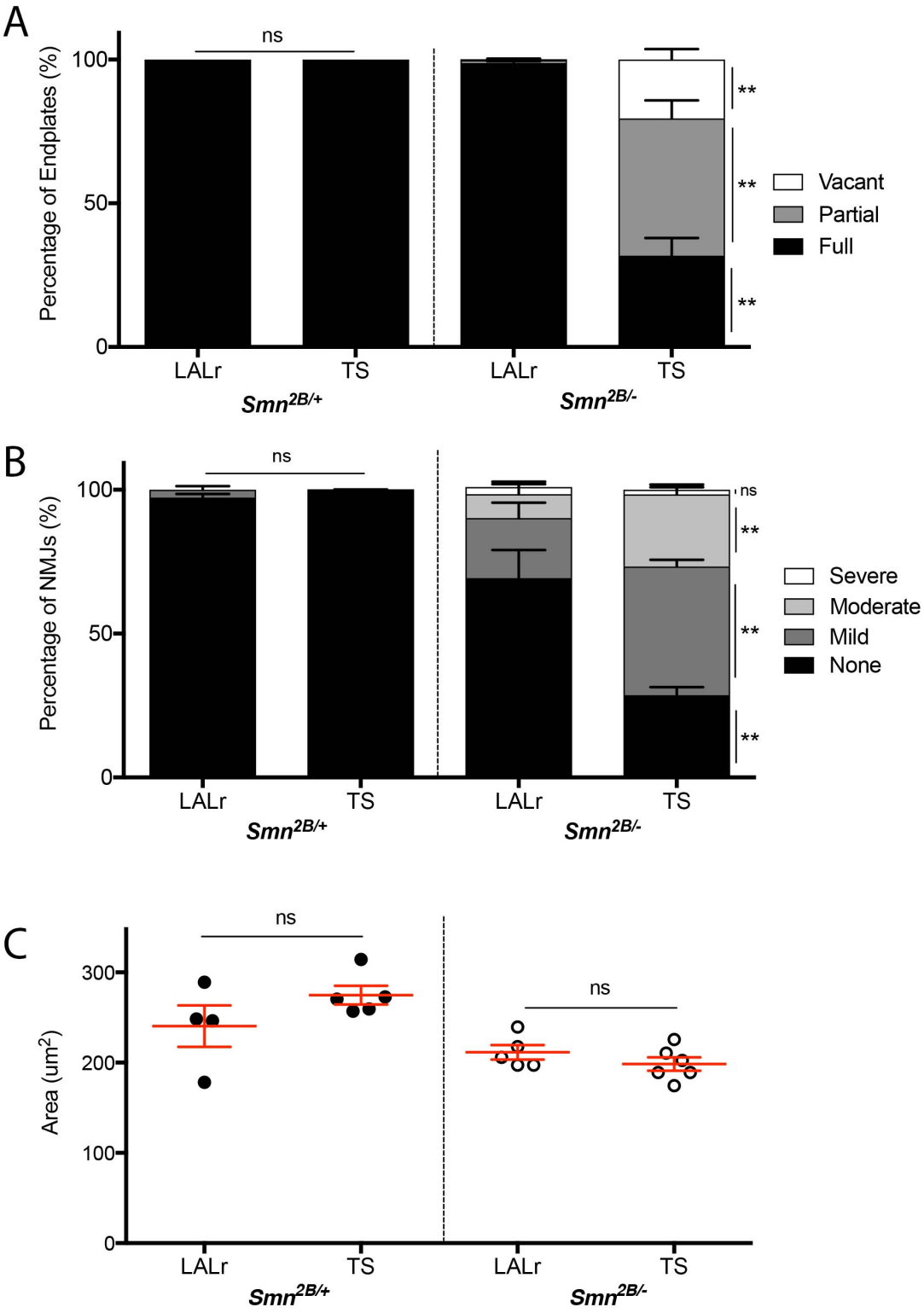
A
ns
Percentage of Endplates (%)
100
50
0
**
**
**
Vacant
Partial
Full
LALr
TS
LALr
TS
Smn2B/+
Smn2B/-
B
ns
Percentage of NMJs (%)
100
50
0
ns
**
**
**
Severe
Moderate
Mild
None
LALr
TS
LALr
TS
Smn2B/+
Smn2B/-
C
ns
ns
Area (um2)
300
200
100
0
LALr
TS
LALr
TS
Smn2B/+
Smn2B/-

Figure 4.10: The TS muscle displays significantly more pathology than the LALr muscle in P18 *Smn$^{2B/-}$* mice (**A**) The bar chart (Mean ± SEM) compares the occupancy of endplates in the LALr and the TS muscles for *Smn$^{2B/+}$* and *Smn$^{2B/-}$* mice. In *Smn$^{2B/+}$* mice, there is no significant denervation in both the LALr and TS muscles. In *Smn$^{2B/-}$* mice, there is a significant decrease in the percentage of fully occupied endplates and a significant increase in the percentage of partially occupied and vacant endplates in the TS muscle when compared to the LALr (by Mann Whitney-U test; ns>0.05, **p<0.01; n= 6 TS per genotype, 4 LALr for *Smn$^{2B/+}$*, 6 LALr for *Smn$^{2B/-}$*). (**B**) The bar chart (Mean ± SEM) compares pre-synaptic swelling in the LALr and the TS muscles for *Smn$^{2B/+}$* and *Smn$^{2B/-}$* mice. In *Smn$^{2B/+}$* mice, there is no significant swelling in both the LALr and TS muscles. In *Smn$^{2B/-}$* mice, there is a significant decrease in the percentage of NMJs with no pre-synaptic swelling and a significant increase in the percentage of NMJs displaying mild and moderate pre-synaptic swelling in the TS muscle when compared to the LALr (by Mann Whitney-U test; ns>0.05, *p<0.05; n= 6 TS per genotype, 4 LALr for *Smn$^{2B/+}$*, 6 LALr for *Smn$^{2B/-}$*). (**C**) The graph (Mean ± SEM) compares post-synaptic endplate area in the LALr and the TS muscles for *Smn$^{2B/+}$* and *Smn$^{2B/-}$* mice. In *Smn$^{2B/+}$* mice, there is no significant difference in the average endplate area of the LALr and TS muscles. In *Smn$^{2B/-}$* mice, there is also no significant difference in endplate area between the LALr and TS muscles (by Unpaired t-test, ns>0.05, *p<0.05, ***p<0.005; n= 5 TS for *Smn$^{2B/+}$*, 6 TS for *Smn$^{2B/-}$*, 4 LALr for *Smn$^{2B/+}$*, 5 LALr for *Smn$^{2B/-}$*). *Data acquired in collaboration with Roxanna Munir during a MSc project.*

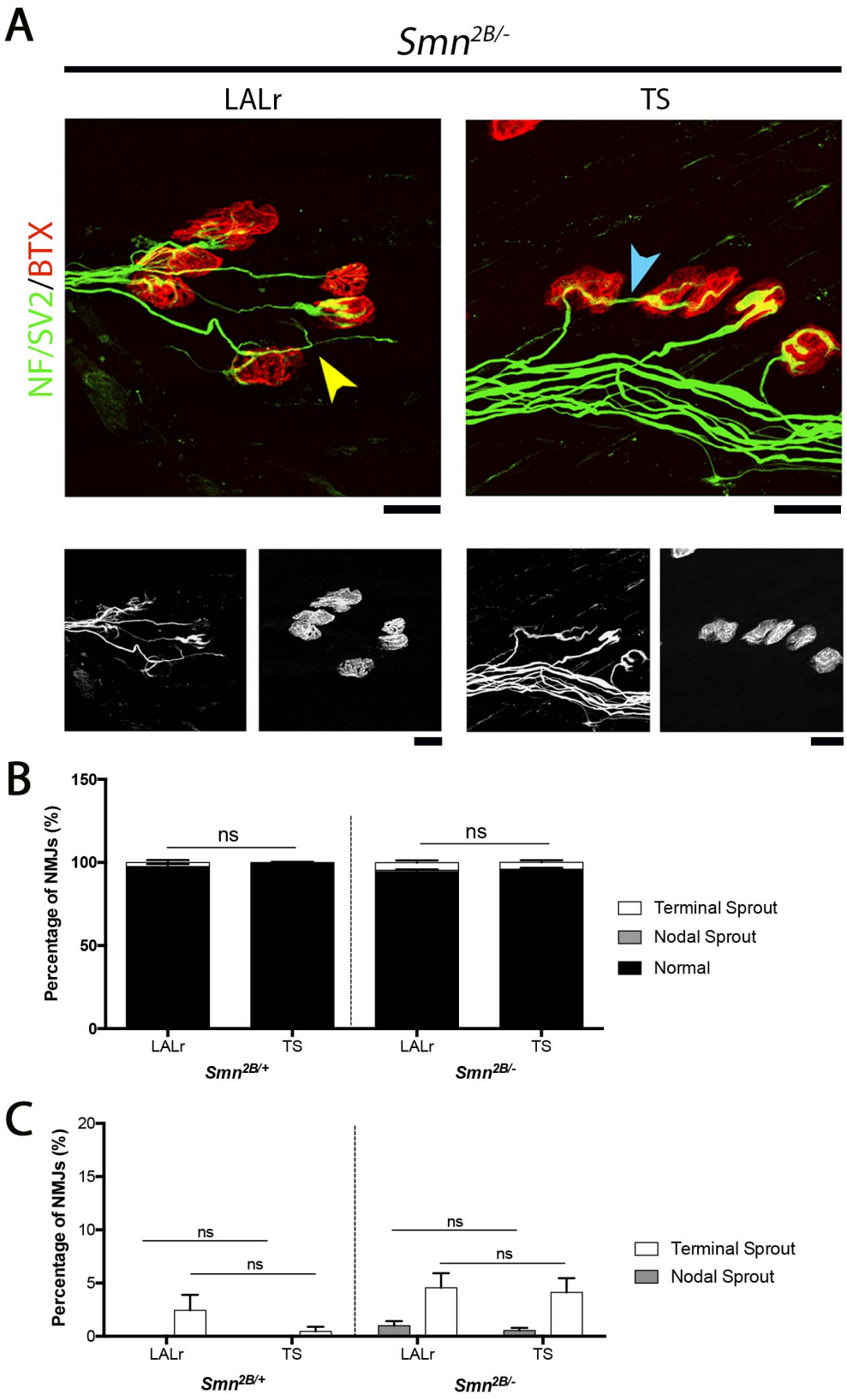
A
Smn2B/-
LALr
TS
NF/SV2/BTX
B
Percentage of NMJs (%)
150
100
50
0
ns
ns
LALr
TS
LALr
TS
Smn2B/+
Smn2B/-
Terminal Sprout
Nodal Sprout
Normal
C
Percentage of NMJs (%)
20
15
10
5
0
ns
ns
ns
ns
LALr
TS
LALr
TS
Smn2B/+
Smn2B/-
Terminal Sprout
Nodal Sprout

Figure 4.11: There is no significant difference in sprouting between the TS and LALr muscles in P18 *Smn$^{2B/-}$* mice (**A**) Images show NMJs from the LALr muscle and TS muscle and highlight examples of sprouting. The arrowheads show terminal sprouts extending from the pre-synaptic terminal of an NMJ. Grey scale images show the separate channels of the images. The small image at the bottom left of each large image is the axons labelled with NF/SV2 and the small image at the bottom right of each large image is the endplate labelled with BTX. Scale bar = 20μm. (**B**) The bar chart (Mean ± SEM) compares the percentage of nodal and terminal sprouts in the LALr and the TS muscles for *Smn$^{2B/+}$* and *Smn$^{2B/-}$* mice. In both *Smn$^{2B/+}$* and *Smn$^{2B/-}$* mice there is no significant difference in the level of sprouting observed in the TS muscle when compared to the LALr (by Mann Whitney-U test; ns>0.05; n= 6 TS per genotype, 4 LALr for *Smn$^{2B/+}$*, 6 LALr for *Smn$^{2B/-}$*) (**C**) The graph shows the percentage of terminal and nodal sprouts in each muscle. These bars have been pulled out from the graph in (B) in order to show the low percentage in more detail. *Data acquired in collaboration with Roxanna Munir during a MSc project.*

4.2.3 Motor unit reconstructions show that pathology is asynchronous in motor units of the LALr muscle in $Smn^{2B/-}$ mice

Schaefer *et. al.* proposed that in a mouse model of ALS, there are subpopulations of large motor neurons that have sprouted to compensate for the degeneration of other small motor neurons (Schaefer et al. 2005). In addition, they show that degenerating axons and axonal sprouts are rarely found in the same motor unit. Therefore, in this mouse model, it appears that 'healthy' motor neurons are compensating for degenerating motor neurons by sprouting. If this is the case then it could be proposed that pathological features of NMJs, such as denervation, pre-synaptic swelling and endplate shrinkage will be restricted to subsets of motor neurons.

In order to address whether there are compensatory subpopulations of motor neurons the *$Smn^{2B/-}$;YFP-H* mouse model was utilised. Prior to the examination of YFP expression, I had aimed to trace and assess individual motor neurons within a variety of differentially vulnerable muscles within this mouse model. However, due to the YFP expression in this mouse model, only motor neurons within in the LALr muscle were traceable. Entire motor units in this muscle were individually imaged, reconstructed and traced (Figure 4.12). From the trace of the motor unit a tree diagram was created, to show the structure and branching pattern of the motor unit (Figure 4.12C). The morphology (including endplate occupancy, pre-synaptic swelling, endplate size and maturation and sprouting) of each individual NMJ in the 6 motor units that were traceable was assessed. NMJs were only quantified if they were clearly visible and in the correct orientation to ensure consistency of measurements.

In 3 of the 6 motor units that were assessed, there was evidence of denervation (Figure 4.13 & Figure 4.14). In one of these motor units, 2 out of 19 (10.5%) NMJs had partially occupied endplates. In the other two motor units, there were retraction bulbs, as evidenced by branches that did not

supply an endplate and had a bulbous end, suggesting the withdrawal of this axon from the NMJ. It must be noted that quantifying vacant endplates was not possible within *Smn$^{2B/-}$;YFP-H* mice (whose muscles have not been stained to label all axons) as YFP expression is within only a subset of motor neurons. Therefore, endplates that appear vacant in YFP-H mice are not necessarily vacant and may be supplied by another, non-YFP expressing motor neuron. It is therefore possible that there is an undercounting of denervation. However, the average percentage of fully occupied endplates for the 6 motor units combined is 95.15%, which is in keeping with whole muscle occupancy analysis of the LALr, which shows that ~96% of endplates are fully occupied in the LALr of *Smn$^{2B/-}$* mice (Whole muscle average from Figure 4.7; also displayed in Figure 4.14).

For future analysis of motor unit pathology, the 6 motor units were categorised based on their denervation status; those that contained signs of denervation and those that did not. All endplates in motor units 1-3 were fully occupied and so these motor units therefore fell into the 'non-denervated' category. Motor units 4 and 6 contained retraction bulbs while motor unit 5 had partially occupied endplates. Therefore, these three motor units fell into the 'denervated' category. By doing this, motor unit pathology between non-denervated and denervated motor units could be compared.

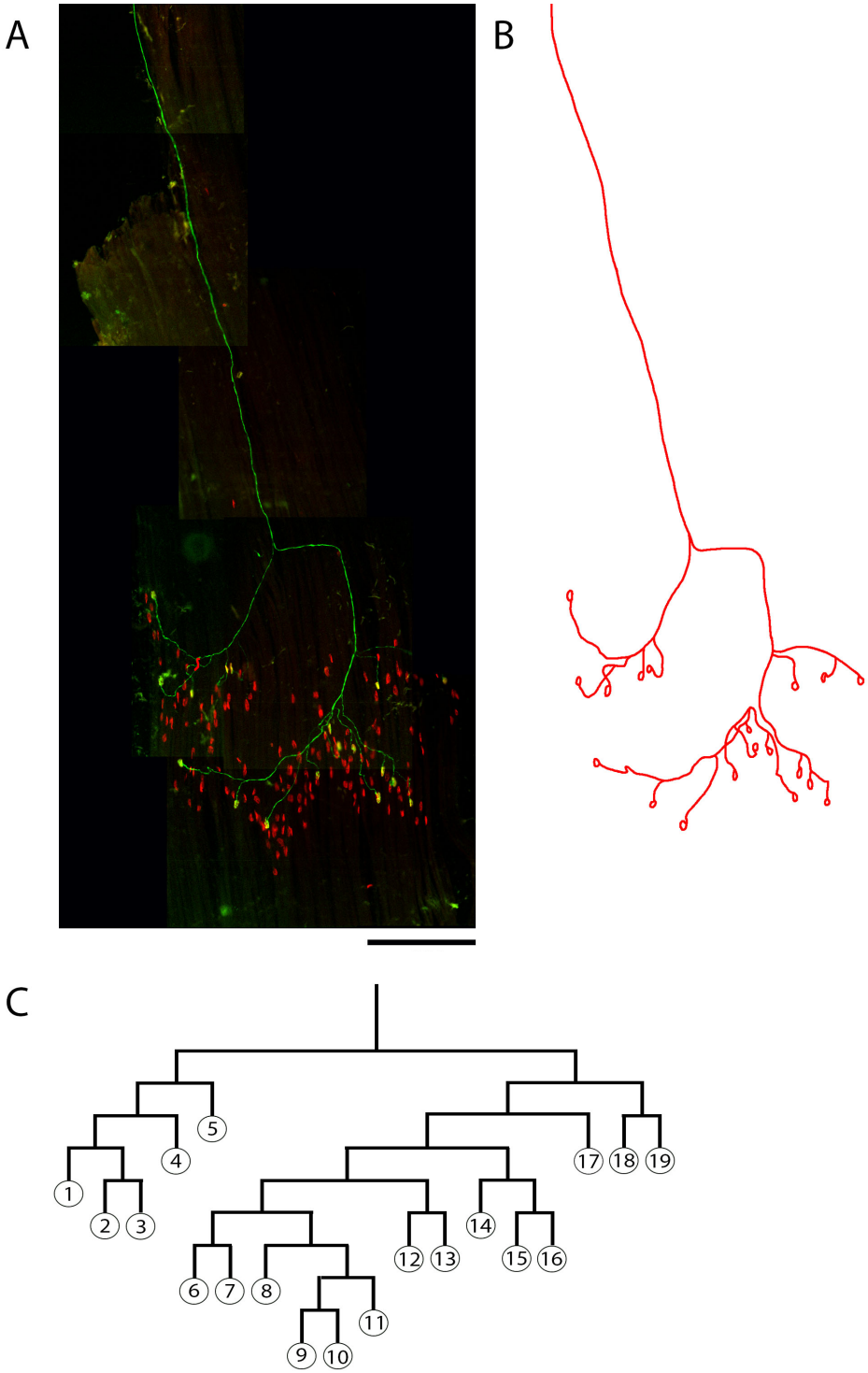

Figure 4.12: YFP allows individual motor neurons to be traced. (**A**) A montage of a motor unit was created by stitching together images taken, on a fluorescent microscope, at x20 magnification in Adobe Photoshop. Scale bar =300μm. (**B**) The montage was traced in Adobe Photoshop to show the layout of the motor unit as a single line drawing. (**C**) Tree diagrams were created from the line drawing of the motor unit, showing the branching pattern and assigning a number to individual NMJs within the motor unit. This allowed various features of these NMJs to be assessed.

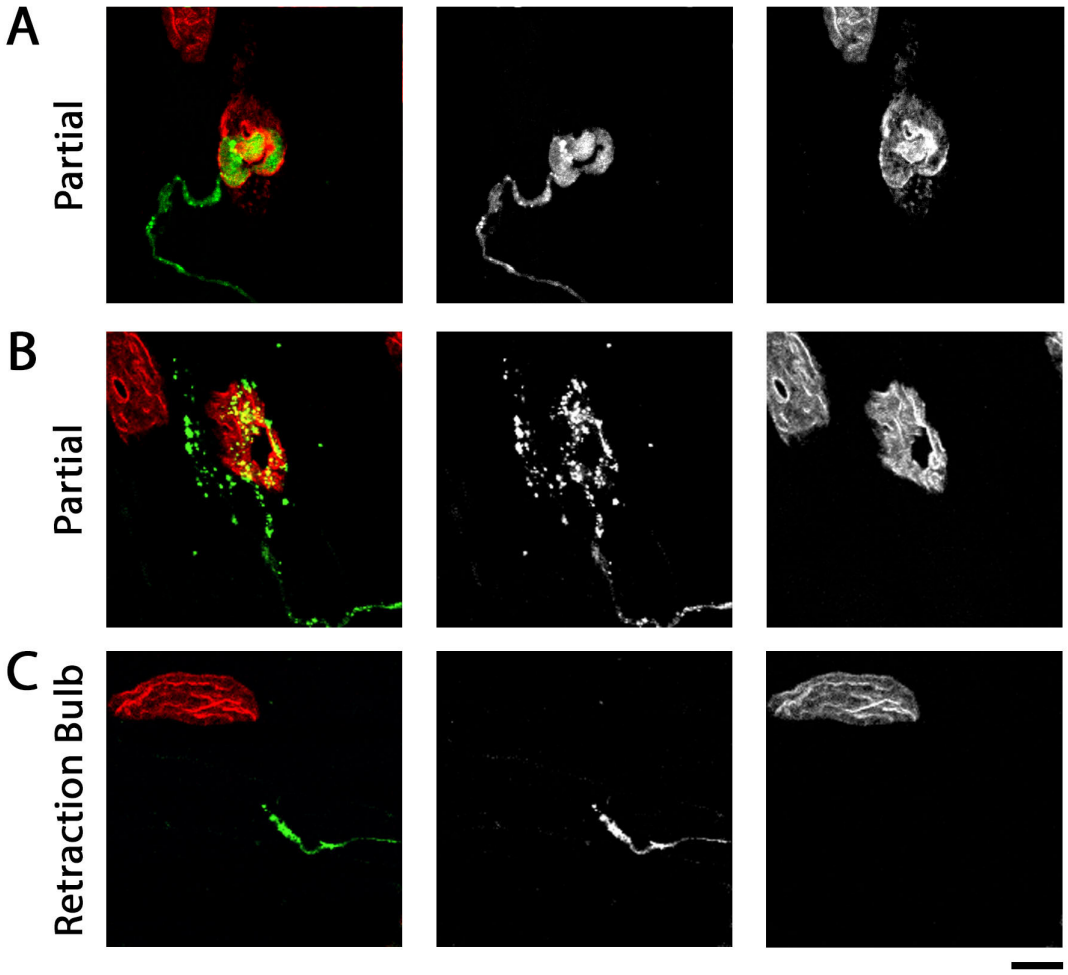

Figure 4.13: Features of denervation were visible using YFP expression in motor neurons (**A**) Representative image of a NMJ that has a partially occupied post-synaptic endplate (on the left). (**B**) Image shows an NMJ that had a partially occupied endplate. Note the unusual appearance of this pre-synaptic terminal. (**C**) Representative image of a retraction bulb visualised using YFP. Note the bulbus end of the axon as it withdraws away from a post-synaptic endplate. Scale bar (for all) = 10μm.

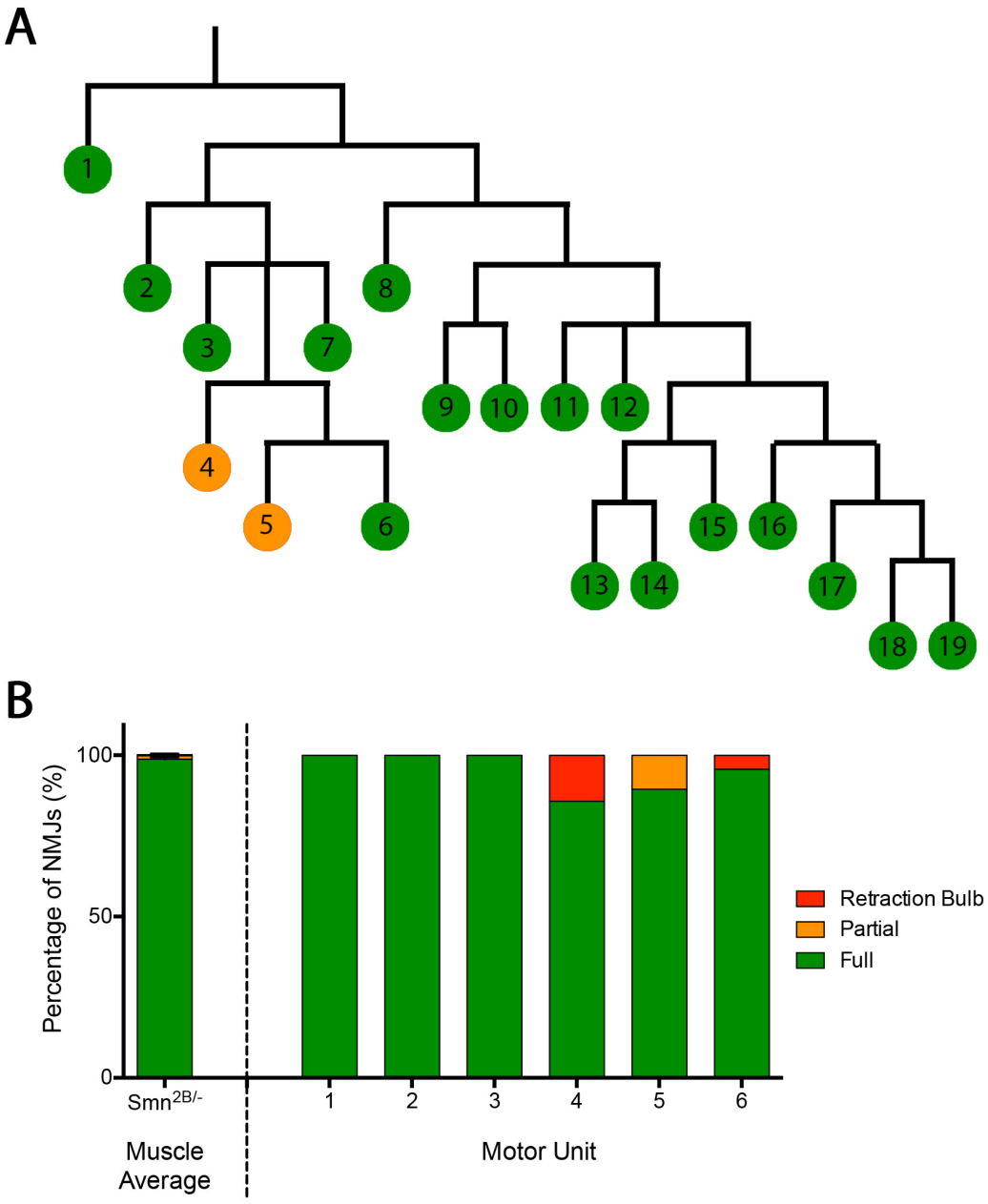

Figure 4.14: Denervation was visible in 50% of LALr motor units analysed in *Smn$^{2B/-}$;YFP-H* mice. (**A**) Example of a tree diagram showing the occupancy endplates in motor unit 5. One of these tree diagrams was created for all 6 motor units analysed. By colour coding full and partial occupancy pathology across the entire motor unit can be visualised. (**B**) Bar chart stacks the percentage of fully and partially occupied endplates as well as the percentage of retraction bulbs in each of the 6 motor units assessed. In 2 of the 6 motor units there were retraction bulbs and in 1 of the 6 motor units there was partial occupancy of endplates. The percentage of occupancy for the entire muscle is shown on the left of the bar chart (Mean ± SEM, n= 6 muscles).

I wished to determine whether pre-synaptic swelling was synchronous throughout motor units within the LALr of *Smn$^{2B/-}$;YFP-H* mice. Therefore, pre-synaptic swelling was quantified in each of the motor units (Figure 4.15 & Figure 4.16). It was observed that the overall percentage of NMJs with no, mild, moderate and severe swelling varied between motor units and within each of the motor units there was evidence of NMJs with and without swelling. In addition, the NMJs that had evidence of swelling were scattered throughout the motor unit rather than being confined to one area (Figure 4.16). As a result, it appears that with regards to pre-synaptic swelling there are not bimodal populations of motor neurons in the LALr of *Smn$^{2B/-}$;YFP-H* mice.

Previously in this thesis, it was found that the percentage of NMJs with no pre-synaptic swelling for the muscle as a whole is approximately 69.3% (Figure 4.9). When the average percentage of NMJs displaying no pre-synaptic swelling for the six motor units assessed is combined, 52.4% of NMJs displayed no pre-synaptic swelling. Due to the use of different pre-synaptic terminal markers, this data should not be directly compared. However, the difference in pre-synaptic swelling between NF/SV2 stained and YFP expressing motor units may suggest that the latter display more severe pre-synaptic swelling than the whole muscle average.

Additionally, the percentage of NMJs with no, mild, moderate and severe pre-synaptic swelling was compared between non-denervated and denervated motor units (Figure 4.16C). This showed that there was no significant difference in the percentage of each of these categories between non-denervated and denervated motor units.

Subsequently, the area of endplates within each motor unit was measured (Figure 4.15). To observe the spread of endplate area across a motor unit tree endplate size was categorised into groups; 1-100μm, 101-200μm, 201-300μm and 301-400μm. Collating this data into a bar shows that motor units

contain endplates of a variety of different sizes, with the most common categories being 101-200μm and 201-300μm (Figure 4.17 A&B). The area of the individual endplate measured within each motor unit was also plotted, alongside the area of endplates measured within the whole of the LALr (Figure 4.17C). From this, it appears that the endplate area within these motor units is relatively consistent with the spread of endplate areas observed within the muscle as a whole. There does not appear to be divergent subpopulations of motor neurons, when considering endplate area.

Furthermore, the area of endplates for non-denervated and denervated motor units was collated. This shows that the spread of endplate area between denervated and non-denervated endplates was comparable and not significantly different (Figure 4.17D). In addition, the average endplate area for non-denervated and denervated motor units was also not statistically different (Figure 4.17E). This therefore shows that post-synaptic endplate area is not based upon the denervation status of the motor unit.

The maturity of endplates within the motor units was also staged to determine whether this was synchronous across motor units in the LALr of *Smn$^{2B/-}$;YFP-H* mice. Stage 1 denotes the most mature endplates and stage 4 denotes the least mature. It was found that most endplates expressed stage 2 or 3 maturity (Figure 4.18). Two of the six motor units contained stage 4 endplates and one of these motor units also contained stage 1, immature endplates. This therefore shows that the maturity of endplates within motor units can vary. Motor units were again categorised into denervated or non-denervated and this showed that although there was no statistical difference in the maturity of endplates within these groups of motor units, there was greater variability in the maturity of endplates in denervated motor units (Figure 4.16C).

I wished to determine whether there are subpopulations of motor units that sprout to compensate for the degeneration of other motor units. Therefore,

sprouting was assessed within the motor units of the LALr of *Smn$^{2B/-}$;YFP-H* mice. Micro-sprouts, nodal sprouts and terminal sprouts were quantified. Micro-sprouting was a feature only observed in YFP expressing motor neurons, it had not previously seen in motor neurons stained using immunofluorescent techniques, and appeared as a 'speckling' of YFP that extended from the pre-synaptic terminal (Figure 4.19). While some motor units expressed a large degree of sprouting, others showed no evidence of sprouting (Figure 4.20B). Although not all motor units containing denervation expressed high levels of sprouting, motor unit 5 was of particular interest due to its high degree of pathology (although it still expressed variability in pathology throughout) and high degree of sprouting activity. This is contrary to the original hypothesis, which stated that denervation and sprouting occurs in different motor units. Micro-sprouting was still observed in one of the motor units that did not contain any denervation but no terminal or nodal sprouting was found in non-denervated motor units (Figure 4.20B).

The level of sprouting in these motor units was compared with the average level of sprouting observed in the LALr as a whole (Figure 4.20B). The average percentage of nodal and terminal sprouts in the whole muscle was ~6% whilst the average for the six motor units was ~9%, suggesting that these motor units are comparable to the muscle as a whole.

Moreover, by collating the data for motor units 1-3 (non-denervated) and motor units 4-6 (denervated), sprouting between non-denervated and denervated motor units was compared. Although there is no statistical significance in sprouting between these two groups, there does appear to be a trend towards an increase in sprouting within denervated motor units (Figure 4.20C).

Overall, it appears that pathology is asynchronous within a motor unit and it does not appear that there are pathologically divergent populations of motor neurons. It does not appear that apparently 'healthier' motor units are

sprouting to mask the degeneration of other motor units and in fact, motor units with greater pathology may exhibit greater levels of sprouting. In addition, it should be considered that sprouting is a motor neuron dependent activity since the muscle environment of these motor neurons is consistent yet the sprouting observed is not consistent across all motor units.

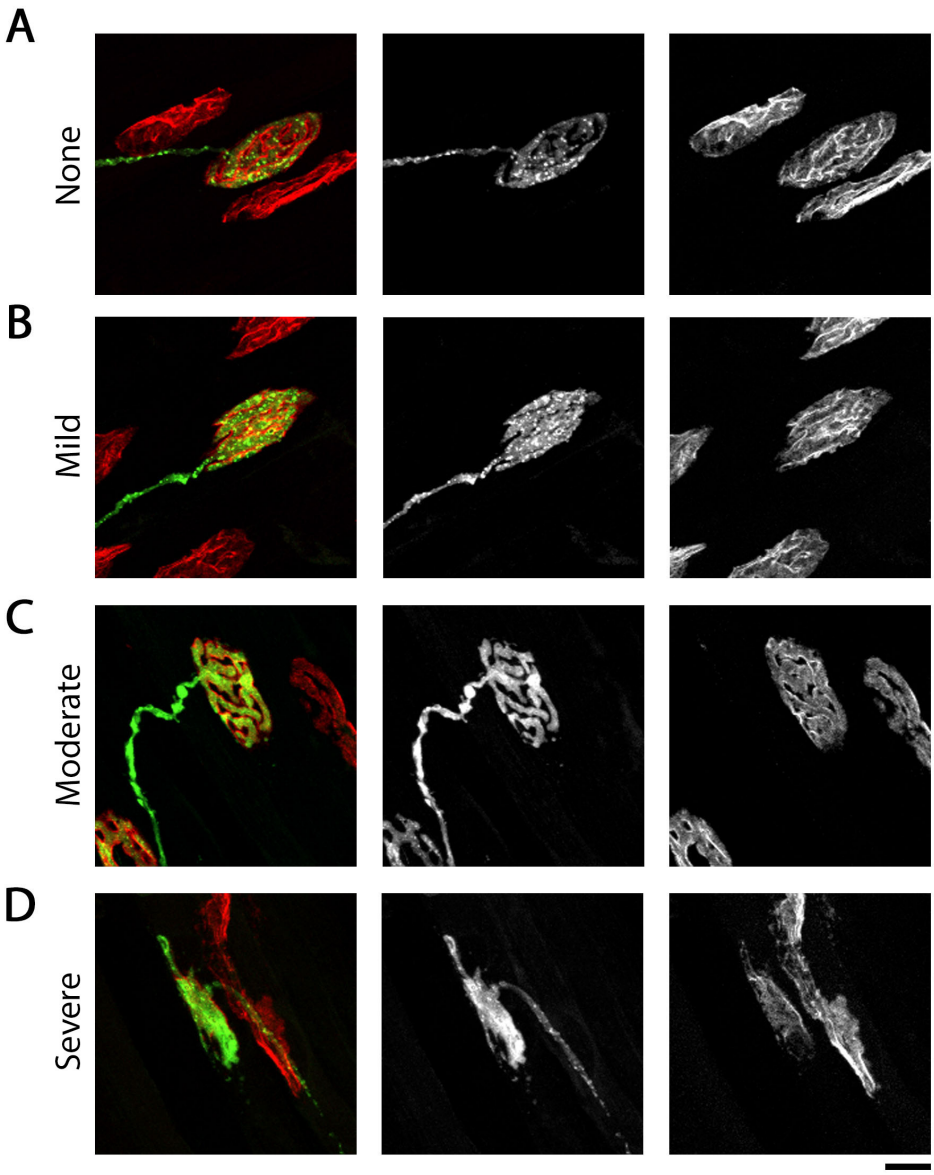

Figure 4.15: Pre-synaptic swelling can be observed in motor neurons expressing YFP. Representative image of non, mild, moderate and severe pre-synaptic swelling in motor neurons expressing YFP. (**A**) No pre-synaptic swelling: Pre-synaptic terminal and axon have a uniform expression of YFP. (**B**) Mild pre-synaptic swelling: YFP expression is increased at the terminal. (**C**) Moderate pre-synaptic swelling: YFP expression is increased at the terminal and there is some axonal swelling. (**D**) Severe pre-synaptic swelling: Pre-synaptic swelling is increased and obscures the endplate. Scale bar (for all images) = 10μm.

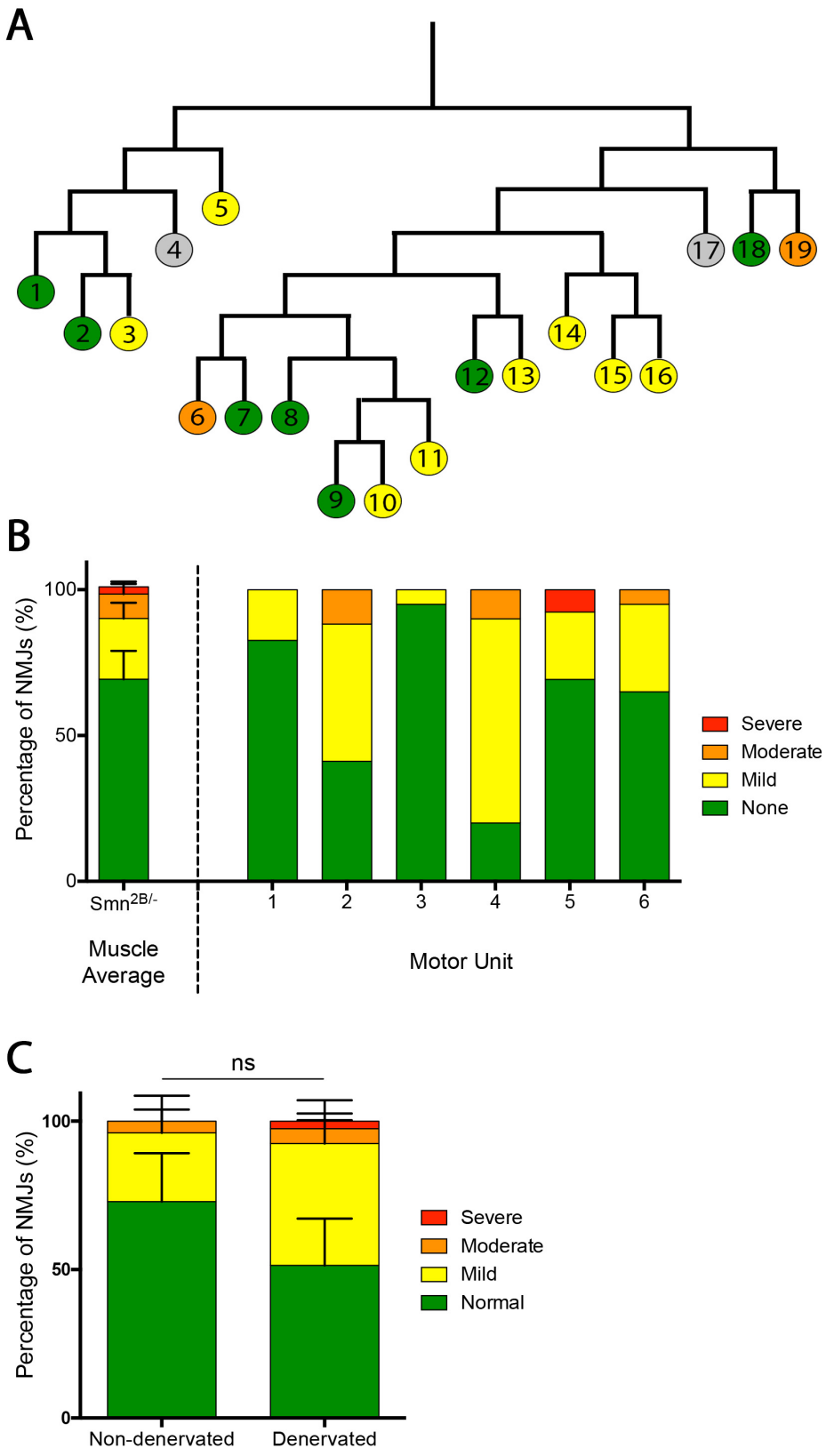
A
5
4
17
18
19
1
2
3
14
12
13
15
16
6
7
8
11
9
10
B
100
50
0
Percentage of NMJs (%)
Smn2B/-
1
2
3
4
5
6
Muscle Average
Motor Unit
Severe
Moderate
Mild
None
C
ns
100
50
0
Percentage of NMJs (%)
Non-denervated
Denervated
Severe
Moderate
Mild
Normal

Figure 4.16: Pre-synaptic swelling severity is not synchronous within motor units of *Smn$^{2B/-}$;YFP-H* mice. (**A**) The tree diagram shows the severity of pre-synaptic swelling at each NMJ of motor unit 2. One of these tree diagrams was created for each of the 6 motor units analysed. By colour coding each stage of pre-synaptic swelling pathology across the entire motor unit can be visually inspected. It appears that pathology is asynchronous within the motor unit and is not clustered in one location. (**B**) Bar chart stacks the percentage of pre-synaptic terminals with no, mild, moderate and severe swelling in motor units 1-6. It appears that the level of swelling varies across each of the motor units assessed. The average pre-synaptic swelling appearance for the muscle is shown at the left of the bar chart (mean ±SEM, n= 6 muscles). (**C**) When the percentage of no, mild moderate and severe swelling is collated for motor units displaying no denervation and denervation, there is no statistically significant difference between the two groups in terms of the severity of swelling. Note the trend towards an increase in severity in motor units displaying denervation. (ns>0.05 by Mann Whitney U test; n= 3 motor units)

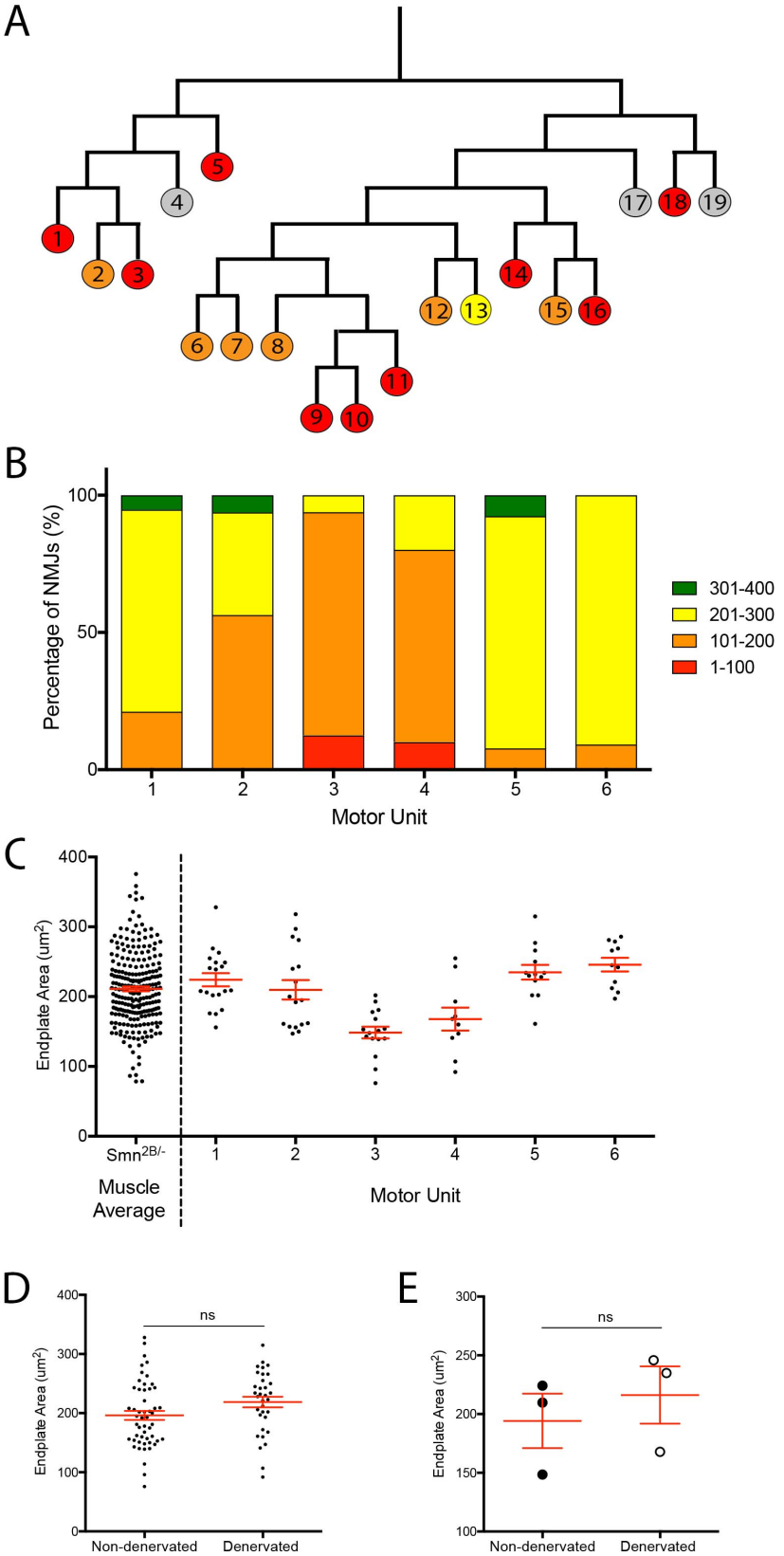
A
5
4
17
18
19
1
2
3
14
12
13
15
16
6
7
8
11
9
10
B
Percentage of NMJs (%)
100
50
0
1
2
3
4
5
6
Motor Unit
301-400
201-300
101-200
1-100
C
Endplate Area (um2)
400
300
200
100
0
Smn2B/-
Muscle Average
1
2
3
4
5
6
Motor Unit
D
Endplate Area (um2)
ns
Non-denervated
Denervated
E
Endplate Area (um2)
ns
Non-denervated
Denervated

Figure 4.17: The area of post-synaptic endplates varies throughout a motor units of *Smn$^{2B/-}$;YFP-H* mice. (**A**) Example of a tree diagram showing the endplate area of NMJs in motor unit 2. One of these tree diagrams was created for each of the 6 motor units analysed. By categorising the area measured into groups and colour coding each group (1-100μm (red), 101-200μm (yellow), 201-300μm (orange) and 301-400μm (green)), the area of endplates across the entire motor unit could be visualised. It appears that endplate size varies throughout the motor unit and smaller endplates are not clustered in one location. (**B**) Bar chart stacks the percentage of endplates with and area of 1-100μm, 101-200μm, 201-300μm or 301-400μm in motor units 1-6. It appears that the area of endplates varies across each of the motor units assessed, but the most common size categories are 101-200μm and 201-300μm. (**C**) The graph (Mean ± SEM) shows the area of each individual endplate within motor units 1-6. The average for the LALr is shown at the left of the graph. Note that the area of endplate across the six motor units appear consistent with the area of endplates across the whole LALr muscle in *Smn$^{2B/-}$* mice (ns>0.05 by Unpaired t-test; n= 3 motor units; muscle average = n of 5 muscles) (**D**) The area of endplates for motor units displaying no denervation and denervation is comparable and not statistically significant between the two groups (by Unpaired t-test, ns>0.05; n= 34/52 endplates for non-denervated/ denervated motor units) (**E**) The average endplate area of motor units displaying no denervation and denervation was also not significantly different (by Unpaired t-test, ns>0.05; n= 3 motor units).

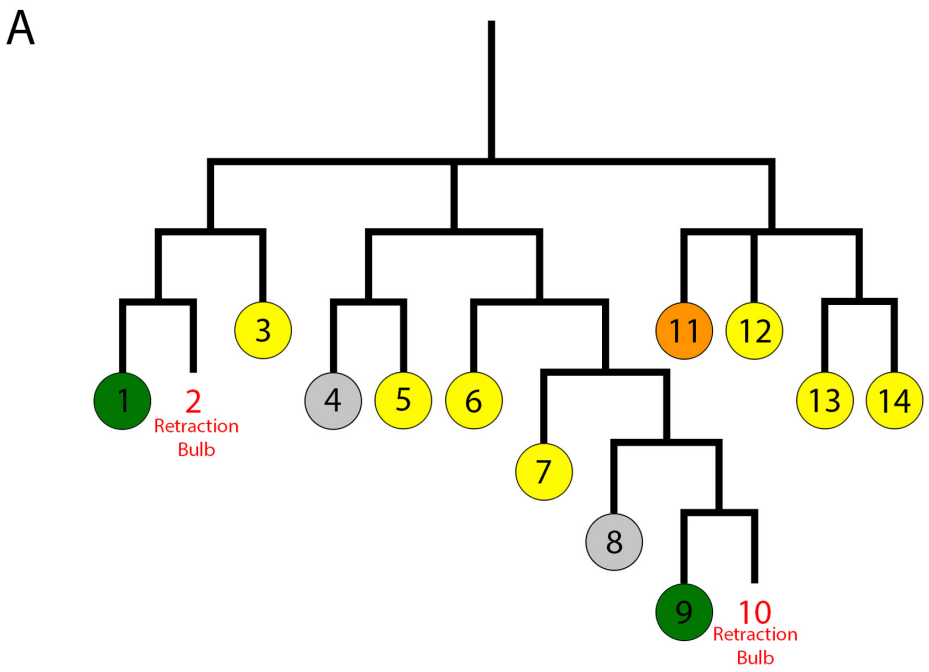
A
1
2
Retraction
Bulb
3
4
5
6
7
8
9
10
Retraction
Bulb
11
12
13
14

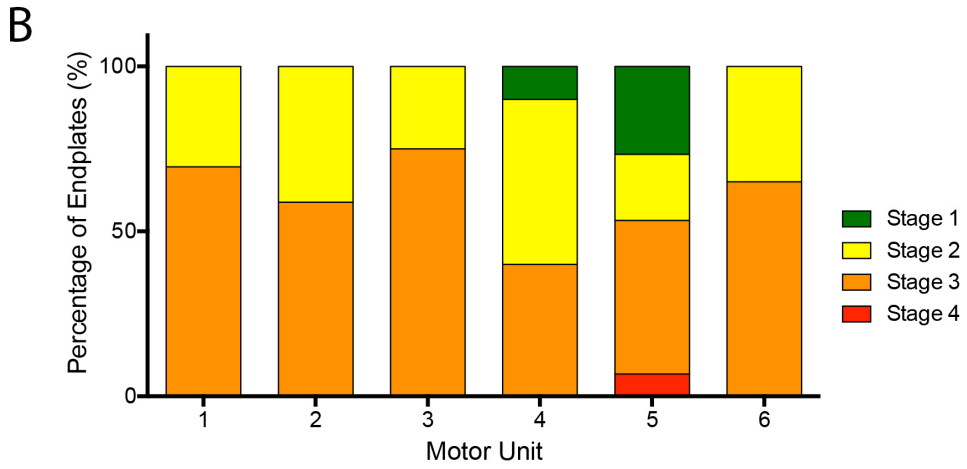
B
Percentage of Endplates (%)
100
50
0
1
2
3
4
5
6
Motor Unit
Stage 1
Stage 2
Stage 3
Stage 4

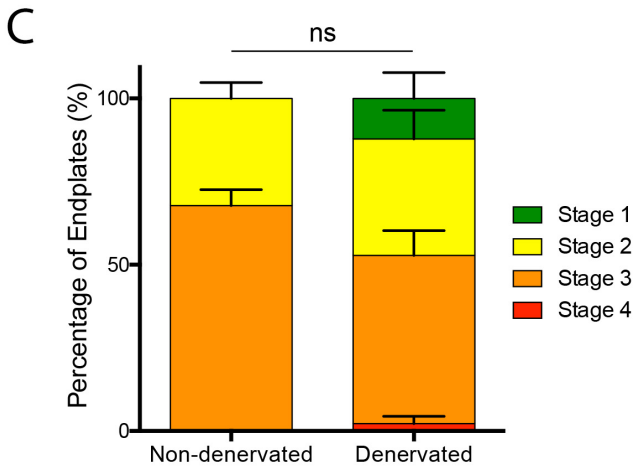
C
ns
Percentage of Endplates (%)
100
50
0
Non-denervated
Denervated
Stage 1
Stage 2
Stage 3
Stage 4

Figure 4.18: Endplate maturation varies within motor units of *Smn$^{2B/-}$;YFP-H* mice. (**A**) The tree diagram shows the stage of maturation of each post-synaptic endplate of motor unit 2 (least mature (stage 1) to most mature (stage 4)). One of these tree diagrams was created for each of the 6 motor units analysed. By colour coding each stage of maturation the pathology across the entire motor unit can be visualised. It appears that pathology is asynchronous within the motor unit and is not clustered in one location. Most pre-synaptic endplates were stage 2 or 3 maturity. (**B**) Bar chart stacks the percentage of endplates displaying stage 1 to 4 endplate maturity in motor units 1-6. The level of maturation appears to vary across each of the motor units assessed. (**C**) When the percentage of stage 1-4 endplate maturation is collated for motor units displaying no denervation and denervation, there is no statistically significant difference between the two groups (ns>0.05 by Mann Whitney U test; n= 3 motor units). However, it is interesting that non-denervated motor units consistently display stage 2 and 3 maturity while motor units that do have on going denervation have more variability with these motor units also showing endplates with stage 1 and stage 4 maturity.

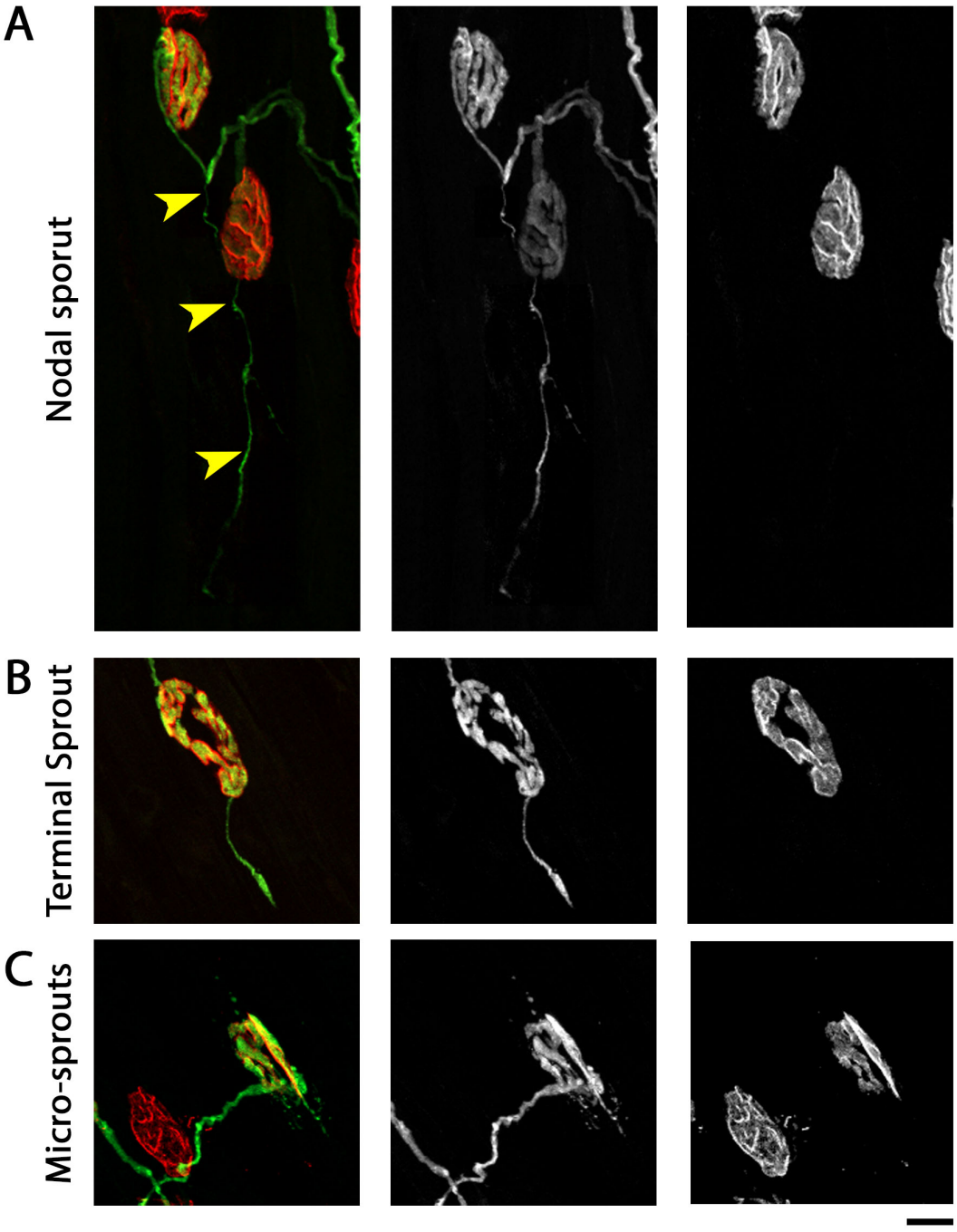

Figure 4.19: Sprouting can be observed in motor neurons expressing YFP. (**A**) Representative image of a nodal sprout extending from an axon (highlighted using yellow arrowheads placed along its length). (**B**) Representative image showing a terminal sprout extending from the pre-synaptic terminal of the NMJ. (**C**) Representative image showing micro-sprouting, a feature that has only been observed through YFP expression. Scale bar (for all images) = 10μm.

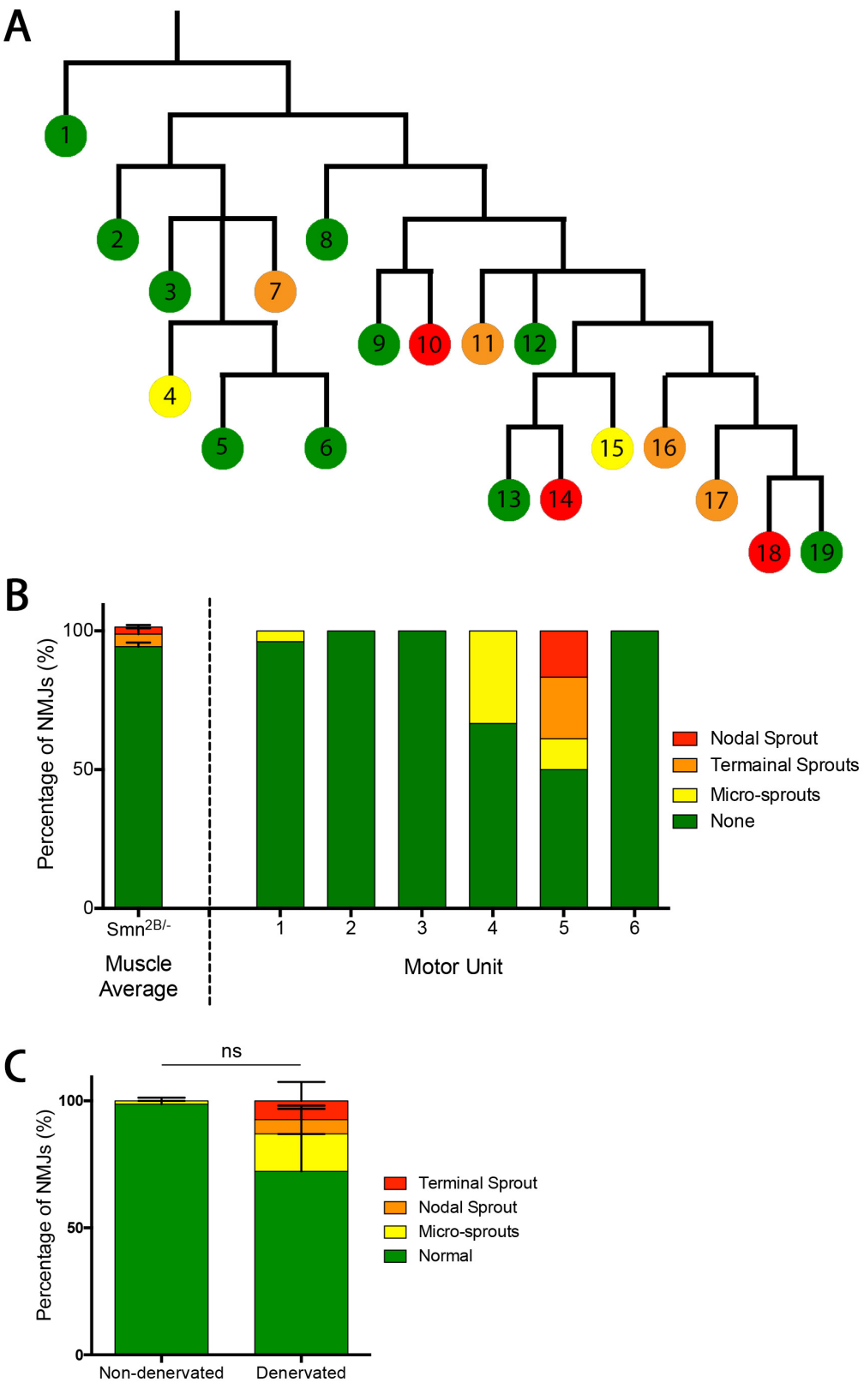
A
1
2
3
4
5
6
7
8
9
10
11
12
13
14
15
16
17
18
19
B
Percentage of NMJs (%)
100
50
0
Smn2B/-
Muscle Average
1
2
3
4
5
6
Motor Unit
Nodal Sprout
Termainal Sprouts
Micro-sprouts
None
C
ns
Percentage of NMJs (%)
100
50
0
Non-denervated
Denervated
Terminal Sprout
Nodal Sprout
Micro-sprouts
Normal

Figure 4.20: Sprouting appears to be motor neuron dependent in *Smn$^{2B/-}$;YFP-H* mice. (**A**) Example of a tree diagram showing sprouting at NMJs in motor unit 5. One of these tree diagrams was created for all 6 motor units analysed. By colour coding the different types of sprouts sprouting across the entire motor unit can be visualised. (**B**) Bar chart stacks the percentage NMJs that show either micro-, nodal or terminal sprouts in the 6 motor units assessed. There was sprouting apparent in 3 of the 6 motor units, however, this did not correlate with the 3 motor units that expressed denervation. At the left of the bar chart is the average percentage of nodal and terminal sprouting for the LALr in the *Smn$^{2B/-}$* mouse model. Note that this displays only nodal and terminal sprouting and not micro-sprouts. (**C**) When the percentage of micro-, nodal and terminal sprouts is collated for motor units displaying no denervation and denervation, there is no statistically significant difference between the two groups. However, there does appear to be a trend towards there being more sprouting in motor units displaying denervation. (ns>0.05 by Mann Whitney U test; n= 3 motor units)

4.3 Discussion

4.3.1 Overview of Results

In this chapter, the uses and limitations of *YFP-H,* for the purposes of this experiment, were defined. The original aim was to examine the morphology of individual motor units in differentially vulnerable muscles and various mouse models. These mouse models included the *Smn*$^{2B/-}$ mouse model of SMA, at the late symptomatic time point of P18, as well as mouse models that have reduced Smn but are asymptomatic, at a variety of time points ranging from 3 months to 1 year of age (Bowerman et al. 2012a; Simon et al. 2010). Therefore, YFP expression in differentially vulnerable muscles of the *Smn*$^{2B/-}$*;YFP-H* mouse model at P18 and the *Smn*$^{+/+}$*;YFP-H* mice, at 3 months, 6 months and 1 year of age was evaluated. This showed that YFP expression increases with age, with an increase in the percentage of YFP expressing muscle as well as an increase in the average number of YFP positive axons entering individual muscles. It was also found that YFP expression varied between different muscles as no YFP expression was observed within the TVA muscle at any age and there was variability in the expression pattern between the different cranial muscles. This increase in expression over time and variability between muscles is consistent with previous reports (Feng et al. 2000).

Furthermore, previous reports that YFP is not biologically inert were considered. The effect of YFP on motor units of the *Smn*$^{2B/-}$ mouse model of SMA was examined. Quantifying pathology at the NMJ in motor neurons that were YFP negative in the *Smn*$^{2B/-}$*;YFP-H* mouse model, and comparing this with pathology in *Smn*$^{2B/-}$ mice, showed that carrying the YFP-H transgene did not have an adverse effect on the motor unit. In addition, NMJ pathology in motor neurons that expressed YFP and in motor neurons that did not express YFP was compared. This showed that YFP expression within a

motor neuron had no adverse effect on the pathology that was observed. Moreover, motor neurons that are positive for YFP do not appear to be excessively stressed when compared to those that were negative for YFP expression in the spinal cord of *Smn$^{2B/-}$;YFP-H* mice, as evidenced by the lack of a significant change in pH2AX expression.

In this chapter, I subsequently investigated whether compensatory sprouting masks denervation in apparently resistant muscles and contributes to the observed phenomenon of differentially vulnerable muscles in the *Smn$^{2B/-}$* mouse model of SMA. By comparing NMJ morphology and sprouting in a muscle that displays vast denervation (TS) to a muscle that displays lower levels of denervation (LALr), in the *Smn$^{2B/-}$* mouse model of SMA, it was shown that, despite evidence of sprouting in both muscles, the level of sprouting observed could not account for the significant difference in denervation.

In addition, by tracing and analysing individual motor units in the LALr muscle of the *Smn$^{2B/-}$;YFP-H* mouse model, it was found that varying levels of pathology can occur within a single motor unit. Pathologically divergent subpopulations of motor neurons were not observed and therefore, it does not appear that apparently 'healthier' motor units are sprouting to mask the degeneration of other motor units.

4.3.2 Assessing YFP expression and its effects on the motor unit

The expression of *Thy1*, and as a result the expression of YFP, is reportedly developmentally regulated and increases with age (Feng et al. 2000; Porrero et al. 2010). The findings that are presented above support this, as it is shown that as mice age there is an increased incidence of muscles expressing YFP. For example, while no YFP positive axons were observed in the AS muscle at 3 and 6 months of age in *Smn$^{+/+}$;YFP-H* mice, 50% of AS muscles from 1 year old *Smn$^{+/+}$* mice were positive for YFP.

This finding may lead to the assumption that in order to increase the chance of obtaining muscles that are positive for YFP expression, for motor unit tracing, older mice should be used, wherever possible, for the collection of tissue. However, it was also found during this analysis that as age increases the average number of motor neurons expressing YFP in a single muscle also increases and determining what axons belong to which motor unit becomes increasingly difficult. Often, if there are two YFP positive motor neurons within the muscle, varying intensities of YFP expression within these motor neurons can allow them to be separated from each other (Murray et al. 2008). However, in the case of the AS muscle from 1 year old *Smn*$^{+/+}$ mice, in which there was an average of ~10 axons entering the muscle, it becomes impossible to trace a single motor neuron. I originally wished to examine motor units in older, asymptomatic mice however, the increase in the average number of YFP positive axons entering a muscle hindered the tracing of individual motor units at older time points.

In addition, differential expression of YFP within muscles of mice carrying the *YFP-H* transgene was observed. Within the cranial musculature, while the only evidence of YFP expression in the AS was in *Smn*$^{+/+}$;*YFP-H* mice at 1 year of age, there was evidence of YFP expression in the LALr muscle at all of the ages examined, including in P18 *Smn*$^{2B/-}$*;YFP-H* and *Smn*$^{2B/+}$*;YFP-H* mice. YFP was not observed within the abdominal TVA muscle of *YFP-H* mice at any of the ages assessed. This is in-keeping with findings from Thomson *et. al.* who excluded the TVA muscle from their analysis due to poor YFP expression in ~22 week old *YFP-H* mice (Thomson et al. 2012). YFP is reportedly expressed in a random subset of motor neurons in *YFP-H* mice however, these findings appear to suggest otherwise (Feng et al. 2000). Ideally, motor units would have been examined in a variety of differentially vulnerable muscles but due to the lack of expression within these differentially vulnerable muscles this was not possible. Despite being limited to the LALr muscle due to YFP expression, the lesser degree of pathology and denervation of the LALr muscle actually makes it ideal to perform motor

unit analysis. Muscles with vast denervation would have fewer motor units available and therefore be less informative when looking to determine the pattern of pathology within individual motor units.

As I wished to examine pathology within these YFP expressing motor units, the effects of the *YFP-H* transgene and its expression on the motor unit of the *Smn*$^{2B/-}$ mouse model of SMA were considered. The insertion site of the YFP transgene within the genome varies between the various YFP lines (Feng et al. 2000). This is due to the insertion site being completely random upon transfection of the embryo with the *Thy1-YFP* vector and this is thought to play a part in altering the expression pattern of the different YFP mouse lines (Feng et al. 2000). The insertion site of the transgene is often unknown however, it is known that sometimes this random insertion can disrupt other genes impacting on phenotype (Yong et al. 2015; Kolossovski 2017). As it had been reported that there was NFA in *YFP-H* and *YFP-16* mice, NFA was investigated in the *Smn*$^{2B/-}$*;YFP-H* mouse model. This investigation began by addressing whether simply carrying the *YFP-H* transgene affected NMJ pathology in the *Smn*$^{2B/-}$*;YFP-H* mouse model. To do so, a muscle that did not exhibit any YFP expression (TVA muscle) was used to exclude the possibility that the visible expression of YFP within the motor neuron causes increased abnormal NFA. This analysis showed that *Smn*$^{2B/-}$*;YFP-H* mice did not exhibit an increase in the severity of NFA compared to *Smn*$^{2B/-}$ mice. Therefore, it is believed that carrying the YFP transgene at its current insertion site does not adversely affect NFA at the pre-synaptic terminal in the *Smn*$^{2B/-}$ mouse model of SMA.

Whether foreign fluorescent proteins are biologically inert is debated topic. GFP, a well-known spectral variant of YFP, has been simultaneously expressed in various tissues within mouse models and has shown no toxic effects (Okabe et al. 1997). However, GFP has also been reported to increase apoptosis of cultures cells as well as increase the risk of cardiac defect in mice that express GFP exclusively within the heart (Huang et al.

2000). Similarly, YFP has been was thought to be biologically inert in *Thy1-YFP* mouse lines, displaying no morphological changes in synaptic structure, yet Comley *et. al.* report that YFP expression within the motor neuron leads to an increase in abnormal NFA at their pre-synaptic terminals (Feng et al. 2000; Comley et al. 2011). In this study, no increase in abnormal NFA was found in YFP expressing motor neurons of *Smn$^{2B/-}$;YFP-H* mice. In fact, there was a trend towards pre-synaptic terminals of YFP positive motor neurons displaying less severe NFA. These results may suggest that there is a slight reduction in NFA in YFP positive pre-synaptic terminals.

Comely *et. al.* also reported that YFP expression can increase cellular stress in motor neurons of these mouse models (Feng et al. 2000; Comley et al. 2011). In our study, there was no increase in the intensity of pH2AX staining in the cell bodies of YFP positive motor neurons compared to YFP negative motor neurons, in *Smn$^{2B/-}$;YFP-H* mice. As this protein is recruited to sites of DNA damage and DNA damage is a common feature of cellular stress, it does not appear that motor neurons expressing YFP in the *Smn$^{2B/-}$;YFP-H* mouse model at P18 are experiencing excess cellular stress (Fulda et al. 2010; Sharma et al. 2012). The lack of adverse effects from YFP expression in this analysis is likely due to a dose dependent effect of YFP (Comley et al. 2011). The *Smn$^{2B/-}$;YFP-H* mouse model has very low levels of YFP expression compared to that used by Comley *et. al.* and therefore, it is likely that YFP expression is below the threshold required for the onset of adverse effects.

4.3.3 Sprouting cannot account for the reduction in denervation observed in the LALr muscle of *Smn$^{2B/-}$* mouse model of SMA

In this chapter, I aimed to investigate whether neuronal sprouting is a phenotypic modifier in SMA. In patients of SMA, sprouting is thought to occur in those with milder forms of the disease but not in those with very severe SMA (Crawford & Pardo 1996). In mouse models, there are reported

differences in the quantity of terminal and nodal sprouting that is observed in muscles that are differentially vulnerable to degeneration (Murray et al. 2012). Therefore, the possibility that compensatory sprouting could be masking any ongoing denervation, resulting in these muscles displaying reduced levels of denervation, was addressed.

The findings presented in this thesis suggest that sprouting does not account for the differences in denervation observed in various muscle of the *Smn*$^{2B/-}$ mouse model of SMA. A significant difference in the severity of pathology was observed between the TS and the LALr muscles, with the more vulnerable TS muscle displaying an increase in both denervation and pre-synaptic swelling compared to the less vulnerable LALr muscle. However, despite rigorous quantification and analysis of sprouting in both of these muscles, there was no significant difference in the level of sprouting when they were compared. Therefore, it does not appear that increased sprouting is responsible for the reduction in denervation in the LALr.

The level of sprouting that was observed in the LALr muscle is similar to what has previously been reported (Murray et al. 2012). Murray *et. al.* also quantified sprouting in the TVA muscle and had suggested that sprouting correlated with the vulnerability of the muscle. Muscles with increased denervation showed increased terminal sprouting and decreased nodal sprouting while those with less denervation showed decreased terminal sprouts and increased nodal sprouts (Murray et al. 2012). However, the findings presented in this thesis do not support this correlation between the differential vulnerability of muscle and the sprouting that is observed within them. Here, the TS and LALr show differential vulnerability yet have similar levels of both terminal and nodal sprouting. There are a many possible reasons for the variation in findings, including the difference in age at which this analysis was performed.

Furthermore, in the LALr of *Smn*$^{2B/-}$*;YFP-H* mice, it did not appear that there were subpopulations of motor units compensating for the degeneration of others, as Schaefer *et. al.* had reported in their mouse model of ALS (Schaefer et al. 2005). Pathology was not restricted to only some motor neurons and rather it was variable within each motor unit. For example, motor neurons had NMJs that had no pre-synaptic swelling as well as NMJs that displayed very severe pre-synaptic swelling. Furthermore, sprouting did not appear to be regulated by the denervation status of the motor neuron. This may suggest that sprouting is a motor neuron dependent activity, as the muscle environment of these motor neurons is consistent yet the level of sprouting observed is not consistent across all motor units. It is known that following denervation muscles release proteins that are involved in initiating sprouting (English 2003). Perhaps upon denervation, motor neurons become more sensitised to these proteins and therefore sprouting is increased.

Based on this data it is not believed that sprouting is responsible for the decreased denervation observed in the LALr muscle. Another possible reason for the decreased denervation that was observed could be that there is an increase in synaptic stability at the NMJs of this muscle. Many factors and pathways contribute to the stability of the synapse, including ubiquitin homeostasis and mitochondrial energy metabolism (Gillingwater & Wishart 2013; Groen et al. 2018b). In motor neuron populations that are less vulnerable to degeneration, there is an increase in mitochondrial-related transcripts (Murray et al. 2015; Boyd & Gillingwater 2017). Increasing mitochondrial biogenesis in a zebrafish model of SMA had a beneficial effect on phenotype (Boyd & Gillingwater 2017). Furthermore, ubiquitination pathways are also implemented in SMA with a decrease in transcripts of ubiquitin-conjugating enzyme (Ube) observed in motor neuron populations that are vulnerable to degeneration (Murray et al. 2015). When the ubiquitin-like modifier activating enzyme (Uba1) was systemically increased in a mouse model of SMA, it caused a marked improvement in the phenotype (Powis et al. 2016). The altered regulation of these pathways between

differentially vulnerable motor neuron populations provides evidence that increased NMJ stability may contribute to the reduced denervation observed in some muscle groups (Murray et al. 2015; Boyd & Gillingwater 2017).

4.3.4 Conclusion

In this chapter, I have shown that the expression of YFP in *Smn*$^{+/+}$*;YFP-H* increases with age and shown that YFP expression varies between musculature. I subsequently discussed the limitations of this finding and how these impact on our uses for *YFP-H*. I found that carrying the YFP-H transgene and expressing YFP did not have an adverse effect on motor unit pathology in *Smn*$^{2B/-}$ mice. This is in contrast to previous reports addressing whether YFP is inert, and I conclude that this is due to the low dose of YFP within the *Smn*$^{2B/-}$*;YFP-H* mouse model.

Furthermore, by addressing motor neuron degeneration and sprouting in differentially vulnerable muscles I conclude that sprouting cannot account for the reduction in denervation in the LALr muscle of the *Smn*$^{2B/-}$ mouse model of SMA at P18, compared to the TS muscle. I also addressed how pathology occurs within individual motor units and provide some interesting data that may suggest that, in contrast to mouse model of ALS, there does not appear to be subpopulations of compensatory motor neurons in the *Smn*$^{2B/-}$ mouse model of SMA.

Chapter 5

Investigating motor units of mouse model that have reduced Smn but are asymptomatic

Summary

In this chapter, I wished to investigate compensatory sprouting in asymptomatic mouse models that have reduced Smn expression. MNCB loss and compensatory sprouting have previously been reported in the *Smn*$^{+/-}$ mouse model, which has 50% of normal Smn. However, in *Smn*$^{2B/2B}$ mice, which have a further reduction in Smn, to approximately 30% of normal levels, there is no reported loss of MNCBs and there has been no investigation into sprouting. Therefore, to clarify this paradoxical data and to investigate compensatory sprouting in mouse models that have reduced Smn but are asymptomatic, analysis of both degenerative and regenerative processes, including NMJ morphological analysis and MNCB counts, was performed in *Smn*$^{+/-}$ and *Smn*$^{2B/2B}$ mouse models.

The results that are detailed in the following chapter show that:

1. In contrast to reports in the literature, there is no significant loss of MNCBs in the thoracic spinal cord of *Smn*$^{+/-}$ mice
2. There is no significant degenerative or regenerative NMJ phenotype in *Smn*$^{+/-}$ mice
3. In keeping with previous findings, there is no significant loss of MNCBs in the thoracic spinal cord of *Smn*$^{2B/2B}$ mice
4. There is no significant degenerative or regenerative NMJ phenotype in *Smn*$^{2B/2B}$ mice

Although these results may appear to show no significant result, they in fact address the paradoxical data on MNCB loss in these asymptomatic mouse models with reduced Smn and suggest that there is no significant difference in the remodelling of the NMJ of these mouse models compared to controls.

5.1 Introduction

The *Smn*$^{+/-}$ mouse model expresses approximately 50% of normal levels of Smn protein yet it does not develop any symptoms and remains phenotypically normal throughout its life span (Simon et al. 2010). It does not display any defects in splicing, which is common in symptomatic SMA mouse models, and shows no reduction in gems within the nucleus of motor neurons (Jablonka et al. 2000). However, it has been reported that *Smn*$^{+/-}$ mice do display a reduction in MNCBs, although, the extent of this loss appears to vary with the reported literature (Jablonka et al. 2000; Simon et al. 2010; Bowerman et al. 2014; Udina et al. 2017). While one study reports a 54% loss of MNCBs at 1 year old, another reports a 19% loss at the same age compared to controls (Jablonka et al. 2000; Udina et al. 2017). Additionally, it has been reported that there is in fact no significant loss of MNCBs from this mouse model compared to controls at 1 year (Bowerman et al. 2014).

Simon *et. al.* reported that the lack of an abnormal motor phenotype in the *Smn*$^{+/-}$ mouse model despite the reduction in MNCB number, is due to increased axonal sprouting of motor neurons. They report that there is an increase in the average single motor unit action potential (SMUAP) as well as increased axonal branching within the gastrocnemius muscle in the *Smn*$^{+/-}$ mouse model when compared to *Smn*$^{+/+}$ mice. They also investigate the role of ciliary neurotrophic factor (CNTF), a neurotrophic factor released from Schwann cells in response to denervation, in sprouting within *Smn*$^{+/-}$ mice (English 2003; Simon et al. 2010). Simon *et. al.* show that knocking out CNTF in the *Smn*$^{+/-}$ mouse model has an adverse effect on the level of sprouting in the gastrocnemius muscle and the grip strength of this mouse model and as a result attribute the increased sprouting to CNTF (Simon et al. 2010). However, it has also been shown that knocking out CNTF in *Smn*$^{+/+}$ mice has an adverse effect on MNCB number and grip strength (Masu et al. 1993).

The *Smn*$^{2B/2B}$ mouse model has a further reduction in Smn protein expression when compared to *Smn*$^{+/-}$ mice. It has approximately 30% of normal Smn levels and, like *Smn*$^{+/-}$ mice, does not display any abnormal motor phenotype (Bowerman et al. 2012a). In contrast to *Smn*$^{+/-}$ mice, it has been reported that in the *Smn*$^{2B/2B}$ mouse model there is no reduction in MNCBs in the lumbar spinal cord, when compared to *Smn*$^{+/+}$ controls (Bowerman et al. 2012a). This is perhaps surprising due to the further reduction in Smn protein within this mouse model when compared to the *Smn*$^{+/-}$ mouse model.

However, the lack of MNCB loss in this mouse model does not necessarily mean that there cannot be ongoing remodeling, including withdrawal and sprouting, occurring at the level of the NMJ. It has been shown in this thesis, that these compartments of the motor neuron can be altered independently. This finding is corroborated by literature that reports that synapses can be regulated without cell body involvement (Bettini et al. 2007).

Therefore, I wished to not only clarify this paradoxical data regarding MNCB loss in *Smn*$^{+/-}$ and *Smn*$^{2B/2B}$ mice, but also investigate ongoing degeneration and regeneration within motor units of these mouse models to determine whether a reduction of Smn causes increased motor unit remodeling.

5.2 Results

5.2.1 There is no significant degenerative or regenerative phenotype in motor units of *Smn*$^{+/-}$ mice

I wished to confirm previous findings that there is a loss of MNCBs from the spinal cord, in 1 year old *Smn*$^{+/-}$ mice, and that subsequent compensatory sprouting is responsible for masking a phenotype (Simon et al. 2010). Therefore, the number of MNCB in the ventral horn of the spinal cord of 1 year old *Smn*$^{+/-}$ and *Smn*$^{+/+}$ mice was counted. Sections of spinal cord segments T8-T12 were stained for Nissl and with DAPI and, in every 10th section, the number of MNCBs within the ventral horn was counted. This analysis showed that there was no significant difference in the number of MNCBs between *Smn*$^{+/-}$ and *Smn*$^{+/+}$ mice at 1 year of age (Figure 5.1).

Despite a lack of alterations at the level of the MNCB, it is still possible that there is ongoing degeneration and regeneration at the level of the NMJ. Therefore, NMJ morphology within the *Smn*$^{+/-}$ mouse model was also analysed. Endplate occupancy, NFA and endplate area as well as nodal and terminal sprouting was quantified in the LALr muscle of 1 year old *Smn*$^{+/-}$ and *Smn*$^{+/+}$ control mice.

Denervation within the *Smn*$^{+/-}$ mouse model has previously been observed by Simon *et. al*., however no quantification data was provided in support of this observation (Simon et al. 2010). Quantification of denervation here found that there was no significant difference in the occupancy of post-synaptic endplates, with all endplates remaining fully occupied by the pre-synaptic terminal, in the LALr muscle of *Smn*$^{+/-}$ mice and *Smn*$^{+/+}$ controls at 1 year old (Figure 5.2 & 5.4A). This suggests that there is no denervation occurring within this mouse model with reduced SMN.

There was also no significant difference in the severity of pre-synaptic NFA or in the area of post-synaptic endplates in *Smn*$^{+/-}$ mice when compared to *Smn*$^{+/+}$ controls (Figure 5.2 & Figure 5.4). On average, 37% and 38% of NMJs for *Smn*$^{+/-}$*;YFP-H* and *Smn*$^{+/+}$*;YFP-H* mice, respectively, displayed 'mild' NFA and therefore NFA was not significantly different (Figure 5.4B). This data suggests that there is no evidence of NMJ pathology or denervation in the LALr muscle of *Smn*$^{+/-}$ mice compared to *Smn*$^{+/+}$ controls at 1 year old.

In order to investigate the possibility that spouting could be masking denervation, the occurrence of distinct types of sprouts was quantified. Terminal and nodal sprouting was quantified in the LALr of *Smn*$^{+/-}$ and *Smn*$^{+/+}$ mice at 1 year of age. There was no evidence of terminal or nodal sprouting in the LALr of *Smn*$^{+/-}$ and *Smn*$^{+/+}$ mice at 1 year old (Figure 5.4D). As previous results suggested that some types of sprouting were more readily visualised when labelled with YFP compared to NF, sprouting was also quantified using YFP positive motor neurons in the cranial musculature (including LAL, AS and AAL) of *Smn*$^{+/-}$;*YFP-H* mice and *Smn*$^{+/+}$;*YFP-H* mice (Figure 5.3 & Figure 5.4E). YFP expressing terminal, nodal and micro-sprouts were quantified. As before, terminal sprouts extend from a pre-synaptic terminal while nodal sprouts extend from an axon and appear thin, compared to other axonal branches (Figure 5.3). Micro-sprouts appear as a 'speckling' of YFP that extends from the pre-synaptic terminal and are not visible when staining for NF (Figure 5.3). Micro-sprouts were observed in both *Smn*$^{+/-}$;*YFP-H* mice and *Smn*$^{+/+}$;*YFP-H* mice and terminal and nodal sprouts in *Smn*$^{+/+}$;*YFP-H* mice. However, the occurrence was very low, with incidence ranging from 0 - 7% of NMJs displaying sprouts within the cranial musculature. Therefore, although evidence of sprouting was noted, the prevalence was not increased in *Smn*$^{+/-}$;*YFP-H* mice (Figure 5.3 & Figure 5.4E).

Overall, no significant pathology was observed in the LALr of 1 year old *Smn*$^{+/-}$ mice when compared to *Smn*$^{+/+}$ controls. There was also no significant increase in sprouting in the LALr of *Smn*$^{+/-}$ mice compared to *Smn*$^{+/+}$ mice. This is in contrast to reports by Simon *et. al.* that increased sprouting of motor neurons is responsible for a lack of an SMA phenotype (Simon et al. 2010). Rather, the results presented here suggest that there is no loss of MNCB and no significant difference in remodelling of the NMJ compared to controls.

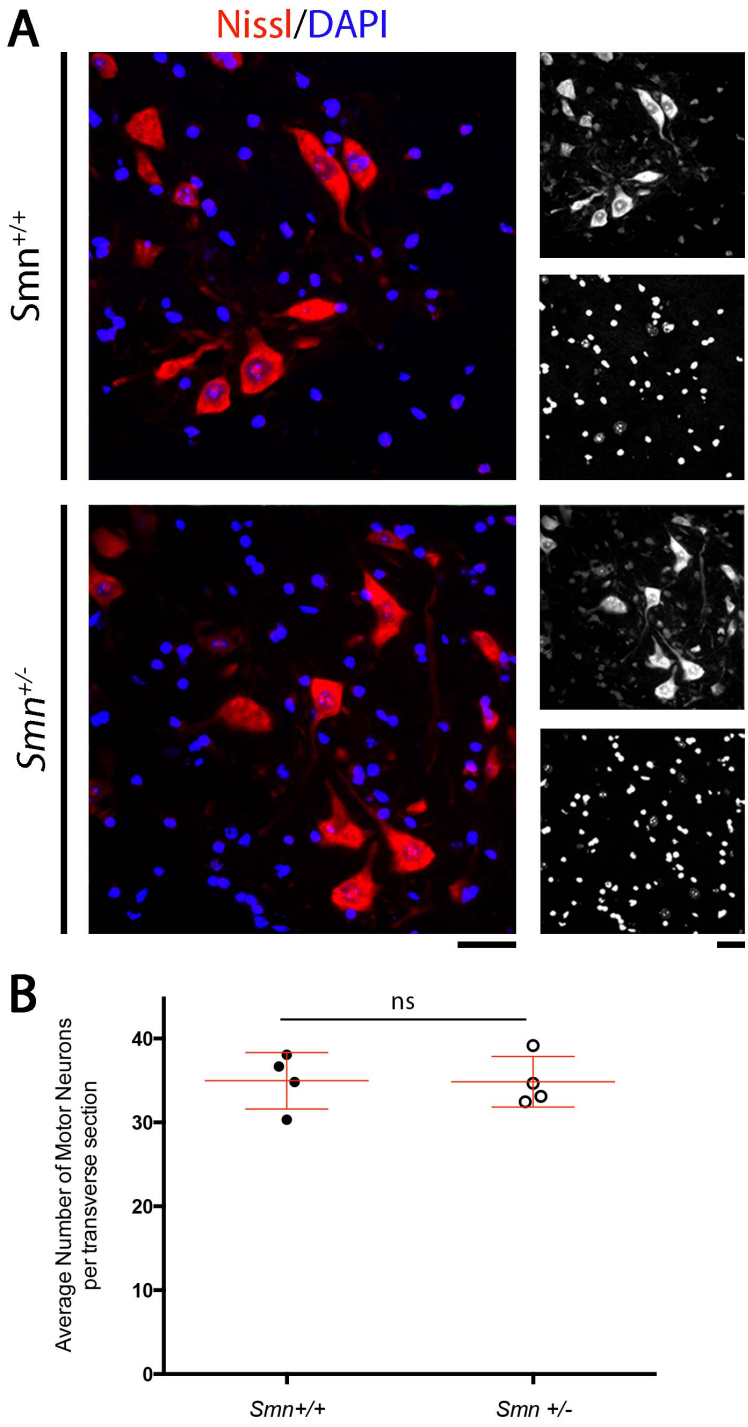

Figure 5.1: There is no significant difference in the number of MNCBs in *Smn*$^{+/-}$ mice compared to *Smn*$^{+/+}$ mice at 1 year old. (**A**) Representative images of MNCBs in the ventral horn of the spinal cord of 1 year old *Smn*$^{+/-}$ and *Smn*$^{+/+}$ mice. Greyscale images to the right show the separated channels; first and third images from the top are Nissl stained MNCBs and the second and forth images from the top are nuclei stained with DAPI. (Scale bar=30μm). (**B**) The graph (Mean ± SEM) shows that there is no significant difference in the average number of MNCBs per transverse section, in the ventral horns of the spinal cord of 1 year old *Smn*$^{+/-}$ and *Smn*$^{+/+}$ mice. (by Unpaired t-test, ns>0.05; n=4 mice per genotype)

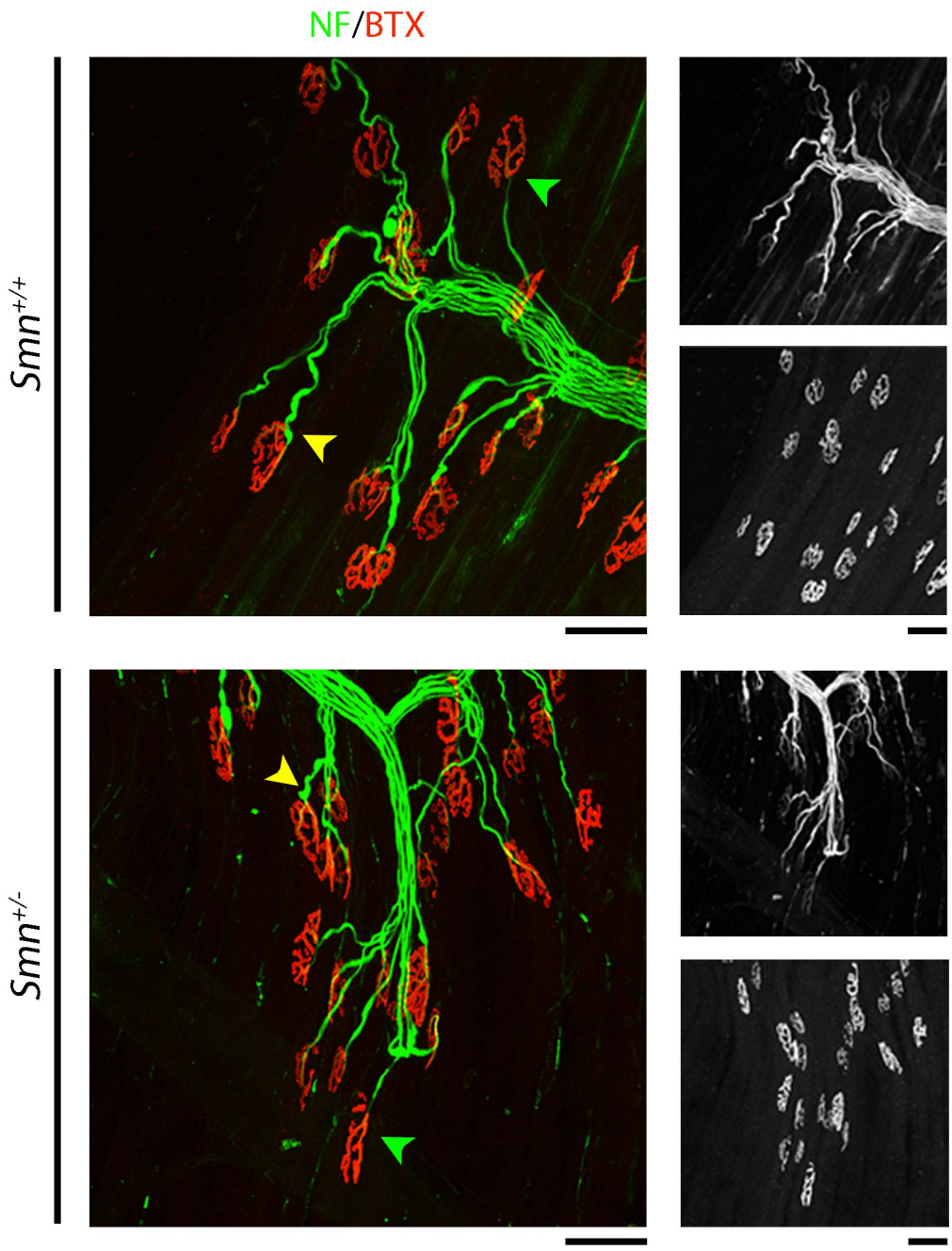

Figure 5.2: There is no significant degenerative or regenerative NMJ phenotype observed in *Smn*$^{+/-}$ mice at 1 year old. Images show NMJs from the LALr of 1 year old *Smn*$^{+/-}$ and *Smn*$^{+/+}$ mice. Note that there is no discernable difference between the two muscles in terms of degenerative or regenerative features. The arrowheads show examples of NMJs with no NFA (green) and mild NFA (yellow). Greyscale images to the right show the separated channels; axons (first and third image from the top) that were stained with NF and post-synaptic endplates (second and forth image from the top) that were stained with a fluorescent-conjugated bungarotoxin. (Scale bars = 10μm).

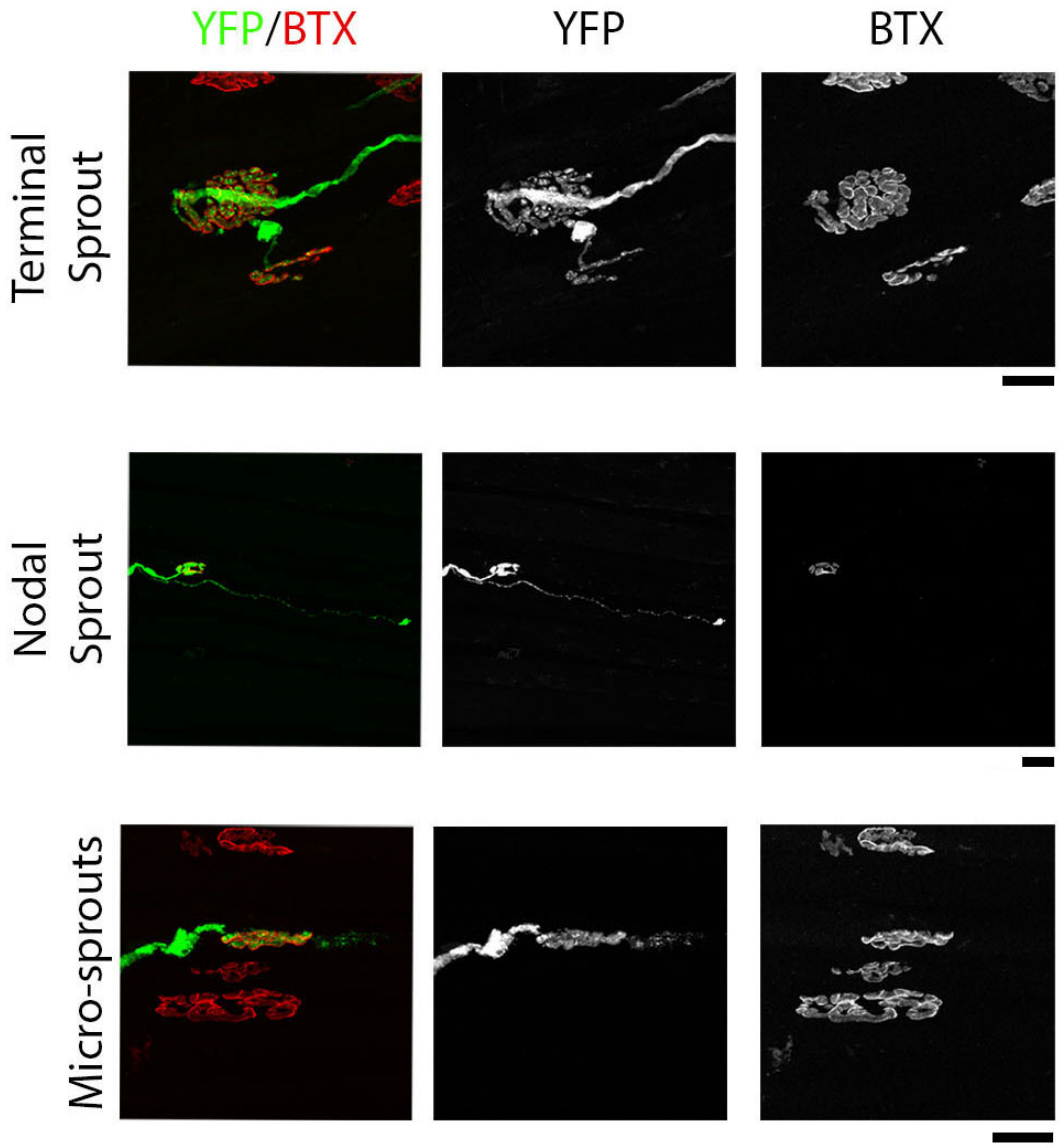

Figure 5.3: YFP positive NMJs of *Smn*$^{+/-}$ mice were examined for morphological alterations. Images show examples of features that were quantified using YFP. Pre-synaptic swelling: the pre-synaptic terminal appears to be swollen and obscuring the endplate. Terminal sprout: axon branched from the pre-synaptic terminal of a NMJ. Nodal sprout: branch extending from another axon. Micro-sprouts: A 'speckling' of YFP that extends from the pre-synaptic terminal. (Scale bars = 10μm).

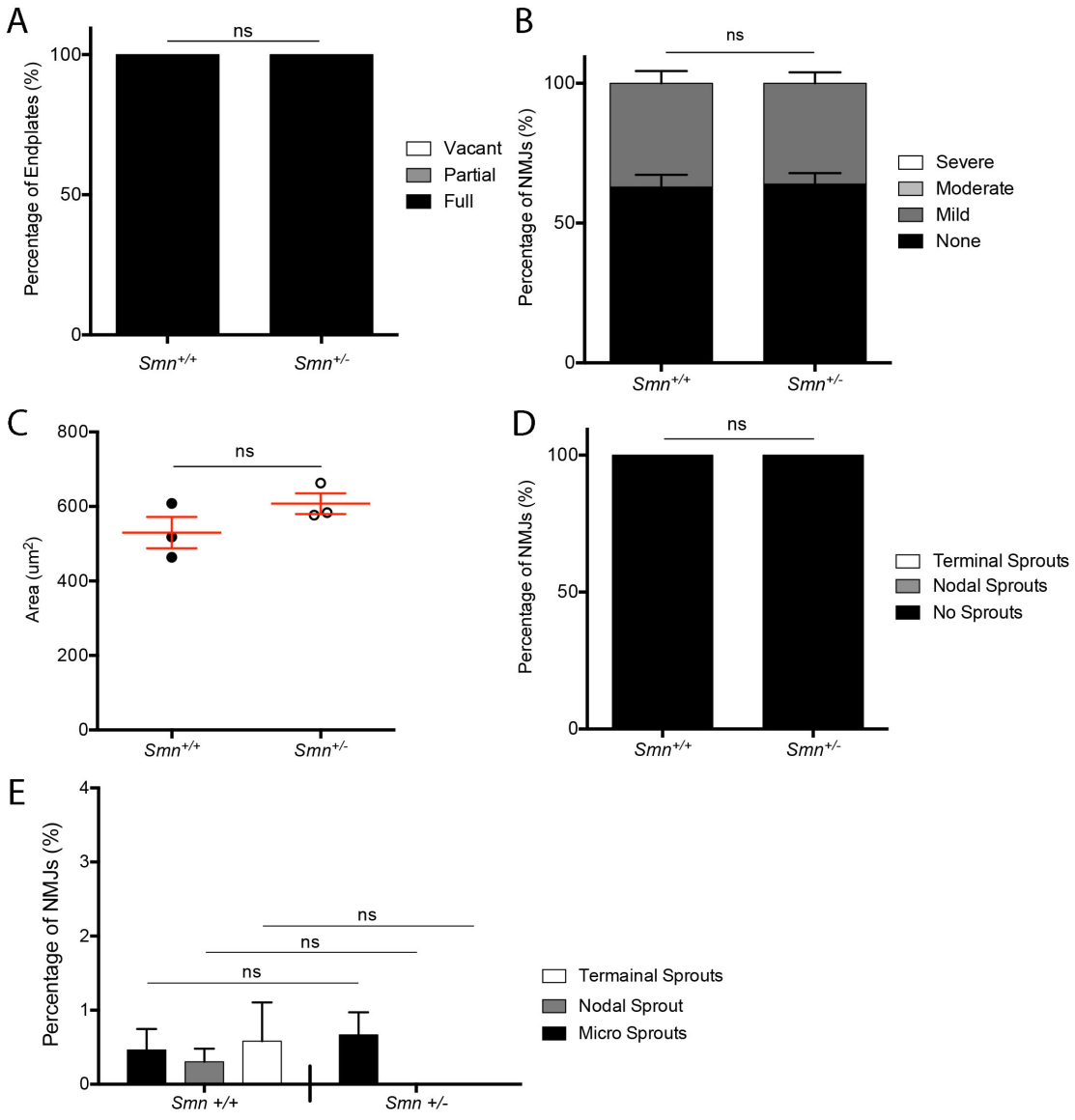
A
ns
100
50
0
Percentage of Endplates (%)
Vacant
Partial
Full
Smn+/+
Smn+/-
B
ns
100
50
0
Percentage of NMJs (%)
Severe
Moderate
Mild
None
Smn+/+
Smn+/-
C
800
600
400
200
0
Area (um2)
ns
Smn+/+
Smn+/-
D
ns
100
50
0
Percentage of NMJs (%)
Terminal Sprouts
Nodal Sprouts
No Sprouts
Smn+/+
Smn+/-
E
4
3
2
1
0
Percentage of NMJs (%)
ns
ns
ns
Termainal Sprouts
Nodal Sprout
Micro Sprouts
Smn +/+
Smn +/-

Figure 5.4: There is no significant degenerative or regenerative phenotype in the LALr muscle of *Smn*$^{+/-}$ mice at 1 year old compared to age matched *Smn*$^{+/+}$ controls. (**A**) The bar chart (Mean ± SEM) shows that there is no significant denervation present in in the LALr muscle of *Smn*$^{+/-}$ and *Smn*$^{+/+}$ mice at 1 year old as 100% of post-synaptic endplates were fully occupied (by Mann Whitney-U test; ns>0.05; n= 6 muscles per group). (**B**) The bar chart (Mean ± SEM) shows that there is no significant difference in pre-synaptic swelling between the LALr muscle of *Smn*$^{+/-}$ and *Smn*$^{+/+}$ mice at 1 year old. There is evidence of mild pre-synaptic swelling however this was consistent in *Smn*$^{+/-}$ and *Smn*$^{+/+}$ mice (by Mann Whitney-U test; ns>0.05; n= 6 muscles per group). (**C**) The bar chart (Mean ± SEM) shows that there is no significant difference in the area of endplates in *Smn*$^{+/-}$ mice compared to *Smn*$^{+/+}$ mice at 1 year old (by Unpaired t-test, ns>0.05; n=3 mice per group). (**D**) The bar chart (Mean ± SEM) shows that there was no significant sprouting observed in the LALr muscle of *Smn*$^{+/-}$ when compared to *Smn*$^{+/+}$ mice at 1 year old. All NMJs in both *Smn*$^{+/-}$ and *Smn*$^{+/+}$ mice showed no evidence of sprouts associated with them (by Mann Whitney-U test, ns>0.05; n=6 muscles per group). (**E**) The bar chart (Mean ± SEM) shows that in 1 year old *Smn*$^{+/}$*;YFP-H*$^{-}$ and *Smn*$^{+/+}$*;YFP-H* mice micro-sprouts, nodal sprouts and terminal sprouts were observed as well as pre-synaptic swelling in YFP positive motor neurons in the cranial musculature. However, there was no significant difference in swelling, nodal, terminal and micro- sprouts in *Smn*$^{+/-}$*;YFP-H* when compared to *Smn*$^{+/+}$*;YFP-H* mice (by Mann Whitney-U test; ns>0.05; n=5 mice per genotype). Note the small scale on the graphs meaning that these features are present in very small quantities.

5.2.2 There is no significant degenerative or regenerative phenotype in motor units of Smn$^{2B/2B}$ mice

The *Smn*$^{2B/2B}$ mouse model has a 70% reduction in Smn but, as with the *Smn*$^{+/-}$ mouse model, is asymptomatic (Bowerman et al. 2012a). No sprouting analysis has, to our knowledge, been performed in this mouse model and therefore the impact of a further reduction in Smn on this process has not been determined. However, due to the paradoxical reports that, despite a further reduction in Smn, this mouse does not display MNCB loss I wished to confirm this finding and further investigate motor unit pathology within this mouse model.

Pilot data suggested that there was a subtle change in the area of the post-synaptic endplates of 3 month old *Smn*$^{2B/2B}$ mice compared to *Smn*$^{+/+}$ control mice. As a result, analysis was carried out in *Smn*$^{2B/2B}$ mice at 3 months of age.

The number of MNCBs within the ventral horn of the spinal cord was investigated. The number of MNCB in segments T8-T12 of 3 month old *Smn*$^{2B/2B}$ mice was counted and compared to age matched *Smn*$^{+/+}$ mice. Spinal cord sections were stained for Nissl and with DAPI. In keeping with findings from Bowerman *et. al.*, it was found that there was no significant difference in the number of MNCBs between *Smn*$^{2B/2B}$ and *Smn*$^{+/+}$ mice at 3 months of age (Bowerman et al. 2012a).

Again, no loss of MNCBs may not necessarily mean that there is no ongoing remodelling at the NMJ. Therefore, morphology of NMJs within the *Smn*$^{2B/2B}$ mouse model was analysed. As before, endplate occupancy, pre-synaptic swelling and endplate area as well as nodal and terminal sprouting were quantified. To increase the scope of this study, the NMJs of both the LALr and the TS muscles of *Smn*$^{2B/2B}$ and *Smn*$^{+/+}$ mice were analysed, as they both show varying levels of denervation in the *Smn*$^{2B/-}$ mouse model of SMA (Figure 5.5).

In the LALr muscle, there was no significant difference in endplate occupancy between *Smn*$^{2B/2B}$ and *Smn*$^{+/+}$ mice, with all endplates fully occupied (Figure 5.6 & 5.7A). Pre-synaptic swelling was observed in both *Smn*$^{2B/2B}$ and *Smn*$^{+/+}$ with 23% and 25% of NMJs displaying mild pre-synaptic swelling respectively, however this was not significantly different (Figure 5.7B). There was also no significant difference in post-synaptic endplate size in the LALr of *Smn*$^{2B/2B}$ mice when compared to *Smn*$^{+/+}$ mice (Figure 5.7C). This data suggests that there is no evidence of NMJ pathology or denervation in the LALr muscle of *Smn*$^{2B/2B}$ mice compared to *Smn*$^{+/+}$ controls at 3 months old.

In addition, no evidence of terminal or nodal sprouting was found in the LALr of *Smn*$^{2B/2B}$ mice at 3 months of age (Figure 5.7D). Sprouting was also examined in *Smn*$^{2B/2B}$*;YFP-H* mice, using the same criteria detailed for analysis in the LALr of *Smn*$^{+/-}$;*YFP-H* mice, to ensure some types of sprouts that are more readily visible when labelled with YFP compared to NF were not overseen. Terminal, nodal and micro- sprouting in the cranial musculature (including LAL, AS and AAL) of 3 month old *Smn*$^{2B/2B}$;*YFP-H* and *Smn*$^{+/+}$;*YFP-H* mice was quantified. No terminal or nodal sprouting was observed in either *Smn*$^{2B/2B}$;*YFP-H* or *Smn*$^{+/+}$;*YFP-H* mice. Micro-sprouting was observed in *Smn*$^{2B/2B}$;*YFP-H* mice however, the occurrence of this was very low, with incidence ranging from 0 – 9% of NMJs exhibiting sprouts within the cranial musculature, which was not significantly different to controls (Figure 5.7E).

In the TS muscle, there was also no significant difference in endplate occupancy in *Smn*$^{2B/2B}$ mice when compared to *Smn*$^{+/+}$, with all endplates fully occupied (Figure 5.6 & 5.8A). Again, pre-synaptic swelling was noted in the TS muscle of both *Smn*$^{2B/2B}$ and *Smn*$^{+/+}$ mice, with 23% and 24% displaying mild pre-synaptic swelling respectively, but this was not significantly different (Figure 5.8B). There was also no significant difference in post-synaptic endplate size in the TS of *Smn*$^{2B/2B}$ mice when compared to *Smn*$^{+/+}$ mice (Figure 5.8C). This data suggests that there is no evidence of NMJ pathology or denervation in the TS muscle of *Smn*$^{2B/2B}$ mice compared to *Smn*$^{+/+}$ controls at 3 months old.

In terms of sprouting, there was no evidence of terminal or nodal sprouting in the TS muscle of *Smn*$^{2B/2B}$ and *Smn*$^{+/+}$ mice, and as a result there was no significant difference between *Smn*$^{2B/2B}$ and *Smn*$^{+/+}$ mice (Figure 5.8D).

Despite the suggestion from preliminary data that there may be morphological alterations at the NMJ of *Smn*$^{2B/2B}$ mice at 3 months, the in-

depth study of NMJ morphology, in two different muscles of *Smn*$^{2B/2B}$ mice, revealed no increase in degeneration or regeneration, when compared to *Smn*$^{+/+}$ mice. There was also no difference in the number of MNCBs in *Smn*$^{2B/2B}$ mice compared to *Smn*$^{+/+}$ controls. As with *Smn*$^{+/-}$ mice it is still possible that ongoing denervation is being masked by sprouting, however based on the lack of significant sprouting observed within both the LALr and TS of *Smn*$^{2B/2B}$ mice it is not believed that the asymptomatic phenotype of this mouse model is due to increased sprouting.

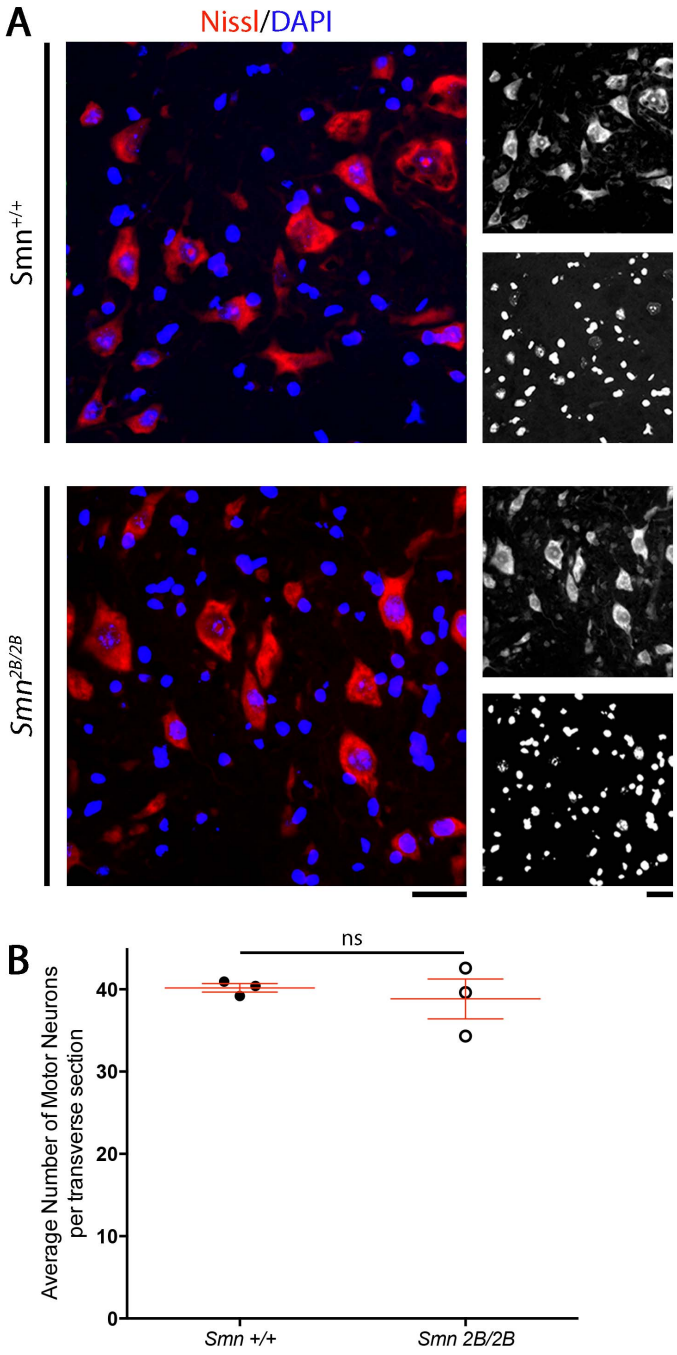

Figure 5.5: There is no significant difference in the number of MNCBs in *Smn*$^{2B/2B}$ mice compared to *Smn*$^{+/+}$ mice at 3 months old. (**A**) Representative images of MNCBs in the ventral horn of the spinal cord of 3 month old *Smn*$^{2B/2B}$ and *Smn*$^{+/+}$ mice. Greyscale images to the right show the separated channels; first and third images from the top are Nissl stained MNCBs and the second and forth images from the top are nuclei stained with DAPI. (Scale bar =30μm). (**B**) The graph (Mean ± SEM) shows that there is no significant the average number of MNCBs per transverse section, in the ventral horns of the spinal cord of 3 month old *Smn*$^{2B/2B}$ and *Smn*$^{+/+}$ mice by Unpaired t-test, ns>0.05; n=3 mice per genotype). *Data acquired in collaboration with Roxanna Munir (MScR student).*

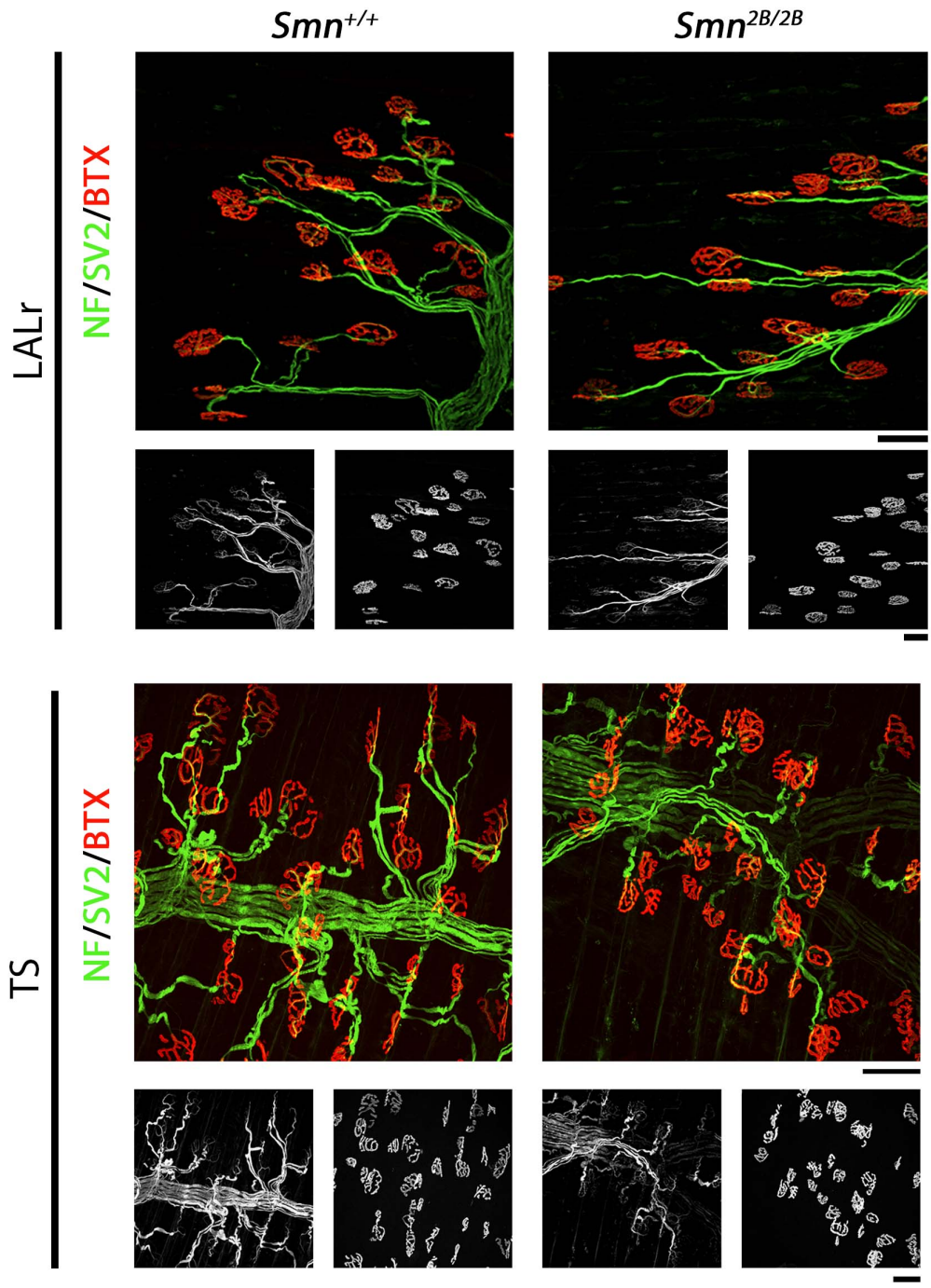

Figure 5.6: There is no significant degenerative or regenerative NMJ phenotype observed in *Smn*$^{2B/2B}$ mice. Images show NMJs from the LALr and TS of 3 month old *Smn*$^{2B/2B}$ mice. Note that there is no difference between the two muscles in terms of degenerative or regenerative features. Greyscale images show the separated channels; bottom left of each image shows axons stained for NF/SV2 and bottom right of each image shows post-synaptic endplates stained with BTX. (Scale bar = 10μm).

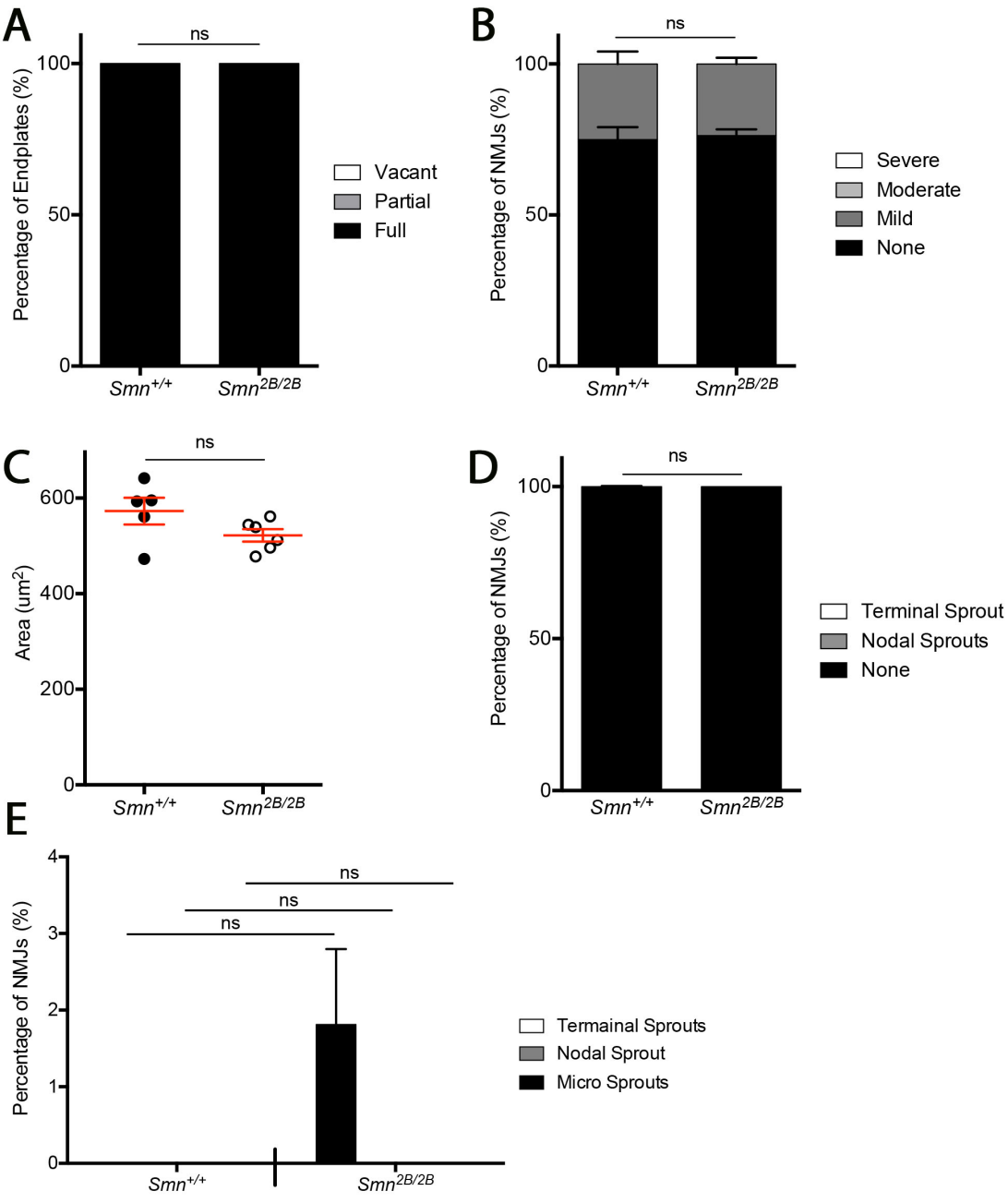
A
ns
Percentage of Endplates (%)
100
50
0
Vacant
Partial
Full
Smn+/+
Smn2B/2B
B
ns
Percentage of NMJs (%)
100
50
0
Severe
Moderate
Mild
None
Smn+/+
Smn2B/2B
C
ns
Area (um2)
600
400
200
0
Smn+/+
Smn2B/2B
D
ns
Percentage of NMJs (%)
100
50
0
Terminal Sprout
Nodal Sprouts
None
Smn+/+
Smn2B/2B
E
ns
ns
ns
Percentage of NMJs (%)
4
3
2
1
0
Termainal Sprouts
Nodal Sprout
Micro Sprouts
Smn+/+
Smn2B/2B

Figure 5.7: There is no significant degenerative or regenerative phenotype in the LALr muscle of *Smn*$^{2B/2B}$ mice at 3 months old compared to age matched *Smn*$^{+/+}$ controls. (**A**) The bar chart (Mean ± SEM) shows that there is no significant denervation present in in the LALr muscle of *Smn*$^{2B/2B}$ and *Smn*$^{+/+}$ mice at 3 months old as 100% of post-synaptic endplates were fully occupied (by Mann Whitney-U test; ns>0.05; n= 6 muscles per group). (**B**) The bar chart (Mean ± SEM) shows that there is no significant difference in pre-synaptic swelling between the LALr muscle of *Smn*$^{2B/2B}$ and *Smn*$^{+/+}$ mice at 3 months old. There is evidence of mild pre-synaptic swelling however this was consistent in *Smn*$^{2B/2B}$ and *Smn*$^{+/+}$ mice (by Mann Whitney-U test; ns>0.05; n= 6 muscles per group). (**C**) The graph (Mean ± SEM) shows that there is no significant difference in the area of endplates in *Smn*$^{2B/2B}$ mice compared to *Smn*$^{+/+}$ mice at 3 months old (by Unpaired t-test, ns>0.05; n=6 muscles per group). (**D**) The bar chart (Mean ± SEM) shows that the bar chart shows that there was no significant sprouting observed in the LALr muscle of *Smn*$^{2B/2B}$ when compared to *Smn*$^{+/+}$ mice at 3 months old. All NMJs in both *Smn*$^{2B/2B}$ and *Smn*$^{+/+}$ mice showed no evidence of sprouts associated with them (by Mann Whitney-U test, ns>0.05; n=6 muscles per group). (**E**) The bar chart (Mean ± SEM) shows that there was no significant difference in the percentage of nodal, terminal or micro- sprouts in 3 month old *Smn*$^{2B/2B}$*;YFP-H* mice when compared to *Smn*$^{+/+}$*;YFP-H* mice. Micro-sprouting was observed in YFP positive motor neurons in the cranial musculature however, this was not significant when compared to *Smn*$^{+/+}$*;YFP-H* mice (by Mann Whitney-U test; ns>0.05; n=5 muscles per genotype). Note the small scale on the graphs meaning that these features are present in very small quantities.

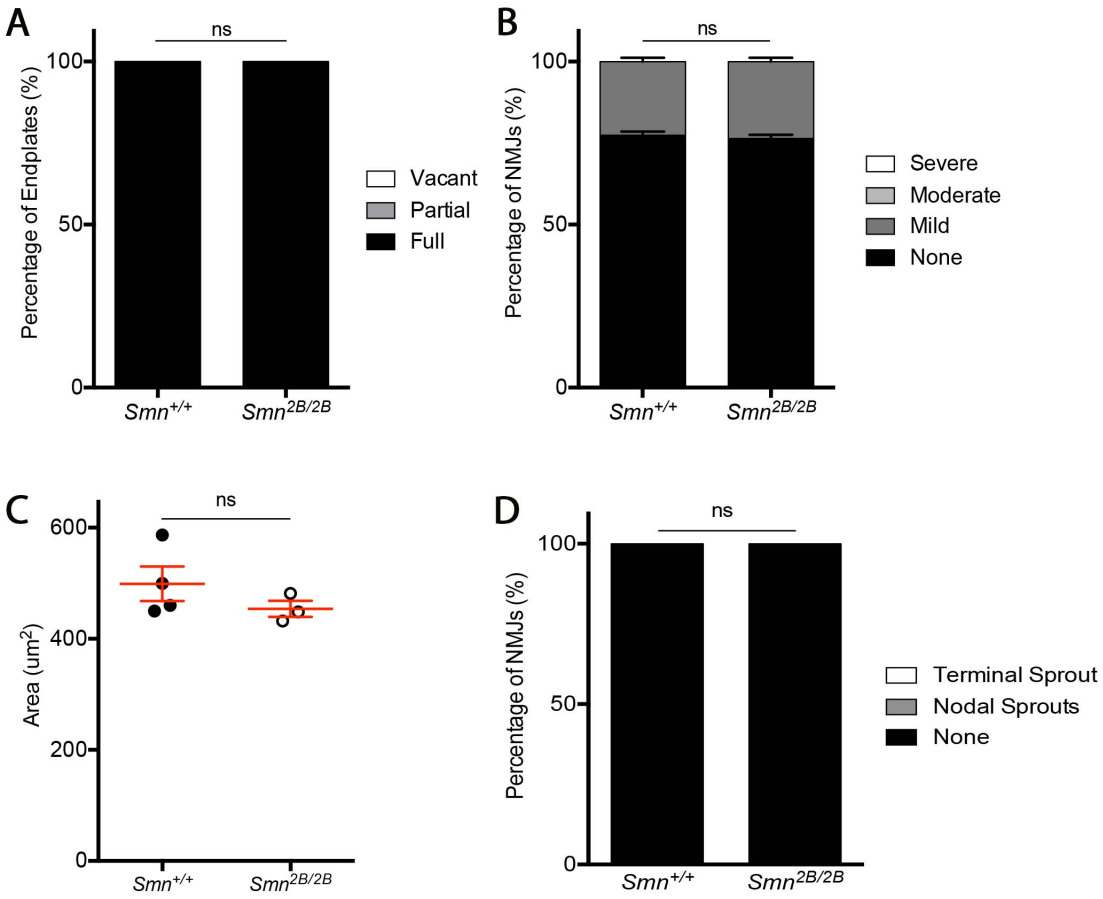

Figure 5.8: There is no significant degenerative or regenerative phenotype in the TS muscle of *Smn*$^{2B/2B}$ mice at 3 months old compared to age matched *Smn*$^{+/+}$ controls. (**A**) The bar chart (Mean ± SEM) shows that there is no significant denervation present in in the TS muscle of *Smn*$^{2B/2B}$ and *Smn*$^{+/+}$ mice at 3 months old as 100% of post-synaptic endplates were fully occupied (by Mann Whitney-U test; ns>0.05; =3 (*Smn*$^{2B/2B}$) or 4 (*Smn*$^{+/+}$) mice per group). (**B**) The bar chart (Mean ± SEM) shows that there is no significant difference in pre-synaptic swelling in the TS muscle of *Smn*$^{2B/2B}$ compared to *Smn*$^{+/+}$ mice at 3 months old. There is evidence of mild pre-synaptic swelling however this was consistent in *Smn*$^{2B/2B}$ and *Smn*$^{+/+}$ mice (by Mann Whitney-U test; ns>0.05; =3 (*Smn*$^{2B/2B}$) or 4 (*Smn*$^{+/+}$) mice per group). (**C**) The graph (Mean ± SEM) shows that there is no significant difference in the area of endplates in the TS of *Smn*$^{2B/2B}$ mice compared to the TS of *Smn*$^{+/+}$ mice at 3 months old (by Unpaired t-test, ns>0.05; n=3 (*Smn*$^{2B/2B}$) or 4 (*Smn*$^{+/+}$) mice per group). (**D**) The bar chart (Mean ± SEM) shows that there was no significant sprouting observed in the TS muscle of *Smn*$^{2B/2B}$ when compared to *Smn*$^{+/+}$ mice at 3 months old. All NMJs in both *Smn*$^{2B/2B}$ and *Smn*$^{+/+}$ mice showed no evidence of sprouts associated with them (by Mann Whitney-U test, ns>0.05; n=3 (*Smn*$^{2B/2B}$) or 4 (*Smn*$^{+/+}$) mice per group). *Data acquired in collaboration with Roxanna Munir (MScR student).*

5.3 Discussion

5.3.1 Overview of Results

In this chapter, I investigated MNCB number and NMJ remodeling in asymptomatic mouse models that have reduced Smn levels. In contrast to previous reports there was no evidence of MNCB loss, denervation or sprouting in the *Smn*$^{+/-}$ mouse model, which has 50% of normal Smn (Jablonka et al. 2000; Simon et al. 2010; Udina et al. 2017). However, it is in keeping with another report that also found no significant loss of MNCBs in the *Smn*$^{+/-}$ mouse model (Bowerman et al. 2014).

In *Smn*$^{2B/2B}$ mice, which have a further reduction in Smn levels to approximately 30% of normal, there is no reported loss of MNCBs and there has been no investigation into sprouting (Bowerman et al. 2012a). In keeping with these reports, I found that there was also no loss of MNCBs in the *Smn*$^{2B/2B}$ mouse model (Bowerman et al. 2012a). Degeneration and regeneration at the NMJ was also investigated in two different muscles, which show varying levels of degeneration in a symptomatic SMA mouse model, and found that neither of these muscles displayed evidence of degeneration or sprouting.

5.3.2 Smn levels in asymptomatic mouse models are above the required threshold

As there was no obvious degeneration or on going sprouting in both the *Smn*$^{+/-}$ and *Smn*$^{2B/2B}$ mouse model that have reduced Smn but are asymptomatic it is possible that the Smn levels in these mouse models are adequate to sustain motor neuron survival. This is in keeping with the theory that there is a tissue-dependent threshold requirement for Smn protein (Sleigh et al. 2011). This theory suggests that some tissues, specifically

motor neurons, may have a higher requirement for Smn than other tissues and as a result are more sensitive to changes in the expression of SMN. Other tissues, that have a lower requirement for Smn protein, are able to sustain survival when there is a reduction of this protein (Sleigh et al. 2011). This theory is supported by recent findings that show that different tissues have different levels of Smn (Groen et al. 2018a). Interestingly, the brain and spinal cord had the greatest levels of Smn in *Smn*$^{2B/+}$ control mice at P15, therefore presenting a reason for the increased susceptibility of neuronal tissue when the expression of SMN is reduced (Groen et al. 2018a).

Furthermore, this theory of a tissue-specific threshold requirement for SMN is supported by observations from SMA patients. While those with type I SMA, who have very low levels of SMN protein, have an increased susceptibility to heart defects, those with types II, II and IV SMA, who have increased SMN levels, are no more likely to develop heart defects than the general population (Shababi et al. 2014; Deguise et al. 2016). This suggests that only when SMN is very low, do cardiac tissue becomes more susceptible.

It may also be possible that, due to the known differential vulnerability of motor neurons in symptomatic SMA mouse models, that some motor neurons require more Smn that others (Murray et al. 2008). Therefore, it cannot be ruled out that while the LALr muscle in 1 year old *Smn*$^{+/-}$ mice does not show degeneration and sprouting, that the muscles examined by others in the literature, do experience these morphological changes.

However, in the *Smn*$^{2B/2B}$ mouse model, two different muscles, which show differential vulnerability in the symptomatic *Smn*$^{2B/-}$ mouse model (refer to Section 4.2.2), were assessed. Both of these muscles showed no significant alterations in NMJ morphology. It could be argued that morphological changes may occur in this mouse model at a later time point to that examined in this study. However, these results are consistent with findings from Bowerman *et. al.*, who found no significant alterations in MNCB number

or NMJ morphology in this mouse model at 8 months and 1 year of age (Bowerman et al. 2012a).

Furthermore, an adjacent study from our lab has assessed the level of proteins involved in sprouting, including CNTF and IGF2 in the RA muscle of *Smn*$^{2B/2B}$ and *Smn*$^{+/-}$ mice (Munir 2017). When compared to age-matched *Smn*$^{+/+}$ controls, this quantification showed no significant change in the level of CNTF and IGF2 in the RA muscle of 3 month old *Smn*$^{2B/2B}$ as well as 6 month and 1 year old *Smn*$^{+/-}$ mice (Munir 2017). Since elevated levels of CNTF and IGF2 are associated within increased sprouting, this finding suggests that sprouting is not increased in the RA muscle of *Smn*$^{+/-}$ compared to *Smn*$^{+/+}$ mice (English 2003; Simon et al. 2010).

Moreover, this also supports the findings that show no significant loss of MNCBs in the thoracic region of the spinal cord, and suggests that there is a lack of motor neuron degeneration in these mouse models with reduced Smn. Interestingly, it is noted that over time the percentage loss of MNCBs that has been published appears to decrease. While the first report saw a 54% loss of MNCBs subsequent reports saw a 40% and a 19% loss of MNCB from the lumbosacral region of the spinal cord (Jablonka et al. 2000; Simon et al. 2010; Udina et al. 2017). This has been highlighted in order to advise those who wish to use this mouse model as a mild model of SMA to perform appropriate investigation into the defects that their mouse exhibits, prior to pursuing further research interests.

5.3.3 Conclusions

These findings from *Smn*$^{2B/2B}$ and *Smn*$^{+/-}$ mice suggest that there is no on-going motor neuron loss that is being masked by compensatory sprouting. Based on these results, I believe that these mouse models have an appropriate level of Smn to sustain motor neuron survival and remain asymptomatic.

Chapter 6

General Discussion and Conclusions

6.1 Overview of results

At the beginning of this thesis I detailed three main aims and subsequently presented the work that was carried out in order to address those aims.

The first aim investigated the timing of motor neuron pathology in the *Smn*$^{2B/-}$ mouse model of SMA. I performed a temporal analysis of NMJ and MNCB pathology in the *Smn*$^{2B/-}$ mouse model, to determine the relationship between the pathological hallmarks of motor neurons in SMA. I found that, in the *Smn*$^{2B/-}$ mouse model of SMA, the onset of NMJ pathology coincides with the onset of phenotypic symptoms and precedes a decrease in the number and area of MNCBs. This analysis has clarified an important issue in the SMA research field by confirming that motor neuron degeneration in SMA occurs in a distal to proximal manner.

Furthermore, I showed that the onset of NMJ pathology coincides with the up-regulation of transcripts involved in the P53 signalling pathway in the spinal cords of *Smn*$^{2B/-}$ mice. By reducing the expression of P53 in the *Smn*$^{2B/-}$ mouse model of SMA I found that although this does not improve the overall phenotype of the mouse model or decrease the loss of MNCBs, it does result in a decrease in the level of denervation observed at the level of the NMJ. This implies that P53 plays a role in synaptic withdrawal in this mouse model of SMA.

The second aim in this thesis investigated whether there are compensatory subpopulations of motor neurons in the *Smn*$^{2B/-}$ mouse model that are responsible for masking degeneration in muscles that are less vulnerable to

degeneration and contributing to the observed phenomenon of differentially vulnerable muscles. By comparing NMJ morphology and sprouting in a muscle that displays vast denervation (TS) to a muscle that displays lower levels of denervation (LALr), in the *Smn*$^{2B/-}$ mouse model of SMA, I found that, despite evidence of sprouting in both muscles, the level of sprouting observed could not account for the significant difference in denervation. I also found that in the LALr there are not pathologically divergent subpopulations of motor neurons and therefore, it does not appear that apparently 'healthier' motor units are sprouting to mask the degeneration of other motor units in this mouse model.

The third aim investigated MNCB number and NMJ remodeling in asymptomatic mouse models that have reduced Smn levels. I found no evidence of MNCB loss, denervation or sprouting in *Smn*$^{+/-}$ and *Smn*$^{2B/2B}$ mice, which express only 50% and 30% of normal SMN protein levels respectively. This suggests that there is no on-going motor neuron loss that is being masked by compensatory sprouting. Based on these results, I believe that these mouse models have an appropriate level of Smn to sustain motor neuron survival and remain asymptomatic.

6.2 Importance of findings

Therapeutics are currently at the forefront of SMA research. The approval of Spinraza as the first treatment for SMA was a huge milestone however, work is still required to improve its efficacy (Shorrock et al. 2018). It is believed, based on research in mouse models, that Spinraza must be administered early, preferably pre-symptomatically, to improve its effectiveness (Lutz et al. 2011; Robbins et al. 2014). Clinical trials are currently underway to determine the effects of early intervention with Spinraza in patients (Hwu et al. 2017). However, it is also hypothesised that the efficacy of Spinraza may be increased through the use of combinational therapies that are SMN-independent (Bowerman et al. 2017). A variety of targets that are known to

be phenotypic modifiers have now been identified. For example, targeting the RhoA-ROCK pathway, which can regulate actin dynamics, in the *Smn*$^{2B/-}$ mouse model of SMA was shown to improve muscle pathology and increased lifespan (Bowerman et al. 2010; Bowerman, et al. 2012b). Furthermore, systemically increasing Uba1, which is known to be decreased in SMA mouse models, using gene therapy techniques increased the survival and improved the NMJ phenotype of the Taiwanese mouse model (Powis & Gillingwater 2016). It is thought that targeting these pathways in combination with Spinraza may increase the therapeutic benefits to patients (Shorrock et al. 2018).

In this thesis, the effects of P53 reduction on the motor unit were addressed. A natural question to ask would be whether P53 could be a potential target for combinational therapies. Since the long-term inhibition of P53 can lead to the formation of tumors it may be an unlikely target for combinational therapy in patients (Donehower 1996). However, as the results presented in this thesis implicate P53 in synaptic withdrawal, further investigation into how P53 controls synaptic withdrawal may determine whether there are neuron specific molecules that are involved in this pathway and may be possible therapeutic targets. It is perhaps possible that P53-inhibition could be used as a short-term therapy to try and promote the persistence of synaptic connections while a long-term SMN therapy is administered (Benkafadar et al. 2017).

In this thesis, I also addressed compensatory sprouting of motor neurons in SMA. As the mechanism of motor neuron sprouting was not specifically addressed, the therapeutic benefit of increasing compensatory sprouting cannot be verified and therefore this may still be effective as a combinational therapy. Given that symptomatic administration of an SMN-dependent therapy will mean that there is already NMJ loss, then the increased growth of motor neurons through sprouting may help to restore those synapses that had been lost due to the low levels of SMN. Moreover, since the results that

have been presented here show that sprouting is not responsible for the differential vulnerability of muscles in the *Smn*$^{2B/-}$ mouse model of SMA, there are likely to be other targets that do regulate this differential vulnerability, which may also be viable combinational therapies (Murray et al. 2015).

Furthermore, these results also support the findings that there is an SMN-threshold and above this threshold motor neurons remain stable, as demonstrated in *Smn*$^{+/-}$ and *Smn*$^{2B/2B}$ mice. It is understood that in patients this threshold is variable. While some individuals that have 3 copies of *SMN2* and no functional *SMN1* are symptomatic, others with the same *SMN* genetics remain asymptomatic (Oprea et al. 2008). A large-scale study to determine the average threshold of SMN to sustain normal functioning within the human population would be informative, giving a target to which we would be required to increase SMN to in SMA patients. Increasing the levels of SMN above this threshold will be key to ensuring the stability of motor neurons and the future success of SMN-dependent treatments in SMA.

6.3 Concluding remarks

I conclude this thesis by emphasising that despite recent advances in therapeutics for SMA we must remember that increasing our basic understanding of SMA pathogenesis remains incredibly important. All research to date has been paramount to the recent success in the SMA field. Therefore, by continuing to increase our knowledge we strengthen our chance of finding further ways to improve the lives of SMA patients. The work I have presented in this thesis has provided an insight into the pattern of motor neuron degeneration and remodeling in SMA and therefore I have provided significant contribution to the SMA research field.

References

Aliouat-Denis, C.-M. et al., 2005. p53-Independent Regulation of p21Waf1/Cip1 Expression and Senescence by Chk2. *Molecular Cancer Research*, 3(11), pp.627–634. Available at: http://www.ncbi.nlm.nih.gov/pubmed/16317088 [Accessed October 25, 2018].

Allodi, I. et al., 2016. Differential neuronal vulnerability identifies IGF-2 as a protective factor in ALS. *Scientific Reports*, 6, p.25960. Available at: http://www.nature.com/articles/srep25960 [Accessed August 18, 2016].

Anderton, R.S. et al., 2011. Survival of motor neuron protein over-expression prevents calpain-mediated cleavage and activation of procaspase-3 in differentiated human SH-SY5Y cells. *Neuroscience*, 181, pp.226–233. Available at: https://www.sciencedirect.com/science/article/pii/S0306452211001734?via%3Dihub [Accessed September 3, 2018].

Babin, P.J., Goizet, C. & Raldúa, D., 2014. Zebrafish models of human motor neuron diseases: Advantages and limitations. *Progress in Neurobiology*, 118, pp.36–58. Available at: https://www.sciencedirect.com/science/article/pii/S0301008214000410?via%3Dihub [Accessed August 13, 2018].

Baumbach-Reardon, L., Sacharow, S.J. & Ahearn, M.E., 2012. *Spinal Muscular Atrophy, X-Linked Infantile*, University of Washington, Seattle. Available at: http://www.ncbi.nlm.nih.gov/pubmed/20301739 [Accessed July 25, 2018].

Bäumer, D. et al., 2009. Alternative splicing events are a late feature of pathology in a mouse model of spinal muscular atrophy. *PLoS genetics*, 5(12), p.e1000773. Available at: http://journals.plos.org/plosgenetics/article?id=10.1371/journal.pgen.1000773 [Accessed July 20, 2015].

Benkafadar, N. et al., 2017. New Strategies for Improving the Quality of Life of Cancer Survivors: Reversible p53 Inhibition. *Journal of Cancer Science & Therapy*, 09(06), pp.490–491. Available at: https://www.omicsonline.org/open-access/bioactivity-and-cytotoxic-effect-of-cyanobacterial-toxin-againsthepatocellular-carcinoma-1948-5956-1000464.php?aid=90699 [Accessed December 4, 2018].

Bertini, E. et al., 2017. Safety and efficacy of olesoxime in patients with type 2 or non-ambulatory type 3 spinal muscular atrophy: a randomised, double-blind, placebo-controlled phase 2 trial. *The Lancet Neurology*, 16(7), pp.513–522.

Available at: http://www.ncbi.nlm.nih.gov/pubmed/28460889 [Accessed August 13, 2018].

Bettini, N.L. et al., 2007. Dynamic remodelling of synapses can occur in the absence of the parent cell body. *BMC neuroscience*, 8, p.79. Available at: http://www.ncbi.nlm.nih.gov/pubmed/17897464 [Accessed November 20, 2018].

Biros, I. & Forrest, S., 1999. Spinal muscular atrophy: untangling the knot? *Journal of medical genetics*, 36(1), pp.1–8. Available at: http://www.ncbi.nlm.nih.gov/pubmed/9950358 [Accessed September 3, 2018].

Boon, K.-L. et al., 2009. Zebrafish survival motor neuron mutants exhibit presynaptic neuromuscular junction defects. *Human molecular genetics*, 18(19), pp.3615–25. Available at: http://www.ncbi.nlm.nih.gov/pubmed/19592581 [Accessed August 13, 2018].

Bordet, T. et al., 2010. Olesoxime (TRO19622): A Novel Mitochondrial-Targeted Neuroprotective Compound. *Pharmaceuticals (Basel, Switzerland)*, 3(2), pp.345–368. Available at: http://www.ncbi.nlm.nih.gov/pubmed/27713255 [Accessed August 13, 2018].

Bowerman, M. et al., 2010. Rho-kinase inactivation prolongs survival of an intermediate SMA mouse model. *Human Molecular Genetics*, 19(8), pp.1468–1478. Available at: https://academic.oup.com/hmg/article-lookup/doi/10.1093/hmg/ddq021 [Accessed August 13, 2018].

Bowerman, M. et al., 2012a. A critical smn threshold in mice dictates onset of an intermediate spinal muscular atrophy phenotype associated with a distinct neuromuscular junction pathology. *Neuromuscular Disorders*, 22(3), pp.263–276. Available at: https://www.sciencedirect.com/science/article/pii/S0960896611013459 [Accessed August 13, 2018].

Bowerman, M., Murray, L.M., et al., 2012b. Fasudil improves survival and promotes skeletal muscle development in a mouse model of spinal muscular atrophy. *BMC medicine*, 10, p.24. Available at: http://www.ncbi.nlm.nih.gov/pubmed/22397316 [Accessed September 3, 2018].

Bowerman, M., Swoboda, K.J., et al., 2012c. Glucose metabolism and pancreatic defects in spinal muscular atrophy. *Annals of neurology*, 72(2), pp.256–68. Available at: http://www.ncbi.nlm.nih.gov/pubmed/22926856 [Accessed October 22, 2018].

Bowerman, M. et al., 2014. Defects in pancreatic development and glucose metabolism in SMN-depleted mice independent of canonical spinal muscular

atrophy neuromuscular pathology. *Human molecular genetics*, 23(13), pp.3432–44. Available at: http://www.pubmedcentral.nih.gov/articlerender.fcgi?artid=4049303&tool=pmcentrez&rendertype=abstract [Accessed November 12, 2014].

Bowerman, M. et al., 2017. Therapeutic strategies for spinal muscular atrophy: SMN and beyond. *Disease models & mechanisms*, 10(8), pp.943–954. Available at: http://www.ncbi.nlm.nih.gov/pubmed/28768735 [Accessed December 4, 2018].

Bowerman, M. et al., 2018. Pathogenic commonalities between spinal muscular atrophy and amyotrophic lateral sclerosis: Converging roads to therapeutic development. *European Journal of Medical Genetics*, 61(11), pp.685–698. Available at: https://www.sciencedirect.com/science/article/pii/S1769721217306742?via%3Dihub [Accessed November 12, 2018].

Boyd, P.J. & Gillingwater, T.H., 2017. Axonal and Neuromuscular Junction Pathology in Spinal Muscular Atrophy. *Spinal Muscular Atrophy*, pp.133–151. Available at: https://www.sciencedirect.com/science/article/pii/B9780128036853000082 [Accessed September 13, 2018].

Boyer, J.G. et al., 2014. Myogenic program dysregulation is contributory to disease pathogenesis in spinal muscular atrophy. *Human molecular genetics*, 23(16), pp.4249–59. Available at: http://hmg.oxfordjournals.org/content/early/2014/04/15/hmg.ddu142.full [Accessed August 20, 2015].

Bruce, A.K. et al., 1995. Hypoglycaemia in spinal muscular atrophy. *Lancet (London, England)*, 346(8975), pp.609–10. Available at: http://www.ncbi.nlm.nih.gov/pubmed/7651007 [Accessed October 22, 2018].

Brzustowicz, L.M. et al., 1990. Genetic mapping of chronic childhood-onset spinal muscular atrophy to chromosome 5q1 1.2–13.3. *Nature*, 344(6266), pp.540–541. Available at: http://www.nature.com/doifinder/10.1038/344540a0 [Accessed July 25, 2018].

Burghes, A.H.M. & Beattie, C.E., 2009. Spinal muscular atrophy: why do low levels of survival motor neuron protein make motor neurons sick? *Nature reviews. Neuroscience*, 10(8), pp.597–609. Available at: http://www.pubmedcentral.nih.gov/articlerender.fcgi?artid=2853768&tool=pmcentrez&rendertype=abstract [Accessed November 24, 2014].

Bürglen, L. et al., 1996. Structure and Organization of the Human Survival Motor Neurone (SMN) Gene. *Genomics*, 32(3), pp.479–482. Available at: http://www.ncbi.nlm.nih.gov/pubmed/8838816 [Accessed November 12, 2018].

Cajigas, I.J. et al., 2012. The local transcriptome in the synaptic neuropil revealed by deep sequencing and high-resolution imaging. *Neuron*, 74(3), pp.453–66. Available at: http://www.ncbi.nlm.nih.gov/pubmed/22578497 [Accessed August 13, 2018].

Calucho, M. et al., 2018. Correlation between SMA type and SMN2 copy number revisited: An analysis of 625 unrelated Spanish patients and a compilation of 2834 reported cases. *Neuromuscular Disorders*, 28(3), pp.208–215. Available at: https://www.sciencedirect.com/science/article/pii/S096089661730490X?via%3Dihub [Accessed October 16, 2018].

Carpenter, S. et al., 1978. *Pathological Involvement of Primary Sensory Neurons in Werdnig-Hoffmann Disease*, Available at: https://link.springer.com/content/pdf/10.1007/BF00690973.pdf [Accessed November 26, 2018].

Chan, Y.B. et al., 2003. Neuromuscular defects in a Drosophila survival motor neuron gene mutant. *Human molecular genetics*, 12(12), pp.1367–76. Available at: http://www.ncbi.nlm.nih.gov/pubmed/12783845 [Accessed August 13, 2018].

Chang, H.C.-H. et al., 2008. Modeling spinal muscular atrophy in Drosophila. *PloS one*, 3(9), p.e3209. Available at: http://www.ncbi.nlm.nih.gov/pubmed/18791638 [Accessed August 13, 2018].

Cifuentes-Diaz, C., 2002. Neurofilament accumulation at the motor endplate and lack of axonal sprouting in a spinal muscular atrophy mouse model. *Human Molecular Genetics*, 11(12), pp.1439–1447. Available at: http://hmg.oxfordjournals.org/content/11/12/1439.abstract [Accessed October 27, 2015].

Comley, L.H. et al., 2011. Induction of cell stress in neurons from transgenic mice expressing yellow fluorescent protein: implications for neurodegeneration research. *PloS one*, 6(3), p.e17639. Available at: http://www.pubmedcentral.nih.gov/articlerender.fcgi?artid=3050905&tool=pmcentrez&rendertype=abstract [Accessed November 2, 2015].

Coovert, D., 1997. The survival motor neuron protein in spinal muscular atrophy. *Human Molecular Genetics*, 6(8), pp.1205–1214. Available at: http://hmg.oxfordjournals.org/content/6/8/1205.long [Accessed November 11, 2015].

Côté, F., Collard, J.-F. & Julien, J.-P., 1993. Progressive neuronopathy in transgenic mice expressing the human neurofilament heavy gene: A mouse model of amyotrophic lateral sclerosis. *Cell*, 73(1), pp.35–46. Available at: https://www.sciencedirect.com/science/article/pii/009286749390158M?via%3Di

hub [Accessed September 13, 2018].

Crawford, T.O. & Pardo, C.A., 1996. The Neurobiology of Childhood Spinal Muscular Atrophy. , 110(0010), pp.97–110.

Crawford, T.O. et al., 1999. Abnormal fatty acid metabolism in childhood spinal muscular atrophy. *Annals of Neurology*, 45(3), pp.337–343. Available at: http://doi.wiley.com/10.1002/1531-8249%28199903%2945%3A3%3C337%3A%3AAID-ANA9%3E3.0.CO%3B2-U [Accessed October 22, 2018].

Cusack, C.L. et al., 2013. Distinct pathways mediate axon degeneration during apoptosis and axon-specific pruning. *Nature Communications*, 4(1), p.1876. Available at: http://www.nature.com/articles/ncomms2910 [Accessed October 25, 2018].

Czaplinski, K., 2014. Understanding mRNA trafficking: Are we there yet? *Seminars in Cell & Developmental Biology*, 32, pp.63–70. Available at: https://www.sciencedirect.com/science/article/pii/S1084952114000962 [Accessed August 13, 2018].

d'Errico, P. et al., 2013. Selective vulnerability of spinal and cortical motor neuron subpopulations in delta7 SMA mice. *PloS one*, 8(12), p.e82654. Available at: http://www.ncbi.nlm.nih.gov/pubmed/24324819 [Accessed August 13, 2018].

Dale, J.M. et al., 2011. The spinal muscular atrophy mouse model, SMAΔ7, displays altered axonal transport without global neurofilament alterations. *Acta neuropathologica*, 122(3), pp.331–41. Available at: http://www.ncbi.nlm.nih.gov/pubmed/21681521 [Accessed September 10, 2018].

Darabid, H., Perez-Gonzalez, A.P. & Robitaille, R., 2014. Neuromuscular synaptogenesis: coordinating partners with multiple functions. *Nature Reviews Neuroscience*, 15(11), pp.703–718. Available at: http://www.nature.com/articles/nrn3821 [Accessed October 10, 2018].

Deguise, M.-O. et al., 2016. Differential induction of muscle atrophy pathways in two mouse models of spinal muscular atrophy. *Scientific Reports*, 6(1), p.28846. Available at: http://www.nature.com/articles/srep28846 [Accessed August 13, 2018].

Deguise, M.-O. et al., 2017. Immune dysregulation may contribute to disease pathogenesis in spinal muscular atrophy mice. *Human molecular genetics*, 26(4), pp.801–819. Available at: http://www.ncbi.nlm.nih.gov/pubmed/28108555 [Accessed October 22, 2018].

Deguise, M.-O. & Kothary, R., 2017. New insights into SMA pathogenesis: immune dysfunction and neuroinflammation. *Annals of clinical and translational neurology*, 4(7), pp.522–530. Available at: http://www.ncbi.nlm.nih.gov/pubmed/28695153 [Accessed October 22, 2018].

DiDonato, C.J. et al., 2001. Regulation of murine survival motor neuron (Smn) protein levels by modifying Smn exon 7 splicing. *Human Molecular Genetics*, 10(23), pp.2727–2736. Available at: https://academic.oup.com/hmg/article-lookup/doi/10.1093/hmg/10.23.2727 [Accessed August 13, 2018].

Dominguez, E. et al., 2011. Intravenous scAAV9 delivery of a codon-optimized SMN1 sequence rescues SMA mice. *Human Molecular Genetics*, 20(4), pp.681–693. Available at: https://academic.oup.com/hmg/article-lookup/doi/10.1093/hmg/ddq514 [Accessed August 13, 2018].

Donehower, L.A., 1996. The p53-deficient mouse: a model for basic and applied cancer studies. *Seminars in Cancer Biology*, 7(5), pp.269–278. Available at: https://www.sciencedirect.com/science/article/pii/S1044579X96900358?via%3Dihub [Accessed December 4, 2018].

Donlin-Asp, P.G. et al., 2017. The Survival of Motor Neuron Protein Acts as a Molecular Chaperone for mRNP Assembly. *Cell reports*, 18(7), pp.1660–1673. Available at: http://www.ncbi.nlm.nih.gov/pubmed/28199839 [Accessed August 13, 2018].

Dubowitz, V., 1999. Very severe spinal muscular atrophy (SMA type 0): an expanding clinical phenotype. *European Journal of Paediatric Neurology*, 3(2), pp.49–51. Available at: https://www.sciencedirect.com/science/article/pii/S1090379899800129 [Accessed August 13, 2018].

Dubowitz, V., 2009. Ramblings in the history of spinal muscular atrophy. *Neuromuscular Disorders*, 19(1), pp.69–73. Available at: https://www.sciencedirect.com/science/article/pii/S096089660800672X?via%3Dihub [Accessed July 25, 2018].

Elmore, S., 2007. Apoptosis: a review of programmed cell death. *Toxicologic pathology*, 35(4), pp.495–516. Available at: http://www.ncbi.nlm.nih.gov/pubmed/17562483 [Accessed August 27, 2018].

English, A.W., 2003. Cytokines, growth factors and sprouting at the neuromuscular junction. *Journal of neurocytology*, 32(5–8), pp.943–60. Available at: http://link.springer.com/10.1023/B:NEUR.0000020634.59639.cf [Accessed April 26, 2016].

Ernest, N.J., Habela, C.W. & Sontheimer, H., 2008. Cytoplasmic condensation is both necessary and sufficient to induce apoptotic cell death. *Journal of cell science*, 121(Pt 3), pp.290–7. Available at: http://www.ncbi.nlm.nih.gov/pubmed/18198188 [Accessed October 25, 2018].

Eshraghi, M. et al., 2016. Effect of genetic background on the phenotype of the Smn2B/- mouse model of spinal muscular atrophy. *Human molecular genetics*, 25(20), pp.4494–4506. Available at: http://www.ncbi.nlm.nih.gov/pubmed/28172892 [Accessed October 10, 2018].

Fallini, C., Bassell, G.J. & Rossoll, W., 2012. Spinal muscular atrophy: the role of SMN in axonal mRNA regulation. *Brain research*, 1462, pp.81–92. Available at: http://www.sciencedirect.com/science/article/pii/S0006899312001266 [Accessed July 20, 2015].

Fallini, C. et al., 2016. Deficiency of the Survival of Motor Neuron Protein Impairs mRNA Localization and Local Translation in the Growth Cone of Motor Neurons. *The Journal of neuroscience : the official journal of the Society for Neuroscience*, 36(13), pp.3811–20. Available at: http://www.ncbi.nlm.nih.gov/pubmed/27030765 [Accessed August 13, 2018].

Fayzullina, S. & Martin, L.J., 2014. Skeletal Muscle DNA Damage Precedes Spinal Motor Neuron DNA Damage in a Mouse Model of Spinal Muscular Atrophy (SMA) T. H. Gillingwater, ed. *PLoS ONE*, 9(3), p.e93329. Available at: http://dx.plos.org/10.1371/journal.pone.0093329 [Accessed August 13, 2018].

Fei, P., Bernhard, E.J. & El-Deiry, W.S., 2002. Tissue-specific induction of p53 targets in vivo. *Cancer research*, 62(24), pp.7316–27. Available at: http://www.ncbi.nlm.nih.gov/pubmed/12499275 [Accessed October 25, 2018].

Feng, G. et al., 2000. Imaging Neuronal Subsets in Transgenic Mice Expressing Multiple Spectral Variants of GFP. *Neuron*, 28(1), pp.41–51. Available at: http://www.sciencedirect.com/science/article/pii/S0896627300000842 [Accessed June 30, 2015].

Fink, S.L. & Cookson, B.T., 2005. Apoptosis, pyroptosis, and necrosis: mechanistic description of dead and dying eukaryotic cells. *Infection and immunity*, 73(4), pp.1907–16. Available at: http://www.ncbi.nlm.nih.gov/pubmed/15784530 [Accessed August 27, 2018].

Finkel, R.S. et al., 2016. Treatment of infantile-onset spinal muscular atrophy with nusinersen: a phase 2, open-label, dose-escalation study. *Lancet (London, England)*, 388(10063), pp.3017–3026. Available at:

http://www.ncbi.nlm.nih.gov/pubmed/27939059 [Accessed August 13, 2018].

Finkel, R.S. et al., 2017. Nusinersen versus Sham Control in Infantile-Onset Spinal Muscular Atrophy. *New England Journal of Medicine*, 377(18), pp.1723–1732. Available at: http://www.nejm.org/doi/10.1056/NEJMoa1702752 [Accessed August 13, 2018].

Fisher, E.M.C. et al., 2009. New approaches for modelling sporadic genetic disease in the mouse. *Disease models & mechanisms*, 2(9–10), pp.446–53. Available at: http://www.ncbi.nlm.nih.gov/pubmed/19726804 [Accessed July 25, 2018].

Foust, K.D. et al., 2010. Rescue of the spinal muscular atrophy phenotype in a mouse model by early postnatal delivery of SMN. *Nature biotechnology*, 28(3), pp.271–4. Available at: http://www.ncbi.nlm.nih.gov/pubmed/20190738 [Accessed August 13, 2018].

Fulda, S. et al., 2010. Cellular stress responses: cell survival and cell death. *International journal of cell biology*, 2010, p.214074. Available at: http://www.ncbi.nlm.nih.gov/pubmed/20182529 [Accessed November 20, 2018].

Gabanella, F. et al., 2007. Ribonucleoprotein assembly defects correlate with spinal muscular atrophy severity and preferentially affect a subset of spliceosomal snRNPs. *PloS one*, 2(9), p.e921. Available at: http://www.ncbi.nlm.nih.gov/pubmed/17895963 [Accessed August 13, 2018].

Garbes, L. et al., 2013. VPA response in SMA is suppressed by the fatty acid translocase CD36. *Human Molecular Genetics*, 22(2), pp.398–407. Available at: https://academic.oup.com/hmg/article-lookup/doi/10.1093/hmg/dds437 [Accessed August 13, 2018].

Gavrilina, T.O. et al., 2008. Neuronal SMN expression corrects spinal muscular atrophy in severe SMA mice while muscle-specific SMN expression has no phenotypic effect. *Human molecular genetics*, 17(8), pp.1063–75. Available at: http://www.ncbi.nlm.nih.gov/pubmed/18178576 [Accessed August 13, 2018].

Geden, M.J. & Deshmukh, M., 2016. Axon degeneration: context defines distinct pathways. *Current Opinion in Neurobiology*, 39, pp.108–115. Available at: http://dx.doi.org/10.1016/j.conb.2016.05.002 [Accessed September 26, 2018].

Giavazzi, A. et al., 2006. Neuronal-Specific Roles of the Survival Motor Neuron Protein. *Journal of Neuropathology and Experimental Neurology*, 65(3), pp.267–277. Available at: http://www.ncbi.nlm.nih.gov/pubmed/16651888 [Accessed November 12, 2018].

Gilliam, T.C. et al., 1990. Genetic homogeneity between acute and chronic forms of spinal muscular atrophy. *Nature*, 345(6278), pp.823–825. Available at: http://www.nature.com/doifinder/10.1038/345823a0 [Accessed July 25, 2018].

Gillingwater, T.H. & Wishart, T.M., 2013. Mechanisms underlying synaptic vulnerability and degeneration in neurodegenerative disease. *Neuropathology and Applied Neurobiology*, 39(4), pp.320–334. Available at: http://doi.wiley.com/10.1111/nan.12014 [Accessed November 23, 2018].

Gilman, C.P. et al., 2003. p53 is Present in Synapses Where it Mediates Mitochondrial Dysfunction and Synaptic Degeneration in Response to DNA Damage, and Oxidative and Excitotoxic Insults. *NeuroMolecular Medicine*, 3(3), pp.159–172. Available at: http://link.springer.com/10.1385/NMM:3:3:159 [Accessed September 13, 2018].

Gordon, T., Hegedus, J. & Tam, S.L., 2004. Adaptive and maladaptive motor axonal sprouting in aging and motoneuron disease. *Neurological Research*, 26(2), pp.174–185. Available at: http://www.ncbi.nlm.nih.gov/pubmed/15072637 [Accessed September 4, 2018].

Gould, T.W. et al., 2006. Complete Dissociation of Motor Neuron Death from Motor Dysfunction by Bax Deletion in a Mouse Model of ALS. *Journal of Neuroscience*, 26(34), pp.8774–8786. Available at: http://www.ncbi.nlm.nih.gov/pubmed/16928866 [Accessed October 25, 2018].

Grasl-Kraupp, B. et al., 1995. In situ detection of fragmented DNA (TUNEL assay) fails to discriminate among apoptosis, necrosis, and autolytic cell death: a cautionary note. *Hepatology (Baltimore, Md.)*, 21(5), pp.1465–8. Available at: http://www.ncbi.nlm.nih.gov/pubmed/7737654 [Accessed September 10, 2018].

Groen, E.J.N. & Gillingwater, T.H., 2015. UBA1: At the Crossroads of Ubiquitin Homeostasis and Neurodegeneration. *Trends in molecular medicine*, 21(10), pp.622–632. Available at: http://www.ncbi.nlm.nih.gov/pubmed/26432019 [Accessed August 13, 2018].

Groen, E.J.N. et al., 2018a. Temporal and tissue-specific variability of SMN protein levels in mouse models of spinal muscular atrophy. *Human molecular genetics*, 27(16), pp.2851–2862. Available at: http://www.ncbi.nlm.nih.gov/pubmed/29790918 [Accessed August 13, 2018].

Groen, E.J.N., Talbot, K. & Gillingwater, T.H., 2018b. Advances in therapy for spinal muscular atrophy: promises and challenges. *Nature Reviews Neurology*, 14(4), pp.214–224. Available at:

http://www.nature.com/doifinder/10.1038/nrneurol.2018.4 [Accessed November 23, 2018].

Gubitz, A.K., Feng, W. & Dreyfuss, G., 2004. The SMN complex. *Experimental cell research*, 296(1), pp.51–6. Available at: http://www.ncbi.nlm.nih.gov/pubmed/15120993 [Accessed November 24, 2014].

Hammond, S.M. et al., 2010. Mouse Survival Motor Neuron Alleles That Mimic SMN2 Splicing and Are Inducible Rescue Embryonic Lethality Early in Development but Not Late B. D. McCabe, ed. *PLoS ONE*, 5(12), p.e15887. Available at: http://dx.plos.org/10.1371/journal.pone.0015887 [Accessed August 13, 2018].

Hao, L.T., Burghes, A.H. & Beattie, C.E., 2011. Generation and Characterization of a genetic zebrafish model of SMA carrying the human SMN2 gene. *Molecular neurodegeneration*, 6(1), p.24. Available at: http://www.ncbi.nlm.nih.gov/pubmed/21443782 [Accessed August 13, 2018].

Harada, Y. et al., 2002. Correlation between SMN2 copy number and clinical phenotype of spinal muscular atrophy: three SMN2 copies fail to rescue some patients from the disease severity. *Journal of Neurology*, 249(9), pp.1211–1219. Available at: http://link.springer.com/10.1007/s00415-002-0811-4 [Accessed August 13, 2018].

Harding, B.N. et al., 2015. Spectrum of neuropathophysiology in spinal muscular atrophy type I. *Journal of neuropathology and experimental neurology*, 74(1), pp.15–24. Available at: http://www.ncbi.nlm.nih.gov/pubmed/25470343 [Accessed September 13, 2018].

Hausmanowa-Petrusewicz, I. & Vrbová, G., 2005. Spinal muscular atrophy: a delayed development hypothesis. *Neuroreport*, 16(7), pp.657–61. Available at: http://www.ncbi.nlm.nih.gov/pubmed/15858401 [Accessed October 25, 2018].

Hayashi, S. & McMahon, A.P., 2002. Efficient Recombination in Diverse Tissues by a Tamoxifen-Inducible Form of Cre: A Tool for Temporally Regulated Gene Activation/Inactivation in the Mouse. *Developmental Biology*, 244(2), pp.305–318. Available at: https://www.sciencedirect.com/science/article/pii/S001216060290597X?via%3Dihub [Accessed October 10, 2018].

Hoffman, H., 1950. LOCAL RE-INNERVATION IN PARTIALLY DENERVATED MUSCLE: A HISTO-PHYSIOLOGICAL STUDY. *Australian Journal of Experimental Biology and Medical Science*, 28(4), pp.383–398. Available at:

http://doi.wiley.com/10.1038/icb.1950.39 [Accessed September 13, 2018].

Hsieh-Li, H. et al., 2000. A mouse model for spinal muscular atrophy. *Nature …*, 24(january), pp.66–70. Available at: http://www.nature.com/ng/journal/v24/n1/abs/ng0100_66.html [Accessed November 26, 2014].

Hua, Y. & Zhou, J., 2004. Survival motor neuron protein facilitates assembly of stress granules. *FEBS Letters*, 572(1–3), pp.69–74. Available at: http://doi.wiley.com/10.1016/j.febslet.2004.07.010 [Accessed November 12, 2018].

Huang, W.-Y. et al., 2000. Transgenic expression of green fluorescence protein can cause dilatedcardiomyopathy. *Nature Medicine*, 6(5), pp.482–483. Available at: http://www.nature.com/articles/nm0500_482 [Accessed September 13, 2018].

Hwu, W. et al., 2017. Outcomes after 1-year in presymptomatic infants with genetically diagnosed spinal muscular atrophy (SMA) treated with nusinersen: interim results from the NURTURE study. *Neuromuscular Disorders*, 27, p.S212. Available at: https://www.sciencedirect.com/science/article/pii/S0960896617309975 [Accessed August 13, 2018].

Ito, Y. et al., 2011. New insights into the pathogenesis of spinal muscular atrophy. *Brain and Development*, 33(4), pp.321–331. Available at: https://www.sciencedirect.com/science/article/pii/S0387760410001403 [Accessed September 3, 2018].

Iwahashi, H. et al., 1997. Synergistic anti-apoptotic activity between Bcl-2 and SMN implicated in spinal muscular atrophy. *Nature*, 390(6658), pp.413–417. Available at: http://www.nature.com/articles/37144 [Accessed September 3, 2018].

Jablonka, S. et al., 2000. Reduced survival motor neuron (Smn) gene dose in mice leads to motor neuron degeneration: an animal model for spinal muscular atrophy type III. *Human Molecular Genetics*, 9(3), pp.341–346. Available at: https://academic.oup.com/hmg/article-lookup/doi/10.1093/hmg/9.3.341 [Accessed September 17, 2018].

Jacobs, W.B., Kaplan, D.R. & Miller, F.D., 2006. The p53 family in nervous system development and disease. *Journal of Neurochemistry*, 97(6), pp.1571–1584. Available at: http://doi.wiley.com/10.1111/j.1471-4159.2006.03980.x [Accessed September 10, 2018].

James, P.A. & Talbot, K., 2006. The molecular genetics of non-ALS motor neuron diseases. *Biochimica et Biophysica Acta (BBA) - Molecular Basis of Disease*, 1762(11–12), pp.986–1000. Available at:

https://www.sciencedirect.com/science/article/pii/S092544390600072X [Accessed September 3, 2018].

Kariya, S. et al., 2008. Reduced SMN protein impairs maturation of the neuromuscular junctions in mouse models of spinal muscular atrophy. *Human molecular genetics*, 17(16), pp.2552–69. Available at: http://www.ncbi.nlm.nih.gov/pubmed/18492800 [Accessed August 13, 2018].

Kato, S. & Hirano, A., 1990. Ubiquitin and phosphorylated neurofilament epitopes in ballooned neurons of the extraocular muscle nuclei in a case of Werdnig-Hoffmann disease. *Acta neuropathologica*, 80(3), pp.334–7. Available at: http://www.ncbi.nlm.nih.gov/pubmed/1698008 [Accessed September 13, 2018].

Kelley, K.A. et al., 1994. Expression of Thy-1/ lacZ fusion genes in the CNS of transgenic mice. *Molecular Brain Research*, 24(1–4), pp.261–274. Available at: https://www.sciencedirect.com/science/article/pii/0169328X94901392?via%3Dihub [Accessed November 20, 2018].

Kerr, D.A. et al., 2000. Survival motor neuron protein modulates neuron-specific apoptosis. *Proceedings of the National Academy of Sciences of the United States of America*, 97(24), pp.13312–7. Available at: http://www.ncbi.nlm.nih.gov/pubmed/11078511 [Accessed September 3, 2018].

Khairallah, M.-T. et al., 2017. SMN deficiency negatively impacts red pulp macrophages and spleen development in mouse models of spinal muscular atrophy. *Human molecular genetics*, 26(5), pp.932–941. Available at: http://www.ncbi.nlm.nih.gov/pubmed/28062667 [Accessed October 22, 2018].

Khalil, B. et al., 2018. mRNP assembly, axonal transport, and local translation in neurodegenerative diseases. *Brain Research*, 1693, pp.75–91. Available at: https://www.sciencedirect.com/science/article/pii/S0006899318300829?via%3Dihub [Accessed August 13, 2018].

Khatri, I.A. et al., 2008. Low bone mineral density in spinal muscular atrophy. *Journal of clinical neuromuscular disease*, 10(1), pp.11–7. Available at: https://insights.ovid.com/crossref?an=00131402-200809000-00003 [Accessed October 19, 2018].

Kline, R.A. et al., 2017. Comparison of independent screens on differentially vulnerable motor neurons reveals alpha-synuclein as a common modifier in motor neuron diseases. *PLoS genetics*, 13(3), p.e1006680. Available at: http://www.ncbi.nlm.nih.gov/pubmed/28362802 [Accessed August 13, 2018].

Kolossovski, E., 2017. Oh transgene, where art thou? Mapping transgene insertion.

Taconic. Available at: https://www.taconic.com/taconic-insights/gems-design/mapping-transgene-insertion.html [Accessed November 23, 2018].

Kong, L. et al., 2009. Impaired synaptic vesicle release and immaturity of neuromuscular junctions in spinal muscular atrophy mice. *The Journal of neuroscience : the official journal of the Society for Neuroscience*, 29(3), pp.842–51. Available at: http://www.ncbi.nlm.nih.gov/pubmed/19158308 [Accessed August 13, 2018].

Korinthenberg, R. et al., 1997. Congenital axonal neuropathy caused by deletions in the spinal muscular atrophy region. *Annals of Neurology*, 42(3), pp.364–368. Available at: http://doi.wiley.com/10.1002/ana.410420314 [Accessed September 13, 2018].

Kostic, V. et al., 1997. Bcl-2: prolonging life in a transgenic mouse model of familial amyotrophic lateral sclerosis. *Science (New York, N.Y.)*, 277(5325), pp.559–62. Available at: http://www.ncbi.nlm.nih.gov/pubmed/9228005 [Accessed October 25, 2018].

Le, T.T. et al., 2005. SMNΔ7, the major product of the centromeric survival motor neuron (SMN2) gene, extends survival in mice with spinal muscular atrophy and associates with full-length SMN. *Human Molecular Genetics*, 14(6), pp.845–857. Available at: https://academic.oup.com/hmg/article-lookup/doi/10.1093/hmg/ddi078 [Accessed August 13, 2018].

Lee, Y. Il et al., 2011. Muscles in a mouse model of spinal muscular atrophy show profound defects in neuromuscular development even in the absence of failure in neuromuscular transmission or loss of motor neurons. *Developmental biology*, 356(2), pp.432–44. Available at: http://www.ncbi.nlm.nih.gov/pubmed/21658376 [Accessed February 26, 2019].

Lefebvre, S., 1995. Identification and characterization of a spinal muscular atrophy-determining gene. *Cell*, 80(1), pp.155–165. Available at: http://www.sciencedirect.com/science/article/pii/0092867495904603 [Accessed November 24, 2014].

Li, J. & Yuan, J., 2008. Caspases in apoptosis and beyond. *Oncogene*, 27(48), pp.6194–6206. Available at: http://www.nature.com/articles/onc2008297 [Accessed August 27, 2018].

Li, M. et al., 2000. Functional role of caspase-1 and caspase-3 in an ALS transgenic mouse model. *Science (New York, N.Y.)*, 288(5464), pp.335–9. Available at: http://www.ncbi.nlm.nih.gov/pubmed/10764647 [Accessed October 25, 2018].

Liu, H. et al., 2014. The Smn-independent beneficial effects of trichostatin A on an intermediate mouse model of spinal muscular atrophy. *PloS one*, 9(7), p.e101225. Available at: http://www.ncbi.nlm.nih.gov/pubmed/24984019 [Accessed November 13, 2018].

Liu, Q. & Dreyfuss, G., 1996. A novel nuclear structure containing the survival of motor neurons protein. *The EMBO Journal*, 15(14), pp.3555–3565. Available at: https://onlinelibrary.wiley.com/doi/abs/10.1002/j.1460-2075.1996.tb00725.x [Accessed August 13, 2018].

Logge, W., Kingham, J. & Karl, T., 2014. Do individually ventilated cage systems generate a problem for genetic mouse model research? *Genes, Brain and Behavior*, 13(7), pp.713–720. Available at: http://www.ncbi.nlm.nih.gov/pubmed/24920375 [Accessed October 10, 2018].

Lorson, C.L. et al., 1999. A single nucleotide in the SMN gene regulates splicing and is responsible for spinal muscular atrophy. *Proceedings of the National Academy of Sciences of the United States of America*, 96(11), pp.6307–11. Available at: http://www.ncbi.nlm.nih.gov/pubmed/10339583 [Accessed July 25, 2018].

Lunn, M.R. & Wang, C.H., 2008. Spinal muscular atrophy. *Lancet*, 371(9630), pp.2120–33. Available at: http://www.ncbi.nlm.nih.gov/pubmed/18572081.

Lutz, C.M. et al., 2011. Postsymptomatic restoration of SMN rescues the disease phenotype in a mouse model of severe spinal muscular atrophy. *The Journal of clinical investigation*, 121(8), pp.3029–41. Available at: http://www.pubmedcentral.nih.gov/articlerender.fcgi?artid=3148744&tool=pmcentrez&rendertype=abstract [Accessed June 15, 2015].

Mailman, M.D. et al., 2002. Molecular analysis of spinal muscular atrophy and modification of the phenotype by SMN2. *Genetics in Medicine*, 4(1), pp.20–26. Available at: http://www.nature.com/doifinder/10.1097/00125817-200201000-00004 [Accessed July 25, 2018].

Marques Lopes, J., 2018. Roche Stops Work on Potential SMA Therapy Olesoxime After Disappointing Results in Phase 2 Trial. *SMA News Today*. Available at: https://smanewstoday.com/2018/06/06/roche-stops-development-of-sma-therapy-olesoxime-after-disappointing-trial-results/ [Accessed October 22, 2018].

Marques, M.J., Conchello, J.A. & Lichtman, J.W., 2000. From plaque to pretzel: fold formation and acetylcholine receptor loss at the developing neuromuscular

junction. *The Journal of neuroscience : the official journal of the Society for Neuroscience*, 20(10), pp.3663–75. Available at: http://www.ncbi.nlm.nih.gov/pubmed/10804208 [Accessed October 25, 2018].

Masu, Y. et al., 1993. Disruption of the CNTF gene results in motor neuron degeneration. *Nature*, 365(6441), pp.27–32. Available at: http://www.nature.com/doifinder/10.1038/365027a0 [Accessed November 20, 2018].

Maxwell, G.K. et al., 2018. Developmental and degenerative cardiac defects in the Taiwanese mouse model of severe spinal muscular atrophy. *Journal of Anatomy*, 232(6), pp.965–978. Available at: http://doi.wiley.com/10.1111/joa.12793 [Accessed October 22, 2018].

McGivern, J. V et al., 2013. Spinal muscular atrophy astrocytes exhibit abnormal calcium regulation and reduced growth factor production. *Glia*, 61(9), pp.1418–1428. Available at: http://www.ncbi.nlm.nih.gov/pubmed/23839956 [Accessed October 25, 2018].

McWhorter, M.L. et al., 2003. Knockdown of the survival motor neuron (Smn) protein in zebrafish causes defects in motor axon outgrowth and pathfinding. *The Journal of cell biology*, 162(5), pp.919–31. Available at: http://www.ncbi.nlm.nih.gov/pubmed/12952942 [Accessed August 13, 2018].

Melki, J. et al., 1990. Gene for chronic proximal spinal muscular atrophies maps to chromosome 5q. *Nature*, 344(6268), pp.767–768. Available at: http://www.nature.com/doifinder/10.1038/344767a0 [Accessed July 25, 2018].

Mercuri, E. et al., 2017. Infants and children with SMA treated with nusinersen in clinical trials: an integrated safety analysis. *Neuromuscular Disorders*, 27, p.S210. Available at: https://www.sciencedirect.com/science/article/pii/S0960896617309926 [Accessed August 13, 2018].

Merlo, P. et al., 2014. p53 prevents neurodegeneration by regulating synaptic genes. Available at: www.pnas.org/cgi/doi/10.1073/pnas.1419083111 [Accessed August 29, 2018].

Merritt, A.J. et al., 1997. Apoptosis in small intestinal epithelia from p53-null mice: evidence for a delayed, p53-indepdendent G2/M-associated cell death after γ-irradiation. *Oncogene*, 14(23), pp.2759–2766. Available at: http://www.nature.com/articles/1201126 [Accessed October 25, 2018].

Miller, C.C.J. et al., 2002. *Review Axonal transport of neurofilaments in normal and disease states*, Available at: https://link.springer.com/content/pdf/10.1007/s00018-002-8425-7.pdf [Accessed September 10, 2018].

Mishina, M. et al., 1986. Molecular distinction between fetal and adult forms of muscle acetylcholine receptor. *Nature*, 321(6068), pp.406–411. Available at: http://www.nature.com/articles/321406a0 [Accessed August 13, 2018].

Monani, U.R. et al., 1999. A single nucleotide difference that alters splicing patterns distinguishes the SMA gene SMN1 from the copy gene SMN2. *Human Molecular Genetics*, 8(7), pp.1177–1183. Available at: https://academic.oup.com/hmg/article-lookup/doi/10.1093/hmg/8.7.1177 [Accessed July 25, 2018].

Monani, U.R. et al., 2000. The human centromeric survival motor neuron gene (SMN2) rescues embryonic lethality in Smn-/- mice and results in a mouse with spinal muscular atrophy. *Human Molecular Genetics*, 9(3), pp.333–339. Available at: https://academic.oup.com/hmg/article-lookup/doi/10.1093/hmg/9.3.333 [Accessed July 25, 2018].

Monani, U.R., 2005. Spinal Muscular Atrophy: A Deficiency in a Ubiquitous Protein; a Motor Neuron-Specific Disease. *Neuron*, 48(6), pp.885–895. Available at: https://www.sciencedirect.com/science/article/pii/S0896627305010111?via%3Dihub [Accessed July 25, 2018].

Munir, R., 2017. *Sprouting as a disease modifier in asymptomatic mouse models with reduced Smn*. University of Edinburgh.

Munsat, T.L. & Davies, K.E., 1992. International SMA consortium meeting. (26-28 June 1992, Bonn, Germany). *Neuromuscular disorders : NMD*, 2(5–6), pp.423–8. Available at: http://www.ncbi.nlm.nih.gov/pubmed/1300191 [Accessed July 25, 2018].

Murray, L.M. et al., 2008. Selective vulnerability of motor neurons and dissociation of pre- and post-synaptic pathology at the neuromuscular junction in mouse models of spinal muscular atrophy. *Human Molecular Genetics*, 17(7), pp.949–962. Available at: https://academic.oup.com/hmg/article-lookup/doi/10.1093/hmg/ddm367 [Accessed August 13, 2018].

Murray, L.M., Gillingwater, T.H. & Parson, S.H., 2010. Using mouse cranial muscles to investigate neuromuscular pathology in vivo. *Neuromuscular Disorders*, 20(11), pp.740–743. Available at: http://dx.doi.org/10.1016/j.nmd.2010.06.013.

Murray, L.M. et al., 2012. Defects in neuromuscular junction remodelling in the Smn(2B/-) mouse model of spinal muscular atrophy. *Neurobiology of disease*, 49, pp.57–67. Available at: http://www.ncbi.nlm.nih.gov/pubmed/22960106 [Accessed January 12, 2015].

Murray, L.M. et al., 2015. Transcriptional profiling of differentially vulnerable motor neurons at pre-symptomatic stage in the Smn (2b/-) mouse model of spinal muscular atrophy. *Acta neuropathologica communications*, 3, p.55. Available at: http://www.ncbi.nlm.nih.gov/pubmed/26374403 [Accessed August 13, 2018].

Mutsaers, C. a et al., 2011. Reversible molecular pathology of skeletal muscle in spinal muscular atrophy. *Hum Mol Genet*, 20(22), pp.4334–4344.

Neve, A. et al., 2016. Central and peripheral defects in motor units of the diaphragm of spinal muscular atrophy mice. *Molecular and Cellular Neuroscience*, 70, pp.30–41. Available at: https://www.sciencedirect.com/science/article/pii/S1044743115300336 [Accessed August 13, 2018].

Nichterwitz, S. et al., 2018. LCM-seq reveals unique transcriptional adaption mechanisms of resistant neurons in spinal muscular atrophy. *bioRxiv*, p.356113. Available at: https://www.biorxiv.org/content/early/2018/06/27/356113?rss=1 [Accessed August 31, 2018].

Ogino, S. & Wilson, R.B., 2004. Spinal muscular atrophy: molecular genetics and diagnostics. *Expert Review of Molecular Diagnostics*, 4(1), pp.15–29. Available at: http://www.ncbi.nlm.nih.gov/pubmed/14711346 [Accessed February 26, 2019].

Okabe, M. et al., 1997. 'Green mice' as a source of ubiquitous green cells. *FEBS Letters*, 407(3), pp.313–319. Available at: http://doi.wiley.com/10.1016/S0014-5793%2897%2900313-X [Accessed September 13, 2018].

Oppenheim, R.W., 1991. *CELL DEATH DURING DEVELOPMENT OF THE NERVOUS SYSTEM*, Available at: www.annualreviews.org [Accessed September 7, 2018].

Oprea, G.E. et al., 2008. Plastin 3 is a protective modifier of autosomal recessive spinal muscular atrophy. *Science (New York, N.Y.)*, 320(5875), pp.524–7. Available at: http://www.ncbi.nlm.nih.gov/pubmed/18440926 [Accessed August 13, 2018].

Oskoui, M. et al., 2017. Physician driven variation in the care of children with spinal muscular atrophy type 1. *Pediatric Pulmonology*, 52(5), pp.662–668. Available at: http://doi.wiley.com/10.1002/ppul.23616 [Accessed October 16, 2018].

Parker, G.C. et al., 2008. Survival motor Neuron protein regulates apoptosis in anin vitro model of Spinal muscular atrophy. *Neurotoxicity Research*, 13(1), pp.39–48. Available at: http://link.springer.com/10.1007/BF03033366 [Accessed

September 13, 2018].

Pearn, J., 1978. Incidence, prevalence, and gene frequency studies of chronic childhood spinal muscular atrophy. *Journal of medical genetics*, 15(6), pp.409–13. Available at: http://www.ncbi.nlm.nih.gov/pubmed/745211 [Accessed July 25, 2018].

Pellizzoni, L. et al., 1998. A Novel Function for SMN, the Spinal Muscular Atrophy Disease Gene Product, in Pre-mRNA Splicing. *Cell*, 95(5), pp.615–624. Available at: http://www.sciencedirect.com/science/article/pii/S0092867400816323 [Accessed October 20, 2015].

Pérez-García, M.J. et al., 2017. Developmental Aspects and Pathological Findings in Spinal Muscular Atrophy. In *Spinal Muscular Atrophy*. Elsevier, pp. 21–42. Available at: https://linkinghub.elsevier.com/retrieve/pii/B9780128036853000021 [Accessed September 13, 2018].

Ploner, C., Kofler, R. & Villunger, A., 2008. Noxa: at the tip of the balance between life and death. *Oncogene*, 27 Suppl 1(Suppl 1), pp.S84-92. Available at: http://www.ncbi.nlm.nih.gov/pubmed/19641509 [Accessed October 25, 2018].

Porrero, C. et al., 2010. Mapping of fluorescent protein-expressing neurons and axon pathways in adult and developing Thy1-eYFP-H transgenic mice. *Brain research*, 1345, pp.59–72. Available at: http://www.sciencedirect.com/science/article/pii/S0006899310012424 [Accessed April 25, 2016].

Powis, R.A. et al., 2016. Systemic restoration of UBA1 ameliorates disease in spinal muscular atrophy. *JCI insight*, 1(11), p.e87908. Available at: http://www.ncbi.nlm.nih.gov/pubmed/27699224 [Accessed November 23, 2018].

Powis, R.A. & Gillingwater, T.H., 2016. Selective loss of alpha motor neurons with sparing of gamma motor neurons and spinal cord cholinergic neurons in a mouse model of spinal muscular atrophy. *Journal of anatomy*, 228(3), pp.443–51. Available at: http://www.ncbi.nlm.nih.gov/pubmed/26576026 [Accessed August 13, 2018].

Prior, T.W. et al., 2009. A positive modifier of spinal muscular atrophy in the SMN2 gene. *American journal of human genetics*, 85(3), pp.408–13. Available at: http://www.ncbi.nlm.nih.gov/pubmed/19716110 [Accessed October 16, 2018].

Raoul, C., Henderson, C.E. & Pettmann, B., 1999. Programmed cell death of embryonic motoneurons triggered through the Fas death receptor. *The Journal of cell biology*, 147(5), pp.1049–62. Available at: http://www.ncbi.nlm.nih.gov/pubmed/10579724 [Accessed October 25, 2018].

Robbins, K.L. et al., 2014. Defining the therapeutic window in a severe animal model of spinal muscular atrophy. *Human Molecular Genetics*, 23(17), pp.4559–4568. Available at: https://academic.oup.com/hmg/article-lookup/doi/10.1093/hmg/ddu169 [Accessed August 13, 2018].

Rochette, C., Gilbert, N. & Simard, L., 2001. SMN gene duplication and the emergence of the SMN2 gene occurred in distinct hominids: SMN2 is unique to Homo sapiens. *Human Genetics*, 108(3), pp.255–266. Available at: http://link.springer.com/10.1007/s004390100473 [Accessed August 13, 2018].

Roos, W.P. & Kaina, B., 2006. DNA damage-induced cell death by apoptosis. *Trends in Molecular Medicine*, 12(9), pp.440–450. Available at: https://www.sciencedirect.com/science/article/pii/S1471491406001687?via%3Dihub#bib62 [Accessed August 28, 2018].

Roy, N. et al., 1995. The gene for neuronal apoptosis inhibitory protein is partially deleted in individuals with spinal muscular atrophy. *Cell*, 80(1), pp.167–178. Available at: http://www.sciencedirect.com/science/article/pii/0092867495904611 [Accessed May 18, 2015].

Rudnik-Schoneborn, S. et al., 2008. Congenital heart disease is a feature of severe infantile spinal muscular atrophy. *Journal of Medical Genetics*, 45(10), pp.635–638. Available at: http://jmg.bmj.com/content/45/10/635.long [Accessed October 20, 2015].

Sanes, J.R. & Lichtman, J.W., 2001. Induction, assembly, maturation and maintenance of a postsynaptic apparatus. *Nature Reviews Neuroscience*, 2(11), pp.791–805. Available at: http://www.nature.com/articles/35097557 [Accessed August 13, 2018].

Sareen, D. et al., 2012. Inhibition of Apoptosis Blocks Human Motor Neuron Cell Death in a Stem Cell Model of Spinal Muscular Atrophy T. H. Gillingwater, ed. *PLoS ONE*, 7(6), p.e39113. Available at: http://dx.plos.org/10.1371/journal.pone.0039113 [Accessed September 3, 2018].

Sato, K. et al., 2000. Regions essential for the interaction between Bcl-2 and SMN, the spinal muscular atrophy disease gene product. *Cell Death & Differentiation*, 7(4), pp.374–383. Available at: http://www.nature.com/articles/4400660 [Accessed September 3, 2018].

Schaefer, A.M., Sanes, J.R. & Lichtman, J.W., 2005. A compensatory subpopulation of motor neurons in a mouse model of amyotrophic lateral sclerosis. *The Journal of Comparative Neurology*, 490(3), pp.209–219. Available at: http://

www.ncbi.nlm.nih.gov/pubmed/16082680 [Accessed September 13, 2018].

Schmid, A. & DiDonato, C.J., 2007. Animal Models of Spinal Muscular Atrophy. *Journal of Child Neurology*, 22(8), pp.1004–1012. Available at: http://journals.sagepub.com/doi/10.1177/0883073807305667 [Accessed August 13, 2018].

ScholarRock, 2017. SRK-015 for Spinal Muscular Atrophy (SMA). Available at: http://www.scholarrock.com/pipeline/srk-015-for-sma/intro/ [Accessed August 13, 2018].

Schrank, B. et al., 1997. Inactivation of the survival motor neuron gene, a candidate gene for human spinal muscular atrophy, leads to massive cell death in early mouse embryos. *Proceedings of the National Academy of Sciences of the United States of America*, 94(18), pp.9920–5. Available at: http://www.ncbi.nlm.nih.gov/pubmed/9275227 [Accessed July 25, 2018].

Schreml, J. et al., 2013. Severe SMA mice show organ impairment that cannot be rescued by therapy with the HDACi JNJ-26481585. *European journal of human genetics : EJHG*, 21(6), pp.643–52. Available at: http://www.ncbi.nlm.nih.gov/pubmed/23073311 [Accessed October 22, 2018].

Shababi, M., Lorson, C.L. & Rudnik-Schöneborn, S.S., 2014. Spinal muscular atrophy: a motor neuron disorder or a multi-organ disease? *Journal of anatomy*, 224(1), pp.15–28. Available at: http://www.ncbi.nlm.nih.gov/pubmed/23876144 [Accessed August 13, 2018].

Shafey, D., Côté, P.D. & Kothary, R., 2005. Hypomorphic Smn knockdown C2C12 myoblasts reveal intrinsic defects in myoblast fusion and myotube morphology. *Experimental Cell Research*, 311(1), pp.49–61. Available at: http://www.ncbi.nlm.nih.gov/pubmed/16219305 [Accessed February 26, 2019].

Shanmugarajan, S. et al., 2009. Bone loss in survival motor neuron (Smn(-/-) SMN2) genetic mouse model of spinal muscular atrophy. *The Journal of pathology*, 219(1), pp.52–60. Available at: http://www.ncbi.nlm.nih.gov/pubmed/19434631 [Accessed October 19, 2018].

Sharma, A., Singh, K. & Almasan, A., 2012. Histone H2AX phosphorylation: a marker for DNA damage. *Methods in molecular biology (Clifton, N.J.)*, 920, pp.613–26. Available at: http://www.ncbi.nlm.nih.gov/pubmed/22941631 [Accessed July 27, 2015].

Shorrock, H.K., Gillingwater, T.H. & Groen, E.J.N., 2018. Overview of Current Drugs and Molecules in Development for Spinal Muscular Atrophy Therapy. *Drugs*, 78(3), pp.293–305. Available at:

http://www.ncbi.nlm.nih.gov/pubmed/29380287 [Accessed August 13, 2018].

Simic, G. et al., 2000. Ultrastructural Analysis and TUNEL Demonstrate Motor Neuron Apoptosis in Werdnig-Hoffmann Disease. *Journal of Neuropathology & Experimental Neurology*, 59(5), pp.398–407. Available at: https://academic.oup.com/jnen/article-lookup/doi/10.1093/jnen/59.5.398 [Accessed September 3, 2018].

Simon, C.M. et al., 2010. Ciliary neurotrophic factor-induced sprouting preserves motor function in a mouse model of mild spinal muscular atrophy. *Human molecular genetics*, 19(6), pp.973–86. Available at: http://www.ncbi.nlm.nih.gov/pubmed/20022887 [Accessed August 23, 2015].

Simon, C.M. et al., 2017. Converging Mechanisms of p53 Activation Drive Motor Neuron Degeneration in Spinal Muscular Atrophy. *Cell Reports*, 21(13), pp.3767–3780. Available at: https://www.sciencedirect.com/science/article/pii/S2211124717317990?via%3Dihub [Accessed September 3, 2018].

Singh, N.N., Howell, M.D. & Singh, R.N., 2017. Transcriptional and Splicing Regulation of Spinal Muscular Atrophy Genes. *Spinal Muscular Atrophy*, pp.75–97. Available at: https://www.sciencedirect.com/science/article/pii/B9780128036853000057 [Accessed November 12, 2018].

Slack, J.R., Hopkins, W.G. & Pockett, S., 1983. Evidence for a motor nerve growth factor. *Muscle & Nerve*, 6(4), pp.243–252. Available at: http://www.ncbi.nlm.nih.gov/pubmed/6866006 [Accessed September 13, 2018].

Slack, J.R., Hopkins, W.G. & Williams, M.N., 1979. Nerve sheaths and motoneurone collateral sprouting. *Nature*, 282(5738), pp.506–507. Available at: http://dx.doi.org/10.1038/282506a0 [Accessed November 2, 2015].

Sleigh, J.N., Gillingwater, T.H. & Talbot, K., 2011. The contribution of mouse models to understanding the pathogenesis of spinal muscular atrophy. *Disease models & mechanisms*, 4(4), pp.457–67. Available at: http://www.ncbi.nlm.nih.gov/pubmed/21708901 [Accessed August 13, 2018].

Sleigh, J.N. et al., 2014. Morphological analysis of neuromuscular junction development and degeneration in rodent lumbrical muscles. *Journal of neuroscience methods*, 227, pp.159–65. Available at: http://www.sciencedirect.com/science/article/pii/S0165027014000582 [Accessed April 7, 2016].

Soler-Botija, C. et al., 2002. Neuronal death is enhanced and begins during foetal development in type I spinal muscular atrophy spinal cord. *Brain*, 125(7), pp.1624–1634. Available at: https://academic.oup.com/brain/article-

lookup/doi/10.1093/brain/awf155 [Accessed September 10, 2018].

Somers, E. et al., 2016. Vascular Defects and Spinal Cord Hypoxia in Spinal Muscular Atrophy. *Annals of Neurology*, 79(2), pp.217–230. Available at: http://doi.wiley.com/10.1002/ana.24549 [Accessed October 22, 2018].

Statland, J.M. et al., 2015. Primary Lateral Sclerosis. *Neurologic clinics*, 33(4), pp.749–60. Available at: http://www.ncbi.nlm.nih.gov/pubmed/26515619 [Accessed September 3, 2018].

Sumner, C.J. et al., 2003. Valproic acid increases SMN levels in spinal muscular atrophy patient cells. *Annals of Neurology*, 54(5), pp.647–654. Available at: http://doi.wiley.com/10.1002/ana.10743 [Accessed November 13, 2018].

Sunyach, C. et al., 2012. Olesoxime delays muscle denervation, astrogliosis, microglial activation and motoneuron death in an ALS mouse model. *Neuropharmacology*, 62(7), pp.2346–2353. Available at: https://www.sciencedirect.com/science/article/pii/S0028390812000743 [Accessed August 13, 2018].

Swoboda, K.J. et al., 2009. Phase II Open Label Study of Valproic Acid in Spinal Muscular Atrophy B. D. McCabe, ed. *PLoS ONE*, 4(5), p.e5268. Available at: http://dx.plos.org/10.1371/journal.pone.0005268 [Accessed August 13, 2018].

Szunyogova, E. et al., 2016. Survival Motor Neuron (SMN) protein is required for normal mouse liver development. *Scientific Reports*, 6(1), p.34635. Available at: http://www.nature.com/articles/srep34635 [Accessed October 22, 2018].

Talbot, K., 2002. Motor neurone disease. *Postgraduate medical journal*, 78(923), pp.513–9. Available at: http://www.ncbi.nlm.nih.gov/pubmed/12357010 [Accessed July 25, 2018].

Taylor, J.E. et al., 1998. Correlation of SMNt and SMNc gene copy number with age of onset and survival in spinal muscular atrophy. *European Journal of Human Genetics*, 6(5), pp.467–474. Available at: http://www.nature.com/articles/5200210 [Accessed July 25, 2018].

Thomson, A.K. et al., 2017. Survival of motor neurone protein is required for normal postnatal development of the spleen. *Journal of Anatomy*, 230(2), pp.337–346. Available at: http://doi.wiley.com/10.1111/joa.12546 [Accessed October 22, 2018].

Thomson, S.R. et al., 2012. Morphological characteristics of motor neurons do not determine their relative susceptibility to degeneration in a mouse model of severe spinal muscular atrophy. *PloS one*, 7(12), p.e52605. Available at:

http://www.ncbi.nlm.nih.gov/pubmed/23285108 [Accessed August 13, 2018].

Tsai, M.S. et al., 2006a. Abolishing Bax-Dependent Apoptosis Shows Beneficial Effects on Spinal Muscular Atrophy Model Mice. *Molecular Therapy*, 13(6), pp.1149–1155. Available at: https://www.sciencedirect.com/science/article/pii/S1525001606000530?via%3Dihub [Accessed September 3, 2018].

Tsai, M.S. et al., 2006b. Abolishing Trp53-dependent apoptosis does not benefit spinal muscular atrophy model mice. *European Journal of Human Genetics*, 14(3), pp.372–375. Available at: http://www.nature.com/articles/5201556 [Accessed September 10, 2018].

Udina, E. et al., 2017. Compensatory axon sprouting for very slow axonal die-back in a transgenic model of spinal muscular atrophy type III. *The Authors. The Journal of Physiology C*, 595, pp.1815–1829. Available at: https://www.ncbi.nlm.nih.gov/pmc/articles/PMC5330916/pdf/TJP-595-1815.pdf [Accessed September 18, 2018].

Valori, C.F. et al., 2010. Systemic delivery of scAAV9 expressing SMN prolongs survival in a model of spinal muscular atrophy. *Science translational medicine*, 2(35), p.35ra42. Available at: http://www.ncbi.nlm.nih.gov/pubmed/20538619 [Accessed August 13, 2018].

Verhaart, I.E.C. et al., 2017. A multi-source approach to determine SMA incidence and research ready population. *Journal of neurology*, 264(7), pp.1465–1473. Available at: http://www.ncbi.nlm.nih.gov/pubmed/28634652 [Accessed July 25, 2018].

Vidal, M. et al., 1990. Tissue-specific control elements of the Thy-1 gene. *The EMBO journal*, 9(3), pp.833–40. Available at: http://www.ncbi.nlm.nih.gov/pubmed/1968831 [Accessed September 13, 2018].

Vila, M. & Przedborski, S., 2003. Targeting programmed cell death in neurodegenerative diseases. *Nature Reviews Neuroscience*, 4(5), pp.365–375. Available at: http://www.nature.com/articles/nrn1100 [Accessed August 27, 2018].

Vitte, J.M. et al., 2004. Deletion of murine Smn exon 7 directed to liver leads to severe defect of liver development associated with iron overload. *The American journal of pathology*, 165(5), pp.1731–41. Available at: http://www.ncbi.nlm.nih.gov/pubmed/15509541 [Accessed October 22, 2018].

Vyas, S. et al., 2002. Involvement of survival motor neuron (SMN) protein in cell death. *Human Molecular Genetics*, 11(22), pp.2751–2764. Available at:

https://academic.oup.com/hmg/article-lookup/doi/10.1093/hmg/11.22.2751 [Accessed September 3, 2018].

Wang, C.H. et al., 2007. Consensus Statement for Standard of Care in Spinal Muscular Atrophy Current Problems in the Medical Care of Patients With Spinal Muscular Atrophy Spinal muscular atrophy is a recessively inherited neuro-muscular disease characterized by degeneration of spinal. *Journal of Child Neurology*, 22, pp.1027–1049. Available at: http://jcn.sagepub.comhttp//online.sagepub.com [Accessed October 22, 2018].

Wang, W. et al., 2005. Increased susceptibility of spinal muscular atrophy fibroblasts to camptothecin-induced cell death. *Molecular Genetics and Metabolism*, 85(1), pp.38–45. Available at: https://www.sciencedirect.com/science/article/pii/S109671920500003X [Accessed September 3, 2018].

Williams, A.B. & Schumacher, B., 2016. p53 in the DNA-Damage-Repair Process. *Cold Spring Harbor perspectives in medicine*, 6(5). Available at: http://www.ncbi.nlm.nih.gov/pubmed/27048304 [Accessed August 28, 2018].

Wirth, B., Brichta, L. & Hahnen, E., 2006. Spinal Muscular Atrophy: From Gene to Therapy. *Seminars in Pediatric Neurology*, 13(2), pp.121–131. Available at: https://www.sciencedirect.com/science/article/pii/S1071909106000982?via%3Dihub [Accessed July 25, 2018].

Wood, M.J.A., Talbot, K. & Bowerman, M., 2017. Spinal muscular atrophy: antisense oligonucleotide therapy opens the door to an integrated therapeutic landscape. *Human Molecular Genetics*, 26(R2), pp.R151–R159. Available at: http://academic.oup.com/hmg/article/26/R2/R151/3867126/Spinal-muscular-atrophy-antisense-oligonucleotide [Accessed October 22, 2018].

Wu, D. & Hersh, L.B., 1994. Choline acetyltransferase: celebrating its fiftieth year. *Journal of neurochemistry*, 62(5), pp.1653–63. Available at: http://www.ncbi.nlm.nih.gov/pubmed/8158117 [Accessed October 25, 2018].

Yong, C.S.M. et al., 2015. Embryonic Lethality in Homozygous Human Her-2 Transgenic Mice Due to Disruption of the Pds5b Gene J. P. Lydon, ed. *PLOS ONE*, 10(9), p.e0136817. Available at: https://dx.plos.org/10.1371/journal.pone.0136817 [Accessed November 23, 2018].

Young, P.J. et al., 2002. A Direct Interaction between the Survival Motor Neuron Protein and p53 and Its Relationship to Spinal Muscular Atrophy*. Available at: http://www.jbc.org/ [Accessed August 29, 2018].

Yuan, A. et al., 2012. Neurofilaments at a glance. *Journal of cell science*, 125(Pt

14), pp.3257–63. Available at: http://www.ncbi.nlm.nih.gov/pubmed/10523515 [Accessed September 10, 2018].

Zerres, K. & Rudnik-Schöneborn, S., 1995. Natural History in Proximal Spinal Muscular Atrophy. *Archives of Neurology*, 52(5), p.518. Available at: http://archneur.jamanetwork.com/article.aspx?doi=10.1001/archneur.1995.00540290108025 [Accessed July 25, 2018].

Zhang, H.L. et al., 2003. Active transport of the survival motor neuron protein and the role of exon-7 in cytoplasmic localization. *The Journal of neuroscience : the official journal of the Society for Neuroscience*, 23(16), pp.6627–37. Available at: http://www.ncbi.nlm.nih.gov/pubmed/12878704 [Accessed August 13, 2018].